2025-08-13

Computational Modeling of Magnetic Field Interaction with Superconductors Under High-Field and High-Dissipation Conditions: A TDGL Approach Applied to Nb and Nb3Sn

Aiden Victor Harbick
Brigham Young University

Computational Modeling of Magnetic Field Interaction with Superconductors Under High-Field and High-Dissipation Conditions: A TDGL Approach Applied to Nb and Nb_3Sn

Aiden Victor Harbick

A dissertation submitted to the faculty of
Brigham Young University
in partial fulfillment of the requirements for the degree of

Doctor of Philosophy

Mark Transtrum, Chair
Sam Posen
Benjamin Frandsen
David Neilsen
Blake Barker

Department of Physics and Astronomy

Brigham Young University

ABSTRACT

Computational Modeling of Magnetic Field Interaction with Superconductors
Under High-Field and High-Dissipation Conditions:
A TDGL Approach Applied to Nb and Nb_3Sn

Aiden Victor Harbick
Department of Physics and Astronomy, BYU
Doctor of Philosophy

Superconducting radiofrequency (SRF) cavities are essential components in modern particle accelerators, enabling the efficient acceleration of charged particles for various applications in physics, medicine, materials science, and beyond. The performance of these cavities is significantly influenced by the properties of superconducting materials, such as niobium (Nb) and triniobium-tin (Nb_3Sn), and the defects and surface features present within the material. This dissertation presents a computational study focused on understanding the behavior of SRF cavities, using a sample-specific time-dependent Ginzburg-Landau (TDGL) framework to simulate their performance under realistic material conditions. The research integrates experimental data and density functional theory (DFT) calculations to model the impact of various defects, including hydrides, Sn-deficient islands, grain boundaries, and surface roughness. The calculations reveal how these defects contribute to performance degradation, particularly in terms of dissipation and quality factor (Q). We also investigate the impact of surface layers and roughness on the behavior of Nb_3Sn, finding that surface features play a significant role in influencing cavity performance. In addition, the dissertation explores the generalized TDGL (GTDGL) model, which offers an extension to traditional TDGL theory and enables improved predictions of frequency-dependent phenomena. This work contributes to the development of more accurate computational tools for analyzing SRF cavity performance, providing insights that can guide future efforts in material optimization and accelerator technology.

Keywords: computational, superconductivity, SRF cavities, niobium, Nb3Sn, time-dependent Ginzburg-Landau, TDGL, mesoscopic behavior, material defects, Sn-deficient islands, grain boundaries, surface roughness, quality factor, high-field Q-slope, superheating field, finite element modeling, SRF performance, vortex nucleation, accelerator technology

ACKNOWLEDGMENTS

There are many people throughout my journey to completing this dissertation who deserve my thanks. I can't possibly name them all, but I will do my best to name as many as I can while still meeting the 1-page requirement for this section. First and foremost, I would like to thank my advisor, Mark Transtrum, without whom my life would most likely look completely different right now. From initially agreeing to work with me through BYU's REU program in 2018, offering to let me continue working with him for my senior honors thesis at Willam & Mary, to being my PhD advisor, Mark has been a consistent source of wisdom and encouragement for me, and I really admire the perspective with which he views science and the world in general. I would like to thank my closest CBB collaborators, Nathan Sitaraman, Sarah Willson, and Michelle Kelley. I learned a lot about SRF cavities, superconductors, DFT, chemstry, and beyond from their insights and intuitions and I really appreciated every conversation we had as a part of our collaborations. I want to thank Ritchie Patterson and Joan Curtis for all their help and encouragment with anything CBB related. I would also like to thank the rest of my CBB collaborators, past and present, and particularly those in the SRF theme: Tomàs Arias, Zhaslan Baraissov, Jasper Brown, Robert Burnley, Van Do, Sam Dong, Michal Van Duinen, Rachael Farber, Ben Francis, Gabriel Gaitan, Richard Hennig, Ajinkya Hire, Matthias Liepe, Crisobal Mendez, David Mueller, Thomas Oseroff, Ryan Porter, Sadie Seddon-Stettler, Liana Shpani, Steven Sibener, Zeming Sun, and Caleb Thompson (and I appologize if I missed any names!). Special thanks to my fellow Transtrum group member, Yonatan Kurniawan, for rooming with me at conferences and explaining mahine learned interatomic potentials and uncertainty quantification to me. I want to thank my committee members, Sam Posen, Ben Frandsen, David Neilsen, and Blake Barker for their feedback on my work and their reviews of this dissertation. I also want to thank my wife, Elise, for her ever present love, support, and patience. Finally, I thank my parents, Andrew and Shiree Harbick, who more than anyone else have helped guide me as I have grown into the person I am today.

Contents

List of Figures

List of Tables

Chapter 1

Introduction

The development of particle accelerators has been a cornerstone in advancing our understanding of fundamental physics and enabling numerous technological breakthroughs. From the earliest cyclotrons to the cutting-edge linear accelerators (linacs) of today, these devices have enabled scientists to probe the subatomic world, leading to revolutionary discoveries in particle physics [1], medicine [2, 3], and materials science [4]. Central to the functionality of many modern particle accelerators are superconducting radio-frequency (SRF) cavities, which allow for efficient particle acceleration by minimizing energy loss through their surface resistance, or lack thereof. These cavities, made from high-performance superconducting materials, are critical components in both traditional accelerator systems, such as the Large Hadron Collider (LHC) at CERN, and more modern X-ray Free Electron Lasers (XFELs), such as the LCLS-II at SLAC, which have become indispensable tools for advancing modern materials research. Despite their importance, the performance of SRF cavities is often hindered by issues such as surface defects and material limitations. In this dissertation, we explore the computational modeling of superconducting materials, particularly

Nb_3Sn, to better understand the factors influencing SRF cavity performance. Our work builds on established theories of superconductivity, notably the time-dependent Ginzburg-Landau (TDGL) framework, and aims to provide new insights into how material properties can be optimized to enhance the efficiency and reliability of SRF cavities.

1.1 Brief Overview of Superconductivity

To follow the discussions in this dissertation, it's helpful to have a basic understanding of some key aspects of superconductivity. To make this work more accessible to a wider audience, this section provides a brief overview of the important discoveries and theories in the field. This should provide enough context for readers who may not be as familiar with superconductivity and allow them to better engage with the material that follows.

Superconductivity is characterized by two key phenomena that emerge when a material is cooled below its critical temperature, T_c: resistance-free supercurrent flow (first discovered by Kamerlingh Onnes in 1911 [5]), and perfect diamagnetism, known as the Meissner effect, discovered by Walther Meissner and Robert Ochsenfeld in 1933 [6]. In the context of SRF research—central to this dissertation—the first of these phenomena is a key advantage, while the second can, in certain cases, be a limitation. The ability of superconductors to support resistance-free current is what allows SRF cavities to operate with remarkable efficiency. A key figure of merit for these cavities, which we will explore in detail later, is the cavity quality factor, Q, defined as the ratio of the energy stored in the cavity to the energy dissipated in the cavity walls during each RF period. For comparison, a typical copper (normal-conducting) RF cavity might have $Q \approx 10^5$, whereas a niobium SRF cavity—the current industry standard—typically has $Q \approx 10^{10}$ [7]. The Meissner effect, on the other hand, imposes a limitation in that superconductivity requires the material to maintain its diamagnetic state. If an external magnetic field becomes strong enough to overcome the Meissner effect, the material

could transition to a normal conducting state. As the accelerating fields in SRF cavities increase, the magnetic field that must be screened by the Meissner effect also becomes larger, and if this field surpasses a critical threshold, superconductivity may be lost. Therefore, understanding the critical fields of the SRF material is crucial to assessing the performance of a cavity.

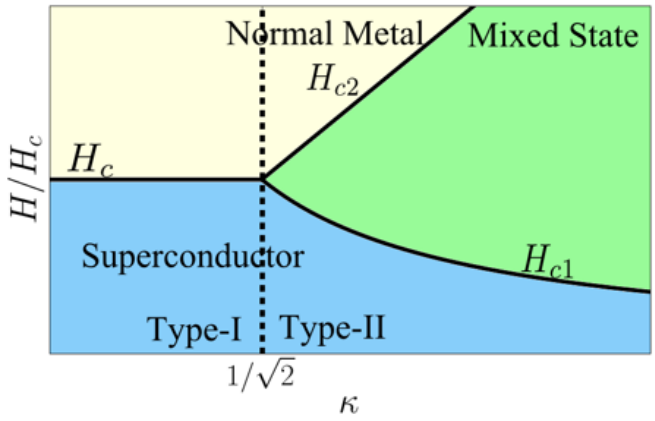

Figure 1.1 A phase diagram for different superconductors at zero temperature (below their T_c). The x-axis represents materials with varying values of κ, the Ginzburg-Landau parameter. The phase boundaries separate superconducting (Meissner), mixed, and normal conducting states. The $\kappa = 1/\sqrt{2}$ value divides Type I and Type II superconductors.

Figure 1.1 shows the phase diagram of superconductors at zero temperature, where different values on the x-axis represent materials with varying Ginzburg-Landau parameters, κ. This parameter is the ratio of a material's penetration depth to its coherence length, which we will discuss in more detail later. For now, κ serves as a parameter that characterizes different superconducting materials. The value $\kappa = 1/\sqrt{2}$ marks the boundary between two types of superconductors. Superconductors with $\kappa < 1/\sqrt{2}$ are classified as Type I, while those with $\kappa > 1/\sqrt{2}$ are Type II. Type I superconductors have a single critical field H_c (the thermodynamic critical field) that separates the superconducting (Meissner) state from the normal conducting state. Type II superconductors, on the other hand, exhibit two critical fields: H_{c1} and H_{c2}, known as the lower and upper critical fields, respectively. Below H_{c1}, the material remains in the Meissner state. Between H_{c1} and H_{c2} lies a new

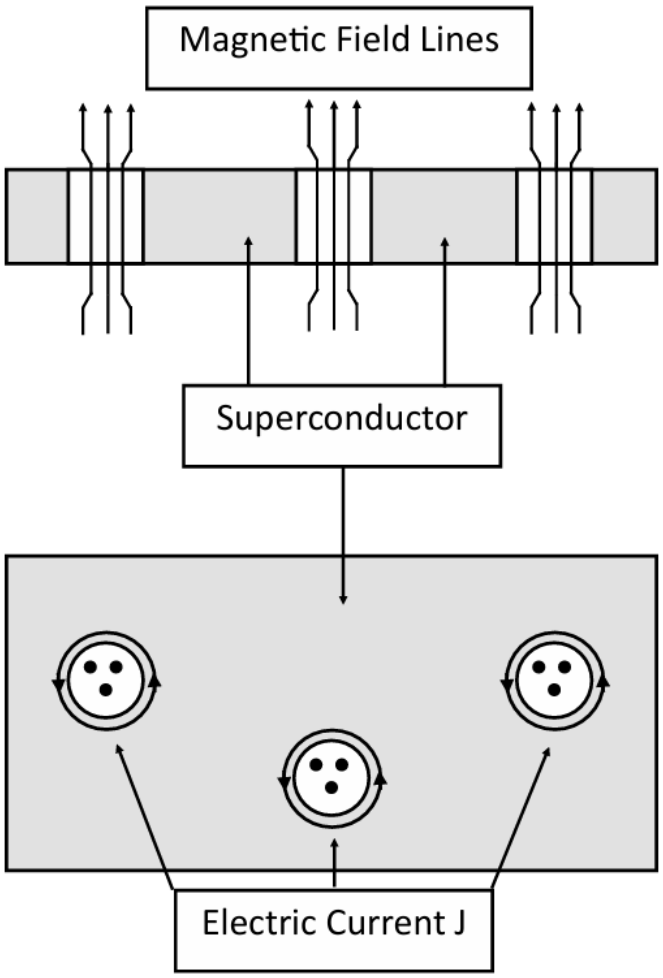

Figure 1.2 A diagram of vortices in a type II superconductor. This figure is borrowed with permission from Alden Pack's masters thesis [8].

mixed state (also referred to as the Abrikosov state), where magnetic flux vortices can penetrate the material. These vortices are regions of magnetic flux where the field lines pass through the material, and supercurrents flow around them in a circular motion. Figure 1.2 illustrates these vortices. The center of the vortices will be locally normal conducting, while the surrounding material can remain superconducting due to the screening of the field by the supercurrents. Above H_{c2}, the material transitions to the normal conducting state. This dissertation will primarily focus on Type II superconductors, as niobium (Nb) and all potential materials for SRF cavity replacements are Type II superconductors. The mixed state, while an interesting phenomenon, presents challenges for SRF cavities since vortex motion leads to energy dissipation [9], causing localized heating and a decrease in the cavity's quality factor. Consequently, it is essential to study methods that keep the material in the vortex-free Meissner state for optimal SRF performance.

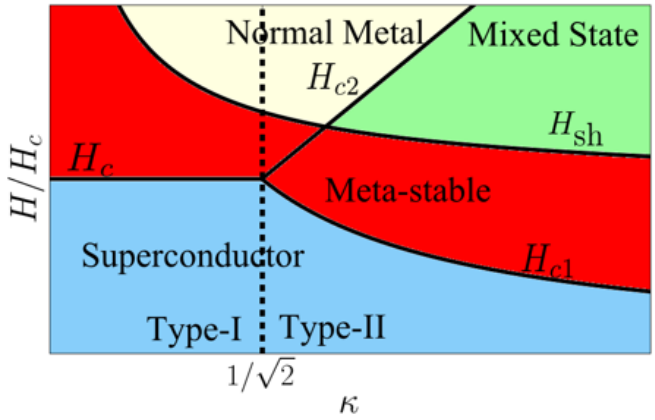

Figure 1.3 An updated phase diagram for different superconductors at zero temperature (below their T_c), incorporating the metastable Meissner state. The x-axis represents materials with different values of κ. The phases are separated into superconducting (Meissner), mixed, metastable, and normal conducting states. The metastable Meissner state is stable above H_{c1}, but can transition to the mixed state above the superheating field, H_{sh}.

While keeping SRF cavity materials in the Meissner state is crucial for performance, the limiting field for SRF cavities is not H_{c1}, as the Meissner state can remain metastable above this field. Figure 1.3 shows an updated phase diagram that includes the metastable state. The Meissner state is locally stable above H_{c1} because there is an energy barrier that prevents the formation of vortices. However, this state becomes unstable when the external magnetic field exceeds a certain threshold, known as the "superheating" field, H_{sh} [10]. The metastable Meissner state is not merely a theoretical concept; many high-power SRF cavities operate within this regime [11]. The superheating field, H_{sh}, serves as the fundamental upper limit for SRF cavity performance. Even in the absence of defects, a pristine SRF cavity will nucleate vortices once the applied magnetic field reaches this critical value.

We now continue our discussion of superconductivity by outlining some important theoretical models. Broadly, superconductivity theories can be divided into two categories: phenomenological theories, which aim to model the observed behaviors of superconductors without delving into the microscopic details, and “microscopic" theories, which attempt to derive models based on first-principles calculations of the underlying physics. The earliest phenomenological theory of superconductivity was the London model [12], developed by Heinz and Fritz London in 1935. This theory incorporated the qualitative features observed by Meissner and Ochsenfeld [6], using Maxwell’s equations to model the decay of the magnetic field beneath the surface of a superconductor. Around the same time, Gorter and Casimir [13] proposed one of the first microscopic theories of superconductivity, now known as the “two-fluid model." This model describes the superconducting state as a superposition of two non-interacting “fluids" of electrons: the normal electrons, which behave like those in any other metal, and the superconducting electrons, which flow with no resistance. Although the two-fluid model lacks a detailed microscopic explanation for the behavior of superconducting electrons, it is often considered one of the first attempts at a microscopic theory.

The most influential phenomenological model is likely the Ginzburg-Landau (GL) theory [14], first published in 1950. Using Lev Landau's theory of second-order phase transitions, GL theory defines an expansion of the superconductor's free energy with respect to the superconducting order parameter, ψ, and the magnetic vector potential, $\mathbf{A}$. This leads to the famous Ginzburg-Landau equations. In this framework, the complex order parameter ψ describes the density of superconducting electrons, with $|\psi|^2$ corresponding to the density of these electrons. The GL theory remains the most widely used phenomenological model and has served as the foundation for many subsequent theories, some of which are central to this dissertation.

However, the most significant development in superconductivity theory is probably the BCS theory [15]. Developed by John Bardeen, Leon Cooper, and John Schrieffer in 1957, BCS theory is the first fully microscopic theory of superconductivity, for which the authors were awarded the 1972 Nobel Prize in Physics. BCS theory describes the formation of Cooper pairs—electron pairs that interact via an effective attractive interaction, allowing them to condense into the ground state, forming a Bose-Einstein condensate. This theory successfully explains many key features of superconductivity, such as zero resistance, the Meissner effect, the existence of a band gap at the Fermi level, and the characteristic heat capacity spike at the superconducting transition. BCS theory also led to a deeper understanding of the GL theory when Lev Gor'Kov derived GL theory from BCS in 1959 [16]. Following Gor'Kov's work, an early calculation by Schmid [17] in 1966 and the subsequent development of the time-dependent Ginzburg-Landau (TDGL) theory by Gor'Kov and Eliashberg [18] further advanced the field. TDGL theory, which is the focus of much of this dissertation, will be discussed in more detail in a later section.

The theoretical study of superconductivity is rich and complex, with BCS theory representing just the beginning of a revolution in the field. Many theories beyond BCS and TDGL have furthered our understanding, such as the work by Eliashberg [19], Larkin and Ovchinnikov [20], Eilenberger [21], and Usadel [22]. However, the primary focus of this work is on the TDGL framework, along with

certain aspects of BCS theory, and we will therefore restrict our discussion to these theories for now. With this theoretical context in mind, we will now turn to a more detailed discussion of the Ginzburg-Landau and time-dependent Ginzburg-Landau theories, as they form the foundation for much of the analysis in this dissertation.

1.2 Ginzburg-Landau Theory

In this section, we will explore Ginzburg-Landau (GL) theory and, later, time-dependent Ginzburg-Landau (TDGL) theory in more detail, as these theories form the foundation for much of the work presented in this dissertation. The content here is primarily informed by two key textbooks: *Introduction to Superconductivity* by Michael Tinkham [23] and *Theory of Nonequilibrium Superconductivity* by Nikolai Kopnin [24]. While we will present the information relevant to this work, readers are encouraged to consult these excellent resources for a more comprehensive treatment of the subject.

GL theory begins with an expression for the free energy of the superconductor, expanded in powers of $|\psi|^2$, in Gaussian units:

$$f = f_{n0} + \alpha|\psi|^2 + \frac{\beta}{2}|\psi|^4 + \frac{1}{2m^*}\left|\left(\frac{\hbar}{i}\nabla - \frac{e^*}{c}\mathbf{A}\right)\psi\right|^2 + \frac{h^2}{8\pi}, \tag{1.1}$$

where f_{n0} is the free energy in the normal state at zero field, α and β are phenomenological parameters (which will be discussed in more detail later), $m^* = 2m$ and $e^* = 2e$ represent the mass and charge of a Cooper pair, $\hbar$ is the reduced Planck constant, c is the speed of light, and h is the external magnetic field. The primary variables are ψ, the superconducting order parameter, where $|\psi|^2$ gives the density of superconducting electrons, and $\mathbf{A}$, the magnetic vector potential. The parameters α and β determine the shape of the free energy. Notably, β must be positive; if

it were negative, the minimum of the free energy would occur at $|\psi|^2 \to \infty$, which is unphysical. The parameter α governs the location of the minima of f. For $\alpha > 0$, the free energy has a single minimum at $\psi = 0$, while for $\alpha < 0$, two minima exist at $|\psi| = \pm\sqrt{\frac{|\alpha|}{\beta}}$, which we define as $|\psi_\infty|^2 = -\frac{\alpha}{\beta}$.

From these parameters, we can define two important length scales: the penetration depth, λ, and the coherence length, ξ:

$$\lambda^2 = \frac{m^* c^2 \beta}{4\pi e^{*2} |\alpha|}, \tag{1.2}$$

$$\xi^2 = \frac{\hbar^2}{2m^* |\alpha|}. \tag{1.3}$$

The penetration depth, λ, defines the characteristic length scale for variations in $\mathbf{A}$, or the decay length of the magnetic field inside the superconductor. The coherence length, ξ, defines the length scale for variations in ψ and can be thought of as the approximate size of a Cooper pair, although Ginzburg and Landau themselves did not have this specific interpretation when developing their theory. In the mixed state, λ corresponds to the size of the region where supercurrent screens the magnetic field from a vortex, while ξ gives the size of the normal core of the vortex. The ratio of these two length scales is known as the Ginzburg-Landau parameter, $\kappa = \frac{\lambda}{\xi}$, which is a key quantity used to characterize superconducting materials. As we saw in the previous section, κ distinguishes Type I and Type II superconductors, and the critical fields are κ-dependent.

Taking the variation of Equation 1.1 with respect to ψ and $\mathbf{A}$ yields the famous Ginzburg-Landau equations:

$$\alpha\psi + \beta|\psi|^2\psi + \frac{1}{2m^*}\left(\frac{\hbar}{i}\nabla - \frac{e^*}{c}\mathbf{A}\right)^2 \psi = 0, \tag{1.4}$$

$$\frac{c}{4\pi}\nabla \times \nabla \times \mathbf{A} - \frac{e^*\hbar}{2m^* i}\left(\psi^*\nabla\psi - \psi\nabla\psi^*\right) + \frac{e^{*2}}{m^* c}|\psi|^2\mathbf{A} = 0. \tag{1.5}$$

It is common to nondimensionalize these equations, and a detailed derivation of this process can be found in Section A.2 of the appendix. The result of this nondimensionalization is:

$$\left(\frac{-i}{\kappa}\nabla - \mathbf{A}\right)^2 \psi - \psi + |\psi|^2\psi = 0, \tag{1.6}$$

$$\nabla \times \nabla \times \mathbf{A} + \frac{i}{2\kappa}(\psi^*\nabla\psi - \psi\nabla\psi^*) + |\psi|^2\mathbf{A} = 0, \tag{1.7}$$

where distances are measured in units of λ, ψ is in units of ψ_∞, and $\mathbf{A}$ is in units of $\sqrt{2}\lambda H_c$ (with the magnetic field $\mathbf{H}$ expressed in units of $\sqrt{2}H_c$).

To transition to the time-dependent Ginzburg-Landau (TDGL) equations, they can technically be derived following the work of Gor'Kov and Eliashberg [18]. However, a full derivation is beyond the scope of our discussion, so we will present the equations in a more heuristic manner. The TDGL equations can be obtained by setting the variations with respect to the GL free energy equal to time derivatives:

$$\Gamma\left(\frac{\partial\psi}{\partial t} + i\kappa\phi\psi\right) = \frac{\delta f}{\delta\psi^*}, \tag{1.8}$$

$$\sigma_n\left(\frac{\partial\mathbf{A}}{\partial t} + \nabla\phi\right) = \frac{\delta f}{\delta\mathbf{A}}, \tag{1.9}$$

where Γ is the relaxation rate of ψ, σ_n is the normal conductivity, and ϕ is the scalar potential. The terms involving ϕ are included to preserve the gauge invariance of the theory. From these, we obtain the TDGL equations (also dimensionless; see Section A.3 of the appendix for more details):

$$\frac{\partial\psi}{\partial t} + i\kappa\phi\psi + \left(\frac{-i}{\kappa}\nabla - \mathbf{A}\right)^2\psi - \psi + |\psi|^2\psi = 0, \tag{1.10}$$

$$\frac{1}{u}\left(\frac{\partial\mathbf{A}}{\partial t} + \nabla\phi\right) + \nabla\times\nabla\times\mathbf{A} + \frac{i}{2\kappa}(\psi^*\nabla\psi - \psi\nabla\psi^*) + |\psi|^2\mathbf{A} = 0, \tag{1.11}$$

where $u = \frac{\tau_\psi}{\tau_j}$ is the ratio of characteristic timescales, similar to κ. Here, $\tau_\psi = \frac{\Gamma}{|\alpha|}$ is the characteristic timescale for changes in the order parameter, and $\tau_j = \frac{\sigma_n m^*\beta}{e^{*2}|\alpha|}$ is the characteristic timescale for changes in $\mathbf{A}$ (and by extension the current, hence the j notation). In these equations, distances are in units of λ, time is in units of τ_ψ, ψ is in units of ψ_∞, ϕ is in units of $\phi_0 = \frac{\hbar\kappa}{e^*\tau_\psi}$, and $\mathbf{A}$ is in units

of $\sqrt{2}\lambda H_c$. These equations are augmented by the following boundary conditions:

$$\left(\frac{i}{\kappa}\nabla\psi + \mathbf{A}\psi\right)\cdot n = 0, \tag{1.12}$$

$$(\nabla\times\mathbf{A})\times n = \mathbf{H}_a\times n, \tag{1.13}$$

$$\left(\frac{\partial\mathbf{A}}{\partial t} + \nabla\phi\right)\cdot n = 0, \tag{1.14}$$

where n is the unit vector normal to the boundary and $\mathbf{H}_a$ is the applied field. Unless explicitly mentioned otherwise, whenever we solve the TDGL equations, we typically use a finite element method, employing the weak formulation proposed by Gao [25]. We also utilize the open-source finite element package FEniCS [26] for these calculations.

When solving the TDGL equations, it is important to consider their limitations. TDGL is only quantitatively valid at temperatures near the critical temperature, T_c, and for gapless superconductors. The latter condition can be addressed using a generalized TDGL formulation, derived by Kramers and Watts-Tobin [27, 28], which will be covered in Chapter 7. However, compared to TDGL, the solutions to the GL equations have a broader range of validity, especially in the dirty limit. This limit can be approximated by setting the effective mass to:

$$m^* = \frac{12\hbar T_c}{\pi\nu(0)v_f\ell}, \tag{1.15}$$

where $\nu(0)$ is the Fermi level density of states, v_f is the Fermi velocity, and ℓ is the electron mean free path. Under the dirty limit, the steady-state solutions of TDGL correspond to the GL solutions, which have a wider range of validity. Despite the more restrictive quantitative validity of TDGL, it remains a popular tool for studying superconducting phenomena because, while it may lack quantitative precision, the qualitative insights it provides are invaluable for understanding the interactions of mesoscopic material features that would otherwise be computationally prohibitive to simulate with more sophisticated theories of superconductivity.

1.3 SRF Cavities and Nb_3Sn

Superconducting radiofrequency (SRF) cavities are key components in particle accelerators, responsible for the acceleration of charged particles. A diagram of a series of SRF cavities is shown in Figure 1.4. A beam of electrons (or other charged particles) enters through the center of the cavities, where the current flowing axially induces standing electromagnetic waves that accelerate the particles. One consequence of the standing wave pattern is that it also bunches the particles. Particles falling behind receive an extra boost, while particles ahead are slightly pushed back, until the particles are grouped into bunches that are optimally accelerated by the maximum field at the center of each cavity.

To date, niobium (Nb) has been the primary material used for SRF cavities. It is a pure elemental superconductor with the highest critical temperature ($T_c = 9.2$ K) among the elemental superconductors. Nb SRF cavities have been optimized through decades of research and are approaching their fundamental limits. Nb has a superheating field of $\mu_0 H_{sh} \approx 220$ mT, with most high-performance Nb SRF cavities reaching peak fields of around 200 mT. While Nb's relatively high T_c is advantageous compared to other elemental superconductors, Nb cavities must still be operated at approximately 2 K, which incurs significant cryogenic costs. These limitations have led researchers to explore alternative superconducting materials that could potentially surpass Nb's performance.

Table 1.1 lists several candidate materials that have been considered as potential replacements for Nb in SRF cavities. While MgB_2 [29, 30] and NbN [31] have seen some consideration, Nb_3Sn has been the subject of the most extensive study. Nb_3Sn is an A15 superconductor [32], named after its crystal structure, and has several promising characteristics. First, it has a superheating field ($\mu_0 H_{sh} =$ 425 mT) more than twice as large as that of Nb, theoretically enabling it to reach accelerating gradients more than twice as large. Additionally, Nb_3Sn has a higher critical temperature of $T_c = 18$ K, nearly twice that of Nb, allowing it to be operated at 4.2 K, significantly reducing cooling costs.

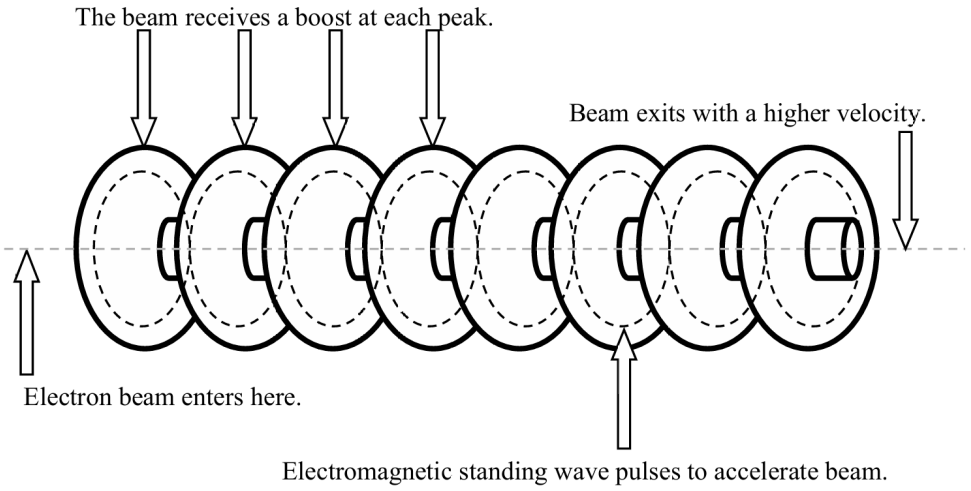

Figure 1.4 A diagram of a line of SRF cavities. An electron beam enters through the center of the cavities, and is accelerated by the standing electric field waves at the center of each cavity. As the electrons pass through the cavities, their energy (and hence speed) increases. This figure is borrowed with permission from Alden Pack's masters thesis [8].

Finally, as we discussed earlier, the efficiency of SRF cavity operation is measured by the quality factor, Q, which is the ratio of the energy stored in the cavity to the energy dissipated in the cavity walls each RF period. Due to the Meissner effect, Q—and thus cavity performance—depends almost entirely on the properties of the thin surface layer of the superconducting material inside the cavity walls. This means that Nb_3Sn cavities can be fabricated by coating the inner surface of an existing Nb cavity with a thin layer of Nb_3Sn, making it a promising alternative to pure Nb.

Most Nb_3Sn cavities are fabricated using the Sn vapor diffusion process [34], in which the cavity is placed in a furnace with a Sn crucible, and the Sn is vaporized and allowed to diffuse into the cavity walls, forming Nb_3Sn. Recently, efforts have been made to develop an electroplating method for Nb_3Sn, which may offer advantages over traditional vapor diffusion methods [35, 36].

Material	$\lambda(T=0)$ [nm]	$\xi(T=0)$ [nm]	$\mu_0 H_{sh}$ [mT]	T_c [K]
Nb	50	22	219	9.2
Nb_3Sn	111	4.2	425	18
MgB_2	185	4.9	170	37
NbN	375	2.9	214	16

Table 1.1 Table of material parameters for superconductors used in SRF cavities. λ is the London penetration depth, ξ is the coherence length, H_{sh} is the superheating field, and T_c is the critical temperature. These values were taken from Reference 33.

While Nb_3Sn holds significant promise, it also has its drawbacks. For one, its coherence length $\xi = 4.2$ nm is much smaller than Nb's, which is around 22 nm. This is problematic because to achieve good performance from the surface layer, material defects need to be controlled down to at least the scale of the coherence length, meaning Nb_3Sn surfaces require much more precise control over their surface features than Nb. Additionally, Nb-Sn systems are highly sensitive to stoichiometry. Even small deviations from the ideal 1:3 ratio in Nb_3Sn can lead to significant degradation in superconducting properties. There are even compositions where the performance is worse than Nb [37, 38]. Furthermore, Nb_3Sn is more brittle than Nb, which increases the likelihood of performance-damaging defects, as well as damage during handling.

Despite these challenges, the potential of Nb_3Sn to outperform Nb has led to significant ongoing research into improving its performance. Although current Nb_3Sn cavities generally underperform their Nb counterparts, with the best-performing Nb_3Sn cavities currently sustaining fields only around 96 mT [39], the promise of ideal Nb_3Sn continues to drive much of the research in this field.

1.4 Research Goals and Dissertation Outline

Now that the context for our research has been established, we can turn to the specific research goals that this dissertation aims to address. When discussing the motivation behind our research, it is essential to consider the broader context in which it is conducted. All the projects presented in this dissertation have, to varying degrees, been funded by and carried out in collaboration with the NSF Center for Bright Beams (CBB). CBB is a National Science Foundation-funded science and technology center with the goal of increasing the brightness of beams used in particle accelerators by a factor of 100, while simultaneously reducing operational costs [40]. CBB's efforts are organized into three main themes: Beam Production, which focuses on the development of photocathodes for electron beam production via the photoelectric effect; Beam Acceleration, which is dedicated to advancing SRF cavity technologies; and Beam Dynamics and Control, which addresses maintaining beam quality as it travels through the complex systems of modern particle accelerators. Our research falls within the Beam Acceleration theme, where we collaborate with five other groups from across the United States.

Several key research questions and goals guided our work. As members of CBB, we have access to a wide range of experts in SRF-related research, including accelerator physicists, condensed matter theorists, and surface chemists. This interdisciplinary collaboration provided us with the opportunity to develop a TDGL framework that integrates knowledge from various fields, such as accelerator physics, condensed matter theory, and surface chemistry. By using experimental materials characterizations and density functional theory (DFT) calculations from condensed matter experts, we could inform the choice of TDGL parameters to simulate sample-specific features. These features may be challenging or impossible to probe experimentally without the use of a mesoscopic-scale computational model.

While Nb_3Sn is one of the central focuses of CBB, our involvement in this collaboration led us to investigate the impact of hydrogen on the surface of Nb SRF cavities. Large hydrogen precipitates, or "hydrides," are already known to cause low-field Q degradation in these cavities, and treatments have been developed to remove these defects. However, recent research has suggested that smaller hydrides may also contribute to Q degradation at high fields, a phenomenon known as high-field Q-slope (HFQS). Motivated by this, we aimed to use our newly developed sample-specific TDGL framework to better understand the mechanisms behind hydride-induced dissipation in Nb SRF cavities.

As discussed in the previous section, Nb_3Sn is one of the most promising next-generation SRF materials. In collaboration with CBB, we sought to investigate the impact of a wide variety of defects that appear on Nb_3Sn surfaces, including excess Sn islands, Sn-deficient regions, surface roughness, grain boundaries, and overall layer structures. Our goal was to understand how these defects affect the performance of Nb_3Sn and contribute to the development of improved growth and treatment procedures that could enhance cavity performance.

Lastly, we aimed to apply a generalized TDGL (GTDGL) model, a theory that has been considered by our group for some time but never fully implemented. Since GTDGL is well-suited for studying non-stationary problems, we used it to investigate the frequency dependence of vortex nucleation in SRF cavities. This allowed us to explore potential benefits—or drawbacks—associated with modifying the frequency of SRF cavity operation.

The remainder of this dissertation is organized as follows. Chapter 2 focuses on the development and application of a sample-specific time-dependent Ginzburg-Landau (TDGL) framework, which forms the core of much of this work. This chapter includes a paper on the topic, which is currently under peer review at *Physical Review B*. In Chapter 3, we delve into the impact of hydrides, on Nb SRF cavities. This chapter contains another paper on the topic, which has been submitted to *Superconductor Science and Technology*. Chapter 4 discusses the role of stoichiometric defects,

as well as some surface roughness, in Nb_3Sn surfaces, and consists of a paper published in *Physical Review Research* on the topic. Chapter 5 explores additional Nb_3Sn defects and features that were studied but did not make it into published work. This includes calculations on grain boundaries and simulations of the Nb_3Sn surface layer. Chapter 6 extends the investigation with multi-domain COMSOL simulations from Chapter 4, exploring important characteristic length scales associated with rough surface features on SRF surfaces. In Chapter 7, we introduce the generalized TDGL (GTDGL) model, compare it with traditional TDGL, and use it to estimate the frequency dependence of the superheating field. Finally, Chapter 8 concludes the dissertation, summarizing our key findings, suggesting potential extensions to this work, and offering concluding remarks on the research presented.

Chapter 2

Sample Specific TDGL

The following chapter is based on a paper we wrote on our framework for sample specific simulation of superconducting materials. The framework uses the results of Density Functional Theory and experimental characterizations to translate the propeprties of realistic sample materials into TDGL parameters which can then be used to model the interactions of such a material with applied magnetic fields. Our framework serves as a mesoscopic link between microscopic material properties and macroscopic cavity performance metrics. This paper also introduces our methods for calculating dissipation and cavity quality factor based on the outputs of TDGL simulations. We use these methods to investigate the impact of Sn-deficient islands in Nb_3Sn. The methods of this paper serve as the basis for the remaining methods in the rest of this dissertation. The contents of the following has been submitted for publication to Physical Review B, and at the time of writing is currently under the second round of peer-review after revisions, a copy is available on arXiv: https://arxiv.org/abs/2410.20078, but we present the full contents here.

2.1 Introduction

Superconducting Radio-Frequency (SRF) cavities are a crucial component of particle accelerators, as they utilize AC electromagnetic fields to accelerate beams of charged particles. Nb has been the industry standard for SRF applications for decades due to its high critical temperature ($\sim$9K) relative to the other elemental superconductors. Within the past decade, the need for SRF cavities with capabilities beyond the limits of Nb cavity performance has led to the study of a variety of alternative SRF materials. Among these materials, Nb_3Sn has emerged as a promising candidate; Nb_3Sn boasts both a higher critical temperature ($\sim$18K) and higher critical fields [41, 42]. One particular advantage of SRF cavities (as compared to traditional normal conducting RF cavities) is their high quality factors (Q) [7]. A major benefit of Nb_3Sn SRF cavities compared to their Nb counterparts is that they can maintain similar Qs (on the order of 10^{10}) at higher temperatures (4.2K vs. 2K) [42], significantly reducing cryogenic costs. NbZr is another promising alternative SRF material which has seen recent attention [43, 44], with most existing NbZr samples exhibiting critical temperatures between 10 and 13K (the theoretical maximum is 17.7K), but this material has not yet been tested at cavity scale. The simulations in this paper focus on Nb_3Sn, but the methods we will present can be generalized to any material of interest.

The oscillating electric fields used for acceleration in SRF cavities induce magnetic fields parallel to the cavity surface, so for large accelerating gradients, the critical magnetic fields of the cavity material are the fundamental limits on cavity performance. Type-II superconductors such as Nb and Nb_3Sn have two critical fields, H_{c1} and H_{c2}. For fields below H_{c1}, the Meissner state is stable and magnetic flux is expelled from the cavity. Between H_{c1} and H_{c2}, there is a mixed state in which superconducting vortices trap lines of magnetic flux, forming normal cores inside the otherwise superconducting state. Under an AC field, as is the case for SRF cavities, the vortices quickly move in and out of the cavity over the course of an AC cycle. This vortex motion leads to large amounts of dissipation [9]. For fields above H_{c2}, the mixed state becomes unstable and in

this state SRF cavities will quench (i.e. go normal conducting). It is important to note that this is not the only mechanism for SRF cavity quench, the dissipation caused by moving vortices in the mixed state can cause heating in the cavity, which can also lead to quenching through a change in cavity temperature. As such, for SRF applications, it is important that the cavity remain within the Meissner state during operation.

While the Meissner state is no longer thermodynamically stable above H_{c1}, it can remain metastable up until the so-called superheating field, H_{sh} [10]. It is well known that many high-power SRF cavities operate in this metastable Meissner state [11]. As such, H_{sh} is the theoretical limiting field for operation of SRF cavities, since the dissipative vortices which are detrimental to SRF performance become unavoidable for fields above H_{sh}. H_{sh} has been studied for decades by condensed matter theorists. These studies have most commonly been within a Ginzburg-Landau (GL) framework [45–48], but the superheating field has also been studied extensively utilizing the Eilenberger equations [49–51].

H_{sh} provides the maximum possible field (and therefore the maximum accelerating gradient) for SRF cavity operation, but local features of a material such as impurities or surface geometries can act as nucleation sites for vortices. This means that in practice, realistic material samples will be limited by what we will call the vortex penetration field, H_{vort}, which is the lowest field at which the material nucleates vortices. This quantity can vary greatly between different samples and depends on a large variety of different effects, so estimation of H_{vort} for realistic sample materials remains a rich area of research. For the case of Nb_3Sn in particular, theoretical H_{sh} calculations suggest that Nb_3Sn cavities could reach accelerating gradients as high as around 100 MV/m, yet the highest accelerating field achieved so far by a Nb_3Sn SRF cavity is around 24 MV/m [39], with most other cavities reaching their quench field well below this. Additionally, many existing cavities exhibit a phenomenon in which Q significantly degrades as the cavity approaches its quench field, a phenomenon dubbed “Q-slope" [52], also sometimes called high field Q-slope (HFQS)

when it occurs primarily at higher fields near the quench field. These performance degradations are the result of material defects introduced during the Nb_3Sn growth process, so understanding how different defects seen within samples affect things like H_{vort} or dissipation more generally is critical to developing better growth techniques.

The need to accurately model specific features such as material impurities within superconducting materials motivates us to develop a framework which will allow us to directly model the spatial variations of superconducting properties due to the material compositions observed in realistic sample materials. To do this, we use time-dependent Ginzburg-Landau (TDGL) theory. TDGL has already proven itself to be a powerful tool for mesoscopic-scale simulations relevant to SRF applications [53–56]. Besides SRF simulations, TDGL has broad application such as in single photon detectors [57, 58], superconducting quantum interference devices (SQUIDs) [59, 60], weak links [61–65], or superconducting nanowires [66–68]. The methods we present in this paper are investigated with full 3D simulations. While prior work has studied vortex dynamics in 3D [69–75], the majority of TDGL research, especially in the context of SRF cavities, has been limited to 2D.

Whenever working with TDGL, it is important to acknowledge its limitations. TDGL is a mesoscopic-scale model which abstracts the microscopic details of superconductivity into quantities which can be used to describe things like vortex dynamics. Much of this abstraction is the direct result of restricting the quantitative validity to gapless superconductivity at temperatures near T_c. This means that outside of this fairly restrictive regime, the quantitative predictions of TDGL are not accurate in general. Despite this, there are three main reasons that TDGL is still has considerable value in a variety of studies, such as those referenced above. Firstly, it is well known that the solutions to the Ginzburg-Landau equations have a much wider range of quantitative applicability when under the dirty limit, and so properties of the TDGL equations which can be derived from steady-state dirty limit solutions, such as H_{sh}, are still valuable quantitative outputs of the theory. Secondly, theories of superconductivity with larger ranges of quantitative accuracy (such as the

Eilenberger equations [49–51] or other quasi-classical approaches) scale extremely poorly in terms of computational complexity when it comes to numerical simulations, whereas TDGL is at least feasible for larger mesoscopic-scale simulations. And finally, TDGL offers qualitative and semi-quantitative predictions that provide useful insight into phenomena which may be difficult or impossible to measure experimentally. For example, it can be used to compare how variations in the size and depth of stoichiometric defects relative to the superconductor's surface affect SRF-relevant metrics such as vortex nucleation and energy dissipation—enabling prioritization of which defect characteristics are most critical to address when perfect control is not possible. In what follows, we apply this approach to a specific class of such defects relevant to Nb_3Sn-coated SRF cavities.

To model sample-specific materials and investigate mechanisms behind Q-slope and other quenching phenomena in Nb_3Sn SRF cavities, we draw on both experimental and theoretical studies that characterize the microscopic properties of Nb_3Sn. There has been a large body of work experimentally characterizing SRF grade vapor-diffused Nb_3Sn samples. The primary suspect for SRF performance degradation comes from defects or other imperfections in the Nb_3Sn surface significantly lowering the barrier to flux penetration [76]. In particular, defects which have been studied are abnormally thin or patchy grains [77–79], Sn-segregated grain boundaries [54, 80, 81], and Sn-deficient regions [77, 78, 82, 83]. In addition to experimental characterizations, there have also been a variety of *ab initio* calculations for Nb_3Sn using density functional theory. In addition to calculations of general properties of Nb_3Sn [84], such as the electron and phonon density of states and Eliashberg spectral function, these quantities have also been estimated with respect to varying intrinsic strain [85] as well as normal resistivity [86]. Variations in the superconducting T_c as well as electron density of states have also been calculated with respect to varying tin concentration [37, 87], which applies to both Sn-segregation at grain boundaries and Sn-deficient regions. These Sn-deficient regions, which we will call Sn-deficient islands, are the primary material defect we will study in order to validate our methods.

Experimental characterizations can give data about the material compositions and physical structure of superconducting materials, and *ab initio* calculations provide detailed descriptions of the electronic/phononic structure and the resulting superconducting properties, both of these a microscopic scale. TDGL plays the role of modeling mesoscopic scale phenomena (such as vortex dynamics) which are difficult or even impossible to measure directly via experiment, and are too large to easily model with microscopic scale theories such as DFT. There have been a number of studies which have used TDGL to model material inhomogenieties [53, 54, 88–92], but these studies did not use the explicit dependencies of the TDGL parameters on microscopic material properties to inform their choice of parameters. The limitation to the approach used in these references is that it requires either looking through a large portion of the TDGL parameter space in order to find values which lead to expected predictions, or more commonly, picking somewhat arbitrary values, which limits confidence in the results.

In this paper, we outline a new framework in TDGL theory which allows us to directly calculate the values of the TDGL parameters based on local properties of the superconductor. This framework enables modeling of realistic features of superconductor samples and supports estimation of critical fields and energy dissipation under dynamic electromagnetic conditions. Under our framework, TDGL serves as a bridge between experimental material characterizations and *ab initio* calculations of material-specific parameters, allowing us to further connect these microscopic characterizations with macroscopic SRF performance metrics in a sample-specific way. Because SRF cavity development is inherently multidisciplinary—bringing together accelerator physicists, materials scientists, and condensed matter theorists—a framework that integrates insights across these domains is particularly valuable. The method presented here enables such integration, offering a pathway to sample-specific predictions grounded in both microscopic characterization and macroscopic application.

This paper is organized as follows. In Section 3.2, we present the TDGL equations and show how to calculate TDGL parameters from material properties. We then describe how spatial variations in these parameters are estimated by combining results from DFT calculations with experimental material characterizations. The section concludes with a discussion of how dissipation can be computed from TDGL solutions and how SRF cavity quality factors can be derived from this dissipation. In Section 2.3, we apply our framework to estimate the critical fields associated with Sn-deficient islands of varying size, position, and stoichiometric composition. We then examine dissipation in the context of Nb SRF cavities and analyze a representative simulation in detail to probe the limits of TDGL. Finally, we demonstrate how combining critical field and dissipation results enables us to estimate high-field Q-slope behavior for Nb_3Sn SRF cavities. Section 2.4 concludes the paper with a discussion of the justification for using TDGL despite its known limitations and the implications of our findings for future SRF cavity research.

2.2 Methods

2.2.1 The Time-Dependent Ginzburg-Landau Equations

Ginzburg-Landau (GL) theory is one of the oldest theories of superconductivity, and it remains relevant today owing to its relative simplicity and direct physical insights into the electrodynamic response of superconductors under static applied fields and currents [93]. The *time-dependent* Ginzburg-Landau (TDGL) equations were originally proposed by Schmid [17] in 1966 and Gor'kov and Eliashberg [18] derived them rigorously from BCS theory later in 1968. The TDGL equations (in Gaussian units) are given by:

$$\Gamma\left(\frac{\partial\psi}{\partial t}+\frac{ie_s\phi}{\hbar}\psi\right)+\frac{1}{2m_s}\left(-i\hbar\nabla-\frac{e_s}{c}\mathbf{A}\right)^2\psi+\alpha\psi+\beta|\psi|^2\psi=0 \tag{2.1}$$

$$\frac{4\pi\sigma_n}{c}\left(\frac{1}{c}\frac{\partial\mathbf{A}}{\partial t}+\nabla\phi\right)+\nabla\times\nabla\times\mathbf{A}-\frac{2\pi ie_s\hbar}{m_sc}\left(\psi^*\nabla\psi-\psi\nabla\psi^*\right)+\frac{4\pi e_s^2}{m_sc^2}|\psi|^2\mathbf{A}=0. \tag{2.2}$$

These equations are solved for the complex superconducting order parameter, ψ, and the magnetic vector potential, $\mathbf{A}$. The magnitude squared of ψ is proportional to the density of superconducting electrons. The parameters α and β are phenomenological, and were originally introduced as coefficients of the series expansion of the Ginzburg-Landau free energy. Additionally, ϕ is the scalar potential; σ_n is the normal electron conductivity; Γ is the phenomenological relaxation rate of ψ. Furthermore, $e_s = 2e$ and $m_s = 2m_e$ represent the total charge and total effective mass of a Cooper pair, respectively. The TDGL equations are subject to boundary conditions

$$\left(i\hbar\nabla\psi + \frac{e_s}{c}\mathbf{A}\psi\right)\cdot\mathbf{n} = 0 \tag{2.3}$$

$$(\nabla\times\mathbf{A})\times\mathbf{n} = \mathbf{H}_a\times\mathbf{n} \tag{2.4}$$

$$\left(\nabla\phi + \frac{1}{c}\frac{\partial\mathbf{A}}{\partial t}\right)\cdot\mathbf{n} = 0, \tag{2.5}$$

where $\mathbf{n}$ is the outward normal vector to the boundary surface and $\mathbf{H}_a$ is the applied magnetic field. Eq. 2.3 ensures no current flows out of the superconducting domain, and noting that $E = -\nabla\phi - \frac{1}{c}\frac{\partial\mathbf{A}}{\partial t}$, Eqs. 2.4 and 2.5 are electromagnetic interface conditions with an applied magnetic field.

The parameters α, β, and Γ were originally introduced into the theory as phenomenological, temperature-dependent constants [94]. It is worth noting that $\alpha < 0$ corresponds to the superconducting state whereas $\alpha \geq 0$ corresponds to the normal state; β is strictly positive regardless of the system's state. The TDGL equations can also be derived from microscopic theory using the time-dependent Gor'Kov equations [18]. A useful consequence of this derivation is that it allows the TDGL parameters to be directly related to experimentally observable properties of the material

in question. The material dependencies are given by Ref. 24:

$$\alpha(\nu(0), T_c, T) = -\nu(0)\left(\frac{1-\frac{T^2}{T_c^2}}{1+\frac{T^2}{T_c^2}}\right) \tag{2.6}$$
$$\approx -\nu(0)\left(1-\frac{T}{T_c}\right)$$
$$\beta(\nu(0), T_c, T) = \frac{7\zeta(3)\nu(0)}{8\pi^2 T_c^2}\left(\frac{1}{1+\frac{T^2}{T_c^2}}\right)^2 \tag{2.7}$$
$$\approx \frac{7\zeta(3)\nu(0)}{8\pi^2 T_c^2}$$
$$\Gamma(\nu(0), T_c) = \frac{\nu(0)\pi\hbar}{8T_c}, \tag{2.8}$$

where $\nu(0)$ is the density of states at the Fermi-level, T_c is the critical temperature, T is the temperature, and $\zeta(x)$ is the Riemann zeta function. Additionally, the effective mass can also be expressed in terms of these same quantities in addition to the Fermi velocity, v_f, and electron mean free path, ℓ:

$$m_s = \frac{12\hbar T_c}{\pi\nu(0)v_f\ell}. \tag{2.9}$$

Equation 2.9 gives the effective mass under the dirty limit.

A major contribution of this paper is to introduce a framework for modeling sample-specific features of superconducting materials by connecting *ab initio* calculations of the material's properties to experimental characterizations of the material. Eqs. 2.6-2.9 determine how the parameters of TDGL depend on the underlying material properties. We allow these parameters to vary spatially to capture the sample-specific features observed from experimental characterizations. When converting these constant coefficient into a spatially-varying ones, it is important to consider how this may alter the TDGL equations due to potential alterations to the functional derivatives of the free energy. In the case of α, β, and Γ, they do not appear on terms of the free energy with spatial gradients. However, m_s does appear in terms including gradients, and so when including spatially-varying

effective mass, Equation 2.1 should be augmented with an additional term:

$$\frac{i\hbar}{2}\nabla\frac{1}{m_s}\cdot(i\hbar\nabla+\frac{e}{c}\mathbf{A})\psi$$

Additionally, when solving the TDGL equations numerically, it is standard to normalize all the parameters of the model in order to obtain dimensionless quantities. In order to satisfy the above requirements, the steps are as follows: Pick a reference value for each of α, β, Γ, m_s, and σ_n, these will most often just be the corresponding values for the bulk material. Label these reference values α_0, β_0, Γ_0, m_0, and σ_{n0}. Define dimensionless spatially varying functions, $a(\mathbf{r})$, $b(\mathbf{r})$, $\gamma(\mathbf{r})$, $\mu(\mathbf{r})$, and $s(\mathbf{r})$, relative to their reference values. Apply the following transformations to Eqs. 2.1 and 2.2:

$$\alpha \longrightarrow \alpha_0 a(\mathbf{r}) \tag{2.10}$$

$$\beta \longrightarrow \beta_0 b(\mathbf{r}) \tag{2.11}$$

$$\Gamma \longrightarrow \Gamma_0 \gamma(\mathbf{r}) \tag{2.12}$$

$$m_s \longrightarrow m_0 \mu(\mathbf{r}) \tag{2.13}$$

$$\sigma_n \longrightarrow \sigma_{n0} s(\mathbf{r}). \tag{2.14}$$

Then proceed with standard nondimensionalization procedures for TDGL (see the Appendix for more details). The advantage of this approach is that the nondimensionalization procedures, when used on these transformed equations, leave behind only the dimensionless functions which capture the spatial variation of the sample material in natural units. The resulting equations are

$$\gamma\left(\frac{\partial\psi}{\partial t}+i\kappa_0\phi\psi\right)+\frac{1}{\mu}\left(\frac{-i}{\kappa_0}\nabla-\mathbf{A}\right)^2\psi+\frac{1}{\kappa_0}\nabla\frac{1}{\mu}\cdot\left(\frac{1}{\kappa_0}\nabla-i\mathbf{A}\right)\psi-a\psi+b|\psi|^2\psi=0 \tag{2.15}$$

$$\frac{s}{u_0}\left(\frac{\partial\mathbf{A}}{\partial t}+\nabla\phi\right)+\nabla\times\nabla\times\mathbf{A}+\frac{i}{2\kappa_0\mu}(\psi^*\nabla\psi-\psi\nabla\psi^*)+\frac{1}{\mu}|\psi|^2\mathbf{A}=0, \tag{2.16}$$

where $\kappa_0=\frac{\lambda_0}{\xi_0}$ is the Ginzburg-Landau parameter of the reference material. The quantity $\lambda_0=\sqrt{\frac{m_0c^2\beta_0}{4\pi e_s^2|\alpha_0|}}$ is the penetration depth of the reference material, and $\xi_0=\sqrt{\frac{\hbar^2}{2m_0|\alpha_0|}}$ is its coherence length. The parameter $u_0=\frac{\tau_{\psi_0}}{\tau_{j_0}}$ is a ratio of characteristic time scales in the reference material, where $\tau_{\psi_0}=\frac{\Gamma_0}{|\alpha_0|}$ is the characteristic relaxation time of ψ in the reference material and $\tau_{j_0}=\frac{\sigma_{n0}m_0\beta_0}{e_s^2|\alpha_0|}$

is the characteristic relaxation time of the current. We have also inserted a minus in front of a, which is just a convention to make positive values of a correspond to the superconducting state (Note: this is the opposite of how α is usually interpreted within Ginzburg-Landau theory, however it is standard to make this change when performing nondimensionalization). The boundary conditions become:

$$\left(\frac{i}{\kappa_0}\nabla\psi + \mathbf{A}\psi\right)\cdot n = 0 \tag{2.17}$$

$$(\nabla\times\mathbf{A})\times n = \mathbf{H}_a \times n \tag{2.18}$$

$$\left(\nabla\phi + \frac{\partial\mathbf{A}}{\partial t}\right)\cdot n = 0. \tag{2.19}$$

It should be noted that $\gamma(\mathbf{r})$ and $s(\mathbf{r})$ allow the local characteristic time relaxations to vary, which only affects the dynamics of the solutions. Where the time dynamics are relevant these parameters cannot be ignored; however, in many cases, the primary interest of TDGL calculations is in determining the energetic stability and critical fields, such as the superheating field. In these cases, the time dynamics are not relevant and γ and s can be safely set to arbitrary constant values, such as unity.

2.2.2 Determining Spatial Variation of TDGL Parameters

In the previous section, we have shown how to introduce spatial variation to the TDGL parameters. The process of calculating the values of $a(\mathbf{r})$, $b(\mathbf{r})$, $\gamma(\mathbf{r})$, and $\mu(\mathbf{r})$ is where we bring in experiment and *ab initio* theory. From Eqs. 2.6-2.8, we know these parameters mostly depend on well-defined microscopic quantities, namely $\nu(0)$, T_c, and v_f. These quantities can be calculated using density-functional theory (DFT). Local densities of states and Fermi velocities are straightforward to compute in DFT, providing local values for $\nu(0)$ and v_f. Superconducting quantities such as T_c are calculated by applying Eliashberg theory within a DFT framework and directly calculating electron-phonon coupling from first principles. Experiment can then give information about the compositions of sample materials, and DFT calculations can determine the $\nu(0)$, v_f, and T_c associated with these

compositions. Using these values in addition to estimates of the electron mean free path (which can be derived from DFT or can come from experimental characterizations), $a(\mathbf{r})$, $b(\mathbf{r})$, $\gamma(\mathbf{r})$,and $\mu(\mathbf{r})$ are calculated from Eqs. 2.6-2.9, and the material geometries from the experimental results determine the spatial variation.

In this paper, we will demonstrate our framework on Sn-deficient islands. These defects have been studied extensively [77, 78, 82, 83] so it is straightforward to find estimates of the general size of these islands and their material compositions in the literature. DFT has also been used to calculate $\nu(0)$, v_f, and T_c for Nb-Sn systems of different concentrations. In this paper we use the DFT values from Ref. 37 to construct $a(\mathbf{r})$, $b(\mathbf{r})$, $\gamma(\mathbf{r})$, and $\mu(\mathbf{r})$ for islands of different Sn concentration. This paper will primarily focus on the results of our TDGL calculations, for further information regarding the details and results from the DFT calculations used in this paper, we refer the interested reader to Refs. 87 and 37.

2.2.3 Simulation Geometry and Numerical Implementation

The simulations in this paper were solved using a finite element formulation of the TDGL equations proposed by Gao [25], under the temporal gauge, which sets the scalar potential $\phi = 0$ (see Du [95] for a more detailed overview of gauge choices in TDGL). All computations were carried out using the open-source finite element software FEniCS [26].

The simulation domain consists of a rectangular cuboid with periodic boundary conditions applied in the x- and y-directions, as indicated by the yellow and light blue highlights in Fig. 2.1. An external magnetic field of constant magnitude H_a is applied in the x-direction on the red surface, while no field is applied on the opposing green surface. For simulations that include Sn-deficient

islands, the island geometry is also shown in Fig. 2.1. These defects are modeled as ellipsoids with equal radii in the x- and y-directions and a z-radius equal to half of the x-radius. The island's distance from the surface, denoted by d, is measured from the surface to the outer edge of the ellipsoid.

All meshes were generated using the open-source mesh generation software Gmsh [96], with cubic tetrahedral elements. For simulations involving Sn-deficient islands, the OpenCASCADE geometry kernel in Gmsh was used to ensure that the mesh conforms to the ellipsoidal shape of the defects.

2.2.4 Dissipation in TDGL

When simulating SRF materials, dissipation is often a physical quantity of interest. Under TDGL, a formula for dissipation can be derived by considering the time derivative of the free energy and the free energy current flux density. A more detailed derivation is found in Ref. 24, but we quote the final result here:

$$D = 2\Gamma \left| \left(\frac{\partial \psi}{\partial t} + \frac{i e_s \phi \psi}{\hbar} \right) \right|^2 + \sigma_n \mathbf{E}^2. \tag{2.20}$$

This quantity is a power density, with the first term corresponding to the superconducting dissipation arising from the relaxation of the order parameter. The second term is the dissipation of normal currents which are largest near the surface where magnetic field can still appreciably penetrate.

It is worth considering how this expression for the dissipation density is related to existing theories of RF power loss and surface resistance. The first term in Eq. 3.20 is associated with the dissipation due to the rate of change of ψ. This term is typically small, except in the vortex state where it becomes the dominant source of dissipation. A dissipation of this form is similar to that proposed by Tinkham [97], who suggested the vortex dissipation should be proportional to $\left(\frac{\partial \psi}{\partial t}\right)^2$. The additional term within the parenthesis in Eq. 3.20 is a result of the gauge invariance of TDGL.

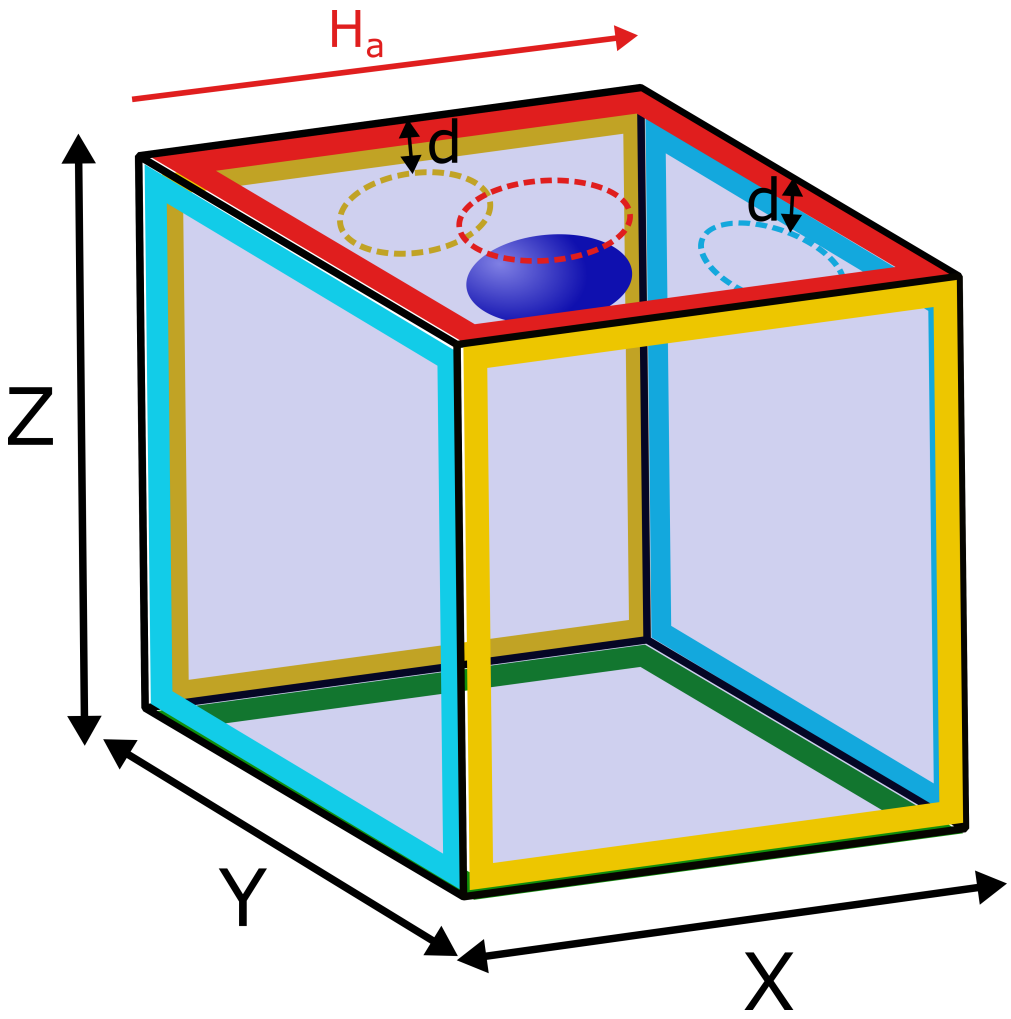

Figure 2.1 Schematic of Simulation Geometry. Like-colored surfaces (yellow and light blue outlines) have periodic boundary conditions. The red and green surfaces indicate the faces where external magnetic field is applied; in simulations, a field is applied to the red surface in the *x*-direction (indicated by the red arrow), with no field applied on the green surface. The Sn-deficient island is shown as a dark blue ellipsoid, with dotted lines indicating its projections into the *xy*, *xz*, and *yz* planes. The distance *d* is measured from the surface to the outer edge of the ellipsoid.

The second term in Eq. 3.20 can be directly related to the phenomenological “two-fluid model," which was first proposed by Gorter and Casimir [13] in 1934 and was applied by London [98] later that year to calculate the power loss of a superconductor. The two-fluid model approximates the electrons of the system as consisting of two non-interacting ‘fluids’: the superconducting electrons, in the form of cooper pairs which carry lossless supercurrent, and the normal electrons, which exist as thermally excited quasiparticles that produce typical dissipative currents. Under the two-fluid model, the normal fluid losses produce dissipation of the form [99, 100]

$$P \propto \sigma_n E^2,$$

which is identical to the second term of Eq. 3.20. For AC applied currents, the electric field is proportional to the frequency and magnetic field, $E \propto \omega H$, meaning that overall the power loss will be of the form

$$P \sim \omega^2 H^2. \tag{2.21}$$

It is also well known that within RF cavities, the power loss is given by

$$P = \frac{1}{2}\oint_A R_s |H(r)|^2 dA, \tag{2.22}$$

where R_s is the surface resistance of the cavity walls and A is the surface area. Comparing Eqs. 2.21 and 2.22, we have that the second term of Eq. 3.20 directly leads to a surface resistance proportional to the square of the frequency, $R_s \propto \omega^2$. In the late 1950s, Mattis and Bardeen [101] as well as Abrikosov, Gor’Kov, and Khalatnikov [102] independently derived the now well-known “BCS resistance." Under the low frequency and low field limit, the BCS resistance reduces to the form [103, 104]

$$R_{bcs} \simeq \frac{\omega^2}{T} e^{\frac{-\Delta}{k_B T}} \tag{2.23}$$

where $\Delta = 1.76 k_B T_c$ is the superconducting energy gap [24]. We thus see that our calculated expression for the surface resistance has the same ω^2 frequency dependence of the BCS prediction in the low frequency and field limit, though the quantitative values may differ.

Given this connection to surface resistance, we now consider how our dissipation estimates can be used to calculate the cavity quality factor, Q, a standard figure of merit in SRF cavity performance.

2.2.5 Estimating Cavity Quality Factor

While TDGL allows us to estimate dissipation, it is important to emphasize that both the dissipation calculations and the quality factor estimates that follow lie well outside the regime of quantitative validity for the theory. In particular, TDGL is strictly valid only near T_c in the gapless limit, and its predictions for dissipation under RF-like dynamic fields at low temperatures should be interpreted with caution. Despite this, we believe the calculations presented here remain qualitatively valuable. They provide a means of linking mesoscopic-scale simulations to macroscopic cavity performance metrics, and enable relative comparisons between different material configurations that may inform experimental priorities.

A particularly relevant quantity that can be estimated from the dissipation is the cavity quality factor, Q, which is given by

$$Q = \frac{2\pi E}{\Delta E}. \tag{2.24}$$

Here, E is the energy stored in the cavity, and ΔE is the energy dissipated in the cavity walls during each RF cycle. It is common to express the quality factor in terms of the surface resistance as

$$Q = \frac{G}{R_s}, \tag{2.25}$$

where R_s is the cavity surface resistance and G is a geometric factor that depends only on quantities which are determined by the cavity geometry. For a typical 1.3 GHz 9-cell Nb TESLA cavity, $G = 270\ \Omega$ [105]. The surface resistance is given by

$$R_s = \frac{\mu_0 \omega \lambda^3}{\tilde{H}_a^2 L_x L_y} \left(I_\psi + \frac{\omega}{\tilde{\omega}} \sigma_n \mu_0 \lambda^2 I_A \right), \tag{2.26}$$

where μ_0 is the permeability of free space, ω is the cavity frequency, λ is the penetration depth, $\tilde{H}_a$ is the maximum applied magnetic field value in simulation units, L_x and L_y are the size of a simulation domain in the X and Y directions respectively, σ_n is the normal conductivity, and $\tilde{\omega}$ is the frequency of the applied field in simulation units. I_ψ and I_A are integrals over the squared time derivatives of ψ and $\mathbf{A}$:

$$I_\psi \equiv \int d\tilde{t} \int d\tilde{x} \int d\tilde{y} \int d\tilde{z} \left| \frac{\partial \tilde{\psi}}{\partial \tilde{t}} \right|^2 \tag{2.27}$$

$$I_A \equiv \int d\tilde{t} \int d\tilde{x} \int d\tilde{y} \int d\tilde{z} \left(\frac{\partial \tilde{\mathbf{A}}}{\partial \tilde{t}} \right)^2 \tag{2.28}$$

where the tilde variables denote ones which are in simulation units. A much more detailed derivation of these equations can be found in the Appendix.

The σ_n appearing in Eq. 2.26 refers specifically to the conductivity of the normal quasiparticles. In general, calculating this quantity from first principles is a complex task that depends sensitively on microscopic material properties, and is largely orthogonal to the rest of the quality factor calculation. For this reason, we choose to treat σ_n as a free parameter in our model, which allows us to explore how dissipation and quality factor vary across a range of plausible conductivity values without relying on potentially oversimplified assumptions. For completeness, we outline a possible approximate derivation of σ_n based on the Drude model in the Appendix, though we emphasize that this is intended primarily as a qualitative reference.

In the derivation of Equation 2.26, it is assumed that the cavity surface is partitioned into small fractional areas, and the dissipated energy is calculated over one of these areas, and then multiplied by the total number of them. If some defect is present in the simulation domain, it would mean that a Q calculation based purely on that value would implicitly assume that such a defect is uniformly distributed over the surface of the cavity. In Equation 2.26, the only thing that changes when simulating a different material or different defect is the value of the quantity in parenthesis, every other part of the process for calculating Q remains the same. This means that we can calculate a

more realistic cavity surface resistance by calculating R_s with Equation 2.26 for a few different simulations, and then taking a weighted average of these values. Let R_i be the surface resistance of the ith simulation, and let p_i be the percentage of the fractional areas partitioning the cavity surface which are represented by this simulation. Then

$$R_{tot} = \sum_i p_i R_i, \tag{2.29}$$

where $\sum_i p_i = 1$. The simplest application for Equation 2.29 is to perform two simulations, one baseline simulation with no defects or material inhomogeneity, and then another simulation containing some defect of interest. Choosing a value p to represent the percentage of fractional areas containing the defect and then following through with the rest of the quality factor calculation provides a simple way to estimate Q for different average defect densities by simply changing the value of p.

The value of Q calculated from TDGL outputs will typically be underestimated at low field. This is because of the assumption of gapless superconductivity, which results in higher surface resistances than is predicted with the BCS surface resistance (Equation 2.23). Despite this, our approach still often predicts quality factors within an order of magnitude of the experimental values. Additionally, the relative behavior of Q at different applied fields, especially when averaging the impact of multiple kinds of defects as described above, qualitatively captures effects such as high field Q-slope. Nonetheless, we emphasize that this quality factor calculation is best treated as a qualitative tool; for quantitatively accurate predictions, more rigorous superconductivity theories should be used.

2.3 Validation Study

2.3.1 Sn-deficient Islands in Nb_3Sn

There has been a considerable amount of work both experimentally and theoretically understanding the various defects present in Nb_3Sn [54,76–83]. For the purposes of this paper, we will focus on Sn-deficient islands, small regions within Nb_3Sn grains that have lower than expected Sn concentrations. To demonstrate the use of our sample specific TDGL framework, we will estimate the potential impact to SRF performance by determining the vortex penetration field, H_{vort}. This field represents the lowest applied field at which a vortex nucleates and generalizes the concept of the superheating field to surfaces containing defects. In the limit of a uniform, flat surface, H_{vort} is equal to the superheating field.

In order to simulate Sn-deficient islands, we require estimates of the material properties within these regions. Such estimates are provided in Ref. 37, which reports values of T_c and $\nu(0)$ for Nb-Sn systems at 18.7, 20.8, and 23.4 at.% Sn. Our v_f estimates for these compositions were obtained via private communication [106]. We first choose a Sn concentration of 18.7 at.% for our islands. Using the corresponding values of T_c and $\nu(0)$, we construct $a(\mathbf{r})$, $b(\mathbf{r})$, and $\gamma(\mathbf{r})$; the values of these quantities in the bulk as well as in the island are reported in Table 2.1. The simulation geometry is the same as depicted in Fig. 2.1, with the domain a cube of side length 10λ. The applied field for these simulations is held constant.

Figure 2.2 depicts vortex nucleation occuring at H_{vort} for a particular island. We find that varying the distance of the island from the surface between 0.1 and 2 penetration depths (i.e. between $\sim$10-200 nm for Nb_3Sn), we observe a reduction in H_{vort} by as much as $\sim$60% below the bulk value of the superheating field for islands very near the surface, as shown in Fig. 2.3. We did this for several different island sizes, and found that the severity of this drop in H_{vort} increases with increasing island size. As such, we conclude that large islands within 200 nm of the cavity

TDGL Parameter and Material Values		
Quantity	Bulk Value	Island Value
T_c (K)	18	6
$\nu(0)$(states/(eV*nm^3))	101.33	40.53
v_f (10^5 m/s)	1.25	1.4
ℓ (nm)	5.5	2.25
a (unitless)	1	0.15
b (unitless)	1	1.8
γ (unitless)	1	1.2
s (unitless)	1	1
μ (unitless)	1	1.79

Table 2.1 A summary of the TDGL parameter and material values used in the results of this paper. All TDGL parameters were calculated from Equations 2.6-2.8 using the higher order temperature dependence and normalized with respect to the bulk value. The T_c and $\nu(0)$ values were taken from Ref. 37 assuming a Sn concentration of 18% for the island. The v_f values came from private correspondence [106], and the bulk value of ℓ was taken from Ref. 107, we set the island value to half of the bulk value. The normal electron conductivity, s, was assumed to remain constant throughout the simulation domain.

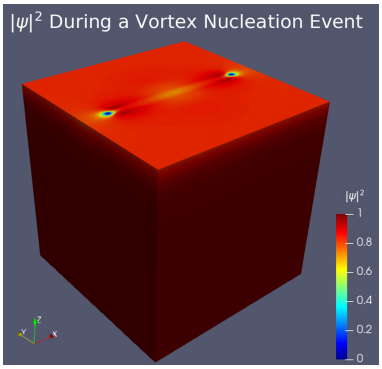

(a) A plot of $|\psi|^2$ during a vortex nucleation event.

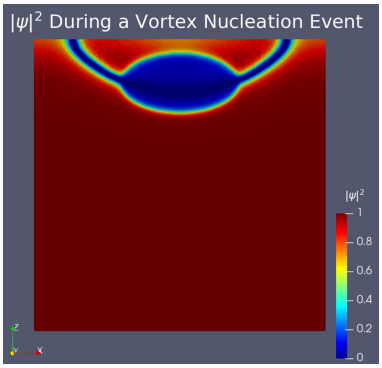

(b) A 2D slice of $|\psi|^2$ in the XZ plane at $\frac{y}{\lambda} = 5$

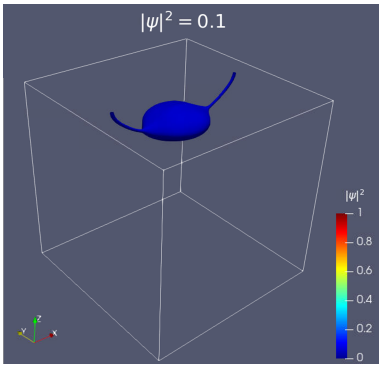

(c) The $|\psi|^2 = 0.1$ isosurface.

Figure 2.2 Example of a Sn-deficient Island Simulation. The domain is a cube with side length 10λ, this particular simulation is for an island 0.5λ from the surface, with a X and Y radius of 2λ and a Z radius of 1λ. The applied field is $\frac{H_a}{\sqrt{2}H_c} = 0.38$, which is the value of H_{vort} for this island size and distance from the surface. (a) depicts a volume plot of $|\psi|^2$ over the whole domain during a vortex nucleation event. (b) is a 2D slice in the XZ plane at $\frac{y}{\lambda} = 5$. (c) is the $|\psi|^2 = 0.1$ isosurface, which shows the shape of the vortex as well as the island that induced the nucleation.

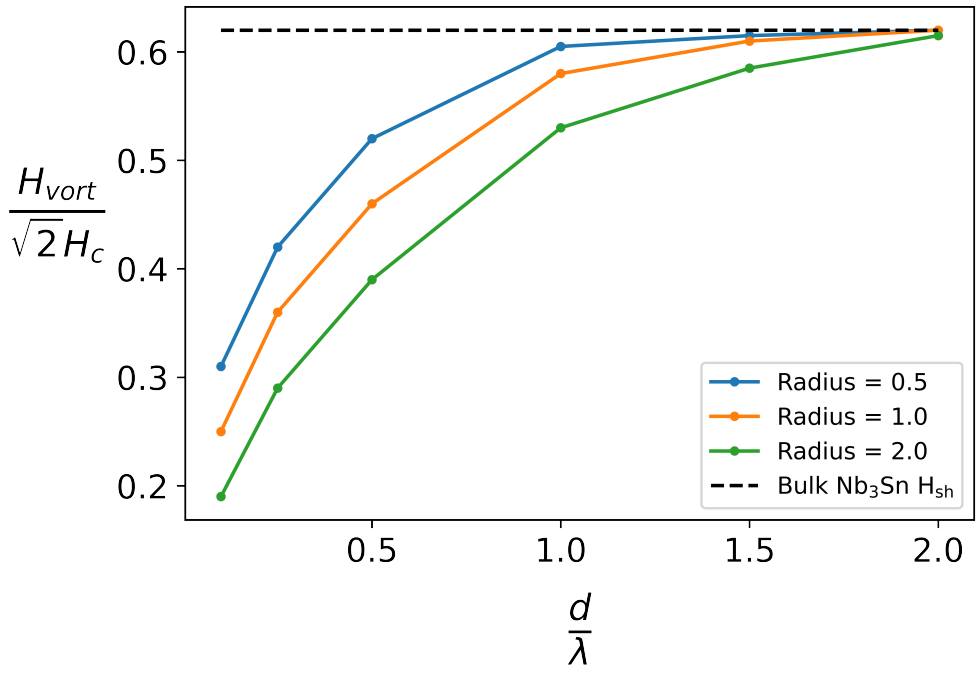

Figure 2.3 Vortex Penetration Field Versus Distance from Surface for Different Island Sizes. We plot our calculated vortex penetration field estimates, varying the distance of the Sn deficient island from the superconductor surface. The field values are reported in units of $\sqrt{2}H_c$ and the distances are in units of penetration depths. We did this for 3 different islands, with x radii of 0.5, 1, and 2 penetration depths. The black dotted line denotes the superheating field of bulk Nb_3Sn. Smaller volume islands have a diminishing impact on H_{vort}.

surface are a potential cause for concern when it comes to SRF performance, particularly ones within 1-2 penetration depths of the surface. Figure 2.4 shows how these effects change with respect to the Sn at.% inside each island. We see that as the Sn deficiency becomes weaker, so does the impact on vortex penetration, though it is worth noting that even an island with 23.4% Sn (only 1.6% off a perfect stoichiometric ratio) has a $\sim$30% reduction in H_{vort} for islands near the surface. Currently, Nb_3Sn-coated SRF cavities are only achieving at most $\sim$25% of their theoretical maximum accelerating fields. There are likely many factors which contribute to this outcome, but these results indicate that Sn-deficient islands are among the defects which contribute to SRF performance degradations.

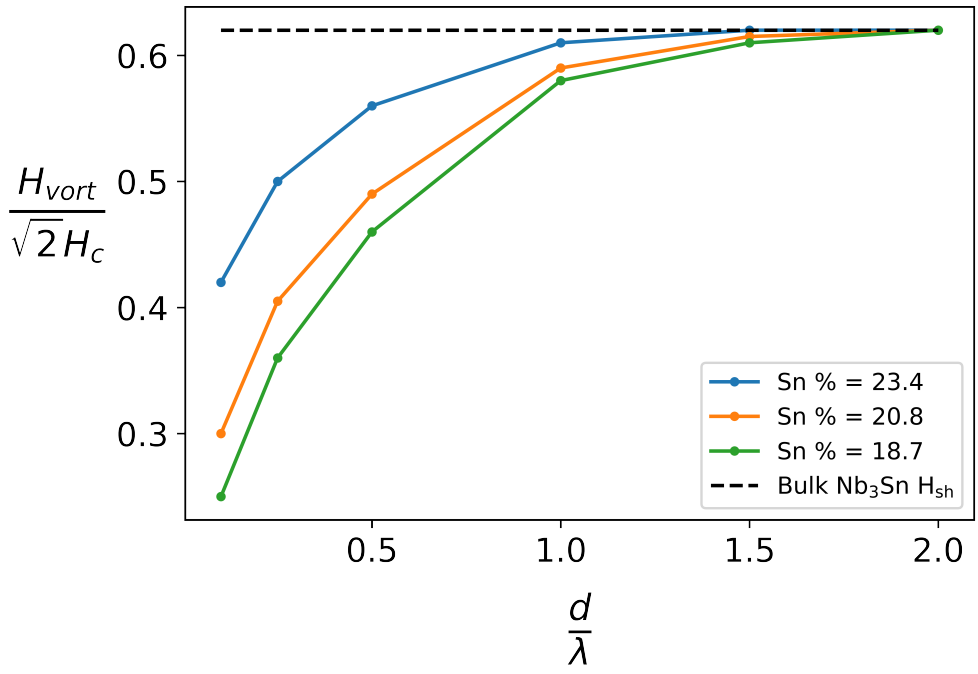

Figure 2.4 Vortex Penetration Field Versus Distance from Surface for Different Island Sn %. We plot our calculated vortex penetration field estimates, varying the distance of the Sn deficient island from the superconductor surface. The field values are reported in units of $\sqrt{2}H_c$ and the distances are in units of penetration depths. We did this for 3 different island Sn percentages, 18.7%, 20.8%, and 23.4%. The black dotted line denotes the superheating field of bulk Nb_3Sn.

2.3.2 Sources of Dissipation in Nb SRF Cavities

In the previous section, we focused on steady-state properties of TDGL in the dirty limit, where the theory is known to have broader quantitative validity. We now extend this framework to examine the two dissipation terms that naturally arise in TDGL simulations. While these calculations fall outside the strict regime of TDGL's quantitative accuracy, particularly at the low temperatures and high frequencies relevant for SRF cavities, they remain *qualitatively* informative. In particular, they allow us to interpret distinct contributions to RF dissipation in a way that parallels the conventional decomposition of surface resistance into BCS and residual components. More broadly, they provide a means of linking mesoscopic TDGL behavior to macroscopic cavity losses, and of understanding how steady-state properties, such as H_{vort} for individual defects, can collectively influence large-scale phenomena like the high-field Q-slope.

It is standard in SRF literature to decompose surface resistance into two components: the BCS resistance, which arises from thermally excited quasiparticles, and a more poorly understood residual resistance, which dominates at low temperatures and is often attributed to trapped flux, impurities, or surface defects. In our TDGL framework, these two types of dissipation emerge naturally. Specifically, in Eq. 2.26, the term proportional to σ_n (involving I_A) captures dissipation due to normal current response, and is the TDGL analog of the BCS resistance. The second term (I_ψ), which arises from relaxation of the superconducting order parameter, reflects dissipation mechanisms not captured by traditional two-fluid or BCS models and can be viewed as a proxy for residual resistance in our simulations. Studying the behavior and interplay of these two terms as a function of applied field and conductivity provides insight into which mechanisms dominate under different conditions.

To establish a baseline for comparison, we simulate a uniform Nb domain subjected to a sinusoidal applied field with period $2000\tau_\psi$. This choice is motivated by the fact that, for Nb at 2 K, we estimate $\tau_\psi \approx 3.7 \times 10^{-13}$ s using Eqs. 2.6 and 2.8 and a value of $\nu(0) = 90$ states/(eV·nm^3) [106], corresponding to a driving frequency of approximately 1.3 GHz—typical of elliptical SRF cavities. The simulation domain is a cube of side length 20λ. In these calculations, we treat the normal conductivity σ_n as a free parameter, and define the dimensionless ratio σ_n/σ_{rt}, where $\sigma_{rt} = 6.7 \times 10^6$ S/m is the room-temperature conductivity of Nb.

Figure 2.5 plots the two dissipation terms as functions of applied field for several values of σ_n/σ_{rt}. The I_A term scales linearly with σ_n, while I_ψ is independent of conductivity and increases more steeply with field. Although we treat σ_n as a free parameter in these simulations, we are nominally modeling Nb, for which a physically meaningful value of σ_n exists. Rigorously determining this value at cryogenic temperatures and GHz frequencies lies beyond the scope of this paper, but physical intuition provides useful bounds: at low field, the BCS-like (i.e., I_A) term should dominate in clean Nb cavities, while at high field, particularly once vortices nucleate, the residual-like (i.e., I_ψ) term should become dominant. These trends imply that the true conductivity is unlikely to differ from σ_{rt} by more than an order of magnitude in either direction. This observation motivates our use of $\sigma_n = \sigma_{rt}$ in the simulations presented in the following section.

While our primary emphasis is on the dissipation terms themselves, we can also use them to estimate quality factors via Eqs. 2.25 and 2.26. As shown in Figure 2.6, the shape of the resulting Q curves depends on the choice of σ_n/σ_{rt}. For moderate and large values (e.g., 1 or 10), the quality factor remains relatively flat at low fields and drops sharply near the superheating field—consistent with expectations for clean Nb cavities. In contrast, for small conductivity values (e.g., 0.1), Q decreases too rapidly with field, indicating unrealistic dissipation behavior. Although lower σ_n values shift the low-field Q magnitude closer to the experimental range of 10^{10}–10^{11}, this comes at the cost of distorting the overall field dependence. Due to the gapless nature of TDGL, we generally

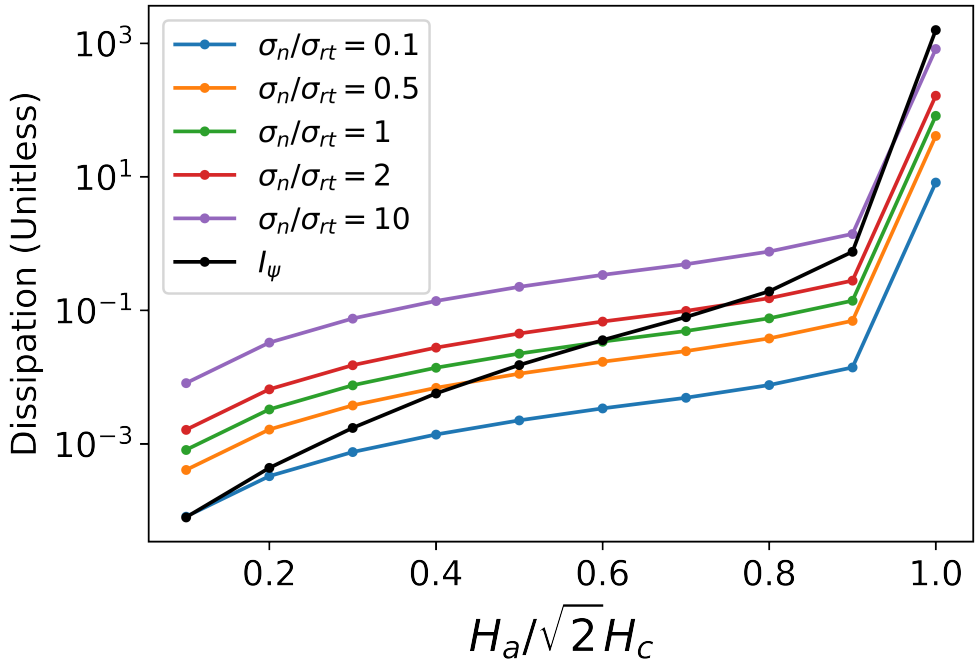

Figure 2.5 Dissipation Contributions from Current Response and Order Parameter Dynamics. The two dissipation terms from Equation 2.26 are plotted separately as functions of applied field, for several values of the normal conductivity σ_n, shown here as ratios to the room-temperature conductivity σ_{rt} of Nb. The term proportional to σ_n and involving I_A represents dissipation from normal current response, while the I_ψ term reflects dissipation due to relaxation of the superconducting order parameter. As field increases, I_ψ grows more rapidly and eventually overtakes I_A. The crossover point depends on the value of σ_n/σ_{rt}: for small values (e.g., 0.1), I_ψ dominates even at low field, while for large values (e.g., 10), the current-induced dissipation remains dominant until vortex nucleation occurs near the superheating field H_{sh}. While σ_n is varied here as a free parameter, this analysis helps illustrate how the relative importance of the two dissipation mechanisms depends on conductivity and field strength within the TDGL framework.

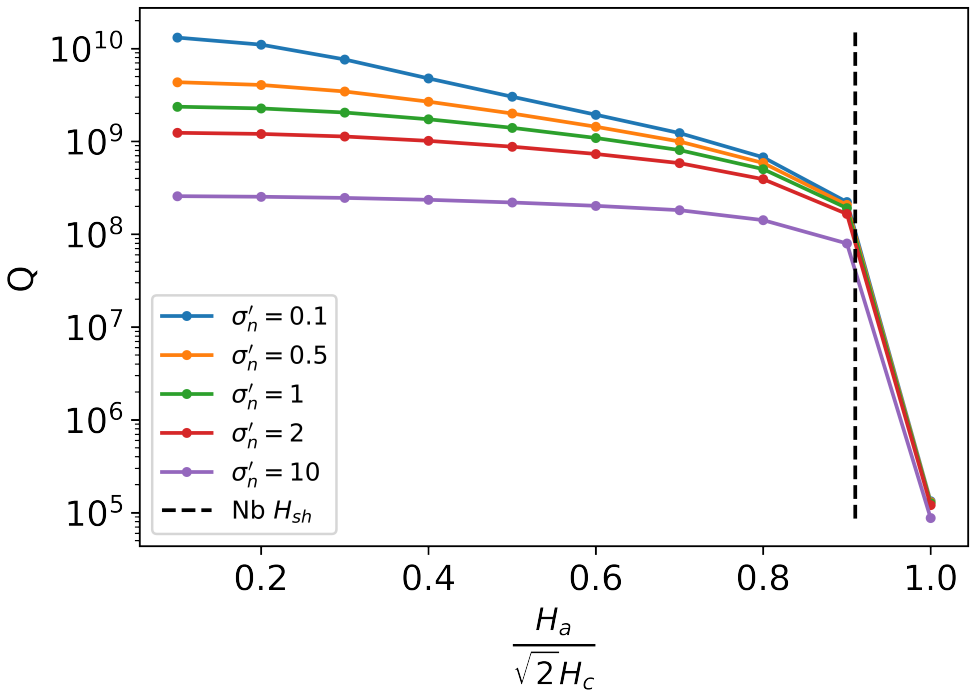

Figure 2.6 Nb SRF Cavity Quality Factor vs. Applied Field. A plot of quality factor for a uniform Nb simulation versus the applied field (in units of $\sqrt{2}H_c$) for several different values of the normal conductivity, given by $\sigma_n = \sigma_{n1} \cdot \sigma_n'$, where σ_{n1} is the room temperature conductivity of Nb. The quality factor is calculated using Eqs. 2.25 and 2.26 with $G = 270\ \Omega$. The calculation for several different values of σ_n' change the low field value, and the shape of the curves, but has much less of an impact near H_{sh}. The dotted black line indicates the superheating field of Nb. Because it is above H_{sh}, vortex nucleation occurred for $\tilde{H}_a = 1.0$ which is the reason for the sharp drop in Q.

expect Q to be underestimated. While we do vary σ_n in these calculations, it is not used as a fitting parameter in the traditional sense—namely, we do not select σ_n to match the low-field Q magnitude from experiment, as we see that doing so would yield qualitatively inaccurate results. Instead, we explore a range of values to identify physically plausible regimes and to qualitatively interpret the resulting dissipation behavior.

These reference simulations validate the dissipation decomposition and demonstrate how our framework reproduces key qualitative features of SRF performance. In the following section, we apply the same methodology to simulations of Sn-deficient islands in Nb_3Sn to investigate how localized stoichiometric defects affect the balance between current-induced and order parameter–related dissipation. Building on this, we introduce an approach for estimating cavity-level losses by linking local vortex nucleation behavior to global quality factor trends.

2.3.3 Dissipation and Quality Factor for Nb_3Sn cavities with Sn-deficient Islands

To explore how localized stoichiometric defects alter RF dissipation, we now apply our framework to a representative simulation of a Sn-deficient island in Nb_3Sn. This case illustrates how such inhomogeneities can shift the balance between current-induced and order parameter–related losses.

To evaluate dissipation in the presence of Sn-deficient islands, we simulate a time-dependent applied field with period $1000\tau_{\psi_0}$, corresponding to a frequency of approximately 5GHz. This is higher than the $\sim$1.3GHz typically used in Nb_3Sn cavities, but was chosen to reduce simulation time for these computationally intensive cases. Each simulation required roughly five weeks of continuous runtime on a computing cluster, making longer periods prohibitively expensive. While

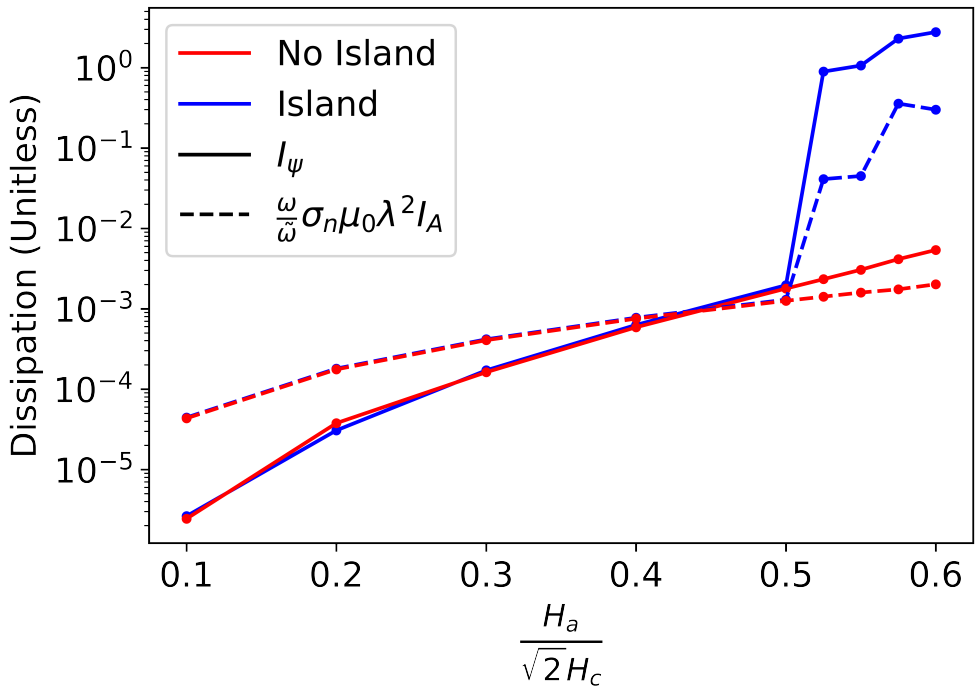

Figure 2.7 Dissipation Terms for Sn-deficient Island Simulations. Dissipation terms I_ψ (solid lines) and I_A (dotted lines) from Eq. 2.26 are plotted as functions of applied field for simulations with (blue) and without (red) a Sn-deficient island. The ellipsoidal island has in-plane radii of 0.5λ, a vertical radius of 0.25λ, and its top edge located 0.5λ beneath the surface. In the island case, vortices nucleate at $H_a \approx 0.525$, causing both dissipation terms—especially I_ψ—to increase sharply by several orders of magnitude. In contrast, the no-island simulation exhibits smoother behavior with more modest growth, and I_ψ exceeds I_A by a smaller factor (typically 2–5$\times$) at high field. These results highlight how local vortex penetration dramatically enhances both forms of dissipation, with I_ψ becoming the dominant contribution.

quantitative estimates of dissipation will differ at lower frequency, we expect the qualitative features of the results to remain representative. To manage computational cost, we model a single island with radius 0.5λ located 0.5λ beneath the surface, using a reduced domain size of $5\lambda \times 2.5\lambda \times 2.5\lambda$ oriented to align the applied field and potential vortex motion along the x-axis.

Figure 2.7 shows the dissipation terms I_ψ and I_A for simulations with and without a Sn-deficient island. Below the vortex penetration field ($H_{vort} \approx 0.525$), both simulations yield nearly identical dissipation, indicating that embedded islands have minimal effect in the Meissner state. Once H_a exceeds H_{vort}, however, the island simulation exhibits an abrupt and sustained increase in both dissipation terms—particularly in I_ψ, which becomes the dominant contribution and rises by several orders of magnitude. The dissipation values above H_{vort} also appear somewhat noisy, which we attribute to numerical variations in vortex entry and dynamics. This binary behavior—where dissipation remains low until vortex entry—appears characteristic of embedded Sn-deficient regions in Nb_3Sn. Whether other types of defects, such as surface-connected grain boundaries, show similar trends remains an open question. Exploring such cases is a clear next direction for future studies.

Building on this result, we develop an approximate method for estimating how a distribution of Sn-deficient islands could collectively affect the quality factor. The dissipation behavior observed in Figure 2.7 suggests that embedded islands have negligible impact below their respective vortex penetration fields, but trigger a sharp increase in dissipation once vortices begin to nucleate. This motivates a two-state approximation: for each island geometry, we assume dissipation follows the defect-free case up to H_{vort}, and then transitions abruptly to constant, elevated values beyond that point. For the vortex state, we use fixed dissipation values of $I_\psi = 2$ and $\frac{\omega}{\bar{\omega}}\sigma_n\mu_0\lambda^2 \cdot I_A = 0.1$, based on the average values from the simulation in Figure 2.7.

Using this approximation, we construct dissipation profiles for each of the simulated island geometries shown in Figure 2.3, focusing on the cases with Sn concentration 18.7%. For each defect, the dissipation follows the defect-free simulation up to its corresponding vortex penetration field H_{vort}, and then transitions to constant values of $I_\psi = 2$ and $\frac{\omega}{\bar{\omega}}\sigma_n\mu_0\lambda^2 \cdot I_A = 0.1$ once vortices nucleate. To estimate the aggregate dissipation and resulting quality factor, we assign weights to

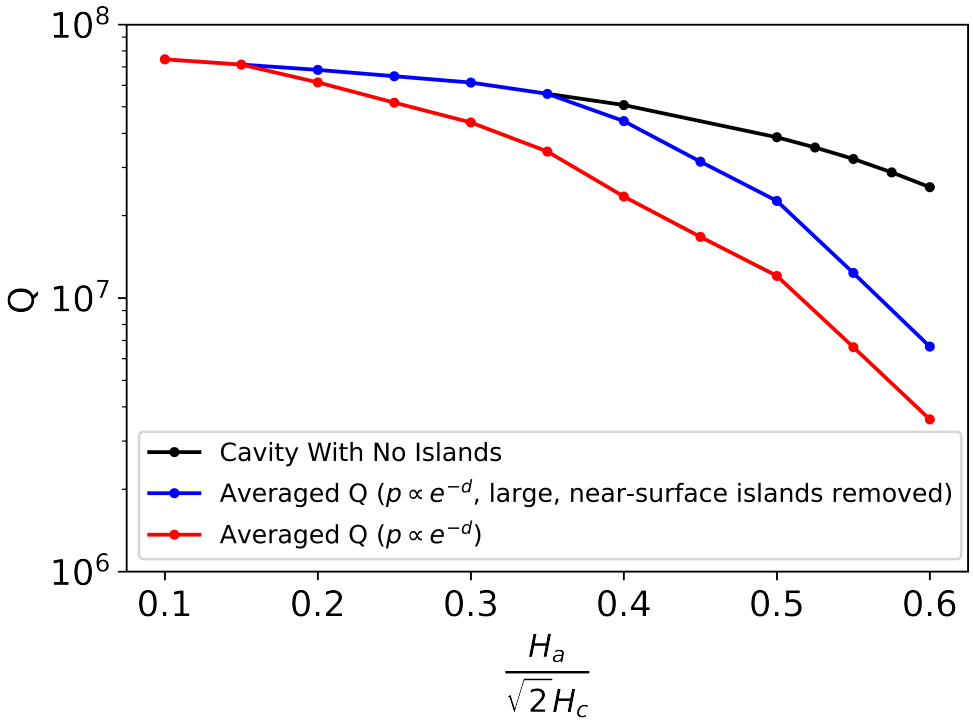

Figure 2.8 Estimated quality factor curves based on weighted dissipation from different Sn-deficient islands. The black curve shows the quality factor for a defect-free cavity. The red curve represents a hypothetical quality factor obtained by averaging dissipation profiles from multiple Sn-deficient island geometries, each transitioning to fixed dissipation values of $I_\psi = 2$ and $\frac{\omega}{\tilde{\omega}}\sigma_n\mu_0\lambda^2 \cdot I_A = 0.1$ above their respective H_{vort}. The weighting assumes all island sizes are equally likely and that the depth d from the surface to the island edge follows an exponential distribution, $p(d) \propto e^{-d}$, normalized so the weights sum to one. The blue curve uses the same assumptions, except that $p(d) = 0$ for the $r = 0.5\lambda$ island when $d \leq 0.1\lambda$, and for the $r = \lambda$ and $r = 2\lambda$ islands when $d < \lambda$. All remaining weights are re-normalized so the distribution still sums to unity. Removing these large, near-surface defects in the model delays the onset of dissipation and improves high-field performance.

each defect based on an assumed distribution and compute a weighted average of the dissipation terms. For the red curve in Figure 2.8, we assume all three island sizes are equally likely and that the depth d from the surface to the outer edge of the island follows an exponential distribution $p(d) \propto e^{-d}$, normalized so the total probability sums to unity.

To evaluate the hypothetical benefit of eliminating large, near-surface defects, we also construct the blue curve in Figure 2.8 using a modified piecewise distribution. In this case, the probability $p(d)$ is defined as

$$p(d) \propto \begin{cases} 0 & \text{for } r = 0.5\lambda \text{ and } d \leq 0.1\lambda \\ 0 & \text{for } r = \lambda \text{ or } 2\lambda \text{ and } d < \lambda \\ e^{-d} & \text{otherwise} \end{cases}$$

and the resulting weights are renormalized to ensure they sum to one. Comparing the red and blue curves illustrates how removing such high-impact defects can delay the onset of increased dissipation and improve the high-field behavior of the cavity.

While the estimated quality factors in Figure 2.8 provide valuable qualitative insight, they should not be interpreted quantitatively. The low-field Q magnitude in our simulations is just under 10^8, significantly lower than the $\sim 10^{10}$ typically observed in Nb3Sn cavities. This discrepancy is primarily due to the higher simulation frequency ($\sim$5 GHz versus 1.3 GHz in practice), though the quantitative limitations of TDGL—such as the assumption of gapless superconductivity and its reduced validity far below T_c—also contribute. Furthermore, we approximate the dissipation above H_{vort} as constant, which neglects the increasing losses and possible thermal effects that would realistically occur as more vortices enter. In practice, such heating could trigger early cavity quench, while in our simulations the dissipation simply continues to increase with field without ever initiating a quench. Despite these simplifications, the structure of the estimated quality factors still captures important qualitative features.

In particular, the onset of high-field Q-slope in these plots arises directly from vortex nucleation, a steady-state property with broader validity in the dirty limit where TDGL is more appropriate. While the precise drop in Q is uncertain, the onset of declining Q in our aggregated curves is governed by the lowest vortex penetration field (H_{vort}) among the defect types with nonzero probability, highlighting how vortex entry from local defects could plausibly contribute to high-field Q-slope in at least some Nb3Sn cavities. More broadly, our results demonstrate a mechanism in which HFQS can emerge from the collective behavior of many small defects. Each defect follows a binary dissipation pattern—remaining nearly inert below H_{vort} and sharply increasing in loss once vortex nucleation occurs—and as the field increases, more defects transition into this high-loss state. The aggregated effect produces a decline in Q that qualitatively resembles the high-field Q-slope observed experimentally. While this is unlikely to be the sole mechanism underlying HFQS, it offers a plausible explanation for how distributed sub-surface defects may contribute to performance degradation in certain cavities, as we elaborate further in the conclusion.

2.4 Conclusion

In this paper, we have demonstrated a framework for incorporating sample-specific information into time-dependent Ginzburg–Landau (TDGL) simulations of superconducting radio-frequency (SRF) cavities. While TDGL is inherently suited for mesoscopic modeling, its application to non-uniform materials often involves arbitrary parameter choices. Our approach addresses this gap by linking TDGL parameters to well-defined microscopic material properties, allowing simulations to reflect characteristics obtained from density functional theory (DFT) or experimental measurements. This enables more realistic modeling of sample-specific features while preserving the computational tractability of TDGL on mesoscopic domains.

In addition to the sample-specific framework, we introduced a method for estimating dissipation and quality factor directly from TDGL simulations. While these estimates are subject to limitations—such as TDGL's quantitative inaccuracy far below T_c and the computational necessity of simulating at higher frequencies—they offer a valuable qualitative connection between mesoscopic defect behavior and macroscopic performance degradation. By decomposing dissipation into physically meaningful components and linking vortex nucleation to high-field Q-slope, our approach provides insight into how distributed material inhomogeneities may impact SRF cavity performance. This type of dissipation-based analysis remains relatively uncommon in the TDGL literature and may serve as a useful tool for future studies aiming to bridge simulation and experiment.

We applied our framework to model Sn-deficient islands in Nb_3Sn and found that they can reduce the vortex penetration field by as much as 60% when located near the surface. This suggests that such sub-surface defects may play a role in limiting the achievable accelerating gradients in Nb_3Sn cavities, particularly given that experimentally observed gradients remain well below the theoretical maximum. To explore this further, we computed the dissipation for representative island configurations and observed sharp increases in both dissipation terms above H_{vort} due to vortex-induced losses. These effects are expected to be even more pronounced for larger or more exposed defects, and in future simulations that incorporate thermal feedback to model cavity quenching. Our method can also be readily extended to other defect types, such as grain boundaries, which are widely believed to impact cavity performance.

To illustrate how these mesoscopic effects might collectively influence macroscopic cavity behavior, we constructed hypothetical quality factor curves by assigning defect-specific H_{vort} thresholds and aggregating their dissipation using simple assumptions about defect size and depth distributions. The resulting Q curves qualitatively resemble the high-field Q-slope observed in

experimental measurements, offering a plausible explanation in which HFQS emerges from the collective activation of many small, embedded defects. This analysis highlights the potential of TDGL-based simulations to inform defect mitigation strategies and guide the development of higher-performance SRF materials.

A recent experimental study by Viklund et al. [108] found that applying centrifugal barrel polishing (CBP) to Nb_3Sn SRF cavities decreased the overall quality factor, lowered the field at which Q-slope began, and reduced the quench field. After an additional Sn vapor deposition, however, the cavity recovered its previous Q performance and reached a higher quench field. Our results offer a potential explanation for these findings. CBP is known to smooth the cavity surface but also removes surface material, which may expose previously buried Sn-deficient islands. As shown in our simulations, bringing such defects closer to the surface significantly enhances their dissipation and lowers H_{vort}, potentially triggering early vortex entry, high-field Q-slope, and premature quenching. The follow-up Sn coating likely fills in these exposed islands, eliminating the source of additional dissipation. This healing process restores Q and enables higher accelerating gradients, consistent with our finding that suppressing near-surface Sn-deficient regions improves both quality factor and vortex-related performance limits.

Whenever TDGL equations are used to model experimental systems, it is important to consider their limitations. The standard TDGL formalism is derived under the assumption of gapless superconductivity, since a gapped density of states introduces a singularity that precludes expansion in powers of the energy gap [23]. Additionally, the equations are only quantitatively valid near the superconducting critical temperature. The former limitation can be addressed by using a generalized TDGL formulation developed by Kramer and Watts-Tobin [27], which extends validity to gapped superconductors. However, several studies have observed conditions in SRF cavities that support the use of conventional TDGL. For example, Proslier et al. [109] reported a broadened density of states at the surface of Nb cavities due to oxide layers, resulting in gapless surface superconductivity.

Further work by Gurevich and Kubo [104, 110] demonstrated that typical material compositions and SRF operating conditions often produce a broadened density of states and suppressed energy gap, reinforcing the relevance of TDGL for SRF applications. Nevertheless, such gapless behavior may come at a cost: broader density of states near the surface could contribute to increased dissipation and reduced quality factors.

The methods presented here for simulating realistic, sample-specific defects and estimating their impact on quality factor provide a new framework for linking microscopic material features to macroscopic SRF performance. While the underlying simulations are conceptually straightforward, their successful application depends on two critical inputs: accurate theoretical models of a material's microscopic properties, and detailed experimental characterization of the defects present in real samples. For this reason, our method is best suited to research contexts where both inputs are available—either in well-studied materials systems or through interdisciplinary collaborations like those found in the NSF Center for Bright Beams, which helped motivate this work. SRF research is particularly well positioned for such integration. SRF cavities are inherently macroscopic devices whose performance depends sensitively on microscopic structure, yet direct experimental probing of such features is often infeasible. The approach we describe enables mesoscopic-scale simulations rooted in real material data, offering a valuable tool for designing and optimizing future generations of SRF cavities.

2.5 Acknowledgement

This work was supported by the US National Science Foundation under Award OIA-1549132, the Center for Bright Beams. We would like to thank Dr. Nathan Sitaraman for helpful conversations and estimates of the Fermi level density of states and Fermi velocities, and Dr. Michelle Kelley for helpful comments about early drafts of the methods section.

Chapter 3

Hydrides in Nb SRF Cavities

The following chapter is based on a paper that covers simulations we performed investigating the impact of hydride precipitates in Nb SRF cavities. This paper with written in collaboration with Nathan Sitaraman from Cornell University. Nathan performed the hydride formation simulations, as well as the DFT estimations of the superconducting properties of NbH. I ran all of the TDGL simulations, and am responsible for the majority of the text of the paper. In this study, we investigate the impacts of hydride size and position (relative to the surface) and conclude that reducing the overall size of hydrides is critical for improving cavity peformance. We also conclude that treatment procedures known to improve cavity performance, such as nitrogen doping, do so by introducing more nucleation sites, which in turn reduces the average size of hydride precipitates, improving cavity performance.

3.1 Introduction

For around half a century, it has been understood that the presence of excess hydrogen in niobium superconducting radiofrequency (SRF) cavities could lead to a variety of deleterious effects on the performance of these cavities [111–113]. Much of the early work on this topic focused on methods to understand and eliminate the so-called “Q-disease," a phenomenon caused by large surface hydrides in which the quality factor of the SRF cavity would be significantly degraded, even at low fields [114, 115]. More recent work on Nb-H systems has focused on understanding how hydrides contribute to high-field Q-slope (HFQS), another phenomenon in which the quality factor of a cavity becomes degraded, but only at higher fields [116–118]. There are two primary treatments for HFQS in Nb SRF cavities: nitrogen doping and low-temperature bakes. These methods have been studied extensively [119–127], yet the exact mechanisms for how they inhibit hydride formation, and how the hydrides themselves lead to HFQS are still open questions.

Hydride formation occurs at cryogenic temperatures in a process analogous to familiar water vapor condensation, where the high-entropy “gas” of interstitial hydrogen minimizes its free energy by organizing into “droplets,” i.e. hydride crystals. These crystals can accurately be described as low-energy ordered configurations of interstitial hydrogen with some accompanying distortion of the niobium lattice [128]. In general, the physics of droplet formation is not trivial because there is a surface energy associated with the droplets which competes with the volume energy associated with the bulk phase transition. The volume energy grows with the cube of hydride radius while the surface energy grows with the square of hydride radius. Thus, for given conditions of hydrogen chemical potential and temperature, there is a “critical" droplet radius above which hydride crystals are stable and below which they are unstable [129]. The fact that sub-critical droplets are unstable

means that the hydrogen atoms must form a super-critical droplet purely by statistical chance, so that there is a free energy barrier to hydride precipitation which is potentially much larger than the thermal energy scale. The rate of droplet nucleation depends exponentially on this ratio and so can potentially be many orders of magnitude slower than the hopping rate of impurities.

The free energy barrier to hydride precipitation depends on the size of the critical droplet, which generally varies throughout a macroscopic sample. Of particular interest are the places where the critical droplet size and corresponding free energy barrier are small enough that hydrides can form quickly relative to the typical timescale (minutes) of cavity cooldown—we will call these places “nucleation sites." Many material defects can potentially affect critical droplet size, including interstitial impurities, as well as more complex defects, such as impurity-vacancy complexes, dislocations and grain boundaries, that we will not describe in detail here. Impurities are of particular interest because their near-surface concentrations can be altered through low-temperature baking, and because first-principles calculations have previously shown that they create low-energy trap sites for hydrogen, potentially encouraging hydride nucleation [119].

We present a new theory for the important physical effects of low-temperature bakes, how they improve cavity performance, and what can be done to further improve high-field quality factors. We use time-dependent Ginzburg-Landau theory to calculate dissipation from sub-surface hydrides, finding good qualitative agreement with experimentally-observed HFQS behavior [121] and a clear relationship between hydride size, position, and HFQS onset field. We argue that increasing the concentration of hydride nucleation sites by impurity doping effectively decreases the typical size of hydrides, delaying the onset of HFQS and improving cavity performance. Our results lend additional credibility to the idea that low-temperature bakes and nitrogen doping affect high-field cavity behavior by controlling the size and distribution of hydride precipitates.

3.2 Methods

3.2.1 The Time-Dependent Ginzburg-Landau Equations

Ginzburg-Landau (GL) theory is one of the oldest theories of superconductivity, and it remains relevant today owing to its relative simplicity and direct physical insights into the electrodynamic response of superconductors under static applied fields and currents [93]. The *time-dependent* Ginzburg-Landau (TDGL) equations were originally proposed by Schmid [17] in 1966 and Gor'kov and Eliashberg [18] derived them rigorously from BCS theory later in 1968. The TDGL equations (in Gaussian units) are given by:

$$\Gamma\left(\frac{\partial\psi}{\partial t}+\frac{ie_s\phi}{\hbar}\psi\right)+\frac{1}{2m_s}\left(-i\hbar\nabla-\frac{e_s}{c}\mathbf{A}\right)^2\psi+\alpha\psi+\beta|\psi|^2\psi=0 \tag{3.1}$$

$$\frac{4\pi\sigma_n}{c}\left(\frac{1}{c}\frac{\partial\mathbf{A}}{\partial t}+\nabla\phi\right)+\nabla\times\nabla\times\mathbf{A}-\frac{2\pi ie_s\hbar}{m_sc}\left(\psi^*\nabla\psi-\psi\nabla\psi^*\right)+\frac{4\pi e_s^2}{m_sc^2}|\psi|^2\mathbf{A}=0. \tag{3.2}$$

These equations are solved for the complex superconducting order parameter, ψ, and the magnetic vector potential, $\mathbf{A}$. The magnitude squared of ψ is proportional to the density of superconducting electrons. The parameters α and β are phenomenological, and were originally introduced as coefficients of the series expansion of the Ginzburg-Landau free energy. Additionally, ϕ is the scalar potential; σ_n is the normal electron conductivity; Γ is the phenomenological relaxation rate of ψ. Furthermore, $e_s=2e$ and $m_s=2m_e$ represent the total charge and total effective mass of a Cooper pair, respectively. The TDGL equations are subject to boundary conditions

$$\left(i\hbar\nabla\psi+\frac{e_s}{c}\mathbf{A}\psi\right)\cdot\mathbf{n}=0 \tag{3.3}$$

$$(\nabla\times\mathbf{A})\times\mathbf{n}=\mathbf{H}_a\times\mathbf{n} \tag{3.4}$$

$$\left(\nabla\phi+\frac{1}{c}\frac{\partial\mathbf{A}}{\partial t}\right)\cdot\mathbf{n}=0, \tag{3.5}$$

where $\mathbf{n}$ is the outward normal vector to the boundary surface and $\mathbf{H}_a$ is the applied magnetic field.

The TDGL equations can also be derived from microscopic theory using the time-dependent Gor'Kov equations [18]. A useful consequence of this derivation is that it allows the TDGL parameters to be directly related to experimentally observable properties of the material in question. The material dependencies are given by Ref. 24:

$$\alpha(\nu(0), T_c, T) = -\nu(0)\left(1 - \frac{T}{T_c}\right) \tag{3.6}$$

$$\beta(\nu(0), T_c, T) = \frac{7\zeta(3)\nu(0)}{8\pi^2 T_c^2} \tag{3.7}$$

$$\Gamma(\nu(0), T_c) = \frac{\nu(0)\pi\hbar}{8T_c} \tag{3.8}$$

$$m_s = \frac{12\hbar T_c}{\pi\nu(0)v_f\ell}, \tag{3.9}$$

where $\nu(0)$ is the density of states at the Fermi-level, T_c is the critical temperature, T is the temperature, $\zeta(x)$ is the Riemann zeta function, v_f is the Fermi velocity, and ℓ is the electron mean free path. Equation 3.9 gives the effective mass specifically under the dirty limit. In order to incorporate spatially varying effective mass in the Ginzburg-Landau free energy variations, Equation 3.1 should be augmented with an additional term:

$$\frac{i\hbar}{2}\nabla\frac{1}{m_s}\cdot(i\hbar\nabla + \frac{e}{c}\mathbf{A})\psi$$

Additionally, when solving the TDGL equations numerically, it is standard to normalize all the parameters of the model in order to obtain dimensionless quantities. To do so we introduce the following transformations:

$$\alpha \longrightarrow \alpha_0 a(\mathbf{r}) \tag{3.10}$$

$$\beta \longrightarrow \beta_0 b(\mathbf{r}) \tag{3.11}$$

$$\Gamma \longrightarrow \Gamma_0 \gamma(\mathbf{r}) \tag{3.12}$$

$$m_s \longrightarrow m_0 \mu(\mathbf{r}) \tag{3.13}$$

$$\sigma_n \longrightarrow \sigma_{n0} s(\mathbf{r}). \tag{3.14}$$

substituting these values into Eqs. 3.1 and 3.2:

$$\gamma\left(\frac{\partial\psi}{\partial t}+i\kappa_0\phi\psi\right)+\frac{1}{\mu}\left(\frac{-i}{\kappa_0}\nabla-\mathbf{A}\right)^2\psi+\frac{1}{\kappa_0}\nabla\frac{1}{\mu}\cdot\left(\frac{1}{\kappa_0}\nabla-i\mathbf{A}\right)\psi-a\psi+b|\psi|^2\psi=0 \quad (3.15)$$

$$\frac{s}{u_0}\left(\frac{\partial\mathbf{A}}{\partial t}+\nabla\phi\right)+\nabla\times\nabla\times\mathbf{A}+\frac{i}{2\kappa_0\mu}\left(\psi^*\nabla\psi-\psi\nabla\psi^*\right)+\frac{1}{\mu}|\psi|^2\mathbf{A}=0, \quad (3.16)$$

where $\kappa_0=\frac{\lambda_0}{\xi_0}$ is the Ginzburg-Landau parameter of the reference material. The quantity $\lambda_0=\sqrt{\frac{m_0c^2\beta_0}{4\pi e_s^2|\alpha_0|}}$ is the penetration depth of the reference material, and $\xi_0=\sqrt{\frac{\hbar^2}{2m_0|\alpha_0|}}$ is its coherence length. The parameter $u_0=\frac{\tau_{\psi_0}}{\tau_{j_0}}$ is a ratio of characteristic time scales in the reference material, where $\tau_{\psi_0}=\frac{\Gamma_0}{|\alpha_0|}$ is the characteristic relaxation time of ψ in the reference material and $\tau_{j_0}=\frac{\sigma_{n0}m_0\beta_0}{e_s^2|\alpha_0|}$ is the characteristic relaxation time of the current. We have also inserted a minus in front of a, which is just a convention to make positive values of a correspond to the superconducting state (Note: this is the opposite of how α is usually interpreted within Ginzburg-Landau theory, however it is standard to make this change when performing nondimensionalization). The boundary conditions become:

$$\left(\frac{i}{\kappa_0}\nabla\psi+\mathbf{A}\psi\right)\cdot n=0 \quad (3.17)$$

$$(\nabla\times\mathbf{A})\times n=\mathbf{H}_a\times n \quad (3.18)$$

$$\left(\nabla\phi+\frac{\partial\mathbf{A}}{\partial t}\right)\cdot n=0. \quad (3.19)$$

3.2.2 Calculating Values for the TDGL Parameters via DFT

To determine appropriate values for $a(\mathbf{r})$, $b(\mathbf{r})$, $\gamma(\mathbf{r})$, and $\mu(\mathbf{r})$, we will consider experimental results from the literature and perform *ab initio* density-functional theory (DFT) calculations where direct experimental measurements are unavailable. From Eqs. 2.6-2.9, we know these parameters mostly depend on well-defined microscopic quantities, namely $\nu(0)$, T_c, v_f, and ℓ all of which can be calculated using DFT. To do so we use the JDFTx software package with the PBE exchange-correlation functional and ultrasoft pseudopotentials [130–132]. In order to perform precise integrals

over the Fermi surface, we use the Wannier function method as implemented in the FeynWann package for JDFTX [133–136]. Fermi-surface integrals immediately give values for $\nu(0)$ and v_f, while T_c is calculated by calculating the phonon dispersion, applying Eliashberg theory, and using the McMillan formula with $\mu* = 0.12$ [137,138]. To estimate electron mean free path ℓ, we consider electron scattering off of the perturbing potential of a hydrogen vacancy as the likely principal defect in NbH, with a defect fraction of 0.075 corresponding to the hydrogen-poor compositional limit of the β hydride phase [139].

Niobium hydride calculations used an 8-atom fcc unit cell with $6 \times 6 \times 9$ k-point folding. Fermi surface integrals for $\nu(0)$, v_f, and ℓ used an energy-conserving delta function width of 5mH, and used the Wannier method to interpolate the k-space mesh to a 16x finer k-space mesh. The Fermi surface integral for T_c used an energy-conserving delta function width of 0.74mH and a 24x finer k-space mesh. For perturbing potentials of phonon modes and hydrogen vacancy defects, we used a 96-atom supercell of this unit cell. a planewave cutoff energy of 20 Hartree, and an effective electron temperature of 5mH.

Experiment can then give information about the compositions of sample materials, and DFT calculations can determine the $\nu(0)$, v_f, and T_c associated with these compositions. Using these values in addition to estimates of the electron mean free path (which can be derived from DFT or can come from experimental characterizations), $a(\mathbf{r})$, $b(\mathbf{r})$, $\gamma(\mathbf{r})$,and $\mu(\mathbf{r})$ are calculated from Eqs. 2.6-2.9, and the material geometries from the experimental results determine the spatial variation.

3.2.3 Dissipation in TDGL

When simulating SRF materials, dissipation is often a physical quantity of interest. While TDGL allows us to estimate dissipation, it is important to emphasize that both the dissipation calculations and the quality factor estimates that follow lie well outside the regime of quantitative validity for the theory. In particular, TDGL is strictly valid only near T_c in the gapless limit, and its predictions

for dissipation under RF-like dynamic fields at low temperatures should be interpreted with caution. Despite this, we believe the calculations presented here remain qualitatively valuable. They provide a means of linking mesoscopic-scale simulations to macroscopic cavity performance metrics, and enable relative comparisons between different material configurations that may inform experimental priorities.

Under TDGL, a formula for dissipation can be derived by considering the time derivative of the free energy and the free energy current flux density. A more detailed derivation is found in Ref. 24, but we quote the final result here:

$$D = 2\Gamma \left| \left(\frac{\partial \psi}{\partial t} + \frac{i e_s \phi \psi}{\hbar} \right) \right|^2 + \sigma_n \mathbf{E}^2. \tag{3.20}$$

This quantity is a power density, with the first term corresponding to the superconducting dissipation arising from the relaxation of the order parameter. The second term is the dissipation of normal currents which are largest near the surface where magnetic field can still appreciably penetrate.

A particularly relevant quantity that can be estimated from the dissipation is the cavity quality factor, Q, which is given by

$$Q = \frac{2\pi E}{\Delta E}, \tag{3.21}$$

where E is the energy stored in the cavity and ΔE is the energy dissipated in the cavity walls each RF period. It is common to express the quality factor as

$$Q = \frac{G}{R_s}, \tag{3.22}$$

where R_s is the cavity surface resistance and G is a geometric factor that depends only on quantities which are determined by the cavity geometry. For a typical 1.3 GHz 9-cell Nb TESLA cavity, $G = 270\ \Omega$ [105]. The surface resistance is given by

$$R_s = \frac{\mu_0 \omega \lambda^3}{\tilde{H}_a^2 L_x L_y} \left(I_\psi + \omega \frac{\sigma_n \mu_0 \lambda^2 T_{sim}}{2\pi} I_A \right), \tag{3.23}$$

where μ_0 is the permeability of free space, ω is the cavity frequency, λ is the penetration depth, $\tilde{H}_a$ is the maximum applied magnetic field value in simulation units, L_x and L_y are the size of a simulation domain in the X and Y directions respectively, σ_n is the normal conductivity, and T_{sim} is the period of the applied field in simulation time units. I_ψ and I_A are integrals over the squared time derivatives of ψ and $\mathbf{A}$:

$$I_\psi \equiv \int d\tilde{t} \int d\tilde{x} \int d\tilde{y} \int d\tilde{z} \left| \frac{\partial \tilde{\psi}}{\partial \tilde{t}} \right|^2 \tag{3.24}$$

$$I_A \equiv \int d\tilde{t} \int d\tilde{x} \int d\tilde{y} \int d\tilde{z} \left(\frac{\partial \tilde{\mathbf{A}}}{\partial \tilde{t}} \right)^2 \tag{3.25}$$

where the tilde variables denote ones which are in simulation units. A much more detailed derivation of these equations can be found in Reference 140.

The value of Q calculated from TDGL outputs will typically be underestimated at low field. This is because of the assumption of gapless superconductivity, which results in higher surface resistances than is predicted with the BCS surface resistance. Despite this, our approach still often predicts quality factors within an order of magnitude of the experimental values. Additionally, the relative behavior of Q at different applied fields qualitatively captures effects such as high field Q-slope. Nonetheless, we emphasize that this quality factor calculation is best treated as a qualitative tool; for quantitatively accurate predictions, more rigorous superconductivity theories should be used.

3.2.4 Estimating Effective TDGL Parameters

In certain situations, a system may behave as if it were a single, homogeneous material, even if it consists of multiple distinct components. One such case occurs when numerous small defects, such as nano-hydrides, are distributed across a surface, leading to a collective behavior that resembles a new effective material. This subsection outlines the method we developed to extract the effective TDGL parameters of such systems, allowing us to estimate how the material's properties evolve when influenced by a large number of small, interacting defects.

The following discussion focuses on the case of a large number of nano-hydrides, though the general approach we describe can be applied to any system in which collective effects result in a new uniform effective material. To model this behavior, we simulate a system with a specific hydrogen concentration, using a smaller domain size of $2\lambda \times 2\lambda \times 8\lambda$ to keep computational costs manageable. The extended z-direction ensures that the order parameter, ψ, can fully reach its zero-field value without experiencing finite-size effects. Hydrides with a radius of 0.05λ are randomly placed within the domain, chosen from a uniform distribution, and added until the desired hydrogen concentration is reached, with no overlap between hydrides.

After placing the hydrides, we solve for the TDGL order parameter ψ at two distinct field conditions: zero field (to estimate the zero-field value, ψ_∞) and a low, non-zero field (to extract the coherence length, ξ). The zero-field value, ψ_∞, provides the ratio α/β through the relation:

$$|\psi_\infty|^2 = \frac{\alpha}{\beta}, \tag{3.26}$$

which is given by Tinkham [23]. However, this relation does not independently determine α or β. To resolve this, we calculate the coherence length, ξ, which depends on α. By determining ξ from the low-field solution of ψ, we can then extract the value of α, and from there, calculate β using the ratio α/β. The coherence length, ξ, is related to α by:

$$\xi^2 = \frac{\hbar^2}{2m_s\alpha}, \tag{3.27}$$

again based on Tinkham [23].

To estimate ξ, we calculate the average value of ψ in the xy-plane for each value of z at low (but non-zero) field. For a uniform material, the order parameter would follow the equation:

$$\psi(z) = \psi_\infty - Ce^{-\sqrt{2}(z_{max}-z)/\xi}, \tag{3.28}$$

where z_{max} is the z-coordinate of the top of the domain where the field is applied, with C and ξ as the fitting parameters. The fitted value of ξ can be used to estimate the coherence length. However, since our system is not truly uniform and ψ_∞ varies slightly due to the random distribution of hydrides, directly using this equation would lead to poor fits. Instead, we modify the approach by fitting the difference $\Delta\psi(z)$ between the calculated $\psi(z)$ and the local value of $\psi_\infty(z)$, where $\psi_\infty(z)$ is the zero-field value of ψ averaged over the xy-plane for each value of z. This modification effectively filters out the noise and isolates the exponential decay associated with ξ:

$$\Delta\psi(z) = \psi(z) - \psi_\infty(z) = -Ce^{-\sqrt{2}(z_{max}-z)/\xi}. \tag{3.29}$$

With ξ now estimated, we can use it to determine the effective value of α from the relationship between ξ and α, as described earlier. From this, we can also estimate β using the ratio α/β, which was determined from the zero-field solution for ψ_∞. Once the effective α and β are determined, we can estimate the critical field H_c using the relation:

$$H_c^2 = \frac{4\pi\alpha^2}{\beta}. \tag{3.30}$$

Since κ can be expressed as a function of β:

$$\kappa^2 = \frac{m_s^2 c^2 \beta}{2\pi\hbar^2 e_s^2}, \tag{3.31}$$

we now have the necessary parameters to calculate the superheating field. The superheating field for the composite material is then estimated using the formula for low κ materials [47]:

$$H_{sh} = 2^{-3/4}\kappa^{-1/2}\frac{1+4.6825120\kappa+3.3478315\kappa^2}{1+4.0195994\kappa+1.0005712\kappa^2}. \tag{3.32}$$

This formula provides an estimate of the superheating field for a system containing many small hydrides, which collectively behave as an effective material with a new κ.

3.2.5 Geometry and Numerical Approach for TDGL Simulations

A schematic of the geometry used in our TDGL simulations is shown in Fig. 3.1. The simulation domain for the large hydride simulations is a $40\lambda \times 40\lambda \times 20\lambda$ cuboid, with periodic boundary conditions applied in the x and y directions (highlighted in yellow and light blue, respectively). An external field is applied to the upper surface in the z-direction (highlighted in red), while the bottom surface (highlighted in green) is free from any applied field. The hydrides, modeled as spheres, are depicted in the figure, with dotted circles showing the projections of the spheres onto the XY, YZ, and ZX planes. These projections help orient the reader to the spatial arrangement of the hydride in three-dimensional space. The distance from the surface to the outer edge of the hydride, denoted by d, is marked on the figure and represents one of the key parameters varied in our simulations to explore how the hydride's position influences its impact on cavity performance. For the nano-hydride simulations, we used a domain of size $2\lambda \times 2\lambda \times 8\lambda$, with the same periodic boundary conditions and applied field.

The simulations were conducted using cubic meshes generated with the open-source mesh generation tool, Gmsh [96]. The OpenCASCADE geometry kernel within Gmsh was employed to adapt the mesh to the shape of the hydride islands. To solve the TDGL equations, we applied the finite element formulation proposed by Gao [25]. All computations were performed using the open-source finite element software FEniCS [26]. A detailed analysis of the methods used for solving the TDGL equations can be found in Harbick and Transtrum [140].

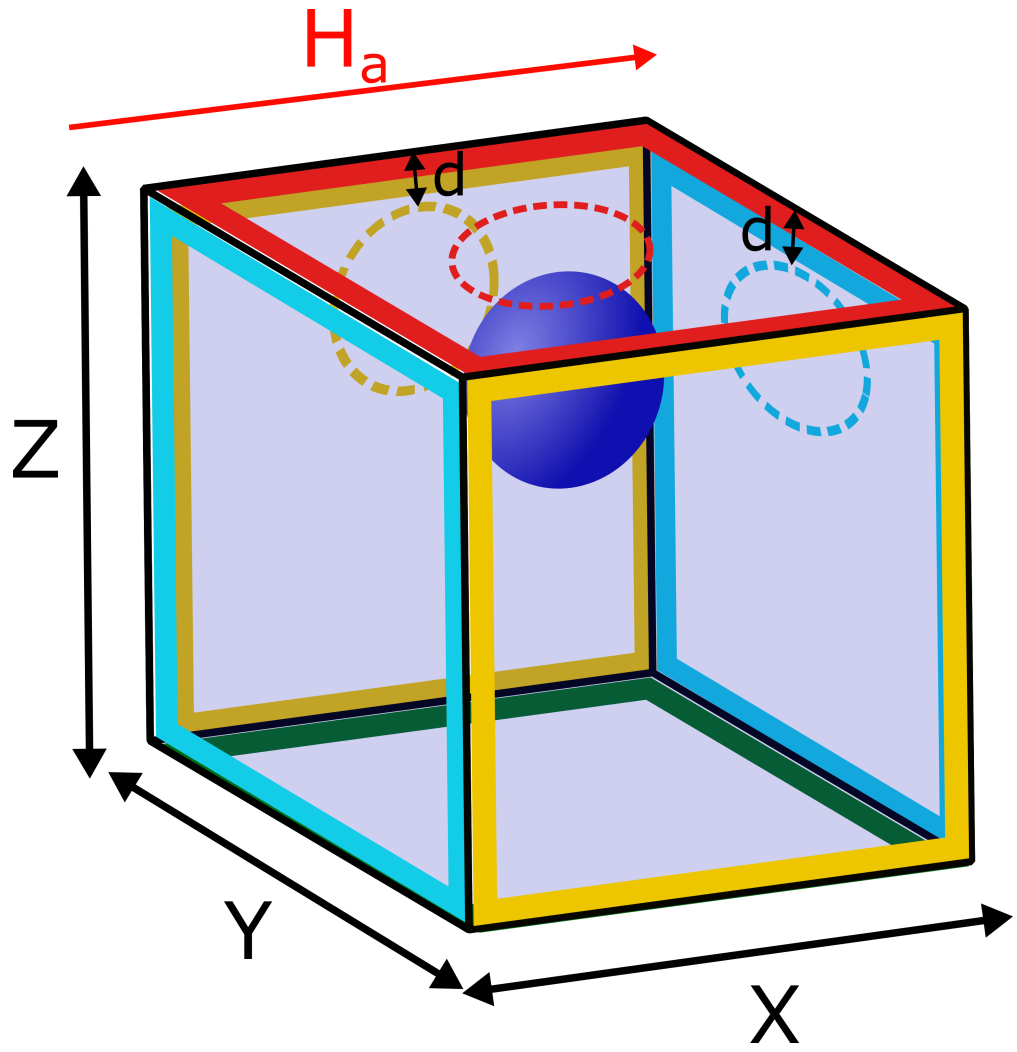

Figure 3.1 Schematic of the simulation geometry (not to scale). Surfaces outlined in yellow and light blue represent the periodic boundary conditions in the x and y directions, respectively. An external field is applied to the surface outlined in red, in the direction indicated by the arrow labeled "H_a". No field is applied to the surface outlined in green. The hydride is modeled as a dark blue sphere, with dotted lines showing the projections of the sphere onto the xy, yz, and zx planes. The color of the dotted circle corresponds to the plane in which the projection occurs. The distance from the surface to the outer edge of the hydride, denoted as d, represents the island's position relative to the surface.

3.2.6 Qualitative Random Walk Simulation of Hydride Formation

To illustrate the possible relationship between impurity-induced disorder and hydride size, we developed a simple random walk simulation of hydride formation. In this simulation, hydride nucleation sites exist at a concentration of 10^{-2} at the surface, and this concentration decays exponentially to $2 * 10^{-6}$ far beneath the surface. We vary the exponential decay constant to simulate different impurity diffusion depths. Hydrogen atoms exist at a concentration of $5 * 10^{-3}$ and undergo random walk movement on the $60 \times 60 \times 1000$ cubic simulation lattice, and become frozen when they are either adjacent to a nucleation site or adjacent to a previously-frozen hydrogen atom.

While this simulation is not rooted in physical atomic interactions and operates at a scale too small to simulate hydrides of the sizes considered in our Ginzburg-Landau simulations, it adequately illustrates the inverse relationship between local nucleation site concentration and typical hydride size. This relationship is important as we will ultimately consider the implications of our Ginzburg-Landau simulation results for developing new experimental recipes. Ongoing research seeks to develop a more physically realistic model of the effect of impurity doping on hydride size distribution.

3.3 Results

3.3.1 Nucleation Sites and Hydride Formation

The distribution of nucleation sites can greatly influence the size and location of hydrides. To illustrate this, we consider a simple classical model of hydride nucleation, which begins with a uniform concentration of free hydrogen interstitial impurities and an exponential profile of nucleation sites, a description of this method is found in Section 3.2.6. In this model, hydrogen atoms freeze if they arrive at a site adjacent to a nucleation site, or if they arrive at a site adjacent to

a frozen hydrogen interstitial. To model a niobium surface which has been impurity-doped to some degree, we take the concentration of nucleation sites to be simply proportional to the concentration of impurities. Figure 3.2 shows the results of this model. We find that a shallow doping depth results in large hydrides near the surface, while a deeper doping depth results in much smaller hydrides near the surface. Generally, hydride size is inversely proportional to nucleation site concentration, as expected.

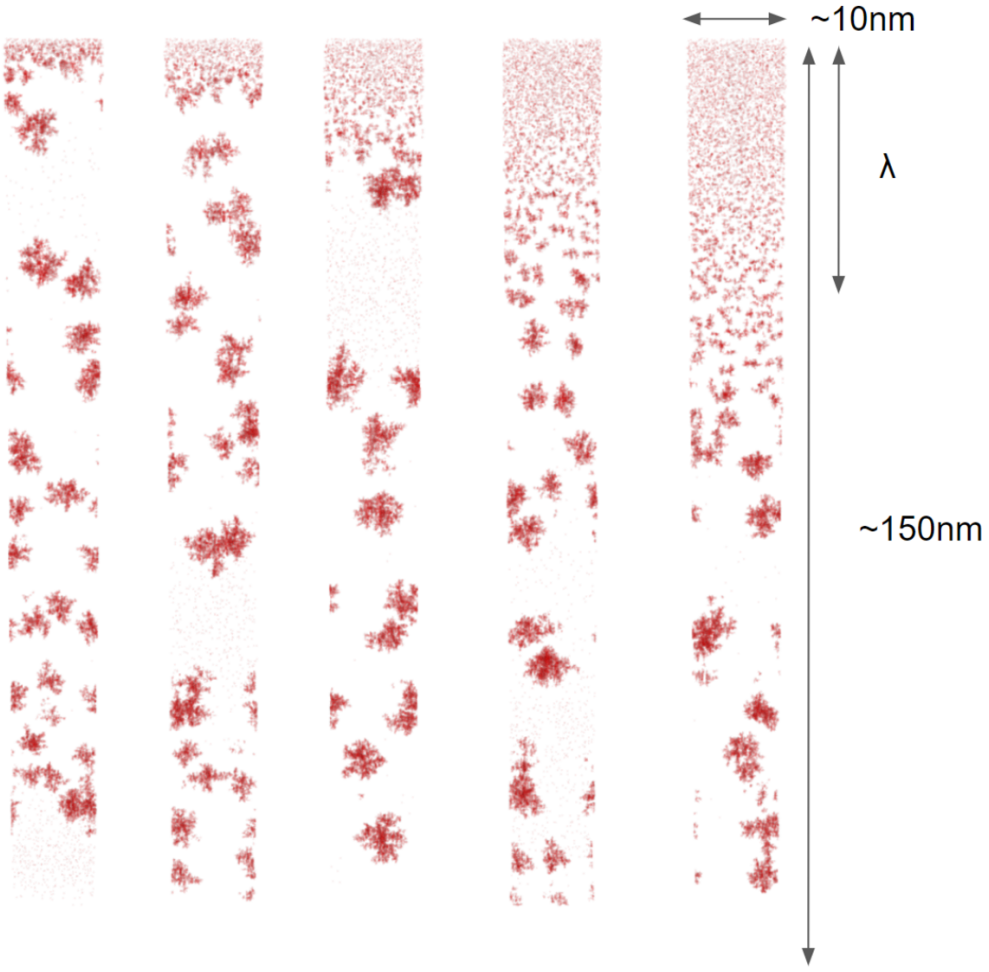

Figure 3.2 Qualitative simulations of hydride nucleation for different exponential nucleation site distributions, from shallowest (left) to deepest (right).

These results demonstrate there are, roughly speaking, two regimes for hydride precipitation: One in which there are a small number of larger, mesoscopic-scale hydrides, and another regime in which there is a large number of microscopic scale nano-hydrides. The following two subsections will address both these regimes.

3.3.2 TDGL Simulations of Mesoscopic Hydrides

To estimate the impact of mesoscopic-scale hydrides, we use density-functional theory to calculate material properties of hydrides [141], and then we perform time-dependent Ginzburg-Landau (TDGL) theory simulations of hydride dissipation, the results of which are detailed in this section.

We find that hydrides have a low-field state in which they dissipate more energy per unit volume than the superconducting niobium, resulting in a lower low-field quality factor Q_0. This dissipation is simply the result of normal currents of Bogoliubov quasiparticles moving through a material of finite resistivity; it does not cause any noticeable Q-slope, and for realistic hydride concentrations the overall effect on dissipation is small.

We find that hydrides have a fundamentally different high-field state in which a more complicated dissipation mechanism occurs, involving penetration of flux vortices. The transition from the low-field state to the high-field state is associated with an abrupt increase in calculated energy dissipation, or an abrupt onset of Q-slope, at a critical value of the peak magnetic field. Vortex penetration occurs because the proximity-coupling effect affects the superconducting properties of the niobium surface above a sub-surface hydride. This creates a weak spot where flux vortex penetration can occur at fields significantly below the superheating field (Fig. 3.3).

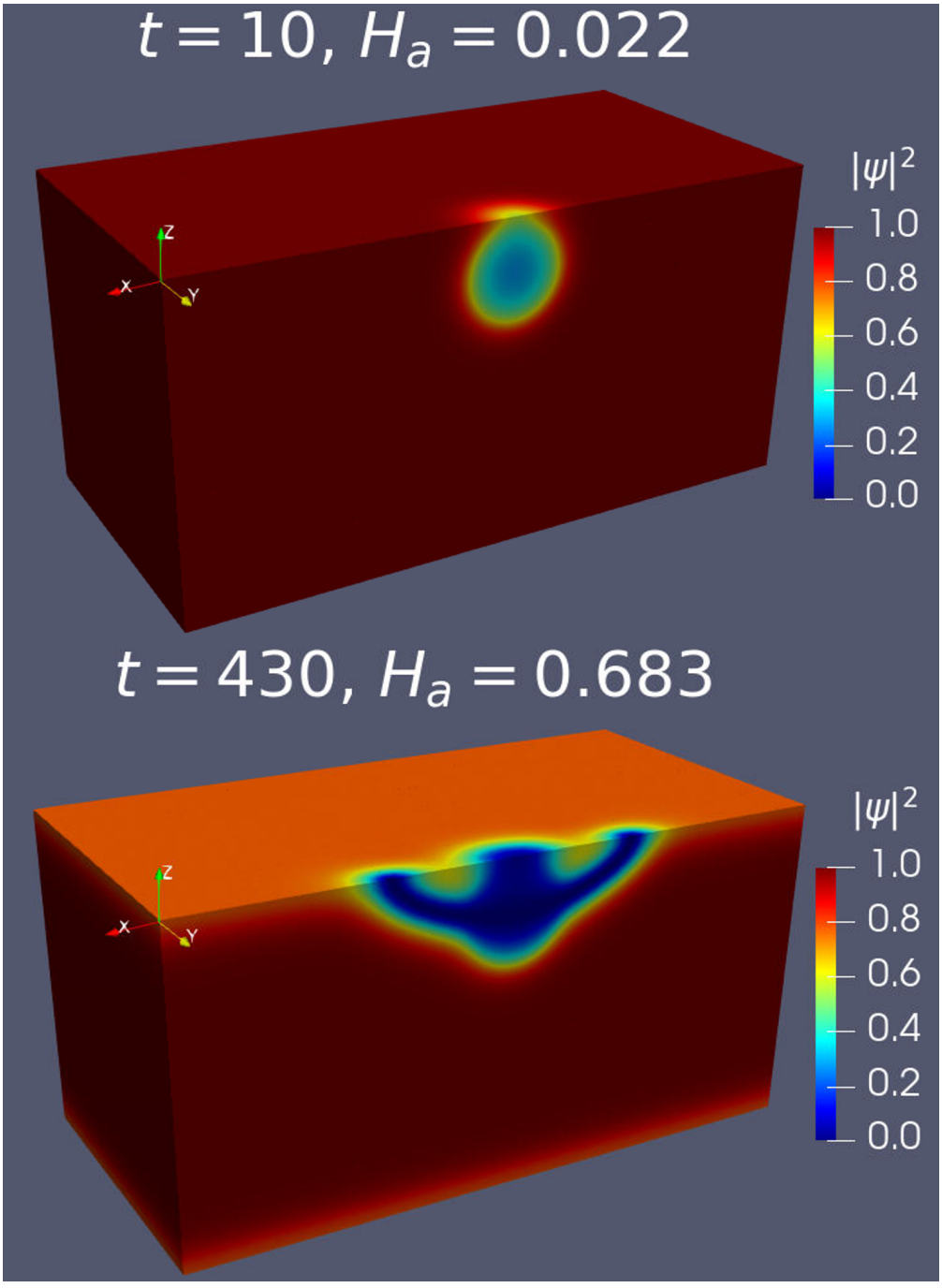

Figure 3.3 Simulations of superconducting order parameter at low field (top), showing a weak spot at the surface, and at high field (bottom) showing flux vortex entry.

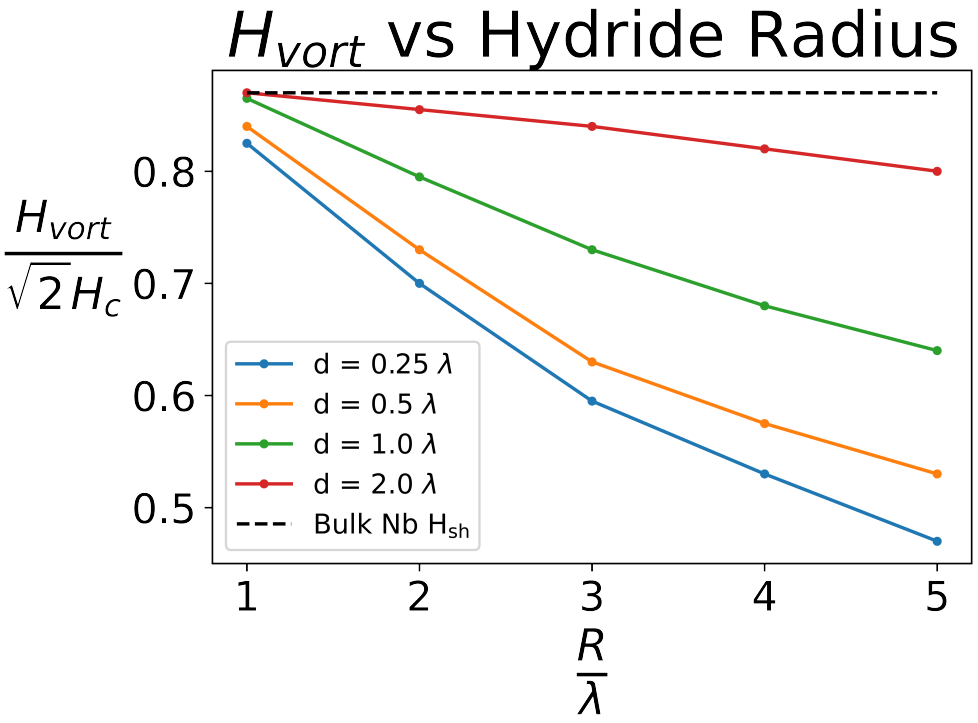

Figure 3.4 Calculated vortex entry field as a function of hydride radius for hydrides at different depths.

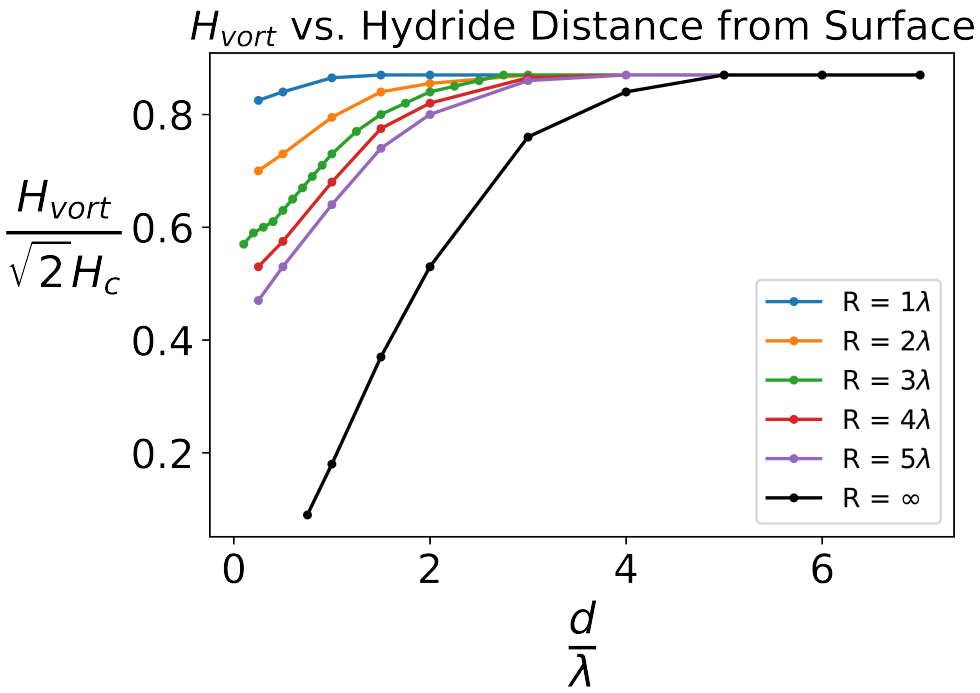

Figure 3.5 Calculated vortex entry field as a function of hydride depth for hydrides of different radii, the infinite radius hydride was simulated using a layered simulation with a layer of Nb of thickness d on top of a NbH layer.

Dissipation from hydrides in the vortex state, unlike dissipation from hydrides in the non-vortex state, is highly field-dependent. This can be explained in part by the fact that, as the field increases beyond the critical field for vortex entry into the hydride, the fraction of the RF cycle at or above this critical field increases rapidly, thus increasing the length of time per cycle that vortex-related dissipation occurs. Additionally, we find that the number of vortices entering a hydride increases with increasing field, further increasing dissipation. Together, these effects result in a steep Q-slope beyond the critical field for vortex entry.

Hydride size and proximity to the surface play a crucial role in determining the critical field for vortex entry into the hydride. Figure 3.4 shows the vortex penetration field H_{vort} versus Hydride radius (R). The vortex penetration field consistently decreases with respect to hydride size, meaning that larger hydrides will achieve the vortex state at lower field thresholds. Additionally, we see that the decrease in H_{vort} with respect to hydride radius becomes larger as the hydrides form closer to the surface. This can also be seen in Figure 3.5, which depicts H_{vort} versus d. Finite-size hydrides with radius $R = 5\lambda$ nucleated vortices $\sim 50\%$ below the bulk superheating field value. We additionally calculated H_{vort} for a hydride of infinite size. This was done by simulating a layer of Nb of thickness d on top of a hydride layer which, due to the periodic boundary conditions, represents a hydride of infinite size. The lowest thickness layer simulated this way was for $d = 0.75\lambda$, which resulted in $H_{vort} = 0.09\sqrt{2}H_c$, for values of d smaller than this, the Nb layer was unable to maintain superconductivity and the whole system would quench for any nonzero applied field. The infinite hydride represents a limiting case for the impact that hydrogen can have on SRF performance, and the behavior we observe in our simulations is consistent with the “Hydrogen Q-disease" which is attributed to large hydride precipitates.

The distribution of hydrides has an important effect on cavity quality factor at high fields, specifically by altering the adverse high-field Q-slope (HFQS) behavior. Our results indicate that even modest changes to the characteristic size of near-surface hydrides can explain experimentally observed changes in the onset field of the high-field Q-slope (Fig. 3.6) [121].

The Q-factor calculations in Fig. 3.6 assume that each cavity contains exclusively one type of hydride, with fixed size and position. To relax this assumption, we can incorporate multiple types of hydrides, making certain assumptions about their distribution within the cavity. By combining the dissipation estimates for each hydride type, we can calculate a weighted average of the dissipation values according to the distribution of hydride types. This yields a new composite Q-slope that reflects the impact of the entire hydride distribution.

Figure 3.7 shows simulations based on these distributions. The black curve represents the quality factor for a simulation with no hydrides. The blue curve corresponds to a uniform distribution of both hydride size and position, meaning all defects are equally likely. The yellow curve assumes hydride size is uniformly distributed, while the distance between hydrides follows an exponential distribution, with a higher likelihood of hydrides near the surface. The green curve assumes a uniform distance distribution, but with hydride sizes exponentially distributed, meaning larger hydrides are more common. Finally, the red curve assumes both hydride size and distance follow exponential distributions, with large hydrides near the surface being most frequent.

These distributions are idealized, and future work could incorporate more detailed experimental characterizations of hydride size and position distributions, as well as simulations of a wider variety of hydride types. Nevertheless, the current results remain qualitatively informative: the simulated quality factor curves are consistent with those observed experimentally. This supports our assertion that the dissipation mechanism responsible for the high-field Q-slope in some Nb cavities is hydride-induced vortex nucleation, and that eliminating large, near-surface hydrides is key to reducing

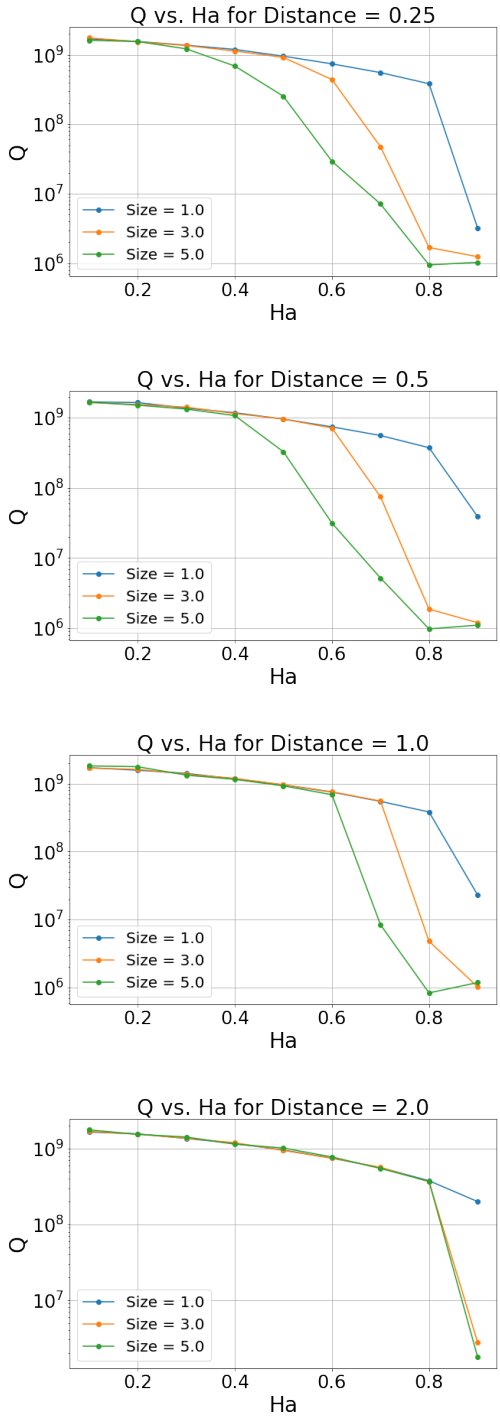

Figure 3.6 Calculated quality factor as a function of field for hydrides at different depths (from shallowest at the top to deepest at the bottom) and of different sizes (different colored lines in each plot).

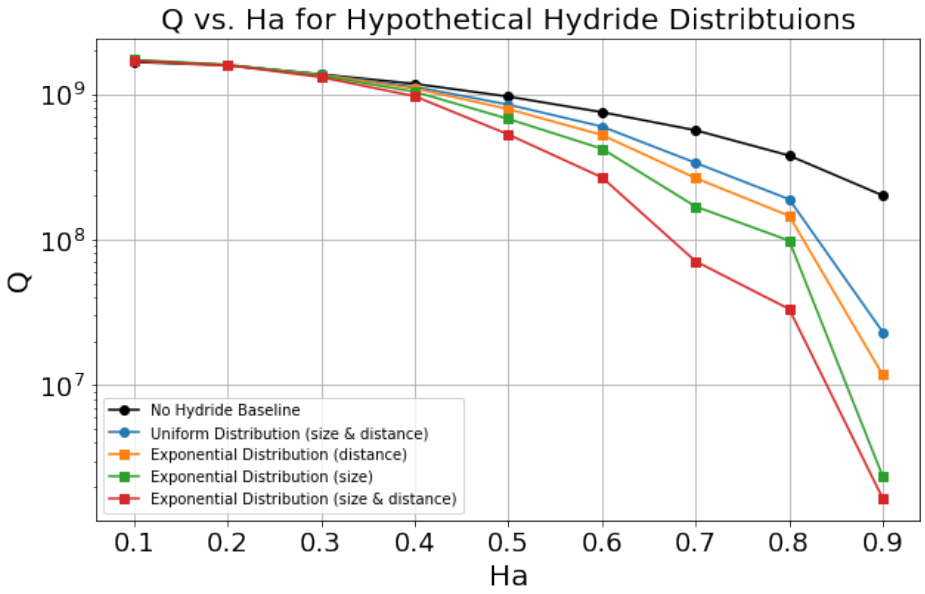

Figure 3.7 Hypothetical quality factor versus applied field curves for different hydride distributions. The black curve represents the baseline simulation with no hydrides. The blue curve assumes a uniform distribution of both hydride size and position. The yellow curve assumes a uniform hydride size distribution and an exponential distribution of hydride distances, with a higher likelihood of hydrides near the surface. The green curve assumes a uniform distribution in distance and an exponential distribution in hydride size, with larger hydrides being more probable. The red curve assumes both hydride size and distance follow exponential distributions, with large hydrides near the surface being most common.

high-field quality slope (HFQS) in Nb SRF cavities. As shown in Fig. 3.2, procedures designed to reduce hydride size might instead lead to the formation of a large number of nano-hydrides. While individual nano-hydrides may have negligible effects, we now turn to explore the potential collective effects when a large number of nano-hydrides are present.

3.3.3 Nano-hydride simulations

In this section, we perform TDGL simulations to investigate the collective effects of a large number of nano-hydrides. The simulations were conducted using the methods described in Section 3.2.4, with a domain size of $2\lambda \times 2\lambda \times 8\lambda$. A nano-hydride radius of 0.05λ was chosen as a representative case for hydrides that, on their own, would be considered negligible. We ran simulations varying the number of nano-hydrides from 0 to 2000, corresponding to hydrogen concentrations between 0% and 3.2%. This range was chosen based on the expectation that typical local hydrogen concentrations in SRF cavities would not exceed 3%.

The hydrogen concentration, C_H, is estimated using the formula:

$$C_H = \frac{V_H}{V_{Nb} + V_H}, \tag{3.33}$$

where V_H is the volume of the hydrides and V_{Nb} is the volume of niobium in the simulation domain. In this case, the entire domain contains niobium, so $V_{Nb} = 32$, and $V_H = \frac{4}{3}\pi(0.05)^3 N$, where N is the number of hydrides in the given simulation.

Following the methods outlined in Section 3.2.4, we calculate $|\psi_\infty|^2$ and ξ as functions of hydrogen concentration (see Fig. 3.8). From these values, we estimate α and β relative to the corresponding values for Nb, and then use Eqs. 3.31 and 3.32 to estimate the critical field H_c and superheating field H_{sh}. The resulting superheating field estimate is shown in Figure 3.9, where we plot H_{sh} relative to the superheating field of pure niobium, H_{sh}^{Nb}.

For hydrogen concentrations below approximately 0.2%, H_{sh} quickly decreases by around 5% from H_{sh}^{Nb}. This is observed in simulations with fewer than 100 hydrides, where the number of hydrides is insufficient to create an effective new material. Once the number of hydrides exceeds 100, the hydrides begin to collectively behave as an effective medium, and H_{sh} stabilizes at about 5% below H_{sh}^{Nb}. Beyond this point, H_{sh} continues to gradually decrease with increasing hydrogen concentration. The fluctuations in H_{sh} are due to variability in the ξ fits across different simulations.

The overall decrease in H_{sh} due to the collective effects of nano-hydrides is around $5\% - 7\%$. This change is significantly smaller than the impact of larger, single hydrides, supporting the idea that smaller hydrides, even in large quantities, result in improved cavity performance. This finding offers a potential explanation for how low-temperature baking and nitrogen doping procedures can reduce high-field Q-slope by promoting the formation of smaller near-surface hydrides, which are less detrimental to cavity performance.

3.4 Conclusions

In this study, we investigated the effects of hydride size and position on the high-field Q-slope (HFQS) in Nb SRF cavities. We performed TDGL simulations of hydrides with varying sizes and distributions, focusing on how these factors influence the superconducting properties of the cavities. Our results show that hydrides, particularly those near the surface, play a significant role in the onset of HFQS. We found that larger hydrides, which transition into the vortex state at lower fields, are the primary contributors to the observed dissipation at high fields. In contrast, smaller hydrides, even in large quantities, have a much smaller impact on vortex nucleation and do not significantly affect the cavity performance.

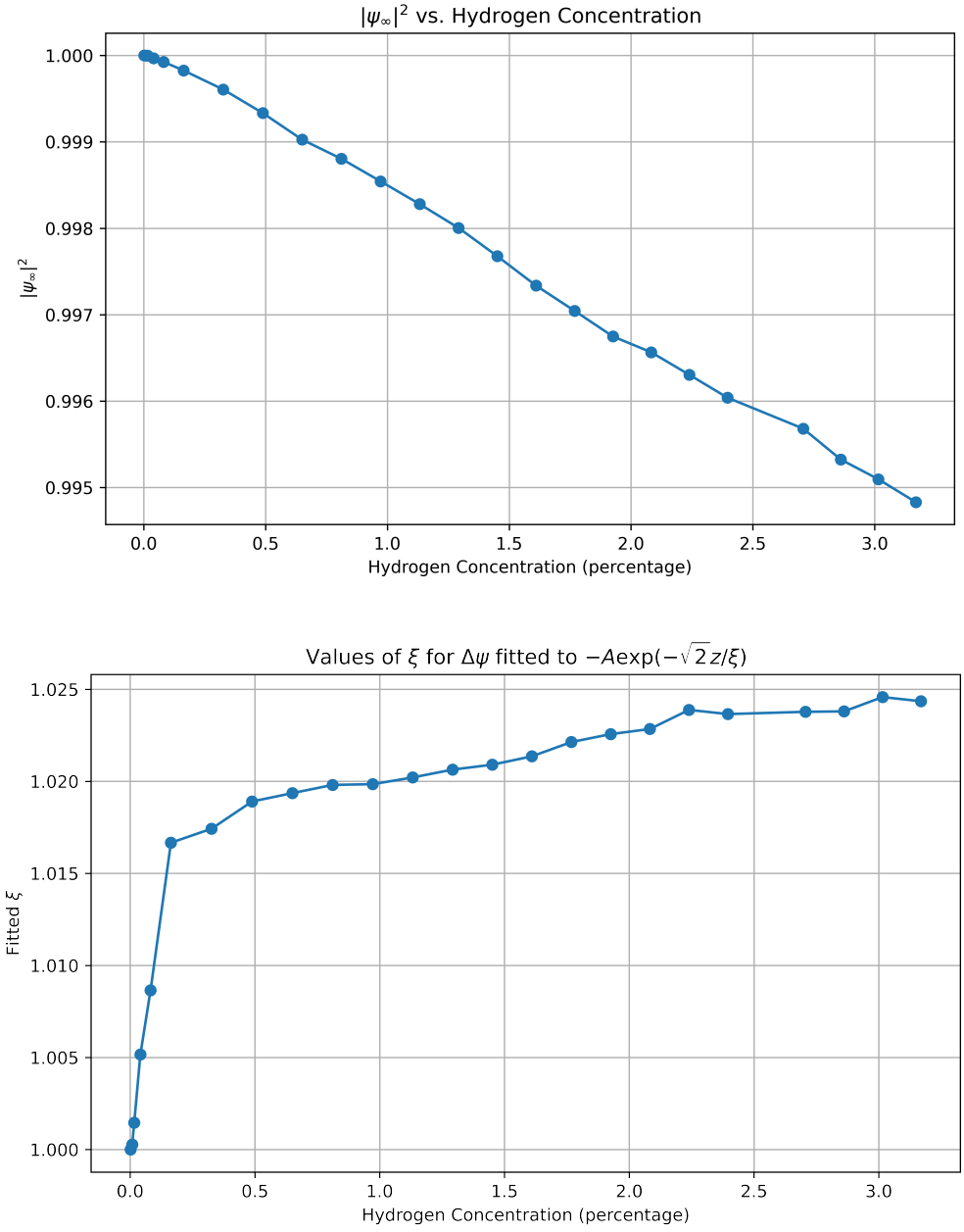

Figure 3.8 Calculated values of $|\psi_\infty|^2$ (top) and ξ (bottom) as functions of hydrogen concentration.

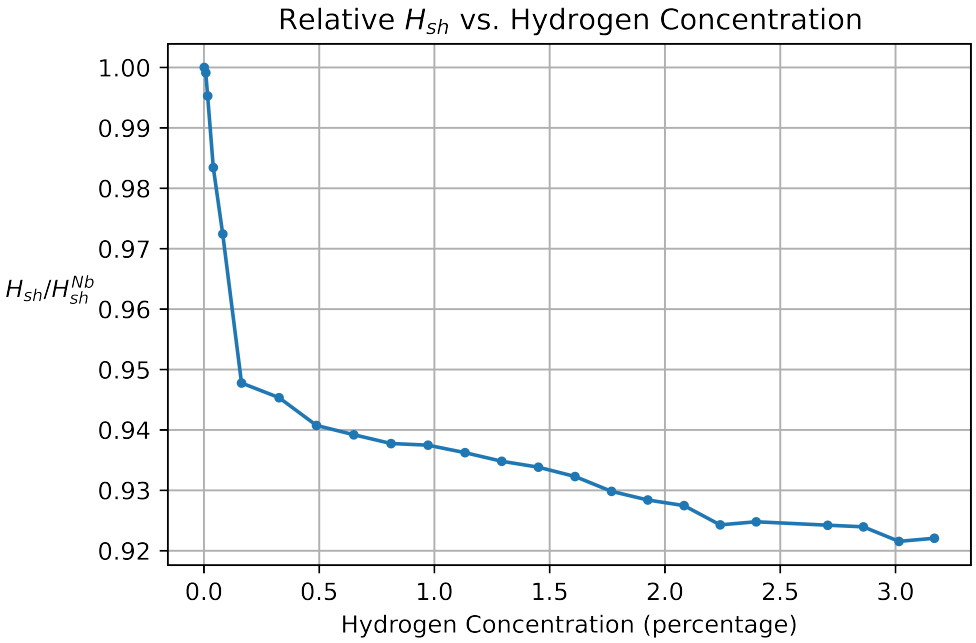

Figure 3.9 Plot of relative H_{sh} versus hydrogen concentration. The relative H_{sh} is shown with respect to the superheating field of pure niobium, H_{sh}^{Nb}. A decrease of approximately 5% in H_{sh} is observed once the hydrogen concentration exceeds 0.2%, slowly decreasing on average with increasing hydrogen concentration.

We expect that in a realistic surface with a distribution of hydride sizes and positions, there will be a gradual transition from low-field behavior with little to no Q-slope to high-field behavior with a steep Q-slope at fields where “typical" near-surface hydrides transition into the vortex state. This trend is qualitatively consistent with experimental Q-slope measurements in low-temperature baked cavities, as well as measurements in “clean" cavities, which do not undergo baking and have very low impurity content. Cavities with low impurity content or relatively short exponential doping profiles typically show a low-field state with little Q-slope, followed by a distinct high-field quality slope (HFQS) state. As noted by other researchers, the onset of HFQS is directly related to impurity doping [142], and our model is consistent with this observation if the characteristic size of hydrides is inversely proportional to impurity concentration.

We emphasize that this mechanism differs subtly from previous proposals, in which impurities were thought to trap near-surface hydrogen and prevent hydride formation. While it is unlikely that impurities can completely prevent hydride formation by trapping hydrogen, our results indicate that it is not necessary to entirely eliminate hydrides to reduce HFQS. The key factor is eliminating large hydrides, which transition into the vortex state significantly below the niobium superheating field. Therefore, counterintuitively, creating more hydride nucleation sites near the surface can be beneficial by reducing the characteristic size of hydrides.

Our simulations support the idea that decreasing the size of hydrides is the most important factor for improving Nb SRF cavity performance, with the distance from the surface being the next most important factor. The dissipation mechanism behind HFQS in our simulations is hydride-induced vortex nucleation, which contrasts with the mechanism proposed in a 2013 study by Romanenko et al. [117], which suggested that proximity breakdown in the hydrides was responsible for HFQS.

While caution is needed in quantitatively interpreting quality factor and dissipation from TDGL simulations, as these are primarily qualitative tools, the simulations provide valuable insights into the underlying mechanisms. The steady-state properties, such as critical fields, offer more quantitative validity, particularly in the dirty limit where our simulations are most relevant.

Overall, our results provide new insights into the role of hydrides in the dissipation mechanisms that cause HFQS in Nb SRF cavities. We hope that these findings can guide future cavity construction and performance refinement, particularly in optimizing hydride size and distribution to improve cavity performance at high fields.

Chapter 4

Stoichiometric Surface Defects in Nb_3Sn

The following paper is one that I wrote in collaboration with several groups from CBB. Sarah Willson from the Sibener group at the University of Chicago and I share co-first authorship over this paper, and the two of us are jointly responsible for most of the text. The UHV-grown samples as well as the SEM and EDS characterizations were done by Sarah Willson, Van Do, and Helena Lew-Kiedrowska in the Sibener group at the University of Chicago. The furnace-grown samples were done by Liana Shpani in the Liepe group at Cornell University. I performed the TDGL simulations and theoretical calulations of superheating field values for differen Sn concentrations. In this paper we demonstrate the impacts that several different surface defects have on Nb_3Sn cavity performance. The paper was published on November 13, 2024 in Phys. Rev. Research **6**, 043133. It is available via open-access at: https://journals.aps.org/prresearch/abstract/10.1103/PhysRevResearch.6.043133. I hereby confirm that the use of this article is compliant with all publishing agreements.

Impact of submicron Nb_3Sn stoichiometric surface defects on high-field superconducting radiofrequency cavity performance

Sarah A. Willson,[1,*,†] Aiden V. Harbick,[2,*] Liana Shpani,[3] Van Do,[1] Helena Lew-Kiedrowska,[1] Matthias U. Liepe,[3] Mark K. Transtrum,[2] and S. J. Sibener[1,‡]

[1]*The James Franck Institute and Department of Chemistry, The University of Chicago, 929 E. 57th Street, Chicago, Illinois 60637, USA*

[2]*Department of Physics and Astronomy, Brigham Young University, Provo, Utah 84604, USA*

[3]*Cornell Laboratory for Accelerator-Based Sciences and Education, Cornell University, Ithaca, New York 14853, USA*

(Received 3 July 2024; accepted 8 October 2024; published 13 November 2024)

Nb_3Sn film coatings have the potential to drastically improve the accelerating performance of Nb superconducting radiofrequency (SRF) cavities in next-generation linear particle accelerators. Unfortunately, persistent Nb_3Sn stoichiometric material defects formed during fabrication limit the cryogenic operating temperature and accelerating gradient by nucleating magnetic vortices that lead to premature cavity quenching. The SRF community currently lacks a predictive model that can explain the impact of chemical and morphological properties of Nb_3Sn defects on vortex nucleation and maximum accelerating gradients. Both experimental and theoretical studies of the material and superconducting properties of the first 100 nm of Nb_3Sn surfaces are complicated by significant variations in the volume distribution and topography of stoichiometric defects. This work contains a coordinated experimental study with supporting simulations to identify how the observed chemical composition and morphology of certain Sn-rich and Sn-deficient surface defects can impact the SRF performance. Nb_3Sn films were prepared with varying degrees of stoichiometric defects, and the film surface morphologies were characterized. Both Sn-rich and Sn-deficient regions were identified in these samples. For Sn-rich defects, we focus on elemental Sn islands that are partially embedded into the Nb_3Sn film. Using finite element simulations of the time-dependent Ginzburg-Landau equations, we estimate vortex nucleation field thresholds at Sn islands of varying size, geometry, and embedment. We find that these islands can lead to significant SRF performance degradation that could not have been predicted from the ensemble stoichiometry alone. For Sn-deficient Nb_3Sn surfaces, we experimentally identify a periodic nanoscale surface corrugation that likely forms because of extensive Sn loss from the surface. Simulation results show that the surface corrugations contribute to the already substantial drop in the vortex nucleation field of Sn-deficient Nb_3Sn surfaces. This work provides a systematic approach for future studies to further detail the relationship between experimental Nb_3Sn growth conditions, stoichiometric defects, geometry, and vortex nucleation. These findings have technical implications that will help guide improvements to Nb_3Sn fabrication procedures. Our outlined experiment-informed theoretical methods can assist future studies in making additional key insights about Nb_3Sn stoichiometric defects that will help build the next generation of SRF cavities and support related superconducting materials development efforts.

DOI: 10.1103/PhysRevResearch.6.043133

I. INTRODUCTION

Extensive resources and research personnel have been put towards optimizing the accelerating gradients in accelerator and high energy collider facilities, such as the LCLS-II at SLAC National Laboratory [1]. Current state-of-the-art linear accelerators utilize niobium (Nb) superconducting radiofrequency (SRF) cavities, enabling 30–35 MV/m gradients with quality factors (Q) of $\sim 10^{10}$ while operating at $\sim$2 K [2–4]. To reduce this cryogenic burden, thereby increasing the accessibility of SRF technology, the accelerator physics community has been exploring alternative SRF materials that can enhance cavity accelerating gradients and Q factors while enabling SRF operation above 4 K. One such potential next-generation SRF material is the $A15$ triniobium-tin alloy (Nb_3Sn), which has a higher critical temperature T_c ($\sim$18 K) and superheating field ($\mu_0 H_{sh}$: 425 mT) than elemental Nb ($T_C \sim 9$ K, $\mu_0 H_{sh}$: 220 mT). Coating the interior walls of an existing Nb SRF cavity with a thin Nb_3Sn film could theoretically enable accelerating gradients as high as $\sim$100 MV/m while operating above 4 K ($Q \sim 10^{10}$) [5].

However, Nb_3Sn-coated SRF cavities have only achieved gradients of 24 MV/m to date [6], underperforming the elemental Nb cavities. The poor SRF performance of Nb_3Sn is attributed to material defects accrued within the films during the standard Sn vapor diffusion growth procedure. Despite the Sn vapor diffusion procedure producing the highest

*These authors contributed equally to this work.

†Present address: KLA, 1 Technology Drive, Milpitas, CA 95035, USA.

‡Contact author: s-sibener@uchicago.edu

performing cavity coatings, the small coherence length (∼4 nm) of Nb_3Sn means that its superconducting behavior is particularly sensitive to material defects, which include regions with inconsistent film growth, stoichiometric deficiencies, and surface roughness [7–13]. Nb_3Sn coatings formed on Nb SRF surfaces exhibit structural and chemical Nb_3Sn inhomogeneities. Combined with the brittleness of the alloy and other practical challenges of growing a high-quality Nb_3Sn film, these inhomogeneities have, to date, limited the use of Nb_3Sn in high-field accelerator applications [14].

Numerous growth studies of the Sn vapor diffusion procedure have resulted in improvements to the material properties of formed Nb_3Sn coatings. One such area of improvement has been identifying that the relatively slow Sn diffusion through Nb_3Sn bulk, as compared to Sn diffusion through Nb_3Sn grain boundaries, results in Sn deficiencies preferentially forming in larger Nb_3Sn grains. Sn-deficient regions of the $A15$ lattice manifest as antisite defects and can lower the Sn atomic percent (at.%) to as low as 18% [10,14]. Cross-sectional energy dispersive spectroscopy (EDS) maps have documented Sn-deficient regions throughout the entirety of the Nb_3Sn film, particularly at the interior of large grains and at the intermetallic interface [7,15–17]. Procedural changes to the vapor deposition procedure, such as increasing the Sn vapor pressure, have been effective in decreasing the incidence of larger, Sn-deficient Nb_3Sn grains [6,18].

While the Nb_3Sn grain sizes are driven by the experimental conditions during nucleation and coating steps, it is the cooldown procedure that primarily dictates the stoichiometry and roughness in the first few nanometers of the films. The Nb_3Sn film surface is particularly prone to forming chemical deviations, such as Sn-rich residues, that likely impact the cavity Q factors [19,20]. However, we lack a thorough experimental realization of how stoichiometric defects form, specifically at the Nb_3Sn surface, where Sn-rich and Sn-deficient regions can form with larger volumes and alter the roughness and morphology of the Nb_3Sn surface. One contribution to the lack of experimental data on chemical defects in the Nb_3Sn surface region is the barriers to experimentally characterizing Nb_3Sn surfaces with surface (<100 nm), spatial (lateral), and chemical sensitivity. To visualize and characterize Nb_3Sn surfaces, spectroscopic tools such as EDS provide chemical contrast information, but lack the spatial (lateral and depth) resolution to accurately probe nanometer-scale surface features. Depending on the electron beam energy and the sample properties, probed x rays used during EDS measurements can originate from hundreds of nanometers below the surface [21]. Alternatively, x-ray photoelectron spectroscopy (XPS) has higher surface sensitivity, usually on the order of nanometers. However, XPS instruments do not typically focus the photon beam to achieve any lateral spatial resolution. Another issue is that XPS measurements can suffer poor quantitative accuracy due to the surface roughness, heterogeneities, and oxidative properties of Nb_3Sn surfaces [22,23]. EDS, XPS, and other common structural analysis tools such as x-ray diffraction (XRD), provide valuable information about the ensemble Nb_3Sn film properties, but lack the lateral and surface sensitivity to examine the volume and geometric distribution of nanometer-scale surface defects. This can result in stoichiometric defects, such as ∼10-nm Sn islands on a Sn-deficient Nb_3Sn surface, being experimentally characterized as near-stoichiometric 25 at.% Sn. To fully capture chemical deviations at both nanometer and micron scales, it may be beneficial to shift the focus to experimentally probing the Nb_3Sn grain morphology rather than solely relying on global chemical analysis to infer the local chemistry at the film surface. For example, large grains with uncharacteristically low surface roughness are almost always Sn deficient. This means that upon observing such grains in future measurements, they can initially be assumed to be Sn deficient. In this sense, experimental observations can alleviate some of the challenges associated with accurately quantifying spectroscopic data. Relating Nb_3Sn surface chemistry with microscopic features can reduce the barriers associated with assessing the Nb_3Sn film's material properties and, ultimately, the SRF performance.

Because of the large variety of geometric and stoichiometric defects that can be present in Nb_3Sn surfaces, and the difficulties associated with experimentally probing local microscopic features, numerical simulation of superconducting fields in the presence of these features can play a powerful role in understanding their impact on SRF performance. Among the most useful outputs of these simulations is the estimation of critical fields for hypothetical Nb_3Sn surfaces. Nb_3Sn is a type-II superconductor, so it has a stable mixed state between its lower and upper critical fields (H_{c1}, H_{c2}) in which magnetic flux vortices can penetrate the surface. These vortices dissipate energy as they are driven by the rf cycle, which degrades SRF cavity quality factors and, in some cases, leads to thermal runaway and cavity quenching (i.e., transitions to normal conducting). However, the lower critical field is not the threshold for vortex nucleation. In practice, an energy barrier against vortex nucleation allows the superconducting (Meissner) state to remain metastable up to the superheating field, H_{sh}, at which point the energy barrier disappears. Above H_{sh}, vortex nucleation is unavoidable, and so the superheating field is the fundamental limit for the maximum accelerating gradient of an SRF cavity. High-field Nb SRF applications are known to operate above H_{c1}, within the metastable Meissner regime [24]. Nb_3Sn cavities, with a lower critical field of ∼38 mT [25], also operate in the metastable state when accelerating gradients exceed ∼9 MV/m. In this state, SRF performance is especially sensitive to material defects that can act as vortex nucleation sites. Because of this, the performance of Nb_3Sn SRF cavities is determined by local stoichiometric and geometric features present in the first few hundred nanometers of the surface. Previous literature demonstrated a strong effect of varying the global Sn percentage on the calculated and measured T_c [5,26]. Additionally, several theoretical studies have investigated the surface topography and Sn volume distribution of Sn-segregated grain boundaries and their superconducting properties [8,27]. However, the lack of predictive modeling limits our ability to connect the wide variety of Sn volume distributions and feature geometries in realistic Nb_3Sn surfaces to specific performance metrics.

We present herein a broad experimental and theoretical investigation of how certain structural variations of Sn-rich and Sn-deficient Nb_3Sn surfaces form during sample growth and their potential impact on SRF performance metrics. In particular, we look at the formation and impact of Nb_3Sn

surfaces which are Sn rich due to Sn islands, and the large, flat, Sn-deficient grains and the nanometer-scale corrugations that appear on them. Vapor-deposited Nb_3Sn films were formed both in an ultrahigh-vacuum (UHV) chamber and in a cavity-coating furnace. Experimental data provide insight into how the critical final cooldown steps of the Nb_3Sn growth procedure can drastically alter the surface stoichiometry, geometric distribution, and topographical profile of nonstoichiometric Nb_3Sn species. These experimental characterizations are modeled as approximate Nb_3Sn surface profiles. Simulation of these profiles shows how realistic surface features alter the critical fields and vortex nucleation behavior of the underlying material. In this way, this study demonstrates how structural and stoichiometric properties in observed surface defects can contribute to decreases in the maximum accelerating gradient of Nb_3Sn-coated SRF cavities.

The paper is outlined in the following order. The Methods section (Sec. II) contains a subsection devoted to the experimental methods (Sec. II A). The UHV Nb_3Sn growth and *in situ* characterization procedures, as well as the furnace Nb_3Sn growth procedure are outlined in Secs. II A 1 and II A 2, respectively. Section II A 3 details the experimental *ex situ* film characterization methods. The theoretical methods are discussed in Sec. II B. The Results and Discussion section (Sec. III) is comprised of three subsections (Secs. III A–III C), each containing an experimental and theory-based component to comprehensively characterize Nb_3Sn surfaces for high-field SRF performance. Section III A outlines the challenges associated with assessing how the Nb_3Sn surface morphology impacts SRF performance from experimental and theory-based perspectives. Section III A 1 outlines how experimental growth conditions can impact the Nb_3Sn stoichiometry throughout the entire film and at the surface. This section also discusses the challenges associated with characterizing the Nb_3Sn Sn at.% using commonly available techniques. In Sec. III A 2, the calculated relationship between the superheating field and the global Nb_3Sn stoichiometry is discussed. In Sec. III B, the formation and superconducting properties of Sn-rich Nb_3Sn surfaces, particularly Sn islands, are described. Finally, Sec. III C addresses the surface morphology and impact of Sn-deficient surfaces on SRF performance.

II. METHODS

A. Experimental methods

1. UHV film growth and in situ characterization (Recipes 1 and 2)

Nb_3Sn films were grown in a UHV chamber equipped with an electron beam evaporator (EFM3T; Focus GmbH) containing a tantalum crucible containing Sn pellets [Fig. 1(a)]. The substrate was a polycrystalline Nb foil (99.9% purity; Goodfellow) that did not undergo any mechanical polishing. Before Sn deposition, the Nb foil underwent repeated Ar^+ sputtering (1.5 keV) and annealing (T_{anneal}: 1630 °C) cycles to form an ordered NbO surface free of carbon contamination. The Nb surface composition was assessed with *in situ* XPS and Auger electron spectroscopy (AES). A 3.00 keV electron source (Staib) was used in AES and a Mg $K\alpha$ photon source (Specs XR 50) was used for XPS. Both AES and XPS photoelectron signals were collected using a cylindrical mirror analyzer (Staib DESA 100). The sampling depth for the Mg $K\alpha$ anode (1253.6 eV) in this setup is approximately 6 nm, whereas the sampling depth (3λ) for our Auger beam is approximately 2 nm [22].

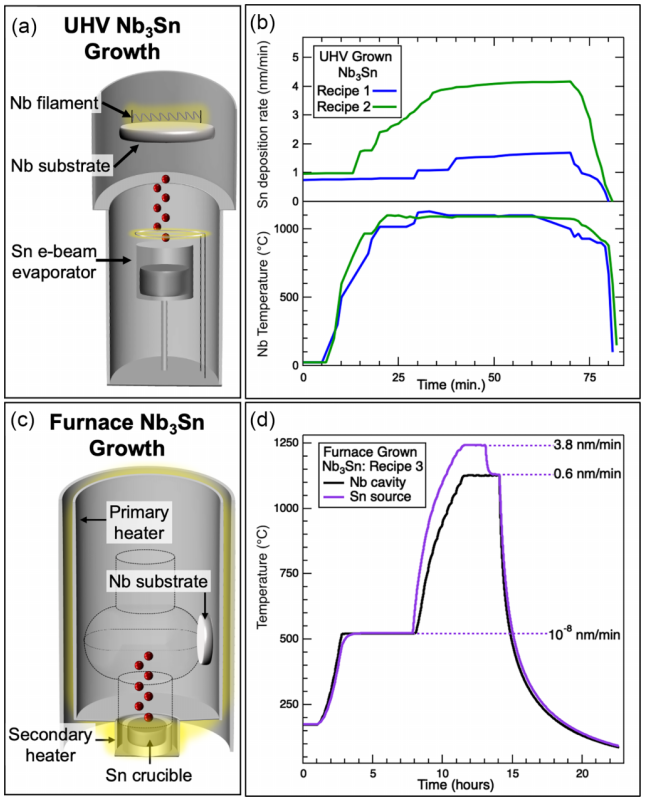

FIG. 1. Three different growth recipes used to form the Nb_3Sn films on Nb substrates. Schematics of experimental setups for (a) e-beam and (c) furnace deposition; (b) e-beam growth conditions for Nb_3Sn film Recipes 1 and 2; (d) furnace temperatures for Nb_3Sn film Recipe 3.

Preceding Sn deposition, the Nb sample was sputtered with 1.5 keV Ar^+ for 15 min at room temperature to increase the density of favorable Sn nucleation sites on the Nb surface [28,29]. The base pressure in the deposition chamber was approximately 10^{-9} torr. During evaporation, the Nb and Sn temperatures were independently controlled using two separate filaments [Fig. 1(a)]. Since the Nb substrate and Sn source were electron beam annealed, the temperatures were able to rapidly quench during the final cooldown steps of the deposition procedure [Fig. 1(b)]. The Nb temperature was monitored using an infrared pyrometer (Mikron Infrared; MG-140). The Sn flux at the substrate in nm/min was found by calibrating the evaporator heating conditions with a quartz crystal microbalance (QCM; INFICON) that was inserted into the same position as the Nb sample during deposition. A summary of the growth recipes used to experimentally grow each Nb_3Sn film can be found in Table I.

Recipes 1 and 2 are the UHV-grown Nb_3Sn films grown at the University of Chicago and were intended to represent condensed versions of the standard Nb_3Sn vapor deposition procedure [6]. The Nb heating conditions were comparable

TABLE I. Preparation of different Nb_3Sn surfaces.

Growth recipe	Deposition environment	Peak T_{Nb}	Peak T_{Sn}	Peak Sn deposition rate	Cooldown period (starting from T_{Nb}: 1100 °C)	Estimated film thickness
1	UHV	1100 °C	1120 °C	1.7 nm/min	<2 min	~275 nm
2	UHV	1100 °C	1175 °C	4.2 nm/min	<20 min	~500 nm
3	Furnace	1130 °C	1243 °C	3.8 nm/min	7 h	~3 μm

for both growth recipes (peak T_{Nb}: 1100 °C). For Recipe 1, the Sn flux was kept intentionally low (peak: 1.7 nm Sn/min) in order to promote the growth of large Sn-deficient grains [30]. For Recipe 2, the Sn flux was higher (peak: 4.2 nm Sn/min) to better simulate the typical Sn impingement rate in the standard Nb_3Sn procedure. In the typical growth furnace, the Sn flux is highly dependent on the location of the Nb cavity with respect to the Sn source, so Recipes 1 and 2 represent how deposition conditions can vary across the Nb SRF cavity surface [30,31]. The main differences from the furnace growth procedure in Recipes 1 and 2 are the shorter growth time, smaller film thickness, and the lack of a $SnCl_2$ nucleating agent during the initial nucleation growth step [hours 2–8 in Fig. 1(d)]. The $SnCl_2$ increases the Sn vapor pressure during the nucleation stage since the Sn source is only at ~525 °C. To compensate, the UHV-grown films had a relatively consistent Sn flux throughout the entire growth procedure. In the Supplemental Material [32], the Sn source temperatures during Recipes 1 and 2 were calculated from the deposition rate and plotted in Fig. S1(a) [33,34].

2. Furnace film growth (Recipe 3)

The Recipe 3 film was prepared using the standard vapor diffusion recipe at Cornell University [35]. High residual resistivity ratio (RRR) niobium samples were electropolished before being placed in the high-vacuum vapor diffusion furnace. The samples were hung from the heat shields to a height of where the equator of a 1.3-GHz cavity would be relative to the Sn source. After degassing the furnace at ~175 °C, the Nb temperature was ramped up to the nucleation temperature of ~500 °C and held there for 5 h. During this time, Sn-rich droplets started to nucleate on the Nb substrate. Utilizing the secondary heater for the Sn source, a temperature gradient of ~170 °C was established before ramping the temperature up for the coating stage. During the coating stage, the temperature of the Sn source was kept at ~1200 °C, while the samples were kept at ~1100 °C for 1.5 h. Lastly, the secondary heater was turned off, and the samples were annealed at 1100 °C for 1 h.

The Sn deposition rates used during Recipe 3 were calculated from the measured temperature of the Sn source during growth and plotted in Fig. S1. Nb_3Sn films were transported to the University of Chicago for analysis.

3. Ex situ film characterization

Scanning electron microscopy (SEM; Zeiss Merlin), EDS (Oxford Ultim Max 100), atomic force microscopy (AFM; Asylum Research Cypher), and XRD (Rigaku SmartLab) measurements were taken *ex situ*. SEM images were acquired using the Everhart Thornley secondary electron (SE), In-lens SE, In-lens, and angle selective backscatter (AsB) detectors. SEM characterization was conducted with a primary beam energy between 1 and 10 keV depending on the desired surface sensitivity and selected detector. The typical primary beam current was 5 nA for all images except for those taken with a 1-kV beam voltage, in which the beam current was lowered to 1–3 nA. Surface topography measurements were conducted using AFM. Images were taken on an atomic force microscope in tapping mode. All image workup and analysis was conducted using GWYDDION, an image analysis software. XRD measurements with taken using Cu $K\alpha$ radiation (1.54 Å).

The Nb_3Sn stoichiometry of each film was assessed with EDS and XRD. During EDS measurements, the primary beam was kept at 7 kV for the films grown with Recipes 1 and 2 and increased to 10 kV for the thick film grown with Recipe 3. The Nb_3Sn films grown using Recipes 1 and 2 are approximately between 250 and 500 nm thick, so EDS measurements were taken at the lowest possible beam energy to increase the surface sensitivity without comprising the EDS energy resolution [21]. It is still possible that the EDS signal probed past the intermetallic Nb_3Sn/Nb interface for these thinner films, so the EDS measurements likely underestimated the Sn concentration in the Recipe 1 and 2 Nb_3Sn films.

B. Theoretical methods

The simulations in this paper were done using the time-dependent Ginzburg-Landau (TDGL) equations,

$$\Gamma\left(\frac{\partial\psi}{\partial t}+\frac{ie_s\varphi}{\hbar}\psi\right)+\frac{1}{2m_s}\left(-i\hbar\nabla-\frac{e_s}{c}\boldsymbol{A}\right)^2\psi + \alpha\psi+\beta|\psi|^2\psi=0, \tag{1}$$

$$\frac{4\pi\sigma_n}{c}\left(\frac{1}{c}\frac{\partial\boldsymbol{A}}{\partial t}+\nabla\varphi\right)+\nabla\times\nabla\times\boldsymbol{A} - \frac{2\pi ie_s\hbar}{m_sc}(\psi^*\nabla\psi-\psi\nabla\psi^*)+\frac{4\pi e_s^2}{m_sc^2}|\psi|^2\boldsymbol{A}=0. \tag{2}$$

These equations (presented here in Gaussian units) are solved for the complex superconducting order parameter, ψ, and the magnetic vector potential, $\boldsymbol{A}$. $|\psi|^2$ is proportional to the density of superconducting electrons. Additionally, α and β are phenomenological parameters related to superconducting properties that we will discuss later, φ is the scalar potential, σ_n is the normal conductivity, Γ is the phenomenological rate of relaxation of ψ, and $e_s=2e$ and $m_s=2m$ are the total

charge and total effective mass of a Cooper pair, respectively. The TDGL equations are subject to boundary conditions:

$$\left(i\hbar\nabla\psi + \frac{e_s}{c}\boldsymbol{A}\psi\right)\cdot\boldsymbol{n} = 0, \tag{3}$$

$$\nabla\times\boldsymbol{A}\times\boldsymbol{n} = \boldsymbol{H}_a\times\boldsymbol{n}, \tag{4}$$

$$\left(\nabla\varphi + \frac{1}{c}\frac{\partial\boldsymbol{A}}{\partial t}\right)\cdot\boldsymbol{n} = 0, \tag{5}$$

where $\boldsymbol{n}$ is the outward normal vector to the boundary surface, and $\boldsymbol{H}_a$ is the applied magnetic field. Equation (3) ensures no current will flow out of the superconducting domain. Noting that $\boldsymbol{E} = -\nabla\phi + \frac{1}{c}\frac{\partial\boldsymbol{A}}{\partial t}$, Eqs. (4) and (5) are standard electromagnetic interface conditions with an applied magnetic field.

The parameters α, β, and Γ are temperature-dependent quantities. While they were originally introduced as phenomenological constants by Ginzburg and Landau, they can be derived from microscopic theories using the time-dependent Gor'kov equations [36]. This microscopic derivation relates these parameters to well-defined, experimentally observable material properties. The approximate material dependencies are given by Kopnin [37]:

$$\alpha(\nu(0), T_c, T) \approx \nu(0)\left(1 - \frac{T}{T_c}\right), \tag{6}$$

$$\beta(\nu(0), T_c, T) \approx \frac{7\zeta(3)\nu(0)}{8\pi^2 T_c^2}, \tag{7}$$

$$\Gamma(\nu(0), T_c) \approx \frac{\nu(0)\pi\hbar}{8T_c}, \tag{8}$$

where $\nu(0)$ is the Fermi-level density of states, T_c is the superconducting critical temperature, and T is the temperature; ζ is the Riemann zeta function. Using spatially varying values for $\nu(0)$, T_c, and T in Eqs. (6)–(8) gives nonuniform profiles for α, β, and Γ. This framework allows us to simulate the impact of material defects, such as Sn islands, on vortex nucleation. It is useful to introduce two other derived quantities, namely, the Ginzburg-Landau parameter κ and the thermodynamic critical field H_c. The Ginzburg-Landau parameter, $\kappa = \frac{\lambda}{\xi}$, relates the London penetration depth λ to the superconducting coherence length, ξ. These quantities can be expressed as functions of α and β [38]:

$$\kappa^2 = \frac{m_s^2 c^2 \beta}{2\pi\hbar^2 e_s^2}, \tag{9}$$

$$H_c^2 = \frac{4\pi\alpha^2}{\beta}. \tag{10}$$

The superheating field is related to these two quantities. Transtrum *et al.* [39] give an asymptotic expression for H_{sh} in the large κ limit:

$$\frac{H_{sh}(\kappa)}{\sqrt{2}H_c} \approx \frac{\sqrt{10}}{6} + \frac{0.3852}{\sqrt{\kappa}}. \tag{11}$$

The κ of Nb_3Sn is approximately ~26, placing it solidly in the large κ limit, so Eqs. (6)–(11) accurately estimate the superheating field for Nb_3Sn directly from $\nu(0)$ and T_c.

The superheating field is a material-specific quantity defined for perfect materials and surfaces. When geometric or stoichiometric defects induce vortex nucleation at a field less than H_{sh}, it is a sample-specific phenomenon. Therefore, we define the sample-dependent field, H_{vort}, as the threshold for vortex nucleation of a specific (simulated) sample. For a uniform surface with no defect, $H_{vort} = H_{sh}$. In the presence of defects, the ratio H_{vort}/H_{sh} quantifies the reduction on the maximum field that the sample can sustain.

The TDGL equations have several important limitations in the context of SRF modeling. First, the equations are only quantitatively valid for temperatures near T_c, but are generally believed to be qualitatively faithful throughout the superconducting state. Next, the equations implicitly assume gapless superconductivity, as the singularity in the density of states for a gapped superconductor prevents the expansion of the free energy in powers of the energy gap [38]. The gapless condition can be lifted with the use of a generalized version of TDGL proposed by Kramer and Watts-Tobin [40], and future work may include implementing these equations. It is also worth noting that Proslier *et al.* [41] found evidence of gapless superconductivity in the surface of some Nb SRF cavities due to Nb oxides. Additionally, Gurevich and Kubo [42,43] have found a generic lowering of the energy gap and broadening of the near-gap density of states under typical SRF operating conditions. We argue that these findings further justify our use of TDGL for SRF applications. Additionally, the computational cost makes more detailed models prohibitively expensive, so TDGL strikes a reasonable balance between fidelity and accuracy. Because of these limitations, however, we only limit ourselves to drawing qualitative conclusions and making *relative* comparisons between different systems.

We solve the TDGL equations using finite-element methods. Most of the simulations were performed using COMSOL's general form partial differential equation solver [44], following the two-domain method laid out by Oripov and Anlage [45]. The fully embedded Sn island simulations were solved using the open-source PYTHON package FENICS [46] with the TDGL weak form originally derived by Gao and Sun [47]. We apply periodic boundary conditions in the X and Y directions of the domains, and a constant field oriented in the X direction is applied to the top surface of the domain. For the plots of two-domain simulations, the solid-filled regions are the superconductors, and everything else is vacuum. All simulations were run on the HPC cluster at Brigham Young University.

In practice, we solve a nondimensionalized version of Eqs. (1)–(5) [48] in which all of the physical constants are absorbed into the fields, and only factors of κ and dimensionless analogs of α, β, and Γ remain. Dimensionless values of α, β, and Γ are expressed relative to their corresponding values for Nb_3Sn. Similarly, Eq. (9) suggests that the value of κ ought to be determined by the reference value for β; however, numerical considerations motivate other choices. In most cases (except where explicitly stated otherwise) simulations use $\kappa = 10$ as the bulk value, which remains within the large κ limit [and thus Eq. (11) is still valid] but is smaller than the actual κ of Nb_3Sn (~26). Large κ leads to simulations with extremely separated length scales that are both technically challenging and computationally expensive. To capture vortex nucleation, the full domain must span several penetration depths, while the element size of the meshes needs to be smaller than the coherence length. A mesh that produces good

solutions for $\kappa = 10$ would need ∼17 times as many elements to produce a similar quality simulation with $\kappa = 26$, and the total simulation time would be over 100 times as long.

Using smaller values of κ introduced controlled approximations into our simulations. As mentioned above, Eq. (9) shows that κ is determined by the value of β, and is independent of α. Referring to Eqs. (6) and (7), at low temperature, decreasing κ is roughly equivalent to increasing the effective T_c of the material. This also means that we are decreasing the value of Γ, but since Γ is a relaxation rate it will only affect the dynamics of the simulation and will have little to no effect on critical fields. So, using $\kappa = 10$ instead of 26 means effectively simulating a material that has the same density of states as Nb_3Sn, but a T_c that is a factor of 2.6 larger. From Eq. (10), H_c is therefore also a factor of 2.6 larger, and thus the corresponding H_{sh} calculated with Eq. (11) is strictly larger. Due to our definition of H_{vort}, there exists a limiting process for any defect in which $H_{vort} \to H_{sh}$. As a result of this, we argue that any given estimate for H_{vort} using $\kappa = 10$ will be strictly larger than the corresponding value for $\kappa = 26$, and the $\kappa = 26$ simulations that we did run corroborate this assertion. In summary, using $\kappa = 10$ allows simulations of superconductors within the large κ limit without the significant additional computational costs incurred by using $\kappa = 26$; while doing so does mean the simulated material is no longer exactly Nb_3Sn, the resulting H_{vort} estimates are still valuable, as they may be treated as upper bounds to the true $\kappa = 26$ values.

III. RESULTS AND DISCUSSION

A. General Nb_3Sn surface stoichiometry

1. *Experiment: Spatial distribution and characterization of* Nb_3Sn *stoichiometries*

Nb_3Sn stoichiometric inhomogeneities are more likely to form at specific regions throughout Nb_3Sn films grown via vapor deposition. For instance, Sn-deficient regions are preferentially located at (1) the intermetallic interface, (2) regions further from grain boundaries, and (3) at the film surface. The relationship between the grain boundary density and Sn stoichiometry is important because it impacts the film composition at all depths. For all three growth recipes, we observe the formation of "abnormal" Nb_3Sn grains that are large, smooth, and Sn deficient (Fig. S2, and Table SI of the Supplemental Material). These abnormal grains have been previously identified in literature as "patchy" and microscopy of film cross sections shows that these grains are also unusually thin and contain Sn deficiencies [11,16,30]. For this study, we focus on the stoichiometry of the first tens of nanometers into the Nb_3Sn surface and the different structural morphologies that form with varying Sn concentrations. While the Nb_3Sn surface does form a surface oxide upon exposure to atmosphere, we focus our discussion of the Nb_3Sn surface composition in terms of the relative Nb and Sn content. The XPS and AES data of the Nb_3Sn surface oxide are shown in Figs. S7 and S8.

To understand how the experimental growth conditions impact the Nb_3Sn surface stoichiometry, we must consider that the film surface morphology is driven by the relative Sn loss and accumulation rates that occur during the final cooldown steps of the growth procedure [Figs. 1(c) and 1(d)]. Throughout the vapor deposition growth procedure, adsorbed Sn vapor on the formed Nb_3Sn surface undergoes multiple diffusive processes including desorption, lateral diffusion, subsurface dissolution, and incorporation into the intermetallic unit cell [49,50]. The interplay and relative rates of these competing surface-mediated processes are primarily dictated by the Nb substrate temperature and Sn vapor flux above the surface. Therefore, the relative cooldown rates of the Nb and Sn heating sources can drastically impact the composition of the first few nanometers of the Nb_3Sn surface. An appreciable Sn vapor pressure is present while the Nb cavity drops below the temperatures required for Sn subsurface incorporation, between 800 °C and 900 °C, which will increase the density of Sn-rich and elemental Sn islands. On the other hand, a premature depletion of the Sn supply will result in excess Sn desorption from the Nb_3Sn surface. Post-deposition thermal treatments have been shown to deplete the Sn surface concentration (Fig. S8), not just by elemental Sn desorption, but from Sn segregating and desorbing from Nb_3Sn. The optimal ratio between the Nb and Sn temperature during the cooldown process is difficult to identify and is likely impossible to achieve experimentally.

For the UHV grown films [Recipes 1 and 2; Fig. 1(b)], the Nb and Sn cooldown process was rapid. The Nb source was cooled from 900 °C to below 300 °C in approximately 2 min. The main experimental differences in Recipe 1 are that the Nb cooldown was more gradual (reduced from 1100 °C to 900 °C in ∼20 min) and that the Sn temperature was slightly reduced about 2 min before the quenching of both Nb and Sn heating sources.

In contrast, the Nb_3Sn surface formed using the standard furnace deposition procedure (Recipe 3) had a much longer cooldown process. Since the Sn crucible was fully depleted, there was a period in which the Nb surface was heated with little to no Sn overpressure above the surface. This may have promoted the precipitation and desorption of Sn from the surface. However, we must also consider that this Nb_3Sn film was grown at a higher Sn flux and over a much longer period than in Recipes 1 and 2. Therefore, we expect fewer Sn-deficient regions within the first 100 nm of the Recipe 3 Nb_3Sn film. Globally, EDS analysis of the Recipe 3 Nb_3Sn film shows that the overall film is Sn rich, with the regular Nb_3Sn grains containing an estimated 26 at.% Sn (Fig. S6). Despite the higher Sn content, we still observe large, abnormal Nb_3Sn grains in the Recipe 3 film that are indicative of Sn deficiencies. These features will be discussed in Sec. III C 1 of the Results and Discussion.

2. *Theory: Effect of global* Nb_3Sn *stoichiometry on SRF performance*

While the specific local features present in Nb_3Sn surfaces will certainly have their own effects on SRF performance metrics, some of which we discuss later in this paper, we first consider the impact of stoichiometry alone. Equations (6)–(11) provide a method for estimating the H_{sh} of a material from the Fermi-level density of states and T_c of the material. Using this method, we can directly estimate the effect that stoichiometry will have on H_{sh}. Sitaraman *et al.* [51] performed DFT calculations on A15 phase Nb-Sn

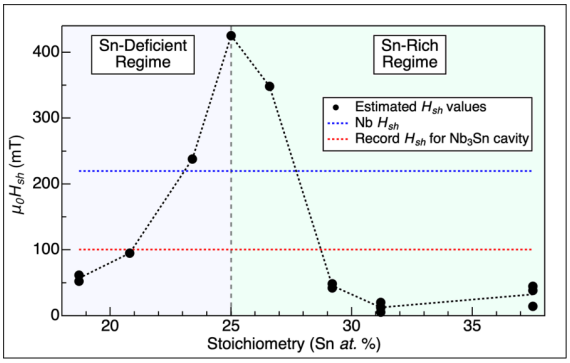

FIG. 2. H_{sh} as a function of Sn percentage. $\mu_0 H_{sh}$ is given in units of millitesla. The superheating field of pure Nb and the maximum field of the record Nb_3Sn cavity performance (documented in Posen *et al.* [6]) are also depicted for comparison.

systems, varying the concentration of antisite defects to estimate the Fermi-level density of states and T_c for different Sn at.%'s. Using these values with Eqs. (6)–(11), we estimate H_{sh} as a function of Nb_3Sn stoichiometry.

Figure 2 gives the bulk superheating field versus stoichiometry. While 25% Sn (perfect stoichiometry Nb_3Sn) has the expected value for $\mu_0 H_{sh}$ of ∼425 mT, off-stoichiometry samples exhibit significant performance degradation. Indeed, Fig. 2 demonstrates why Nb_3Sn is such a difficult material from which to engineer SRF cavities; even small deviations from the perfect stoichiometry can lead to significant reductions in H_{sh}, and by extension the limiting operating fields and maximum accelerating gradients. For example, a Sn stoichiometry of 23.4% cuts the expected H_{sh} nearly in half, and some Sn-rich compositions reduce H_{sh} nearly all the way to zero. The expected value of $\mu_0 H_{sh}$ for pure Nb is ∼220 mT (the blue line in Fig. 2), so not only do stoichiometric variations suppress the potential performance of Nb_3Sn surfaces, but it can even result in Nb_3Sn-coated Nb cavities that underperform elemental Nb. The record performance for a Nb_3Sn SRF cavity (the red line in Fig. 2) is an accelerating gradient of 24 MV/m, which corresponds to a peak magnetic field of ∼100 mT, well below even Nb's H_{sh}.

The H_{sh} values in Fig. 2 are valid for surfaces with a Sn composition that is uniformly distributed within the Nb_3Sn lattice. This assumption holds up well for many Sn-deficient compositions, as the $A15$ phase remains stable down to ∼17.5 Sn at.%; however, it is only stable for Sn-rich compositions up to ∼26% [52]. Compositions with higher Sn concentrations than this have not been observed in bulk, but they are known to appear locally near grain boundaries [9]. While the results in Fig. 2 could serve as an initial guess for the superconducting properties of some local feature, our calculations are only strictly applicable to surfaces that are nearly uniform on scales of several penetration depths (i.e., a few tenths of a micron). Real surfaces can exhibit both stoichiometric and structural variations on much smaller scales than this, which have specific impacts on vortex nucleation. Unfortunately, it is difficult to characterize samples on these scales. Experimental techniques such as EDS or XRD lack the sensitivity to resolve submicron-scale features, and so they must report weighted averages that may show a surface to be broadly Sn rich or Sn deficient. Such surfaces may be mostly good stoichiometry Nb_3Sn with many highly localized Sn-related defects. In these cases, the mechanisms for vortex nucleation are driven by the morphology of the specific defects rather than average stoichiometry. An example of one such surface defect is the presence of Sn islands embedded in the Nb_3Sn, which we cover in Sec. III B of this study. Additionally, variations in the surface geometry of the sample may further induce vortex nucleation. We explore an instance of this in Sec. III C, where we discuss the surface corrugation present on Sn-deficient grains.

B. Sn-rich regions on Nb_3Sn surface: Sn islands

1. Experiment: Partially embedded Sn islands

Sn-residue or Sn-rich regions due to elemental Sn islands or Sn-rich intermetallic phases (Nb_6Sn_5, $NbSn_2$), can often be found on Nb_3Sn surfaces [53,54]. The persistence and chemical identity of the Sn-rich residue is dependent on both the Nb temperature during and after Sn nucleates on the Nb_3Sn surface. Above 930 °C, we expect Sn to diffuse, predominantly through Nb_3Sn grain boundaries, to form the $A15$ Nb_3Sn structure [55].

For the Recipe 1 film, the accumulation of elemental Sn was observed on the surface and is shown in Fig. 3. The Sn islands were confirmed to not contain any detectable Nb with EDS analysis and are morphologically distinct from any Sn-rich intermetallic phase. We observe two distinct geometries for the Sn islands—larger irregular polyhedra and smaller tetrahedra. The SEM image in Fig. 3(a) shows an example of each Sn island geometry. The Nb $L\alpha$ EDS map [Fig. 3(b)] shows a lack of Nb EDS signal in the locations of each island. The Sn $L\alpha$ EDS map [Fig. 3(c)] shows a relative increase of Sn EDS signal at each Sn island. An EDS map depicting the relative Sn proportion is shown in Fig. 3(d) and was calculated by dividing the Sn $L\alpha$ EDS image by the sum of the Sn $L\alpha$ and Nb $L\alpha$ EDS images. In this relative Sn concentration map, the stoichiometric variations within the Nb_3Sn film are distinguishable from the more dramatic increase in Sn concentration due to the Sn islands. The diameter of the Sn islands varies, with the polyhedral islands ranging between 50 and 400 nm and the edge of the tetrahedral Sn islands typically ranging between 80 and 250 nm. Overall, the larger Sn islands conform to the polyhedral shape, with many appearing generally cubic.

Another varying aspect to these Sn islands is their topographic height. AFM images along with respective line scans are shown in Figs. 3(e)–3(h). Overall, the polyhedral island width is typically approximately three times as large as the protruding height. The tetrahedral islands tended to be more deeply embedded into the Nb_3Sn surface with the height only ∼25%−50% of the measured island width. The Sn islands overall have a greater diameter than topographic height which can be due to geometric asymmetry or a degree of embedment into the Nb_3Sn surface. It is worth noting that once these Sn islands form on the Nb_3Sn, removing them, via thermal desorption or incorporation into the Nb_3Sn lattice, is incredibly difficult. Annealing experiments have shown that the thermal stability of elemental Sn islands exceeds the thermal stability of Sn alloyed in the Nb_3Sn unit cell [56]. Thus, heating a

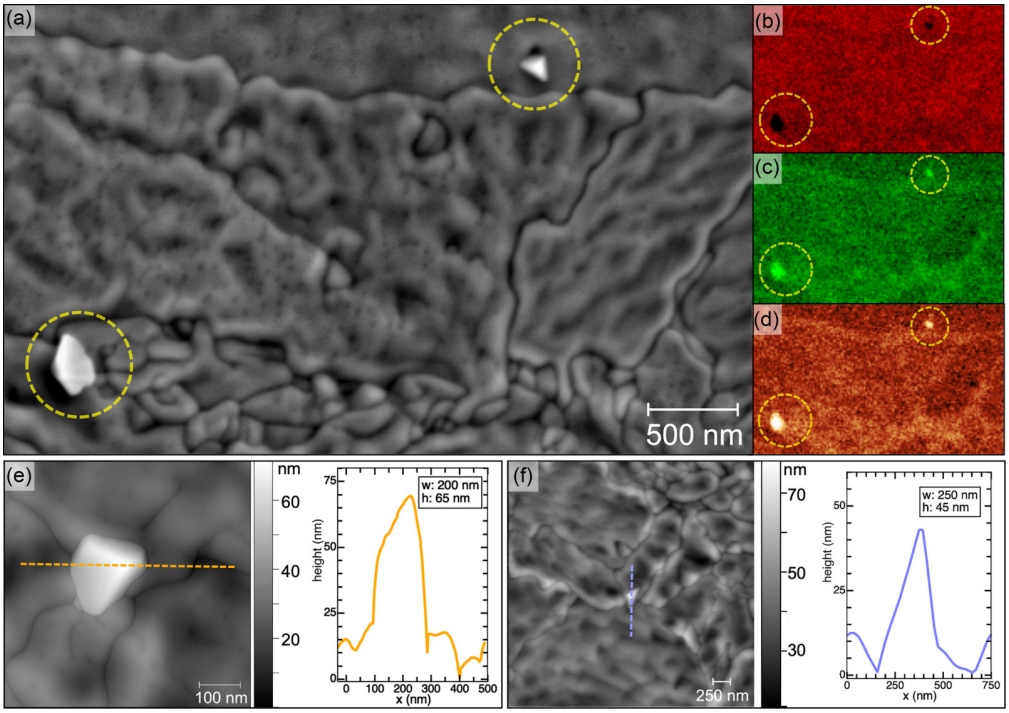

FIG. 3. Experimental data of polyhedral and tetrahedral Sn islands on Nb_3Sn surfaces grown using Recipe 1. SEM image (a) along corresponding EDS maps (b)–(d) show two Sn islands that are marked with the yellow dashed circles. AFM images of polyhedral and tetrahedral Sn island are shown in (e) and (f), respectively, along with corresponding line scans for each image. The inset textbox on each line scan denotes the width (w) and height (h) for each Sn island. Image sizes are denoted by scale bars. (a) SEM image, 4.17 μm×2.5 μm; SE2 detector, 7 keV; (b) Nb $L\alpha$ EDS map, 7 keV; (c) Sn $L\alpha$ EDS map, 7 keV; (d) calculated Sn($L\alpha$)/Nb($L\alpha$)+Sn($L\alpha$) EDS intensity proportion map; (e) AFM image of polyhedral Sn island, 600 nm×600 nm; (f) AFM image of tetrahedral Sn island, 5 μm×5 μm.

Sn-rich surface is likely to induce Sn deficiencies within the Nb_3Sn film at the temperatures necessary for Sn desorption to occur. This eliminates selective elemental Sn desorption through post-deposition thermal treatments as a viable option for reducing Sn-rich surfaces.

2. *Theory: Impact of island geometry and size on vortex nucleation*

We model Sn islands as idealized cubic and tetrahedral volumes embedded in the sample as shown in Figs. 4(a) and 4(d). Table II shows the values used for α, β, and Γ (relative to the corresponding values for Nb_3Sn) both inside and outside the islands as estimated using Eqs. (6)–(8). To determine the impact these Sn islands have on SRF performance, we estimate the lowest field at which vortices spontaneously nucleate, denoted by H_{vort}.

TABLE II. Parameter values used for Sn island simulations. Note that the α, β, and Γ values were defined relative to the respective values for Nb_3Sn to make them unitless for our simulations which use natural units. The values of $\nu(0)$ and T_c were calculated with DFT using the $A15$ phase for Nb_3Sn and the body-centered tetragonal phase for Sn and came from private correspondence.

Parameter	Nb_3Sn	Sn
$\nu(0)$ [states/(eV nm^3)]	101.78	16.8
T_c (K)	18	2.9
α/α_{Nb_3Sn} (unitless)	1	−0.029
β/β_{Nb_3Sn} (unitless)	1	3.907
Γ/Γ_{Nb_3Sn} (unitless)	1	0.803

Figure 4(b) shows one of our simulations for a cubic Sn island with side length λ (where for Nb_3Sn, λ =∼ 100 nm). In this case we found that $H_{\text{vort}} = 322.59$ mT, which is ∼24.2% lower than the superheating field for Nb_3Sn, $\mu_0 H_{\text{sh}} = 425$ mT. As discussed in Sec. II B, the κ for this simulation was 10, but for this size of island we ran another simulation with $\kappa = 26$, and found $H_{\text{vort}} = 304.73$ mT, which is ∼30% lower than the Nb_3Sn H_{sh}; this agrees with our earlier assertion that our $\kappa = 10$ simulation results may be treated as upper bounds (or lower bounds in terms of percentage decreases).

It is instructive to compare the impact of a localized Sn island to that of average stoichiometry. The volume-averaged Sn concentration of this simulation is given by

$$\text{Sn at.\%} = \frac{V_{\text{Sn}}}{3V_{\text{Nb}} + V_{\text{Sn}}}, \tag{12}$$

where V_{Sn} is the volume of the region containing Sn and V_{Nb} is the volume of the region containing Nb. In the case of Fig. 4, $V_{\text{Sn}} = 32.5\lambda^3$ and $V_{\text{Nb}} = 31.5\lambda^3$, resulting in a Sn at.% of ∼25.6%. From Fig. 2, we see that the expected $\mu_0 H_{\text{sh}}$ for a surface with a uniform Sn concentration of 26.5% is about 348 mT, which is only 18% lower than the Nb_3Sn H_{sh} of 425 mT. This means that surfaces with localized stoichiometric defects, such as the one from Fig. 3, may

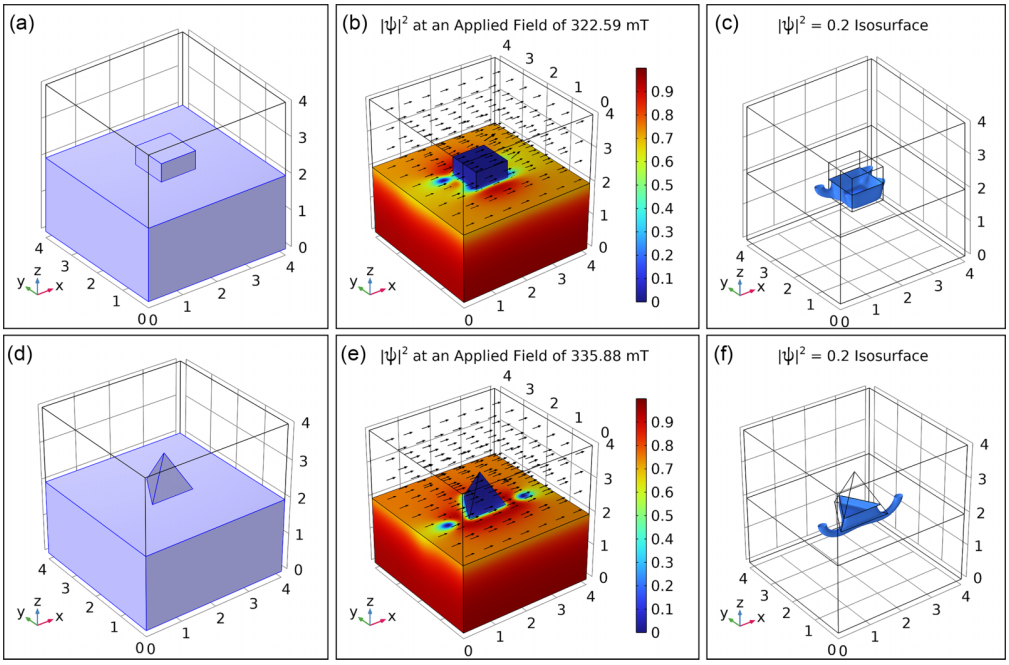

FIG. 4. (a) Simulation geometry of cubic Sn islands. Half of the cubic island is embedded below the surface. We also simulated some islands which were fully embedded, with the top surface of the cube flush with the Nb_3Sn surface (not pictured). (b) A plot of $|\psi|^2$ at an applied field of 348.25 mT. The black arrows show the direction of the magnetic field in the vacuum. (c) An isosurface of $|\psi|^2 = 0.2$ showing the shape of the vortex during nucleation. (d) Simulation geometry of tetrahedron Sn islands. Approximately half of the island's total volume is embedded below the surface. (e) A plot of $|\psi|^2$ at an applied field of 335.88 mT. The black arrows show the direction of the magnetic field in the vacuum. (f) An isosurface of $|\psi|^2 = 0.2$ showing the shape of the vortex during nucleation.

exhibit more significant SRF performance degradation than average stoichiometry alone would imply. In this case, the mechanism behind this degradation comes from Sn island-induced vortex nucleation that occurs 25%–30% below the Nb_3Sn H_{sh}.

We now consider the impact of island size on vortex nucleation. Table III reports the results of simulations with geometries similar to those in Fig. 4 with half of the island protruding above the surface, and the remaining half embedded beneath the surface. Larger islands lead to more significant decreases in H_{vort}. The largest island we simulated was a cube with side length 200 nm corresponding to an average Sn at.% of 30%. A uniform surface with a 30 at.% Sn will have a $\mu_0 H_{sh}$ of around ∼24.6 mT (see Fig. 2), which is an ∼94% decrease relative to the pure Nb_3Sn H_{sh}. Comparatively, the 200-nm side length cubic Sn islands only led to a 29.2% decrease. Thus, relative to uniform surfaces with the same at.% Sn, small Sn islands produce more significant drops in H_{vort} while larger Sn islands produce less significant drops in H_{vort}. An important caveat to this analysis is that the calculated Sn concentration of a simulation depends on both the total volume of the superconducting domain as well as the size of the island. We have chosen our domain size such that it falls within the range of reasonable resolutions for experimental techniques which can estimate material composition, such as EDS. The lateral and surface sensitivity of EDS is material dependent and has a complicated depth dependence which makes it difficult to estimate exactly, but it can reasonably be assumed to fall within a range of several hundred nanometers. Our simulation domains span ∼400 nm, and so the Sn at.% estimates of the compositions of these domains give a rough approximation for the local compositions of similar Sn islands measured experimentally.

We next consider cubic Sn islands fully embedded in the surface, with the top surface of the cube flush with the surrounding Nb_3Sn bulk. These simulations were performed

TABLE III. Results of half-embedded Sn islands.

Cubic island side length (nm)	$\mu_0 H_{vort}$ (mT)	% decrease from Nb_3Sn H_{sh}	Estimated Sn at.%	% decrease from Nb_3Sn H_{sh} for a uniform surface with equal Sn at.%
50	343.4	19.2%	25.07%	0.79%
100 ($\kappa = 10$)	322.59	24.2%	25.59%	6.68%
100 ($\kappa = 26$)	304.73	28.3%	25.59%	6.68%
200	300.9	29.2%	30.0%	94.21%

TABLE IV. Results of fully embedded Sn islands.

Cubic island side length (nm)	$\mu_0 H_{vort}$ (mT)	% decrease from H_{sh}	Estimated Sn at.%	% decrease from Nb_3Sn H_{sh} for a uniform surface with equal Sn at.%
50	313.65	26.2	25.07	0.79
100	274.55	35.4	25.6	6.68
200	228.65	46.2	30.77	96

using FENICS and the weak formulation derived by Gao and Sun [47] and our results are listed in Table IV. Similar to the half-embedded case, larger islands produce larger decreases in H_{vort} overall but have a smaller decrease relative to the Sn at.%, while smaller islands have smaller overall values with larger increases relative to the Sn at.%. It is notable that this fully embedded case reduces H_{vort} more than in the half-embedded case. We conjecture this is because the part of the island which is above the surface in the half-embedded case goes completely normal conducting, and so there is no magnetic field screening in that region. Therefore, from the perspective of the magnetic field, this part of the island is no different than vacuum, and so the island appears to have a smaller effective volume than their fully embedded counterparts. This smaller effective volume leads to lower H_{vort} values in the half-embedded islands.

Finally, we also considered a single tetrahedral Sn island. In this case we used a regular tetrahedron with an edge length of ∼150 nm, with roughly half of the total volume beneath the surface. Our result for $\kappa = 10$ is shown in Figs. 4(e) and 4(f). We found that for this case, $\mu_0 H_{vort} \approx 335.88$ mT, which is ∼26.9% lower than the Nb_3Sn H_{sh}. Notably, the total volume of this island is less than half the total volume of our cubic island with a side length of 100 nm. Even in the cubic case, the vortices tended to nucleate off the corners of the cube, so this result seems to imply that the smaller opening angle of the vertex of the tetrahedron more effectively nucleates vortices than the cube shape, resulting in a lower H_{vort}. We also simulated this island geometry for $\kappa = 26$, for which we found $\mu_0 H_{vort} \approx 304.58$ mT, approximately 28.3% lower than the expected H_{sh}.

C. Sn-deficient Nb_3Sn surfaces: Corrugations

1. Experiment: Formation of surface corrugations resulting from Sn loss

As was discussed in Sec. III A 1, the "abnormal," large Nb_3Sn grains contained some degree of Sn-deficient stoichiometries throughout the grain volume. However, the Sn composition within the first 100 nm drastically influences vortex nucleation. To assess the Nb_3Sn grain properties, we turn to structural morphology to augment our compositional characterization. SEM images of an abnormal, large grain formed from each film recipe are shown in Fig. 5. On the Recipe 1 film in Fig. 5(a), there are sporadically distributed 10-nm-sized pores on the surface. These pores were found on all of the Nb_3Sn films but were difficult to visualize with SEM with beam voltages exceeding 7 kV.

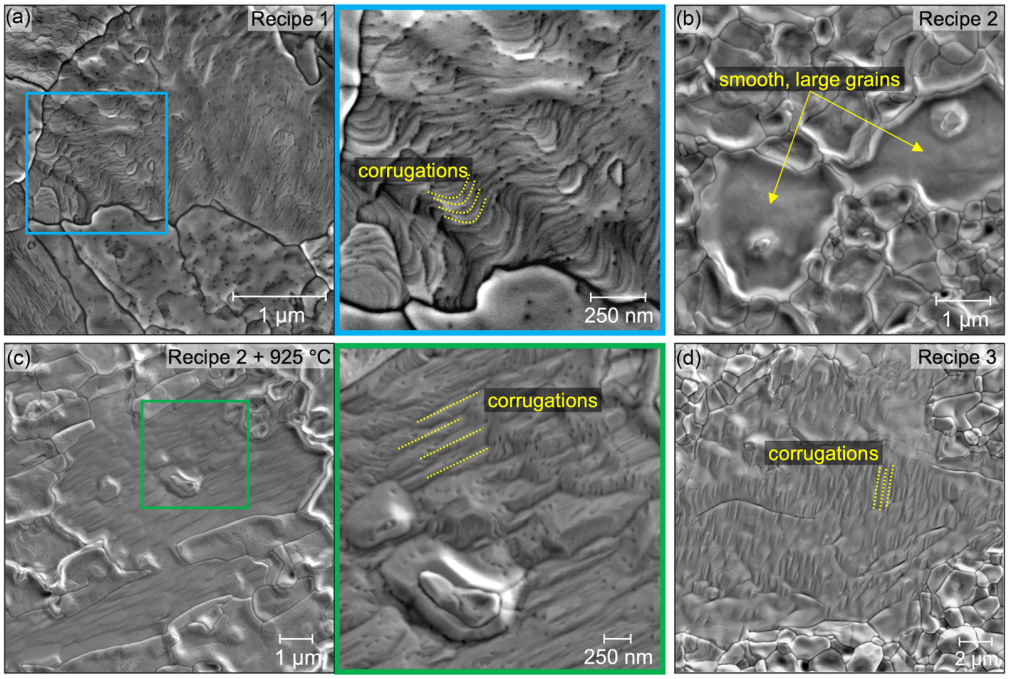

FIG. 5. SEM images of Nb_3Sn surfaces grown on polycrystalline Nb substrates with varying Sn deposition conditions. Image sizes are denoted by scale bars. (a) Recipe 1, UHV growth, 1.7 nm/min Sn flux, inset SEM area denoted with blue box, InLens detector, 3 kV; (b) Recipe 2, UHV growth, 4.2 nm/min Sn flux, SE detector; (c) Recipe 2+60-min UHV anneal at 925 °C, UHV growth, 4.2 nm/min Sn flux, SE detector; (d) Recipe 3, furnace growth, 3.8 nm/min Sn flux, SE detector.

For the UHV grown films, the surface area distributions of the abnormal Sn-deficient grains were comparable (Table SI). The main morphological distinction between the Recipe 1 and 2 films was that the Recipe 1 grains formed periodic corrugations [Fig. 5(a)], whereas the Recipe 2 large grains were smooth and absent of these features [Fig. 5(b)]. The corrugations on the Recipe 1 grains are periodic, with the peaks typically separated by 30–50 nm. The depth of the corrugations varies as well; the depth is highly unlikely to exceed the peak width. Not all of the large grains in Recipe 1 are corrugated; roughly 50% of the abnormal, Sn-deficient grains exhibited this corrugated surface morphology. There does seem to be a minor correlation between the grain area and the likelihood of forming surface corrugations. This may suggest that the formations of surface corrugations indicate a more egregious Sn deficiency, potentially for Nb_3Sn grains with close to the minimum 18 Sn at.% for the $A15$ structure.

For the abnormal, Sn-deficient grains formed using the Recipe 2 surface, the only distinguishable features were the nanopores and sporadic Sn-rich aggregates. The lack of corrugated grains on the large Recipe 2 Nb_3Sn grains (grown at a higher Sn flux) support that the formation of these corrugations is related to the Sn composition within the first 100 nanometers of the surface. If the formation of surfaces corrugations was only dependent on the Nb_3Sn grain surface area, we would expect at least some of the Recipe 2 grains to contain corrugations since the surface area distributions were not significantly different from Recipe 1 (Table SI). It is possible that the more rapid cooldown process used in Recipe 2 may have prevented Sn loss from the surface.

To test whether the corrugations are indicative of (1) an overall Sn deficiency based on the large grain area or (2) Sn deficiencies within the first 100 nanometers of the surface, we conducted post-deposition annealing experiments on the Recipe 2 Nb_3Sn film (AES data in Fig. S8). An SEM image of the Recipe 2 Nb_3Sn film that was annealed at 925 °C to induce Sn loss is shown in Fig. 5(c). Many of the large, abnormal grains now contain corrugations that appear shallower and more widely separated than the corrugations that were formed on the Recipe 1 film. During any Nb_3Sn annealing without a considerable Sn overpressure, Sn desorption dominates over any other diffusion processes [54,56]. Therefore, we can associate these corrugations with a Sn deficiency *specifically* within the first few nanometers of the surface.

Finally, Fig. 5(d) shows a large grain on the furnace grown (Recipe 3) Nb_3Sn film. We observe the shallow corrugations on the grain surface, similar to those formed on the annealed Recipe 2 film [Fig. 5(c)]. These corrugations may be symptomatic of substantial Sn loss from the Nb_3Sn surface. These observed corrugations can serve as a highly surface sensitive structural indicator of severe Sn deficiencies.

2. *Theory: Simulations of corrugated Sn-deficient* Nb_3Sn *surfaces*

We now model the effects that the corrugation geometry has on SRF performance. As a preface to the following discussion, it is important to note that the grains exhibiting these structures tend to be Sn deficient. We can see from Fig. 2 that for 18–24 Sn at.%, this stoichiometry already exhibits a 50%–80% drop in the expected H_{sh} based on the Sn deficiency alone. However, as we will demonstrate, the presence of these geometric corrugations has the potential to degrade this performance even further. We use an idealized geometry shown in Fig. 6(a), varying the height (h) and spacing (d) between the corrugations. This geometry unambiguously defines heights and widths for the corrugations while ignoring potential secondary effects due to curvature. Our primary goal with this part of the study is to qualitatively demonstrate some of the effects that the surface geometry of these corrugations has on SRF performance. Future work may include a more extensive study of the many different geometric factors at play in these simulations. Because of the periodic boundary conditions, these simulations are an infinite series of "boxlike" ridges, which approximate the local shape of the observed corrugations. For the same reasons discussed in Sec. II B, these simulations all use $\kappa = 10$, and the following H_{vort} estimates should be treated as upper bounds to the true values. For the purposes of estimating the critical field values, we assumed the corrugations to have a uniform composition of 18.7 Sn at.%, resulting in a superheating field of $\mu_0 H_{sh} = 57.1$ mT (see Fig. 2).

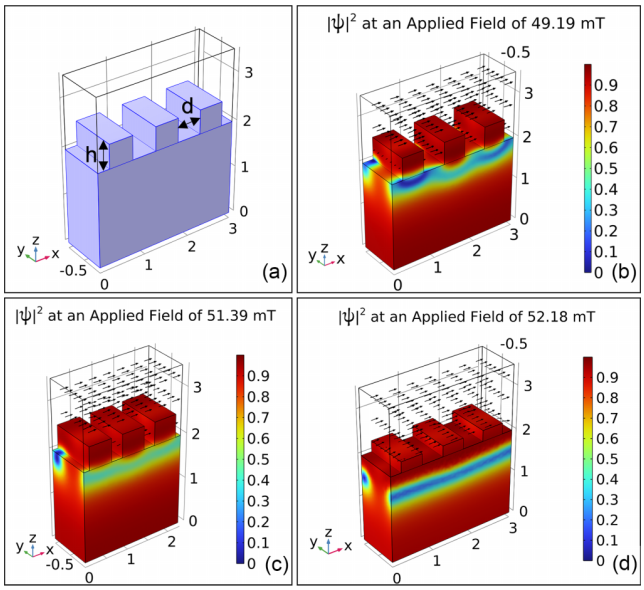

FIG. 6. (a) The geometry used for our corrugation simulations. The solid-filled region is the superconductor, with vacuum in the rest of the domain. Periodic boundary conditions are applied to the outer surfaces in the X and Y directions, and the external field is applied to the top surface of the vacuum domain. The distance labeled by h is the height of the ridges, and the distance labeled by d is the distance between them. (b)–(d) Plots of $|\psi|^2$ during vortex nucleation at different applied fields for different corrugation spacings and heights. The black arrows show the direction of the magnetic field in the vacuum. (b) has $h = 50$ nm, $d = 50$ nm. (c) has $h = 50$ nm, $d = 25$ nm. (d) has $h = 25$ nm, $d = 50$ nm.

In our first corrugation simulations, we used ridges with heights and widths of 50 nm and ran two different simulations: one where the ridges have a 50-nm separation distance [shown in Fig. 6(b)] and the other with a 25-nm separation distance [Fig. 6(c)]. We find that the corrugations lead to a meaningful drop in H_{vort}, with the corrugations shown in Fig. 6(b)

producing an estimated $\mu_0 H_{\text{vort}} \approx 49.19$ mT, which is an $\sim$13.8% decrease below H_{sh}. The corrugations in Fig. 6(c) have an $\mu_0 H_{\text{vort}} \approx 51.39$ mT, a 10% decrease below H_{sh}. The vortex nucleation in this case happens because the ridges act as nucleation sites, with vortices having a much easier time entering the thin ridge. In addition to this, these ridges also exhibit some field enhancement, an effect where the Meissner effect pushing the field out of the material leads to field lines "bunching" up near the outer surface of geometric defects, leading to "enhanced" field magnitude near the defect surface. In this case, the local magnetic field magnitude is slightly larger than the applied field above each ridge, which further improves the possibility of vortex nucleation. The closer spaced corrugations led to a smaller decrease in H_{vort} because the field enhancement is smaller, as well as the surface appearing slightly closer to a flat surface.

We also simulated corrugations with a width of 50 nm and a height of 25 nm, as shown in Fig. 6(d). In this case the smaller ridges produced less field enhancement and were less strong nucleation sites, so the resulting $\mu_0 H_{\text{vort}}$ estimate was 52.18 mT. This is $\sim$8.5% lower than the expected value of H_{sh}, meaning that shallower corrugations have a less pronounced effect on vortex nucleation.

IV. CONCLUSION

In this work, experimental and theoretical results address how deviations in Nb_3Sn stoichiometry can manifest in distinct surface morphologies that have varying impacts on SRF performance. Experimentally, we demonstrate some of the limitations of characterizing Nb_3Sn by relying on global Sn atomic percentage estimates from experimental methods such as XRD or EDS. Not only does the Sn concentration vary drastically as a function of film depth, but the Nb_3Sn surface can contain drastically different surface morphologies with the same estimated chemical makeup. For example, a Sn-rich surface can manifest in micron-diameter Sn residue or sub-100-nm Sn particles that are difficult to characterize using the higher beam voltages ($\geqslant$10 kV) commonly used during SEM/EDS analysis of Nb_3Sn films. Simulated results of the impact of Sn island geometry on vortex nucleation show that smaller Sn islands will nucleate a vortex at a lower applied field as compared to a uniform flat Nb_3Sn surface with the same global Sn at.%. Conversely, we conclude that introducing a larger Sn island has a smaller than expected drop in the vortex nucleation field (H_{vort}) based on a uniform composition, though our estimated values for H_{vort} were still lower than the corresponding values for the small islands. For the Sn-deficient Nb_3Sn grains, we experimentally show that the Nb_3Sn surface develops a corrugated topography that may be used to identify Sn loss within the first few nanometers of the Nb_3Sn surface. While the simulation results show that bump corrugation geometries only minorly contribute to the vortex nucleation field reduction that already occurs on flat, uniformly Sn-deficient Nb_3Sn surfaces, these corrugations may serve as an identifying characteristic of extensive Sn loss from Nb_3Sn. Utilizing structural features to characterize Nb_3Sn surface stoichiometry can compensate for the experimental challenges associated with accurately chemically probing the first 100 nanometers of the Nb_3Sn surface.

Overall, these results demonstrate that local structural differences significantly impact superconducting properties of cavity surfaces, even on length scales smaller than the sensitivities of experimental techniques, such as EDS. The simulations in this study were performed using a smaller Ginzburg-Landau parameter of 10 than the true value of 26 for Nb_3Sn. While this choice was mostly due to technical constraints, our simulations still fall within the same "large κ" regime as Nb_3Sn. Choosing a smaller value for κ is effectively equivalent to increasing the T_c while holding the Fermi-level density of states constant, and the ultimate result of this is that our H_{vort} predictions are likely overestimates of the true values. The $\kappa = 26$ results we did obtain agree with this, as the simulations for a 100-nm Sn island at $\kappa = 26$ had a 28.3% vortex nucleation field reduction compared to 24.4% at $\kappa = 10$. The biggest drop in H_{vort} relative to the Nb_3Sn H_{sh} we estimated was 46.2% for the fully embedded 200-nm island, so the true impact of such an island is likely an even larger drop in performance. This island is still relatively small compared to the scale of many of the defects in Nb_3Sn samples, so it is plausible that larger instances of Sn islands are contributing to the performance limitations which have plagued Nb_3Sn cavities to date.

Future studies should involve simulating more sizes of Sn islands, particularly smaller ones, that may further illuminate performance degradations which can occur for even surfaces which may appear only minimally Sn rich. Also, larger, longer-term simulations done at $\kappa = 26$ may help determine the specific thresholds for vortex nucleation. Collaborative experimental-theory efforts should also be dedicated to understanding how the Nb_3Sn surface oxide, alternative Nb-Sn phases (Nb_6Sn_5, $NbSn_2$), and other film properties affect the expected SRF behavior. It would also be beneficial to simulate how the stoichiometric variations at non-surface-specific features, such as grain boundaries, further contribute to variations in SRF performance [27]. For example, building upon previous studies of vortex nucleation at Nb_3Sn grain boundaries by Carlson *et al.* [8], the SRF performance can be directly correlated to experimental scanning transmission electron microscopy and electron energy loss spectroscopy data of Sn-rich subsurface features.

There currently exists a significant gap between theoretical and experimental Nb_3Sn SRF optimization efforts. Many Nb_3Sn surface defects have been observed throughout the SRF community and have proven immensely difficult to prevent or remove during the fabrication process. Experimentally, it is likely impossible to form a defect-free Nb_3Sn surface on a Nb SRF cavity using the vapor deposition procedure. Despite this, there is relatively little prior theoretical work specifically modeling the effect of the wide variety of observed material defects. In order to continue the monumental progress made towards improving the quality of vapor-deposited Nb_3Sn films, we need to know which stoichiometric defects have the largest impact on accelerating gradients and prioritize reducing their incidence. We argue experiment-informed theoretical models are the best way to determine the impact of defects, since it is generally impossible to isolate microscopic defects for direct measurement. This work provides a systematic approach to close the experiment-theory gap in the SRF community. We developed an intuitive framework to

create predictive models which combine experimental characterizations of defects in Nb_3Sn surfaces with theoretical methods that model the interaction of these defects with applied magnetic fields. These models allow us to estimate how specific submicron-scale defects attenuate high-field SRF performance. While the results we report in this work include specific insights about the growth and impact of Sn islands and Sn-deficient surfaces, our methods provide a general framework for future studies. This study as well as future ones like it will help to guide the development of improved Nb_3Sn fabrication procedures that can enable the next generation of SRF cavities.

ACKNOWLEDGMENTS

We thank Dr. Alexander Filatov of the University of Chicago for help with the x-ray diffraction measurements and Dr. Nathan Sitaraman for conducting DFT calculations for the $\nu(0)$ and T_c values for the $A15$ phase for Nb_3Sn and the body-centered tetragonal phase for Sn. This work was supported by the U.S. National Science Foundation under Award PHY-1549132, the Center for Bright Beams. The infrastructure and facilities from the NSF Materials Research Science and Engineering Center (MRSEC) at the University of Chicago (under Grant No. NSF-DMR-2011854) are also acknowledged.

[1] P. C. Bhat *et al.*, Future high energy colliders and options for the U.S, J. Inst. **18**, P12007 (2023).

[2] C. Antoine, Materials and surface aspects in the development of SRF niobium cavities, in *EuCARD Editorial Series on Accelerator Science* (Warsaw, Poland, 2012).

[3] T. Proslier, J. Zasadzinski, L. Cooley, M. Pellin, J. Norem, J. Elam, C. Z. Antoine, R. A. Rimmer, and P. Kneisel, Tunneling study of SRF cavity-grade niobium, IEEE Trans. Appl. Supercond. **19**, 1404 (2009).

[4] D. Bafia, *Exploring and Understanding the Limitations of Nb SRF Cavity Performance*, Ph.D. thesis, Illinois Institute of Technology, 2020.

[5] A. Godeke, Nb_3Sn *for Radio Frequency Cavities* (Lawrence Berkeley National Laboratory, 2006).

[6] S. Posen, J. Lee, D. N. Seidman, A. Romanenko, B. Tennis, O. S. Melnychuk, and D. A. Sergatskov, Advances in Nb_3Sn superconducting radiofrequency cavities towards first practical accelerator applications, Supercond. Sci. Technol. **34**, 025007 (2021).

[7] R. Porter, D. L. Hall, M. Liepe, and J. T. Maniscalco, Surface roughness effect on the performance of Nb_3Sn Cavities, in *Proceedings of the LINAC2016, East Lansing, MI, USA* (Joint Accelerator Conferences Website (JACoW), 2016), pp. 129–132.

[8] J. Carlson *et al.*, Analysis of magnetic vortex dissipation in Sn-segregated boundaries in Nb_3Sn superconducting RF cavities, Phys. Rev. B **103**, 024516 (2021).

[9] J. Lee, Z. Mao, K. He, Z. H. Sung, T. Spina, S.-I. Baik, D. L. Hall, M. Liepe, D. N. Seidman, and S. Posen, Grain-boundary structure and segregation in Nb_3Sn coatings on Nb for high-performance superconducting radiofrequency cavity applications, Acta Mater. **188**, 155 (2020).

[10] S.-H. Oh, D. Seol, Y.-J. Jeong, S.-H. Na, J. Kim, W.-S. Ko, J. B. Jeon, and B.-J. Lee, Diffusion in A15 Nb_3Sn: An atomistic study, Acta Mater. **234**, 118050 (2022).

[11] Y. Trenikhina, S. Posen, A. Romanenko, M. Sardela, J.-M. Zuo, D. L. Hall, and M. Liepe, Performance-defining properties of Nb_3Sn coating in SRF cavities, Supercond. Sci. Technol. **31**, 015004 (2017).

[12] C. Becker, S. Posen, N. Groll, R. Cook, C. M. Schlepütz, D. L. Hall, M. Liepe, M. Pellin, J. Zasadzinski, and T. Proslier, Analysis of Nb_3Sn surface layers for superconducting radio frequency cavity applications, Appl. Phys. Lett. **106**, 082602 (2015).

[13] E. Viklund, J. Lee, D. N. Seidman, and S. Posen, Three-dimensional reconstruction of Nb_3Sn films by focused ion beam cross sectional microscopy, IEEE Trans. Appl. Supercond. **33**, 1 (2023).

[14] A. Godeke, A review of the properties of Nb_3Sn and their variation with A15 composition, morphology and strain state, Supercond. Sci. Technol. **19**, R68 (2006).

[15] Z. Sun, Z. Baraissov, R. D. Porter, L. Shpani, Y.-T. Shao, T. Oseroff, M. O. Thompson, D. A. Muller, and M. U. Liepe, Smooth, homogeneous, high-purity Nb_3Sn superconducting RF resonant cavity by seed-free electrochemical synthesis, Supercond. Sci. Technol. **36**, 115003 (2023).

[16] U. Pudasaini, G. V. Eremeev, J. W. Angle, J. Tuggle, C. E. Reece, and M. J. Kelley, Growth of Nb_3Sn coating in tin vapor-diffusion process, J. Vac. Sci. Technol. A **37**, 051509 (2019).

[17] P. Zhang, Y. Y. Lau, and R. M. Gilgenbach, Analysis of radio-frequency absorption and electric and magnetic field enhancements due to surface roughness, J. Appl. Phys. **105**, 114908 (2009).

[18] U. Pudasaini, C. Reece, and J. Tiskumara, Managing Sn-supply to tune surface characteristics of vapor-diffusion coating of Nb_3Sn, in *Proceedings of the 20th International Conference on RF Superconductivity* (Joint Accelerator Conferences Website (JACoW), US, 2021).

[19] J. Tiskumara, J. Delayen, U. Pudasaini, C. Reece, and G. Eremeev, Nb_3Sn coating of twin axis cavity for SRF applications, in *Proceedings of the 20th International Conference on RF Superconductivity, East Lansing, MI* (Joint Accelerator Conferences Website (JACoW), 2022).

[20] J. Tiskumara, J. Delayen, G. Eremeev, and U. Pudasaini, Lower temperature annealing of vapor diffused Nb_3Sn for accelerator cavities, in *Proceedings of the 5th North American Particle Accelerator Conference (NAPAC2022)* (Joint Accelerator Conferences Website (JACoW),2022).

[21] S. Burgess, J. Sagar, J. Holland, X. Li, and F. Bauer, Ultra-low kV EDS—A new approach to improved spatial resolution, surface sensitivity, and light element compositional imaging and analysis in the SEM, Microsc. Today **25**, 20 (2017).

[22] C. R. Brundle and B. V. Crist, X-ray photoelectron spectroscopy: A perspective on quantitation accuracy for composition analysis of homogeneous materials, J. Vac. Sci. Technol. A **38**, 041001 (2020).

[23] A. Cano, G. V. Eremeev, J. R. Zuazo, J. Lee, B. Luo, M. Martinello, A. Romanenko, and S. Posen, Selective thermal evolution of a native oxide layer in Nb and Nb_3Sn-coated SRF

grade Nb: An *in situ* XPS study, J. Phys. Chem. C **127**, 19705 (2023).
[24] S. Posen, N. Valles, and M. Liepe, Radio frequency magnetic field limits of Nb and Nb_3Sn, Phys. Rev. Lett. **115**, 047001 (2015).
[25] S. Keckert *et al.*, Critical fields of Nb_3Sn prepared for superconducting cavities, Supercond. Sci. Technol. **32**, 075004 (2019).
[26] H. Devantay, J. L. Jorda, M. Decroux, J. Muller, and R. Flükiger, The physical and structural properties of superconducting A15-type Nb-Sn alloys, J. Mater. Sci. **16**, 2145 (1981).
[27] M. M. Kelley, N. S. Sitaraman, and T. A. Arias, *Ab initio* theory of the impact of grain boundaries and substitutional defects on superconducting Nb_3Sn, Supercond. Sci. Technol. **34**, 015015 (2020).
[28] S. A. Willson, R. G. Farber, A. C. Hire, R. G. Hennig, and S. J. Sibener, Submonolayer and monolayer Sn adsorption and diffusion behavior on oxidized Nb(100), J. Phys. Chem. C **127**, 3339 (2023).
[29] R. G. Farber, S. A. Willson, and S. J. Sibener, Role of nanoscale surface defects on Sn adsorption and diffusion behavior on oxidized Nb(100), J. Vac. Sci. Technol. A **39**, 063212 (2021).
[30] J. Lee, S. Posen, Z. Mao, Y. Trenikhina, K. He, D. L. Hall, M. Liepe, and D. N. Seidman, Atomic-scale analyses of Nb_3Sn on Nb prepared by vapor diffusion for superconducting radiofrequency cavity applications: A correlative study, Supercond. Sci. Technol. **32**, 024001 (2018).
[31] G. Jiang *et al.*, Understanding and optimization of the coating process of the radio-frequency Nb_3Sn thin film superconducting cavities using tin vapor diffusion method, Appl. Surf. Sci. **643**, 158708 (2024).
[32] See Supplemental Material at http://link.aps.org/supplemental/10.1103/PhysRevResearch.6.043133 for additional details of film growth recipes 1-3 and supporting experimental characterization of the Nb_3Sn films.
[33] M. Ohring, *The Material Science of Thin Films* (Academic Press, San Diego, CA, 1992).
[34] C. B. Alcock, V. P. Itkin, and M. K. Horrigan, Vapour pressure equations for the metallic elements: 298–2500 K, Can. Metall. Q. **23**, 309 (1984).
[35] D. Hall, *New Insights into the Limitations on the Efficiency and Achievable Gradients in* Nb_3Sn *SRF Cavities, Dissertation*, (Cornell University, 2017).
[36] L. Gor'Kov and G. Eliashberg, Generalization of the Ginzburg-Landau equations for non-stationary problems in the case of alloys with paramagnetic impurities, Sov. Phys. JETP **27**, 328 (1968).
[37] N. Kopnin, *Theory of Nonequilibrium Superconductivity* (Oxford University Press, New York, 2001), Vol. 110.
[38] M. Tinkham, *Introduction to Superconductivity* (Courier Corporation, North Chelmsford, MA, 2004).
[39] M. K. Transtrum, G. Catelani, and J. P. Sethna, Superheating field of superconductors within Ginzburg-Landau theory, Phys. Rev. B **83**, 094505 (2011).
[40] L. Kramer and R. J. Watts-Tobin, Theory of dissipative current-carrying states in superconducting filaments, Phys. Rev. Lett. **40**, 1041 (1978).
[41] T. Proslier, J. F. Zasadzinski, L. Cooley, C. Antoine, J. Moore, J. Norem, M. Pellin, and K. E. Gray, Tunneling study of cavity grade Nb: Possible magnetic scattering at the surface, Appl. Phys. Lett. **92**, 212505 (2008).
[42] A. Gurevich and T. Kubo, Surface impedance and optimum surface resistance of a superconductor with an imperfect surface, Phys. Rev. B **96**, 184515 (2017).
[43] T. Kubo and A. Gurevich, Field-dependent nonlinear surface resistance and its optimization by surface nanostructuring in superconductors, Phys. Rev. B **100**, 064522 (2019).
[44] COMSOL Inc., *COMSOL Multiphysics* (COMSOL Inc., Burlington, MA, 2023).
[45] B. Oripov and S. M. Anlage, Time-dependent Ginzburg-Landau treatment of rf magnetic vortices in superconductors: Vortex semiloops in a spatially nonuniform magnetic field, Phys. Rev. E **101**, 033306 (2020).
[46] M. S. Alnæs, J. Blechta, J. Hake, A. Johansson, B. Kehlet, A. Logg, C. Richardson, J. Ring, M. E. Rognes, and G. N. Wells, The FEniCS project version 1.5, Arch. Numer. Software **3**, 9 (2015).
[47] H. Gao and W. Sun, A new mixed formulation and efficient numerical solution of Ginzburg–Landau equations under the temporal gauge, SIAM J. Sci. Comput. **38**, A1339 (2016).
[48] A. V. Harbick and M. K. Transtrum, A time-dependent Ginzburg-Landau framework for sample-specific simulation of superconductors for SRF applications, arXiv:2410.20078.
[49] C. T. Campbell, Ultrathin metal films and particles on oxide surfaces: Structural, electronic and chemisorptive properties, Surf. Sci. Rep. **27**, 1 (1997).
[50] D. R. Askeland, *The Science and Engineering of Materials* (Chapman Hall, Oxford, UK, 1996).
[51] N. S. Sitaraman, M. M. Kelley, R. D. Porter, M. U. Liepe, T. A. Arias, J. Carlson, A. R. Pack, M. K. Transtrum, and R. Sundararaman, Effect of the density of states at the Fermi level on defect free energies and superconductivity: A case study of Nb_3Sn, Phys. Rev. B **103**, 115106 (2021).
[52] J. P. Charlesworth, I. Macphail, and P. E. Madsen, Experimental work on the niobium-tin constitution diagram and related studies, J. Mater. Sci. **5**, 580 (1970).
[53] M. N. Sayeed, U. Pudasaini, C. E. Reece, G. V. Eremeev, and H. E. Elsayed-Ali, Properties of Nb_3Sn films fabricated by magnetron sputtering from a single target, Appl. Surf. Sci. **541**, 148528 (2021).
[54] M. N. Sayeed, U. Pudasaini, C. E. Reece, G. Eremeev, and E. H. Elsayed-Ali, Structural and superconducting properties of Nb_3Sn films grown by multilayer sequential magnetron sputtering, J. Alloys Compd. **800**, 272 (2019).
[55] E. Barzi, M. Bestetti, F. Reginato, D. Turrioni, and S. Franz, Synthesis of superconducting Nb_3Sn coatings on Nb substrates, Supercond. Sci. Technol. **29**, 015009 (2015).
[56] S. A. Willson, H. Lew-Kiedrowska, V. Do, and S. J. Sibener, Influence of Nb substrate morphology and atomic structure on Sn nucleation and early Nb_3Sn growth, Appl. Surf. Sci. **664**, 160272 (2024).

Chapter 5

Other Defects in Nb_3Sn

In the previous chapters, we have investigated several different defects in Nb_3Sn. In Chapter 2, we investigated Sn deficient islands, and in Chapter 4 we investigated embedded islands of Sn in Nb surfaces, as well as rough surface features on Sn-deficient grains. We now turn our attention to several other defects that we simulated with TDGL, but that at the time of writing have not been published.

5.1 Nb_3Sn Grain Boundaries

Grain boundaries are widely considered one of the most critical defects to address when improving Nb_3Sn cavity performance [80, 81]. A previous study in Physical Review B by several members of CBB and its collaboraors studied this question in detail [54]. This study concluded that, in agreement with the suspicions of many in the field, grain boundaries are indeed a strong candidate for one of the primary sources of dissipation and peformance drops in Nb_3Sn SRF cavities, concluding that grain boundaries act as both nucleation and pinning sites for vortices, and that it would only require $\sim 0.03\%$ of the grain boundaries in the cavity to be filled with vortices to lead to a drop in Q by an order of magnitude.

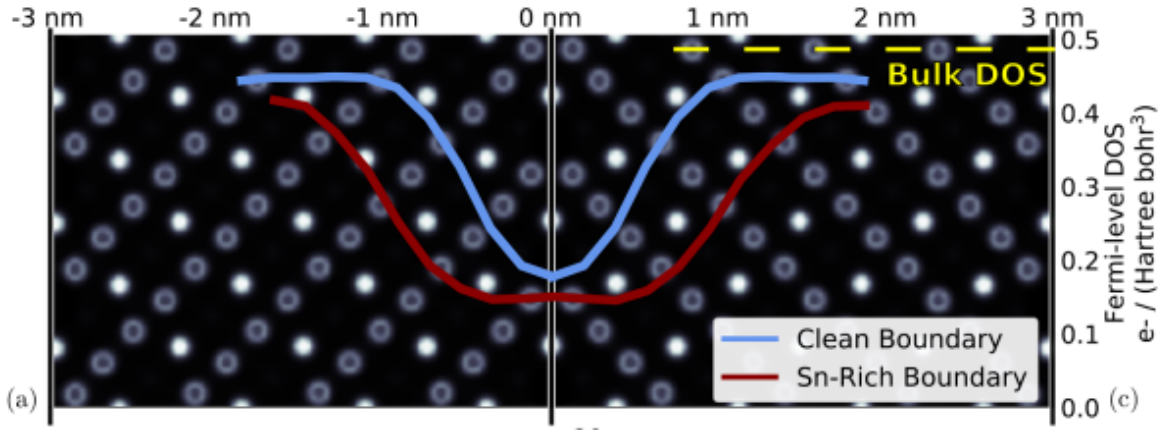

Figure 5.1 Two different profiles of the Fermi-level density of states ($\nu(0)$) for clean and Sn-rich grain boundaries. Image provided courtesy of Dr. Michelle Kelley [87]. The background shows the lattice configuration near the grain boundary, and the blue and red curves show the shapes of the DoS profiles for clean and Sn-rich grain boundaries, respectively.

There were two key things we build upon from this study. Firstly, the TDGL simulations used in this analysis used a more simplified material dependence for the TDGL parameters, setting $\alpha \propto 1 - \frac{T}{T_c}$ and only varying the T_c in the grain boundaries. Now that we have a more sophisticated method for estimating the TDGL parameters for specific materials (described in Chapter 2), we wanted to revist this problem and see how more realistic TDGL parameters would impact these results. Additionally, these calculations only focused on Sn-segregated grain boundaries, grain boundaries in which there is a higher than 25% Sn concentration. We wanted to also compare these grain boundaries to 'clean' grain boundaries, which do not see as significant stoichiometric differences, and only see modified superconducting properties due to local strain fields and other microscopic geometric effects.

Figure 5.1 (provided courtesy of Dr. Michelle Kelley [87]) shows the Fermi-level density of states profiles for clean and Sn-rich grain boundaries. We see that the profile for the clean grain boundary is much more narrow than that of the Sn-rich one. This is a direct result of the larger Sn concentration near the grain boundary for the Sn-rich case leading to a lower density of states

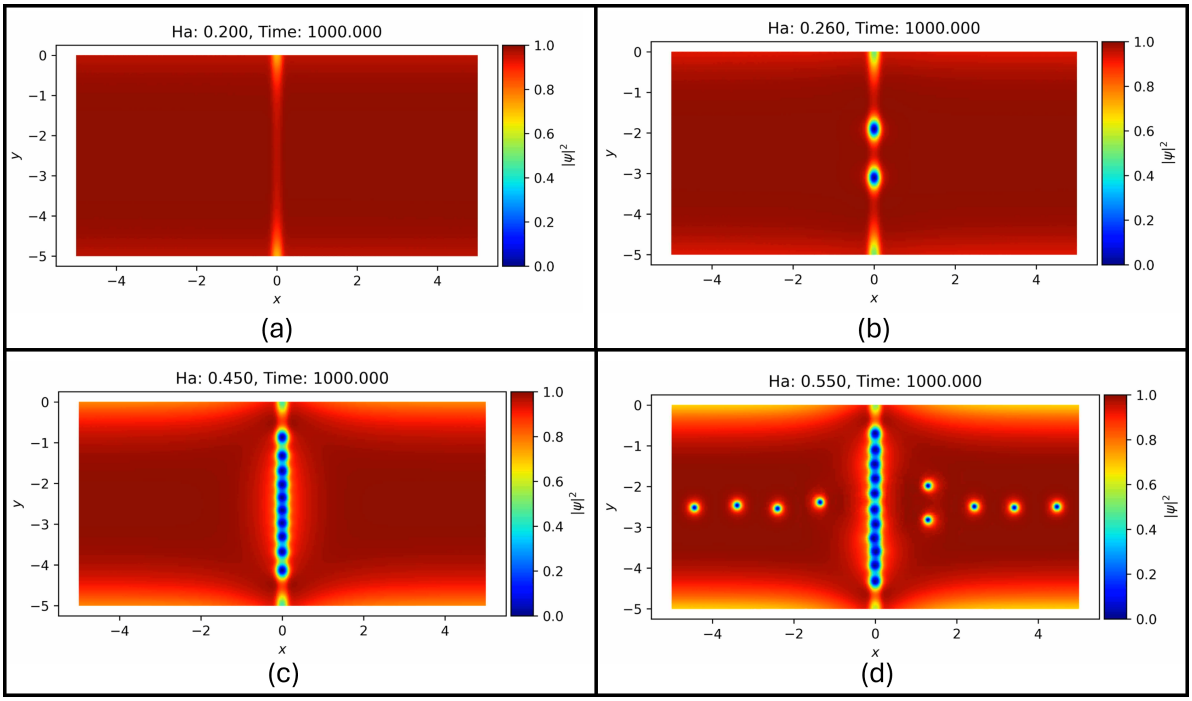

Figure 5.2 Steady State Plots of Sn-Rich Grain Boundaries at Different Applied Fields. The figures depict states in which the grain boundary is (a) vortex free, (b) containing only two vortices after initial nucleation, (c) full of vortices at a higher field, and (d) unable to contain the vortices, in which they spill out into the bulk.

due to the material properies of off-stoichiometry Nb-Sn systems, as opposed to the clean graain boundary, where the supression in the density of states is primarily due to the local strain fields across the boundary. Using these values along with the associated T_c estimates (also courtesy of Michelle Kelley), we construct profiles for α, β, and Γ using the methods described in Chapter 2.

Figure **??** depicts a representative sample of the kinds of behaviors we observed in our simulations, with vortices nucleating into the grain boundary at the vortex penetration field, H_{vort}, then the grain boundary slowly fills up with more vortices until the field reaches the bulk penetration field, H_{bulk} where the grain boundary can no longer contain any more vortices, and so they are pushed into the bulk. It is worth noting that this behavior is the result of a sort of 'buckling' instability,

where when the linear number density of vortices becomes to large, and the line 'buckles' and some vortices are pushed out into the bulk in either direction. This is a fundamentally different mechanism than what is calculated in Ref. [87], where the vortex pinning force was compared against the Lorentz force for a single vortex.

This buckling behavior is consistent with what was observed in the previous grain boundary study with TDGL, which described this system in terms of three states, a flux free state, a pinned flux state, and a bulk flux state. Our simulations reflects this, but there is an interesting subtelty when introducting multiple kinds of grain boundaries, in this case the clean boundary in addition to the Sn-rich one (which is what was simulated in the prior grain boundary study). Table 5.1 shows the results of our critical field calculations compared to those from Ref. 54. Using our sample specific formulation, we find lower results for both the vortex penetration field H_{vort} and the bulk penetration field H_{vort}. The vortex penetration field was lower for the Sn-rich grain boundary than the clean grain boundary, which is what we expect. This is because the clean grain boundary both has a thinner depression in both the Fermi-level density of states as well as T_c, and slightly higher values (compared to the Sn-rich case) for both at the center of the boundary lead to a higher energy barrier against vortex formation. The more surprising result is that both the Sn-rich and clean grain boundaries had essentially the same bulk penetration field $H_{bulk}/H_{sh} = 0.9$. We suspect the reason for this result is that while the clean grain boundary doesn't start nucleating vortices until a higher field value, the weaker pinning of this type of grain boundary also leads to the buckling instability occurring at a lower vortex line density than for the Sn-rich case, meaning both end up reaching their respective H_{bulk} values at the same field. A simple schematic demonstrating this behavior is found in Figure 5.3. The basic picture is that each type of grain boundary nucleates vortices at their

respective H_{vort} above which the vortex density linearly grows (in the limit of infinite size, this is technically a discrete process) until they reach some critical vortex density at H_{bulk} that induces the buckling instability and the vortices enter the bulk, with new vortices that enter the grain boundary displacing existing ones into the bulk, leading to a constant vortex density.

Grain Boundary Type	H_{vort}/H_{sh}	H_{bulk}/H_{sh}
Sn-rich (PRB Results)	0.7	0.95
Sn-rich (Using Sample Specific Formulation)	0.42	0.9
Clean	0.57	0.9

Table 5.1 Results for the vortex penetration field H_{vort} and bulk penetration field H_{bulk} with respect to the superheating field of Nb_3Sn at 4.2 K. The results are compared between the two kinds of grain boundaries we simulated and the results from the PRB article on this topic. We find that using our sample specific formulation, we predict both lower H_{vort} and H_{bulk} values.

The macroscopic interpretation of these two fields is seen in experimentally measured Q vs E_{acc} plots for real cavities. When vortices enter the grain boundary, but stay pinned there they lead to dissipation which causes a drop in Q, thus leading to high-field Q-slope (HFQS). So H_{vort} serves as the field of the onset of HFQS. On the other hand, vortices in the bulk will lead to even more significant runaway dissipation, and represent a cavity-quenching issue. As such H_{bulk} represents the cavity quench field. In this way the distance between these two fields represents how abrupt the HFQS is. We see in real cavities that sometimes the HFQS starts at a relatively lower field, and then the Q slowly drops as the accelerating field increases until it reaches a quench at a much higher field. Conversely, in some cases the Q remains relatively stable until a high field value, at which the Q rapidly drops and quenches soon after. This interpretation lends itself to the picture that a cavity with more Sn-rich grain boundaries may look more like the first of these, whereas cavities with more clean grain boundaries would look closer to the second of these.

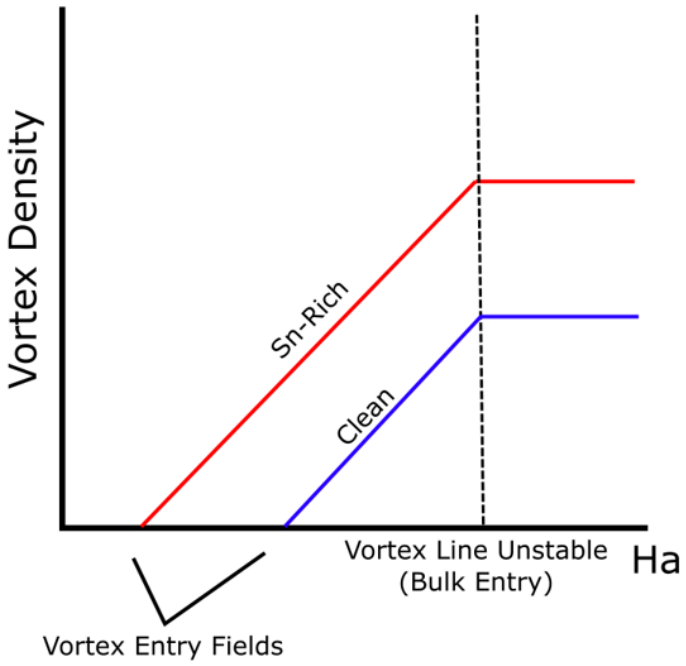

Figure 5.3 A simple schematic of vortex density versus applied field. Both types of grain boundaries start nucleating vortices at their respective H_{vort} values, and then as the field increases the vortex density grows until the vortices in the grain boundary reach the buckling stability, after which any new vortices entering displace existing ones, pushing them into the bulk and leading to a constant vortex density inside the grain boundary.

This picture is augmented by another calculation from Ref. 54, where the authors estimate that the vortices will lead to local heating of the grain boundaries, but it stays contained to within a small distance of the grain boundary. The distance over which this heating is contained still falls outside of our simulation domain, meaning that this heating would be relevant to our simulations. A future goal for our code could include coupling the dissipation from our solutions to a temperature field to simulate this ourselves, but a simple approach that we take here is to just rerun these simulations at the temperature value of the GBs in the vortex state calculated in the PRB article, 10 K. The H_{vort} estimates would not make sense for this case, as the temperature would only reach 10K after vortices already nucleate, so we will only report the H_{bulk} values. We found that for both types of grain boundaries at 10 K, $H_{bulk}/H_{sh} = 0.75$, which decreases the distance between the previous H_{vort} values and this new H_{bulk} value.

To conclude these calculations, it is worth comparing out results to the experimental values. At the time of writing, most Nb_3Sn cavities reach quench at accelerating gradients of $\sim 15-24$ MV/m. This corresponds to $H_{bulk}/H_{sh} \approx 0.15-0.23$ in our unit system. The onset of HFQS varies significantly from cavity to cavity, but on average it tends to occur around $H_{vort}/H_{sh} \approx 0.1-0.15$. These numbers are all a good bit smaller than our calculated values, indicating that there are likely more sources of dissipation at play than just what we have simulated here. Though a significant portion of this discrepancy may also come from the inherent limitations of TDGL, which is not quantitatively accurate for $T << T_c$ and assumes gapless superconductivity. It is possible that a similar analysis with more sophisticated theories of superconductivity, such as Eilenberger or Eliashberg theory, could improve this quantiative discrepancy. Nonetheless, TDGL provides a powerful qualitative tool, providing clear physical insignts into the dissipation mechanisms at play,

and it is also worth pointing out that even if the absolut magnitude of our results is higher than the experimentally measured ones, the relative distance between our estimates for H_{vort} and H_{bulk} are comparable to those of experiment, which lends additional credence to our typical arguments that TDGL does well at predicting relative behaviors even when it is not quantitatively accurate.

These results do not result in overall conclusions which are substantially different than those of Ref. 54, which is why we ultimately opted not to publish these results, but we still believe that they provide some interesting additional insights into the very relevant grain boundary defects in Nb_3Sn SRF cavities.

5.2 Nb_3Sn Surface Layers

Nb_3Sn cavities are constructed by vapor diffusing Sn into a Nb surface creating a relatively thin layer of Nb_3Sn on top of Nb. We have investigated many of the potential defects which may appear within this layer, but we have not yet accounted for the actual shape of this layer itself. We will now cover simulations of Nb_3Sn surface layers we performed to investigate this question. This was a project largely performed by an undergraduate, Aaron Fawley, under my supervision. All simulations and figures in this section were created by Aaron, which I present here with his permission.

We start by simulating a completely flat layer, and just look at the impacts of layer thickness. We solve TDGL in 2D (which assumes a symmetry along the z-axis) and then construct the TDGL parameters α, β, and Γ such that at the surface the material is Nb_3Sn, then at some distance d below the surface the material parameters transition to the corresponding values for Nb. Figure 5.4 shows our results for this calculation. We see that above a layer depth of $d \approx 2.5\lambda$, H_{vort} asymptotes to the superheating field of Nb_3Sn (the dotted black line). For layer depths $d < 2.5\lambda$, H_{vort} starts to drop significantly, eventually reaching the superheating field of Nb for near zero thicknesses. This

behavior is expected, as when the layer is sufficiently thick, it will screen essentially all of the field from the Nb, meaning H_{vort} just looks like the superheating field for Nb_3Sn, and as the layer depth approaches zero, the material will be exclusively Nb and thus should just have the superheating field of Nb.

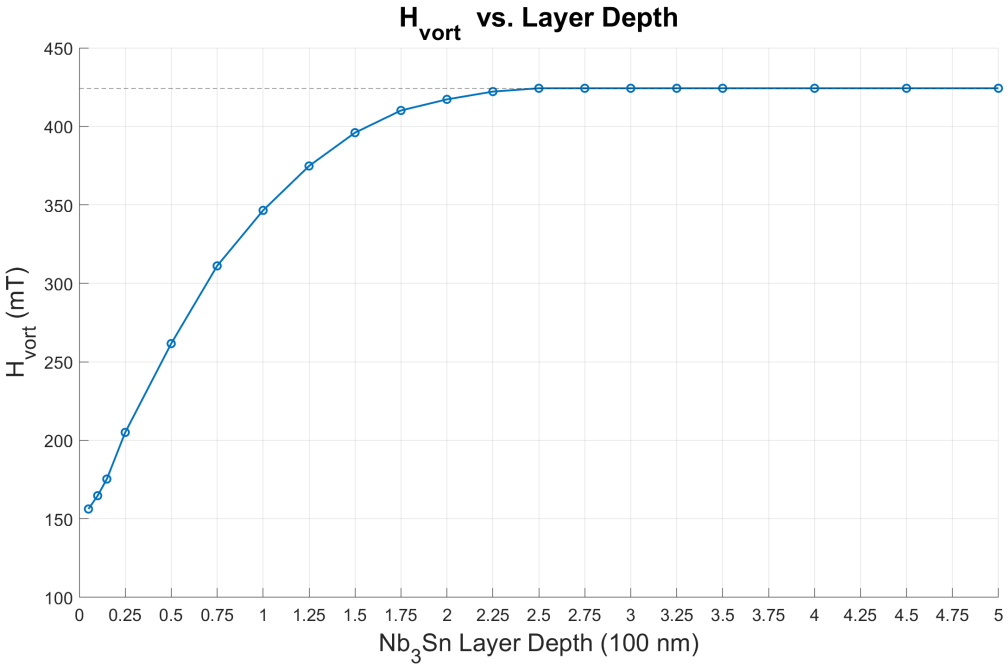

Figure 5.4 A plot of H_{vort} vs. layer depth for flat layers. The value of H_{vort} asymptotes to the superheating field of Nb_3Sn for sufficiently thick layers, and starts to drop for layer depth $d < 2.5\lambda$.

With this baseline in mind, we now consider the shape of the actual layer. To do this, we will simulate layers with a sinusoidal shape of some frequency and estimate how H_{vort} changes with respect to this frequency. Som examples of such simulations are shown in Figure 5.5, which shows some vortex nucleation for simulations of a few wavelengths. To maintain the periodicity of our simulations we had to modify the width of our domain in order to capture several wavelengths for each case we simulated. Of particular concern to these simulations is the notion of the critical wavelength, λ_c, of variations in the order parameter during vortex nucleation. We derive our

expression for the critical wavelength from the corresponding formula for the critical wavenumber, k_c, given by Transtrum et. al. [47]:

$$\lambda k_c \approx 0.9558\kappa^{3/4}, \tag{5.1}$$

where λ and $\kappa = \lambda/\xi$ are the penetration depth and Ginzburg-Landau parameters, respectively. This equation, noting that $\lambda_c \equiv 2\pi/k_c$, results in a critical wavelength given by

$$\lambda_c \approx \frac{2\pi}{0.9558}\lambda^{1/4}\xi^{3/4}. \tag{5.2}$$

The value of λ_c gives the characteristic spacing of vortices during vortex nucleation. For our simulations, we normalize distances with respect to λ, meaning in Equation 5.2 we set $\lambda = 1$, and then since we run at $kappa = 20$ to simulate Nb_3Sn, $\xi = 0.05$. This results in a critical wavelength for our simulations of $\lambda_c = 0.695$, which defines the natural spacing for vortices during nucleation.

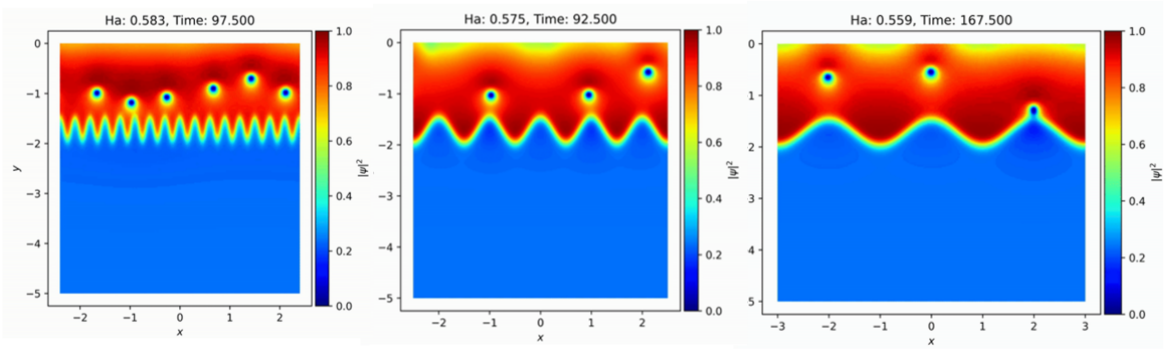

Figure 5.5 Several plots of vortex nucleation for different layer wavelengths.

When vortices enter the simulation domain, they will deviate from this fundamental spacing, both because of numerical effects such as mesh spacing and also more fundamental effects, such as the transition from a 1D arrangement (along the surface) to a 2D lattice arrangement (where the spacing becomes determined by the Abrikosov spacing). In our simulations, the critical nucleation can best be seen in terms of 'proto'-vortices, which is a term we give to the depressions in $|\psi|^2$ near

the surface which may eventually become a vortex, but has not yet fully formed, as shown in Figure 5.6. The spacing between these proto-vortices should go like λ_c though, as we will later discuss, this can vary due to numerical effects. We care about this particular length scale, as we expect that there may be some relevant effects to H_{vort} when the wavelength of the layer matches λ_c.

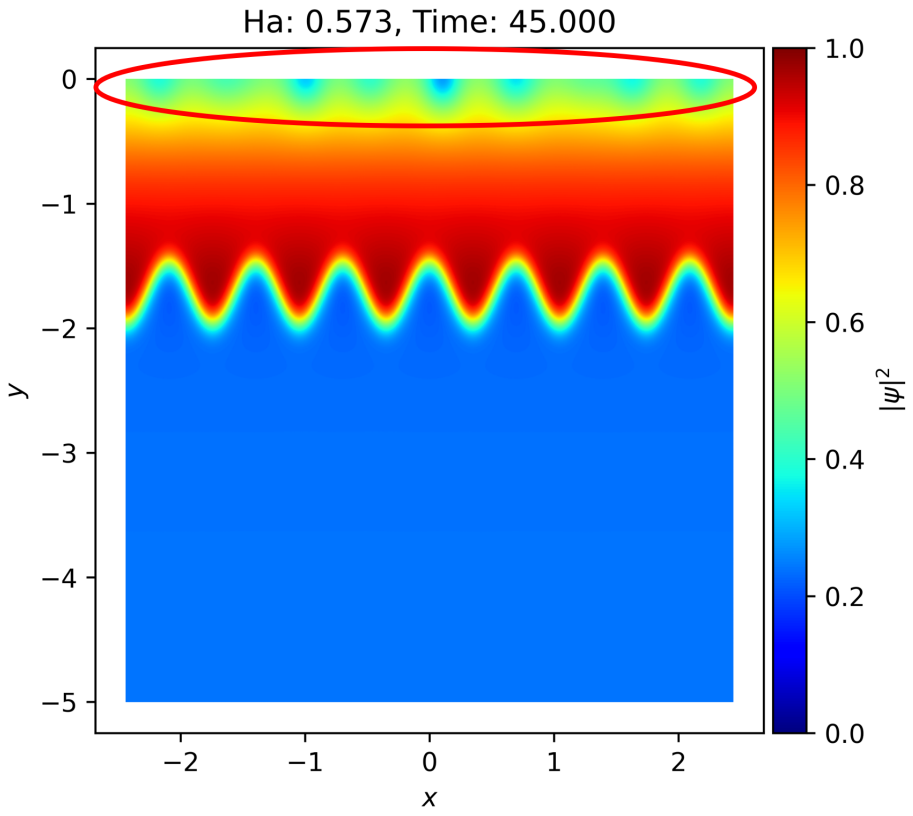

Figure 5.6 A plot of the proto-vortices (circled in red) which form right before vortex nucleation. The spacing between these should theoretically be $\lambda_c \approx 0.695$, though this can vary somewhat due to the numerics.

Figure 5.7 shows our results for estimations of H_{vort} versus layer wavelength, for a sinusoidal layer centered at $d = 1.5\lambda$ below the surface with an amplitude of 0.25λ. We see that there are two asymptotes for large and small wavelengths. At large wavelength the shape of the layer changes slowly enough that it behaves closer to a flat layer, and so vortices nucleate at the same field value

as for a flat layer positioned at the peaks of the sinusoid. In the limit of small wavelength, the shape of the layer is changing fast enough, that it asymptotes to the same value as a corresponding flat layer positioned halfway between the peak and the center value of the sinusoid. As we suspected, there is indeed something happening near λ_c, as well as at some of the higher harmonics. However, our expectation was that there would be a decrease in H_{vort} at λ_c, as the alignment of protovortices with the peaks of the layer should reduce the energy barrier against vortex nucleation relative to other nearby wavelengths which do not perfectly match the shape of the layer. We instead see a peak at λ_c and a depression at a slightly higher wavelength. We believe that this is directly due to finite size effects.

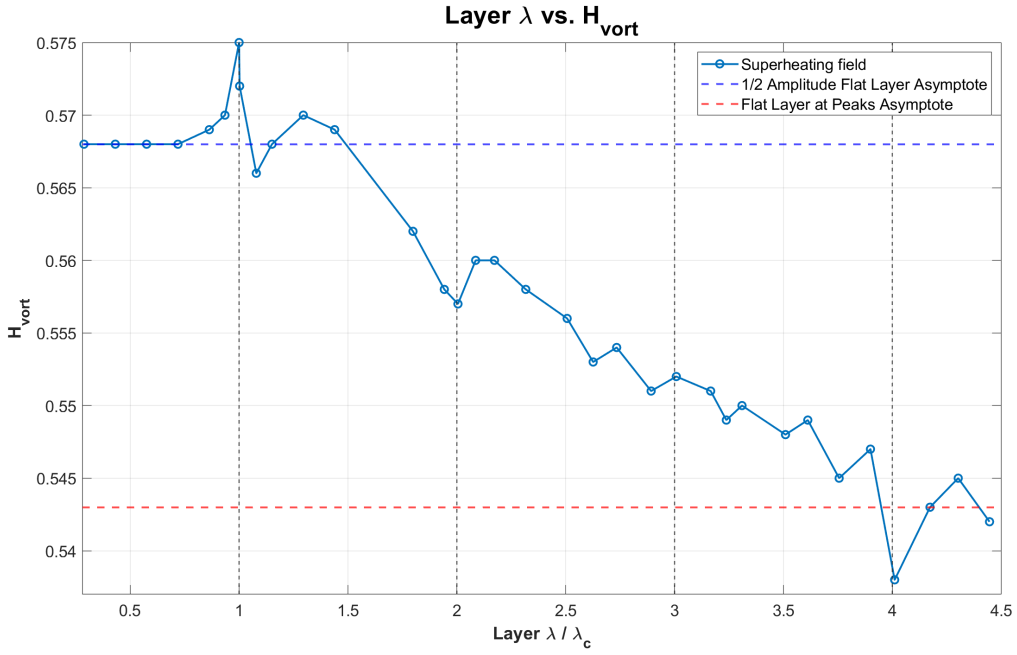

Figure 5.7 Values for H_{vort} versus the wavelength of the layers in our simulations. There are two asymptotes, one at large wavelength where H_{vort} approaches the corresponding value for a flat layer at the peaks of the layer, and another for small wavelengths where H_{vort} approaches the value of a flat layer centered halfway between the peak and center of the sinusoid. The drops below the amplitude for the large wavelength limit are likely the result of numerical noise.

When performing our numerical simulations, we necessarily must use a finite size domain, and we somewhat arbitrarily chose our domain to capture 7 wavelengths of the layer boundary. However, vortex nucleation is inherently a discrete process. Suppose we have a surface which nucleates some number of vortices. If we were to then increase the width of this surface by a small amount and run another simulation, there would still be the same number of vortices, though perhaps no longer spaced in the same way. This is because vortices exert forces on one another, and this would prevent any additional vortices from entering if there is not enough room to fit another one given the force balance. Because of this sort of effect, we suspect that the increase in the curve above the low wavelength asymptote in Figure 5.7 is a numerical artifact resulting from finite size effects, and the shift in the expected depression away from λ_c is the result of the simulation having a different effective λ_c due to uncertainty in k space. This k space uncertainty can be estimated with

$$\Delta k = \frac{2\pi}{W_{sim}}, \tag{5.3}$$

where Δk is the k space uncertainty and W_{sim} is the width of the simulation domain. Using Equation 5.3, for the simulation widths that we used for the simulations in Figure 5.7, $\Delta k \approx 1.2$, while the points around k_c are only separated by about 0.1 in k space. This indicates that we need a much larger mesh to be able to resolve differences of this scale in our simulations. At the time of writing, these simulations are still ongoing, so we do not yet have preliminary results for this adjustment, but it is clear that readjusting our simulations to a larger domain size is the clear next step for our simulations.

In addition to the finite size effects, the results from Figure 5.7 are generally somewhat noisy. This is becasue for these simulations we chose to center the layer at $d = 1.5\lambda$ below the surface, and with an amplitude of 0.25λ. This layer is somewhat deep, and thus there is a relatively small distance between the two asmptotes for the plot, meaning the values are more sensitive to noise in the calculation that can just come from small differences in the mesh. To address this issue, we attempted to repeat this same analysis for a later that is closer to the surface. Doing so led us

to discover a rather interesting phenomenon, depicted in Figure 5.8. Here we see that the vortex nucleation pattern leads to the nucelation of a vortex-antivortex pair at the peaks of the layer, with the antivortices exiting the domain and the vortices travelling further down into the domain. At the time of writing this is again a somewhat preliminary result, but this behavior seems to be robust to refinements in the mesh, as well as under conditions such as a changing applied field, and this modality of vortex nucleation persists even at higher fields, so we are inclined to believe it is not merely a numerical fluke. The exact reason for this behavior is still unclear, but it seems that something about the shape of the peaks near the surface lead to it being more energetically favorable to nucelate this vortex-antivortex pair at the peaks rather than at the surface as usually happens. If this behavior is realistic, it would have meaningful rammifications for SRF performance, namely that the ammount of dissipation in the vortex state would essentially be doubled, as there would be two vortices to dissipate energy as opposed to the usual one in most other cases.

As we have mentioned here a few times, much of the latter part of this work is fairly new at the time of writing, and this work is ongoing. In terms of the implications for SRF research, the primary conclusion is that the Nb_3Sn layer should be as thick as possible, at least until it is $> 2.5\lambda$ thick. This conclusion is not too surprising, but the final result in this section suggests that thin spots in the layer resulting from peaks in the boundary layer shape could potentially be extra problematic. This means that it may be important to prioritize growth procedures which produce a relatively uniform layer, in addition to the thickness. The future outlook for these simulations is that we plan to continue investigating these thinner layers, and also will refine the meshes in some of the earlier calculations to hopefully reduce noise. These calculations, in addition to ones looking at the impact of changing the amplitude of the layer boundary will hopefully constitute results which can be published separately in the future.

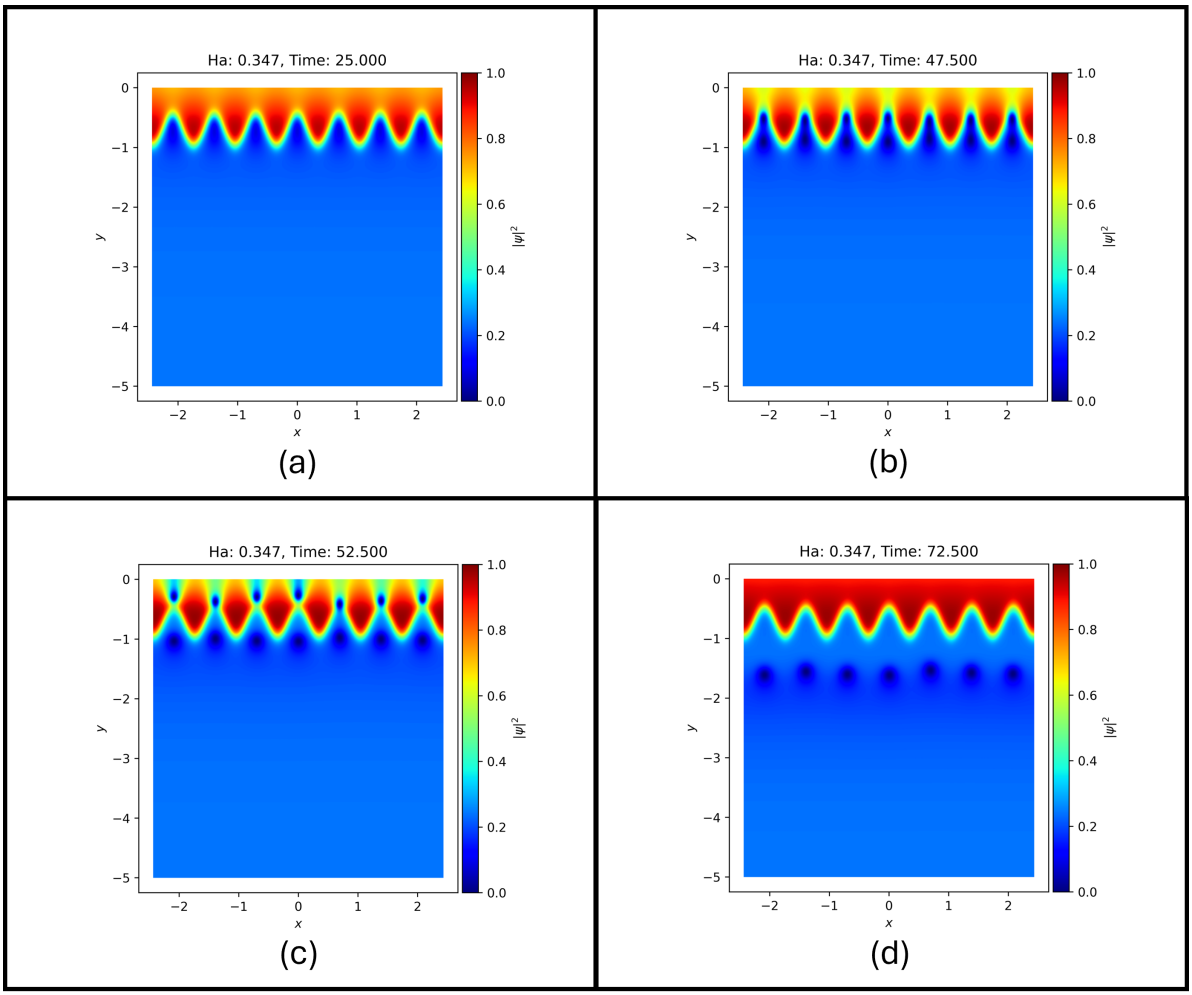

Figure 5.8 Plots of $|\psi|^2$ for the nucleation of a vortex-antivortex pair. The figures depict (a) the layer before vortex nucleation, (b) the initial vortex pair formation, (c) the antivortices being pushed out of the domain while the vortices travel below the layer, and (d) the vortices left behind after the antivortices have been pushed out.

Chapter 6

More Surface Defect Calculations

The following chapter details more of the calculations we did of general surface defects. The simulations in this section utilize the same methods as the simulations from Chapter 4, using the same formulation as Oripov et. al. [55, 56] and running these simulations using COMSOL© Multiphysics. The following sections will cover simulations of “step bump” simulations, where we study surface bumps with a step function shape. We chose this geometry as it allows us to explore the effects of the height and width of surface bumps for a shape where these quantities are unambiguously defined; the only length scales associated with this shape are exactly the height and width, there are no length scales associated with curvature or other effects. In addition to this, “cliff-like" structures have been observed in the surface of real cavities [143], so this kind of structure is not even completely unrealistic. In order to further isolate the length scales of this problem, we will restrict the bulk of our analysis to two primary limits, the “tall bump limit" in which the height of the bump $h >> \lambda > \xi$, and the width of the bump is small comparatively. An example of this limit is shown on the left in Figure 6.1. This limit allows us to explore the length scale associated with

bulk nucleation of vortices. The other limit we explore is the “wide bump limit" in which the width of the bump $w >> \lambda > \xi$, and the height is small. An example of this limit is shown on the right in Figure 6.1 In this limit we explore the length scales ascoiated with the initial vortex nucleation process. We will begin by exploring the tall bump limit.

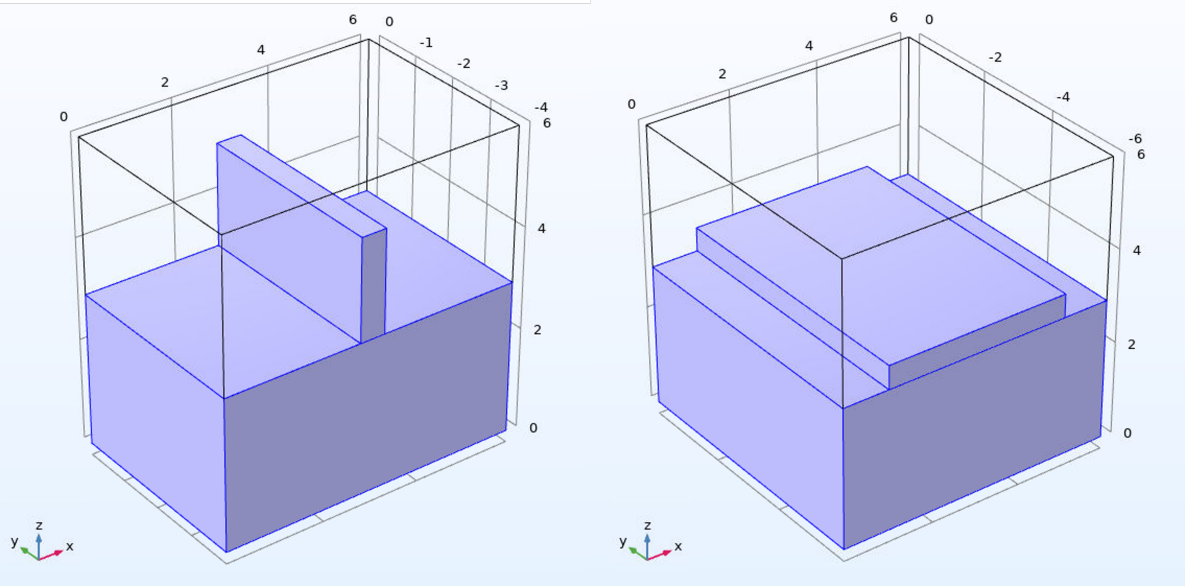

Figure 6.1 Example geometries for the tall (left) and wide (right) bump limits.

6.1 The “Tall Bump Limit"

In this section we run simulations under the tall bump limit. Under this limit, vortices are easily able to nucleate into the bump itself, as the current screening is weak. However, while the energy barrier against the formation of these vortices in the bump itself is small, there is an additional energy barrier required for these vortices to grow and push down into the bulk. This leads to the vortices becoming pinned at the base of the bump. An example of this is shown in Figure6.2, where we see a number of vortices pinned to the base of the bump. More vortices nucleated than could fit at the base of the bump, so the additional vortices sit above the pinned ones inside the bump. Eventually, once

the field is strong enough, the vortex will nucleate into the bulk. We will call this the bulk nucleation field, H_{bulk}. An example of this process is shown in Figure 6.3. Once the field reaches H_{bulk}, the vortices at the base of the bump form a semiloop, which grows until it meets its perodic images, and then straightens out. In terms of the macroscopic SRF picture, this phenomenon is associatied with the quench field for SRF cavities. When vortices are able to enter the bulk material, it will lead to runaway heating and dissipation that will eventually cause a quench, so this calculation tells us what characteristic width of surface defects needs to be controlled in order to prevent early quenches.

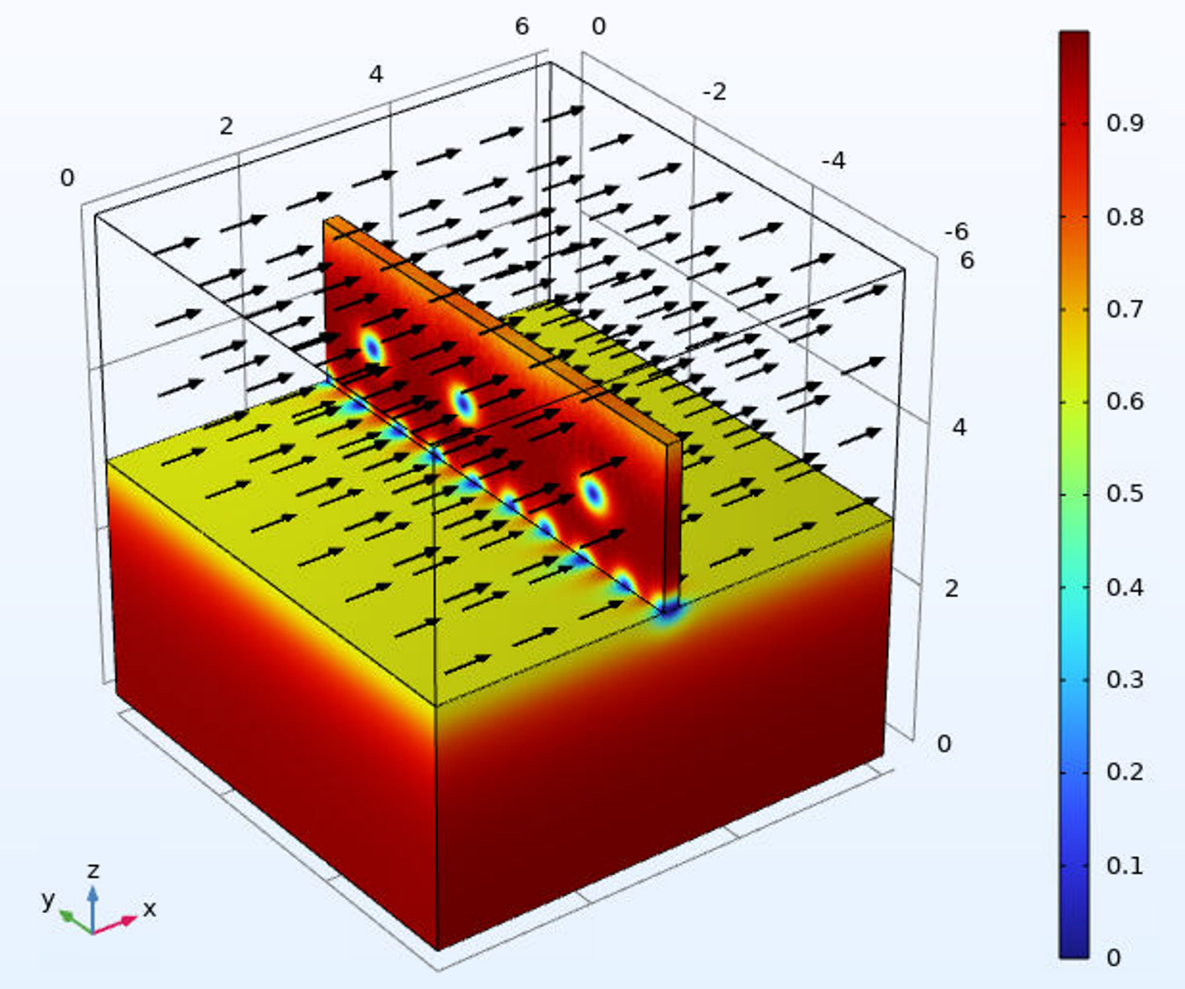

Figure 6.2 A plot of $|\psi|^2$ for a tall bump. The arrows indicate the direction of the magnetic field. Most vortices are pinned to the bottom of the bump, with additional vortices that entered sitting above where there is more space for them.

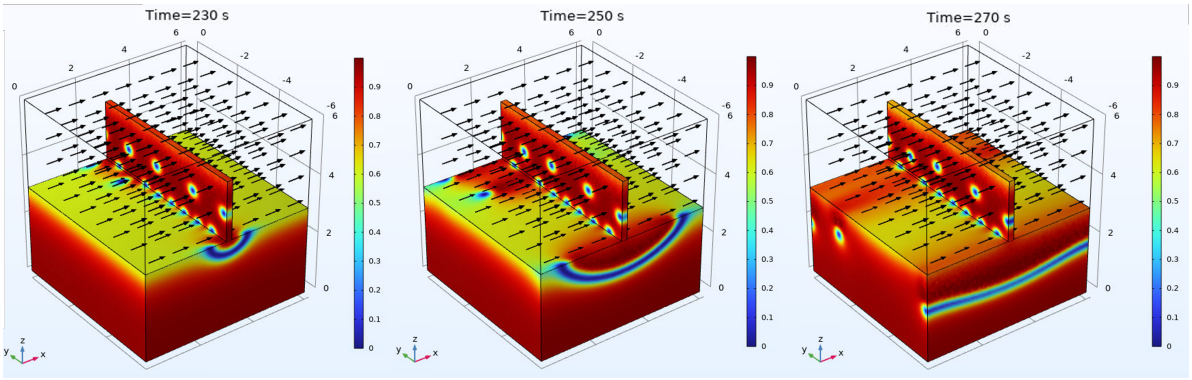

Figure 6.3 Plots of $|\psi|^2$ for a tall bump. The arrows indicate the direction of the magnetic field. The process of a vortex nucleating into the bulk is shown. First a vortex semiloop is formed (left), then it grows in size (middle), and finally it meets the its periodic images and flattens out into a line (right).

In order to extract the length scale of this phenomenon, we consider an expansion of H_{bulk} in terms of the bump width, w,

$$\frac{H_{bulk}}{\sqrt{2}H_c} = A(\kappa) + B(\kappa)\frac{w}{\lambda} + \frac{1}{2}C(\kappa)\left(\frac{w}{\lambda}\right)^2 + \ldots, \tag{6.1}$$

where H_c is the thermodynamic critical field, $\kappa = \frac{\lambda}{\xi}$ is the Ginzburg-Landau parameter, λ and ξ are the penetration depth and coherence lengths, and $A(\kappa)$, $B(\kappa)$, and $C(\kappa)$ are the expansion coefficients, which in general could be functions of κ. We know that if $w = 0$, this represents a completely flat layer, meaning that $A(\kappa) = H_{sh}/\sqrt{2}H_c$. Then the rest of the problem requirest both determining H_{bulk} with respect to small w, and then doing this for multiple values of κ to extract the length scales.

Figure6.4 shows our results for this calculation. We see that at each value of κ, the dominant term of Equation 6.1 is clearly the linear one, and so each set of points is fit to a line. The values of $B(\kappa)$ are plotted in Figure 6.5. We see that B is linear in κ, meaning that $B \propto \kappa$. This means that we can conclude that the expansion of H_{bulk} in small w goes like

$$\frac{H_{bulk}}{\sqrt{2}H_c} = \frac{H_{sh}}{\sqrt{2}H_c} + B'\kappa\frac{w}{\lambda} = \frac{H_{sh}}{\sqrt{2}H_c} + B'\frac{w}{\xi}, \tag{6.2}$$

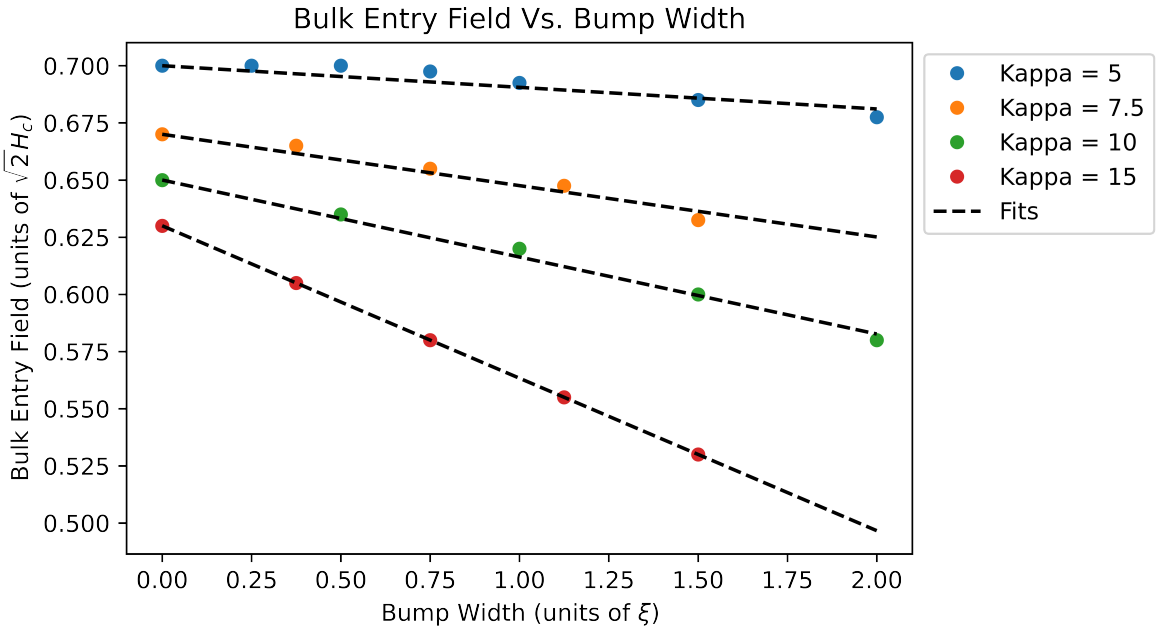

Figure 6.4 Plots of $H_{bulk}/\sqrt{2}H_c$ versus bump width w. Each set of points is fit to a line, showing that the linear term of Equation 6.1 is the dominant term for this effect, the slope also clearly gets steeper with increasing κ.

where B' is the constant of proportionality for B. What this expansion tells us is that the relevant length scale for vortex bulk entry is the coherence length, ξ. This then implies that the quench fields for SRF cavities are impacted by surface defects on the scale of ξ which for Nb_3Sn is $\sim$ 4nm. We will now turn to the wide bump limit

6.2 The “Wide Bump Limit"

In this section we run simulations under the wide bump limit. Inthis limit, the vortices are not as easily able to nucleate into the actual bump as they were in the tall bump limit. Additionally, once vortices do enter the bump the pinning seen in the tall bump limit does not happen, as the vortices already need to form semiloops in order to enter these bumps, and so they can freely enter the bulk from there. This limit therefore allows us to explore the length scale associated with the initial

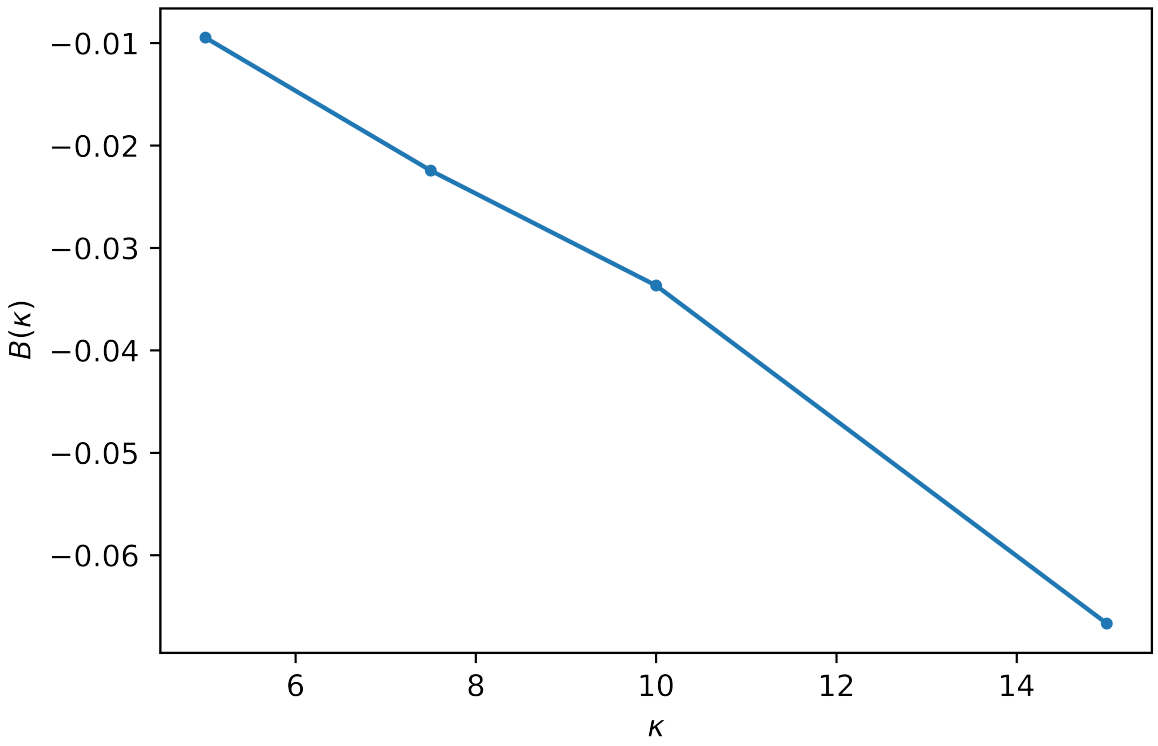

Figure 6.5 Plots of B versus κ, where B is the coefficient of the linear term in Equation 6.1. The κ dependence of B appears to be linear.

nucleation of vortices. An example of the vortex nucleation pattern is shown in Figure 6.6. We see that the vortices form as lines across the bump, then are able to move downward once they have formed. In the SRF picture, the field at which these vortices first nucleate, H_{vort} would represent the ability for a defect to initiate dissipation which leads to high-field Q-slope (HFQS). So this limit can give us the characteristic height for the ability of surface defects to induce HFQS.

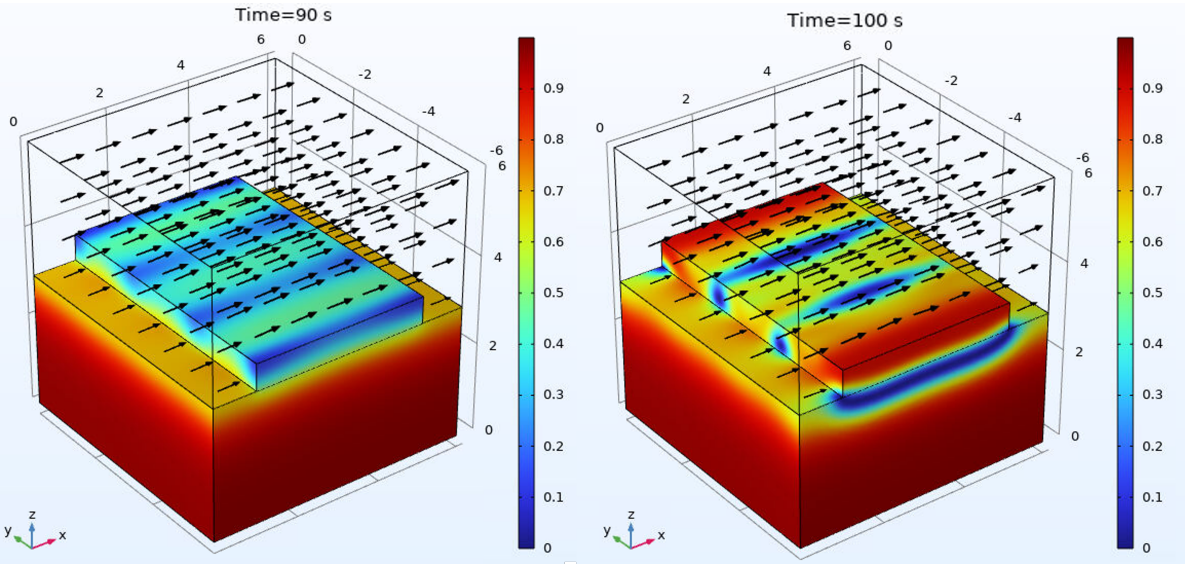

Figure 6.6 A plot of $|\psi|^2$ for a wide bump. The arrows indicate the direction of the magnetic field. Vortices begin to nucleate in lines across the bump (left) and then once they form are able to move downward (right).

Similar to the tall bump limit, we can extract this length scale with an expansion of H_{vort} in the bump height, h,

$$\frac{H_{vort}}{\sqrt{2}H_c} = A(\kappa) + B(\kappa)\frac{h}{\lambda} + \frac{1}{2}C(\kappa)\left(\frac{h}{\lambda}\right)^2 + \ldots, \tag{6.3}$$

where H_c is the thermodynamic critical field, $\kappa = \frac{\lambda}{\xi}$ is the Ginzburg-Landau parameter, λ and ξ are the penetration depth and coherence lengths, and $A(\kappa)$, $B(\kappa)$, and $C(\kappa)$ are the expansion coefficients, which in general could be functions of κ. We again know that if $h = 0$, this is a completely flat layer, so again we have that $A(\kappa) = H_{sh}/\sqrt{2}H_c$. And we will simulate the wide bump limit for several values of κ and extract both the dependence of H_{vort} on h, and the κ dependence of the expansion coefficients.

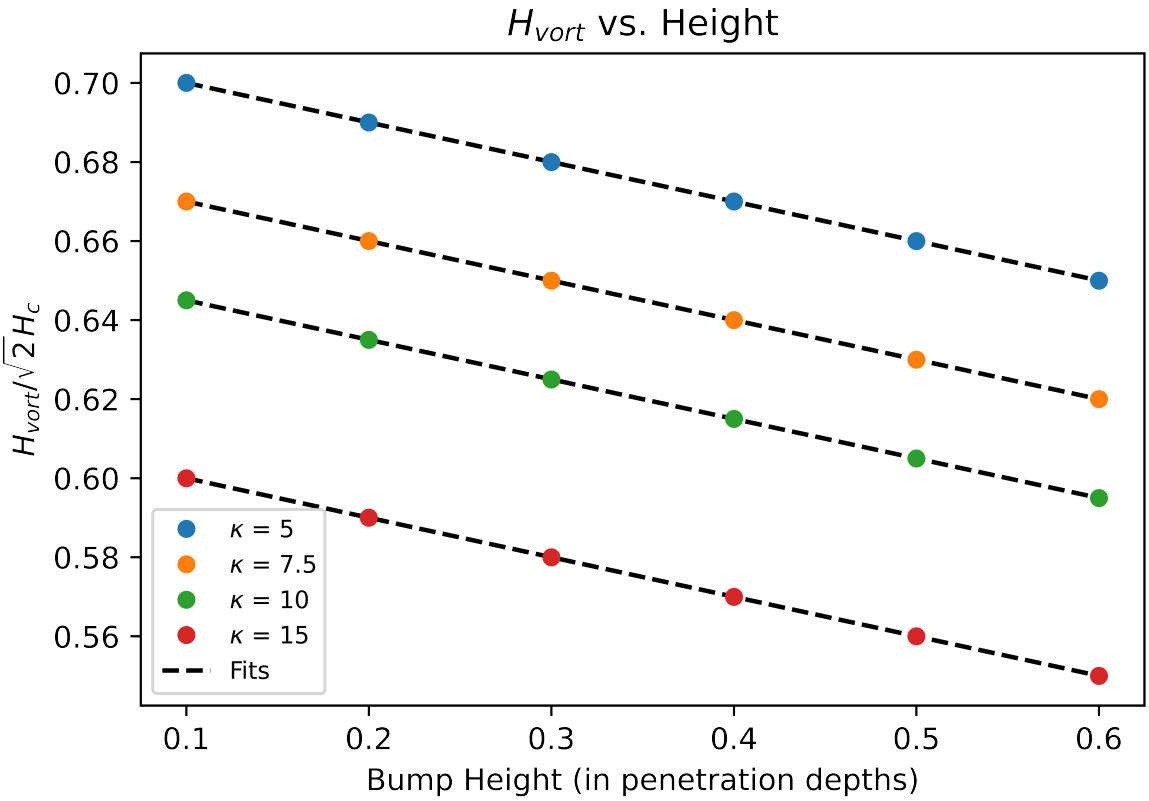

Figure 6.7 Plots of $H_{vort}/\sqrt{2}H_c$ versus bump height h. Each set of points is fit to a line, showing that the linear term of Equation 6.3 is the dominant term for this effect. The slopes are essentially identical, meaning that B is a constant with respect to κ.

Figure 6.7 shows our results for our wide bump limit calculations. We see that at each value of κ the dominant term of Equation 6.3 is clearly the linear term again. However, unlike the tall bump limit case, here all of the slopes are given by $B \approx -0.1$. This means that the expansion becomes

$$\frac{H_{bulk}}{\sqrt{2}H_c} = \frac{H_{sh}}{\sqrt{2}H_c} - 0.1\frac{w}{\lambda}. \tag{6.4}$$

This implies that the relevant length scale for this effect is the penetration depth, λ. This means that variations of the height of defects will have a meaningful impact on the onset of HFQS only over scale of λ or larger.

6.3 Conclusions

In this chapter we have explored two funadmental limits for the size of surface defects. In the tall bump limit we determined that the impact to the bulk nucleation field H_{bulk} is determined by the characteristic length of the coherence length, ξ. This means that controlling the quench fields for SRF cavities requires control over the size of surface variations on the scale of ξ, which is a challenging task for Nb_3Sn, which has $\xi \approx 4$nm. In the wide bump limit, we determined that the characteristic length scale for the vortex penetration field H_{vort} is determined by the penetration depth, λ. This means that controlling the onset of HFQS requires only control over surface variations on the scale of a penetration depth. For Nb_3Sn, $\lambda \approx 100$nm, which is a much more attainable lengh scale for control of the surface roughness. This provides a possible explanation for the behavior of some Nb_3Sn cavities which do not have HFQS but still quench well below the superheating field of Nb_3Sn, it is possible that this is the result of the surface roughness being controlled to within the scale of a penetration depth, but not a coherence length. Meaning there isn't an onset of HFQS to speak of, but once vortices penetrate there is no pinning to the surface defects, so there is runaway dissipation which leads to cavity quenching.

While the simulations in this chapter were run in full 3D, the length scales we captured here really only encapsulate two dimensions, we assumed a symmetry in the third direction for each of these limits to help us isolate a singular length scale. Future work using a similar approach to what we have done here could look at simulating full 3D defects, similar to those that we simulated in Chapter 4, except without any variations in the material stoichiometry. Additionally, these step bump defects (by design) have sharp corners. Adding some curvature to these corners would introduce additional length scales to the problem which would allow for more detailed analysis of the impacts of the actual shapes of rough surface features. Future work could also include simulating full sinusoidal surfaces of different characteristic frequencies/amplitudes. This would allow for a direct comparisons with experimental characterizations of SRF surfaces that decompose the surface into fourier components.

Overall, our results here present a compelling, albeit somewhat preliminary, picture for how simulations of 3D surfaces could explore questions of the important length scales associated with rough surface features. We think our conclusions as they stand already provide valuable insights for experimentalits developing new procedures for smoothing the surfaces of Nb_3Sn cavities, and we hope that future work can extend our approach to more detailed/realistic simulated defects.

Chapter 7

Generalized TDGL and the Frequency Dependence of H_{sh}

Throughout the previous chapters in this dissertation, we have primarily focused on calculations involving time-dependent Ginzburg-Landau theory. As we have emphasized a number of time, TDGL is primarily useful as a *qualitative* tool which allows for mesoscopic scale simulations with reasonable computational costs. This emphasis is largely the result of the restrictions to the quantitative validity of TDGL to temperatures near T_c under the assumption of gapless superconductivity. The latter condition, however, can be remedied with the use of *generalized* TDGL, which will be the focus of this chapter

7.1 Generalized TDGL

The generalized time-dependent Ginzburg-Landau (GTDGL) equations were first introduced by Kramers and Watts-Tobin in the 90s [27, 28]. In this paper, Kramer and Watts-Tobin derive GTDGL by starting with a set of equations from Larkin and Ovchinnikov [144], which come from a version of the Gor'Kov equations under the Keldysh formalism [16, 145]. Using these equations, along

with a corresponding set of kinetic equations augmented with a “mutilated collision operater" with collsion time τ_E [146], Kramer and Watts-Tobin eventually arrive at the generalized TDGL equations. We present the non-dimensionalized versions here

$$\frac{1}{\sqrt{1+\gamma^2|\psi|^2}}\left(\frac{\partial}{\partial t}+i\kappa\phi+\frac{\gamma^2}{2}\frac{\partial|\psi|^2}{\partial t}\right)\psi+\left(\frac{i}{\kappa}\nabla+\mathbf{A}\right)^2\psi-(1-|\psi|^2)\psi=0 \text{ and} \tag{7.1}$$

$$\frac{1}{u}\frac{\partial\mathbf{A}}{\partial t}+\nabla\times\nabla\times\mathbf{A}+\frac{i}{2\kappa}(\psi^*\nabla\psi-\psi\nabla\psi^*)+|\psi|^2\mathbf{A}=0, \tag{7.2}$$

where $u=\tau'_\psi/\tau_j$ is similar to what it was for TDGL, except that τ'_ψ is now the characteristic relaxation time of the *phase* of ψ and κ is the ratio of penetration depth and coherence length, the same as for TDGL. The new parameter $\gamma=2\tau_E\Delta_0$, where τ_E was introduced earlier as part of the derivation of GTDGL and is the inelastic electron-phonon scattering time, and Δ_0 is the zero-field energy gap. Under GTDGL, γ is the main parameter which differentiates it from TDGL, and it serves as a new relaxation time for the magnitude of ψ (as evidenced by its presence as the coefficient on the new time derivative term in Equation 7.1); When $\gamma=0$, the equations reduce to the traditional TDGL equations.

Whereas TDGL assumes gapless superconductivity, GTDGL does not because $\gamma\propto\Delta_0\neq 0$; however, both equations do still assume that $T\approx T_c$. Because of the addition of τ_E into the formulation, some of the simplifying assumptions in Reference 27 result in the additional condition that the inelastic diffusion length $L_E\equiv(D\tau_E)^{1/2}<<\xi$, where $D=v_f\ell/3$ is the diffusion coefficient (v_f and ℓ are the Fermi velocity and electron mean free path, respectively).

It is worthwhile to discuss the differences between GTDGL and TDGL. Firstly, they clearly will have different time dynamics, as TDGL only has a single timescale for the order parameter, whereas GTDGL has a separate timescale for the magnitude and phase. While they have different time dynamics, we can show that any steady-state solution of TDGL also satisfies GTDGL. To do

so we start with both ψ equations:

$$\frac{\partial \psi}{\partial t} = -i\kappa\phi - \left(\frac{i}{\kappa}\nabla - \mathbf{A}\right)^2 \psi + (1-|\psi|^2)\psi \qquad \text{(TDGL)}$$

$$\frac{1}{\sqrt{1+\gamma^2|\psi|^2}}\left(\frac{\partial}{\partial t} + i\kappa\phi + \frac{\gamma^2}{2}\frac{\partial|\psi|^2}{\partial t}\right)\psi = -\left(\frac{i}{\kappa}\nabla - \mathbf{A}\right)^2 \psi + (1-|\psi|^2)\psi. \qquad \text{(GTDGL)}$$

Now let $\psi_0 \neq 0$ be a steady-state solution of TDGL, then we have that $\phi = 0$, and the right hand side of both of the above equations evaluate to zero:

$$\frac{\partial \psi_0}{\partial t} = 0 \qquad \text{(TDGL)}$$

$$\frac{1}{\sqrt{1+\gamma^2|\psi_0|^2}}\left(\frac{\partial}{\partial t} + \frac{\gamma^2}{2}\frac{\partial|\psi_0|^2}{\partial t}\right)\psi = 0. \qquad \text{(GTDGL)}$$

If $\frac{\partial \psi_0}{\partial t} = 0$, then we also have that $\frac{\partial|\psi_0|^2}{\partial t} = 0$, and thus both equations are solved by ψ_0. Since both theories have the same $\mathbf{A}$ equation, any solution to TDGL will trivally also solve GTDGL.

We can also show that for any steady-state solution of TDGL ψ_0, the same solution used in GTDGL will also have the same stability properties. Let $\psi \longrightarrow \psi_0 + \delta\psi$, if we assume that $\delta\psi$ is small, we can linearize the ψ equation of TDGL in terms of $\delta\psi$, which will allow us to define a matrix equation

$$\begin{bmatrix} \frac{\partial \mathrm{Re}(\delta\psi)}{\partial t} \\ \frac{\partial \mathrm{Im}(\delta\psi)}{\partial t} \end{bmatrix} = M \begin{bmatrix} \mathrm{Re}(\delta\psi) \\ \mathrm{Im}(\delta\psi) \end{bmatrix} \tag{7.3}$$

where M is a matrix which defines the system of equations that result from the above substituion. The real part of the eigenvalues of M will give the stability properties of the solution, if the eigenvalues are ≥ 0, then the solution is unstable and if the eigenvalues of M are < 0 then the solution is stable. If we make the exact same substitution for GTDGL, the right hand side of Equation 7.3 will be identical, but there will be an additional matrix on the left hand side:

$$\frac{1}{\sqrt{1+\gamma^2|\psi|^2}} \begin{bmatrix} 1+\gamma^2\mathrm{Re}(\psi_0)^2 & \gamma^2\mathrm{Re}(\psi_0)\mathrm{Im}(\psi_0) \\ \gamma^2\mathrm{Re}(\psi_0)\mathrm{Im}(\psi_0) & 1+\gamma^2\mathrm{Im}(\psi_0)^2 \end{bmatrix} \begin{bmatrix} \frac{\partial \mathrm{Re}(\delta\psi)}{\partial t} \\ \frac{\partial \mathrm{Im}(\delta\psi)}{\partial t} \end{bmatrix} = M \begin{bmatrix} \mathrm{Re}(\delta\psi) \\ \mathrm{Im}(\delta\psi) \end{bmatrix}. \tag{7.4}$$

The new matrix on the left hand side of Equation 7.4 is positive definite (a fact which can be easily determined via Sylvester's Criterion [147]). Because this matrix is positive definite, inverting it and moving it to the right hand side will not change the signs of the real parts of the eigenvalues of M, and thus the stability properties of the solution will also be preserved.

These two results mean that as far as steady-state properties are concerned, GTDGL will not give us any information that we do not already get from regular TDGL. Conversely, this means that the steady state solutions of TDGL have a wider range of validity than the rest of the theory, a fact which is well known, but this is a concrete calculation which demonstrates that a theory with less restrictive assumptions (e.g. GTDGL and the ability to model gapped superconductors) shares steady state solutions with TDGL. Additionally, because GTDGL only differs from TDGL in the transient solutions, this makese it a natural candidate to study phenomena which never reach steady state, which is exactly the case for SRF cavities, where the field is constantly changing. The reason we often still trust the steady state solutions of TDGL for SRF research is because relative to superconducting timescales, the RF period of typical cavities is much slower, and so a DC field is a reasonable approximation. But if we want to study the impacts of frequencies higher than the typical 1.3 GHz, GTDGL is a natural choice.

In the simulations in the following section, we will solve GTDGL using the finite element method. To do so, we adapt the formulation for TDGL by Gao [25] which we use for most of our TDGL simulations. We take Gao's fomulation, and modify the ψ equation to match Equation 7.1. We then use mostly the same function spaces and weak forms, but we use a mixed function space for the real and imaginary parts of ψ, as the additional time derivative in Equation 7.1 causes the two components to mix. We then solve the equations using the same solvers as in our TDGL simulations, modified to accept the mixed function space for the components of ψ. All the computation in this chapter were performed using FEniCS [26]. We will now discuss some of our preliminary studies on the frequency dependence of H_{sh}

7.2 The Frequency Dependence of H_{sh}

The superheating field is often considered a steady state property of a superconductor and this is, in general, true. However in this section we will slightly tweak the definition of H_{sh} to apply to sinusoidal applied fields, as are present in SRF cavities. Normally the superheating field is defined as the lowest field at which the Meissner state becomes thermodynamically unstable, or more heuristically, the lowest field that will nucleate vortices if (slowly) approached from the Meissner state. Along these lines we will use a similar heuristic definition for what we now name the "RF superheating field", H_{shRF}. We define H_{shRF} as the lowest value of the RF field amplitude which will lead to a complete vortex nucleation at some point during the RF period. The emphasis here is on the word 'complete,' as at high frequency there may be situations where 'proto'-vortices (similar to those discussed in Chapter 5, Section 5.2) form, but do not have the time to fully become vortices. The idea here is that H_{shRF} will increase with respect to the cavity frequency, not because vortices couldn't form at the peak amplitudes, but because the vortices do not have the time to fully nucleate before the field changes direction.

Figure 7.1 shows an example of protovortex formation during one of our GTDGL simulations with an RF period of 100. We see that when the applied field reaches its maximum magnitude at $t = 25$, the value of $|\psi|^2$ lags behind, not reaching the lowest surface value of $|\psi|^2$ until several simulation seconds later. This is a direct result of the fact that in this simulation $\gamma = 5$, meaning the magnitude of ψ changes on a timescale that is ~ 5 times slower than the field. We then see that at $t = 40$ as the field is on the way out, protovortices have formed and reached their maximum size. In the next few seconds of the simulation, the field becomes small enough that the protovortices are forced away fairly quickly, and the solution almost reaches a value of $|\psi|^2 = 1$ everywhere at $t = 50$ when the field goes to zero.

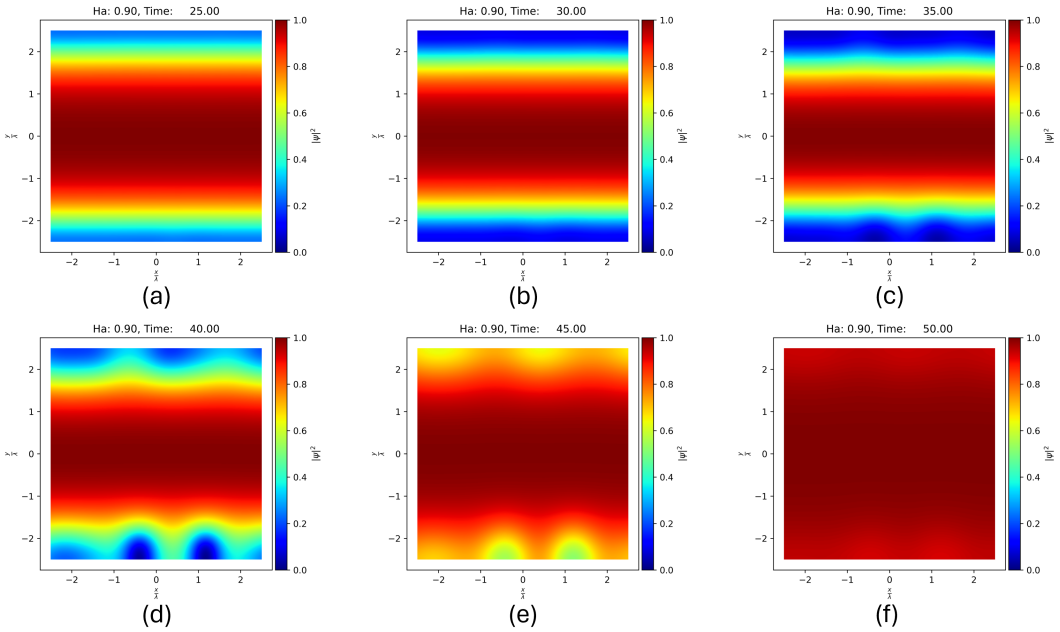

Figure 7.1 Plots of $|\psi|^2$ solved with GTDGL showing proto-vortex formation. The applied field label on the plots refers to the maximum field amplitude. The period of the field for this simulation was 100, (a) shows the solution when the field reaches its maximum at $t = 25$, (b) shows how the ψ solution lags behind the field. In (c) the protovortices begin to form on as the field is on the way down. In (d) the protovortices have reached their maximum size. By (e) the field is low enough that the protovortices are quickly suppressed, and by (f) the solution has almost relaxed fully to $|\psi|^2 = 1$ everywhere as the field reaches zero.

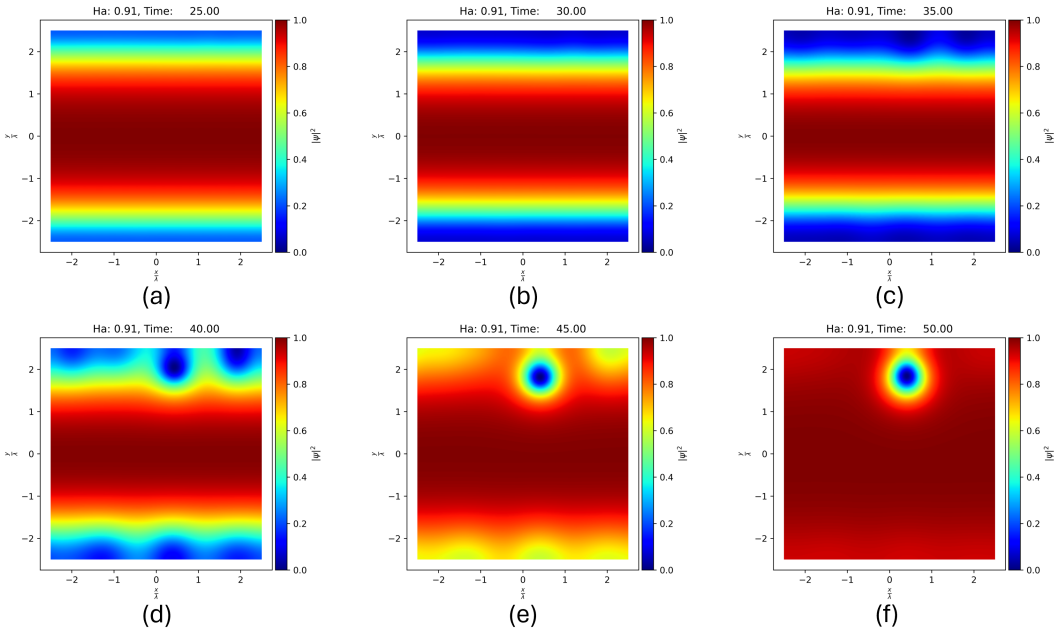

Figure 7.2 Plots of $|\psi|^2$ solved with GTDGL showing vortex nucleation. The applied field label on the plots refers to the maximum field amplitude. The period of the field for this simulation was 100, (a) shows the solution when the field reaches its maximum at $t = 25$, (b) shows how the ψ solution lags behind the field. In (c) the protovortices begin to form on as the field is on the way down. In (d) one of the protovortices has managed to fully nucleate into a vortex. By (e) most of the protovortices have been supressed leaving behind the full vortex, and by (f) only the vortex is left as the field reaches zero. The vortex will soon be pushed out of the domain a few simulation seconds later.

Figure 7.2 shows the same simulation, but at a slightly higher field. Here a vortex is able to fully form, meaning that H_{shRF} has been reached, and for this particular period and value of γ, $H_{shRF} = 0.91$. In this particular case, it is visually clear that a vortex has formed, however, this may not always be the case. To remedy this, we can calculate the number of vortices in a simulation by calculating the winding number of the phase of ψ,

$$N = \frac{1}{2\pi} \oint_P \nabla\theta \cdot d\ell, \tag{7.5}$$

where N is the winding number of the order parameter phase, P is a closed path around the simulation domain, $\theta = \arctan \mathrm{Im}(\psi)/\mathrm{Re}(\psi)$ is the phase of the order parameter, and $d\ell$ is the length element along the path P. Doing this for the simulation shown in Figure 7.2 results in Figure7.3. We see that the number of vortices correctly jumps around as vortices enter and leave the domain. Negative values refer to vortices with field oriented in the negative direction. Using this kind of calculation, we can unambiguously determine whether a vortex has formed, and thus whether or not H_{shRF} has been crossed

Figure 7.4 shows the results of our GTDGL simulations at several different values of γ. We see that in all cases (even $\gamma = 0$ which corresponds to regular TDGL), H_{shRF} increases with respect to the frequency of the applied field. As γ becomes larger, the slope of the roughly linear frequency dependence seems to increase. These results indicate that the maximum field values of SRF cavities could artificially be increased by using higher frequency cavities, and the use of GTDGL further emphasizes this conclusion, as it indicates that the incorporation of gapped superconductivity only strengthens this relation. While such an approach could lead to higher accelerating fields, it is not without downsides. The BCS resistance $R_{bcs} \propto \omega^2$, where ω is the angular frequency of the cavity, so going to higher frequency could significantly lower Q, even at low fields. Additionally a higher

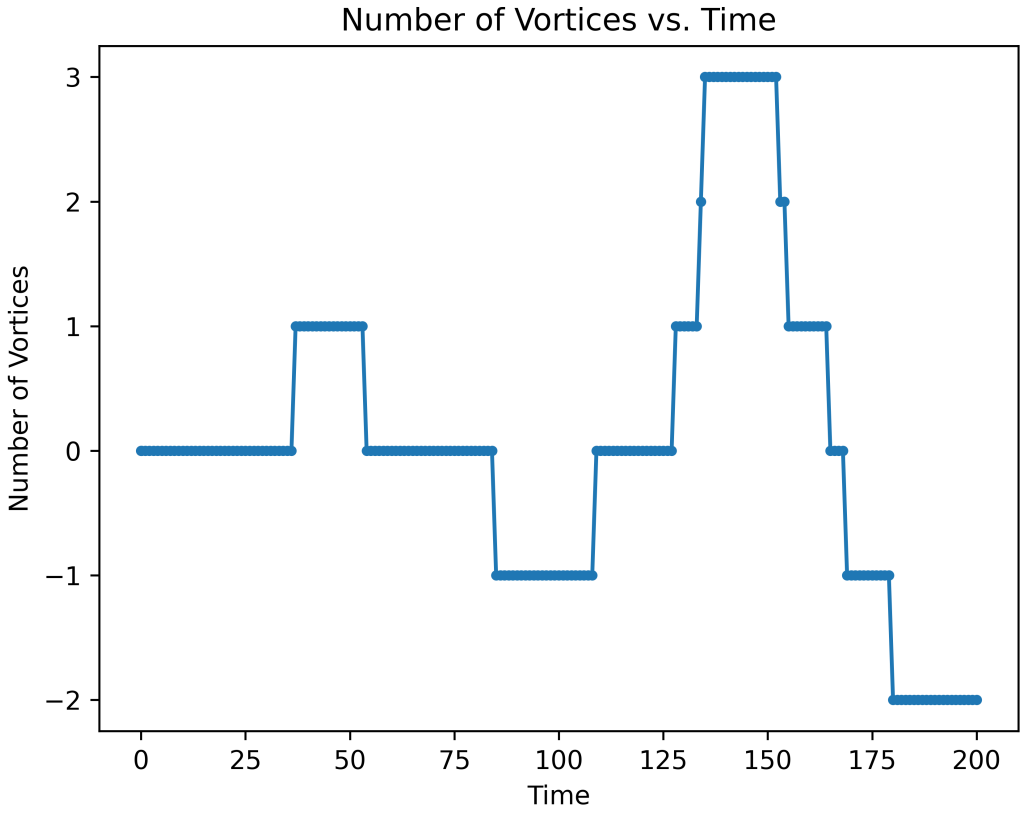

Figure 7.3 A plot of the winding number of the order parameter phase around the simulation shown in Figure 7.2. The winding number was calculated using Equation 7.5, where negative numbers are vortices with field oriented in the negative direction.

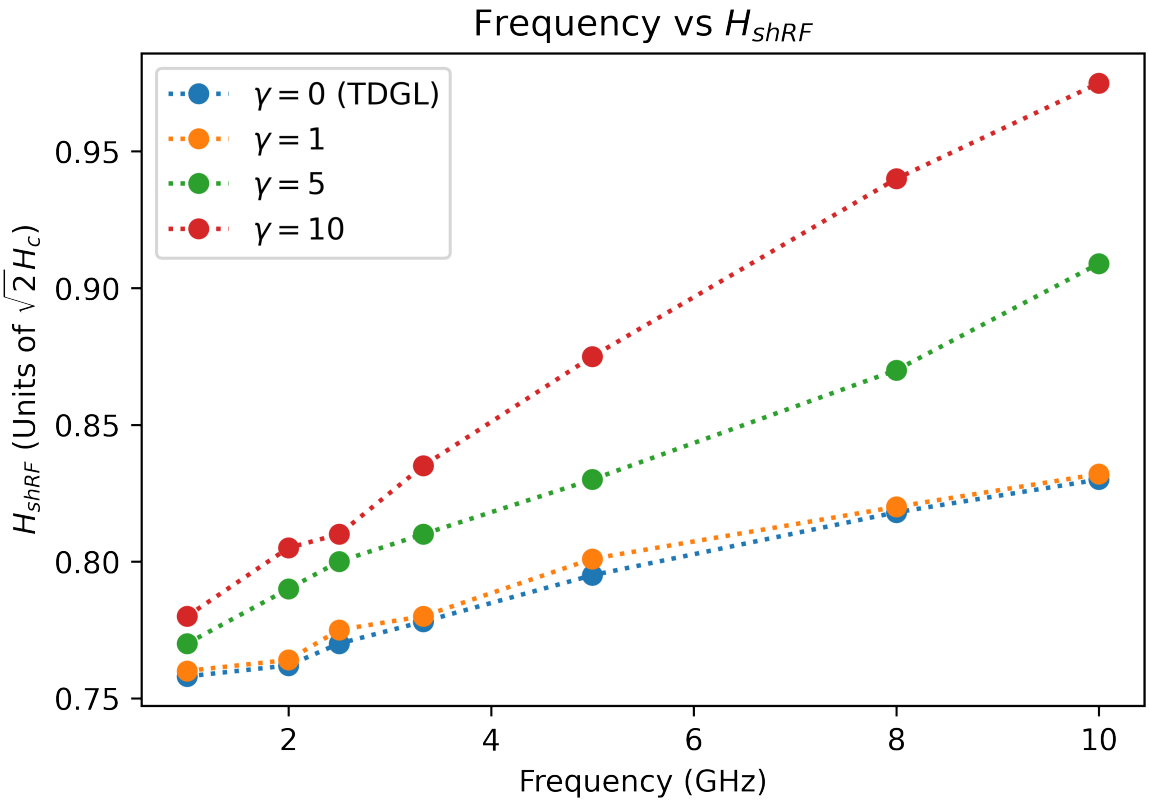

Figure 7.4 A plot of RF frequency versus H_{shRF} for different values of γ. For all values of γ (including $\gamma = 0$, which corresponds to regular TDGL) H_{shRF} increases in a roughly linear fashion, with the slope increasing with respect to γ.

frequency means a smaller cavity, and there are other deleterious effects (such as multipacting [148]) which become much more difficult to manage the smaller a cavity gets. Nonetheless, our results indicate that even a relatively modest increase in frequency could lead to a slight increase in the maximum accelerating gradients allowed by the RF cavity before quench.

Another aspect of this calculation is that we know the microscopic material dependencies of $\gamma = 2\tau_E\Delta_0$. These quantities could be easily estimated with something like DFT; future work would likely include recruiting DFT experts to help us estimate τ_E so that we can work out the accurate value of γ for a given material. GTDGL has recently been used by several groups working on superconducting quantum interference devices (SQUIDs) and superconducting nanowires [59, 60, 149], and in these papers they chose $\gamma = 10$, though it appears this choice may be somewhat arbitrary. To our knowledge, GTDGL is fairly underutilized in the SRF field despite the natural fit of the sorts of time dynamics present in SRF research that GTDGL naturally lends itself to, as we have discussed. It is our hope that this preliminary work, in which we have demonstrated some of the usefulness of GTDGL, will serve as inspiration to future SRF researchers to consider the use of GTDGL for future Ginzburg-Landau type simulations.

Chapter 8

Conclusion

This dissertation provides an in-depth examination of the factors influencing the performance of superconducting radiofrequency (SRF) cavities, with particular focus on niobium (Nb) and niobium-tin (Nb_3Sn) as primary materials. These materials are central to SRF technology, and understanding their behavior, especially at the mesoscopic scale, is critical for optimizing their performance in modern particle accelerators. The work presented here primarily explores the mesoscopic behavior of these materials, using computational models to investigate how material defects, surface characteristics, and superconducting properties interact and influence SRF cavity performance. While experimental methods, conducted by my collaborators, provide valuable insights, the core of this dissertation is grounded in computational research. Using my sample-specific time-dependent Ginzburg-Landau (TDGL) framework, I helped to provide insights into mechanisms that limit cavity performance and identify potential pathways for improvement. The following section summarizes the key findings from each chapter, outlining how the computational approaches and models developed in this dissertation contribute to advancing our understanding of SRF cavity behavior.

8.1 Summary of Key Results

In Chapter 2, we introduced a sample-specific TDGL framework, which forms the core of much of the work presented in this dissertation. This framework allows us to simulate SRF cavity performance under conditions that are representative of real materials, providing a more accurate description of their behavior. We also used this framework to calculate dissipation and quality factors. While the quantitative results are somewhat limited, the framework provides valuable qualitative insights into the factors that influence SRF cavity performance. Additionally, we estimated the impact of Sn-deficient islands on cavity performance. We found that islands several penetration depths in diameter could cause a 60% reduction in the vortex penetration field, H_{vort}, when located within a penetration depth of the surface. We also demonstrated that Sn-deficient islands could cause high-field Q-slope (HFQS) curves that qualitatively resemble those observed in real Nb_3Sn SRF cavities, thus providing a potential mechanism for HFQS and quality factor degradation.

In Chapter 3, we investigated the impact of hydrides in Nb SRF cavities, focusing on their role in high-field Q degradation. We calculated the effect of hydrides of various sizes, again finding that large hydrides—particularly those with diameters several penetration depths—could lead to a drop of 70% or more in H_{vort} if located within half a penetration depth of the surface. Furthermore, we performed simulations with numerous nano-hydrides, and we observed that when their concentration reaches a certain threshold, the material begins to behave as a single effective material. This results in a slight reduction in the superheating field, approximately 7% lower than that of pure Nb, although this is still much less detrimental than the effects of larger hydrides. These results not only provide a mechanism for hydride-induced HFQS, specifically through vortex nucleation and associated dissipation, but also suggest that treatment procedures aimed at improving HFQS in Nb cavities may be effective in increasing the number of hydride nucleation sites, thereby reducing hydride size and improving cavity performance.

Chapter 4 presents a joint experimental-computational approach to investigating the impact of surface defects in Nb_3Sn, focusing on excess Sn and surface roughness. Using our sample-specific TDGL framework and a new multi-domain COMSOL model, we examined how excess Sn and surface roughness affect SRF cavity performance. We performed calculations that allowed us to estimate the expected superheating field for surfaces with varying average Sn concentrations. Our findings suggest that performance degradation due to excess Sn islands embedded in the surface can be more significant than in a uniform surface with the same average Sn concentration. However, for high Sn concentrations, the impact of surface islands was less severe than that of uniform high-Sn surfaces, though it is important to note that high Sn-concentration uniform surfaces likely do not occur regularly due to Sn diffusion properties in Nb. Additionally, we found that surface corrugations on Sn-deficient grains could lead to slight (10%) performance degradation. However, Sn-deficient grains themselves already exhibit significantly poor performance, which aligns with the observed performance of real Nb_3Sn cavities. This suggests that Sn-deficient grains may be a significant contributor to the historically poor performance of Nb_3Sn.

In Chapter 5, we present results on grain boundaries in Nb_3Sn, where we made corrective adjustments to estimates derived from a previous CBB paper published in *Physical Review B*. Our conclusions align closely with the previous paper, namely that vortex nucleation at grain boundaries is a key candidate for one of the main causes of high-field Q-slope (HFQS) in Nb_3Sn SRF cavities. We identified two qualitative features of dissipation in this context: initial vortex nucleation, where vortices become pinned to the grain boundary, contributing to HFQS, and bulk nucleation, where vortices already in the grain boundary enter the bulk, potentially leading to cavity quench (i.e., transitioning to a normal conducting state).

One of the new calculations we performed compared the results of "Sn-rich" grain boundaries, as simulated in the previous *PRB* paper, to "clean" grain boundaries, which do not exhibit Sn segregation. These results represent perturbative corrections to those in the *PRB* paper and reveal some new qualitative insights, such as a decrease in the distance between the vortex penetration field and the bulk entry field due to the dissipative heating estimated in the earlier study. Despite these new insights, our qualitative conclusions remain largely the same, which is why we chose not to publish these results.

We also estimated the impact of Nb_3Sn surface layers, finding that layers thinner than approximately 2.5 penetration depths could start to experience performance drops below what is expected from perfect Nb_3Sn. To further explore this, we simulated sinusoidal-shaped layers, comparing their impacts relative to the "critical wavelength"—the theoretical spacing between vortices during nucleation. In doing so, we observed a situation in which vortex-antivortex pairs would nucleate at the peaks of the layer. This is a preliminary result, but if confirmed, it suggests that rough or thin spots in the Nb_3Sn surface layer could lead to additional dissipation, beyond what is normally expected from vortex nucleation, due to the nucleation of these pairs.

In Chapter 6, we presented additional surface calculations where we explored two limiting cases of idealized step-function-like defects, which we term the “tall bump" and “wide bump" limits. In the wide bump limit, we found that vortices can easily nucleate into the bulk, but they become pinned to the base of the defect. The characteristic length scale associated with vortex nucleation into the bulk, H_{bulk}, was the coherence length. This implies that surface defects capable of nucleating vortices need to be controlled down to the scale of the coherence length in order to mitigate their impact on cavity performance. Furthermore, this result suggests that the field at which cavities quench is primarily determined by defects on the scale of a coherence length, provided the quenching is caused by a surface defect.

In the wide bump limit, we also examined the vortex nucleation field, H_{vort}. In this case, vortices were no longer pinned, allowing us to explore the characteristic length scale associated with the initial vortex nucleation. We concluded that this length scale was the penetration depth, meaning that the initial penetration of vortices—and thus the onset of HFQS—is determined by features on the scale of the penetration depth. This finding underscores the importance of surface features on the scale of the penetration depth in determining the onset of vortex penetration and subsequent dissipation in SRF cavities.

Finally, in Chapter 7, we introduce and discuss the generalized time-dependent Ginzburg-Landau (GTDGL) theory, comparing it to the traditional TDGL model. We show that the additional time derivative in GTDGL decouples the magnitude and phase of the order parameter, leading to two distinct timescales for each. This decoupling makes GTDGL particularly suitable for time-dependent problems. Additionally, we demonstrate that any steady-state solution of the TDGL equations is also a steady-state solution of the GTDGL equations, with both equations having identical stability properties for those solutions. This means that GTDGL does not provide new insights for steady-state conditions beyond those of TDGL, but it also implies that TDGL can still make accurate predictions for gapped superconductors, even though it assumes gapless superconductivity.

We conclude the chapter by using GTDGL to explore the frequency dependence of the "RF superheating field," H_{shRF}, which is the minimum field amplitude of a sinusoidal applied field required to induce vortex nucleation during the RF cycle. Our calculations show that H_{shRF} increases roughly linearly with frequency, with the slope of this dependence becoming steeper as the new parameter γ in GTDGL increases. This result provides valuable insights into how the superheating field behaves in relation to RF frequency, offering potential applications for optimizing SRF cavity operation.

8.2 Potential Future Directions

While this dissertation has made significant strides in understanding the performance of SRF cavities through computational models, there remain many opportunities to expand upon and refine the work presented here. The research has provided valuable insights into the impact of material defects and surface features on SRF cavity performance, but many questions remain, particularly in areas where mesoscopic behavior interacts with macroscopic performance. Future work could build on the findings and models developed here to deepen our understanding of superconducting materials and further enhance the efficiency and effectiveness of SRF cavity technology.

One promising direction for future research is to couple the dissipation estimates to a temperature field. By doing so, we could simulate the dissipative heating of vortices directly during the calculation, allowing for a more dynamic and realistic representation of the heating effects that occur as the vortices move through the superconductor. Currently, the simulations presented in this dissertation analyze the system at fixed temperatures, which limits the ability to capture the full temporal evolution of the system as energy is dissipated. Coupling the dissipation to the temperature field would allow for the calculation of self-consistent temperature distributions in response to the energy dissipated by vortex motion. This approach could reveal more detailed and time-resolved behaviors of SRF cavities, particularly in high-field conditions where dissipation is most pronounced. Moreover, it would provide insights into the thermal feedback mechanisms that may influence the overall performance and stability of the cavity during operation.

The sample-specific framework developed in this dissertation represents a significant contribution to the modeling of SRF cavity performance. By integrating detailed experimental characterizations of various defects, density functional theory (DFT) estimates of the physical properties of these defects, and time-dependent Ginzburg-Landau (TDGL) simulations, this framework offers a more holistic approach to understanding how material defects affect cavity performance. While we have already applied this methodology in various instances throughout the dissertation, a natural

next step would be to scale this approach for a more comprehensive study. By broadening the scope to incorporate a wider range of defect types and material configurations, we could develop a fully realistic—if not quantitatively exact—Q vs. E plot that more accurately reflects the performance of SRF cavities across different conditions.

Increasing the scope of this framework would involve extending the experimental data, DFT calculations, and TDGL simulations to a larger array of sample-specific features, including more complex defect structures and varied material compositions. This expansion would allow for a more complete understanding of how different defects and material properties interact, ultimately improving the accuracy and applicability of the resulting Q vs. E plots. While the results may not be quantitatively exact, they would provide a far more realistic and comprehensive qualitative description of SRF cavity behavior, serving as a powerful tool for guiding experimental designs, improving our understanding of SRF cavity performance, and optimizing cavity technologies for future accelerators.

Additionally, the methods developed in this dissertation could be extended to a broader range of candidate SRF materials. For instance, NbZr is a material of particular interest to CBB [43, 44], but we did not fully incorporate it into this dissertation. While we did perform some preliminary calculations for Nb_3Al as a side project for a collaborator, this material was not extensively analyzed as part of this work. Nb_3Al, although it underperforms compared to Nb_3Sn, offers the advantage of being less sensitive to stoichiometry, which makes it a potential candidate for future research. The reduced sensitivity to compositional variations is a significant benefit, as it could mitigate performance degradation often seen in Nb_3Sn due to variations in the material's composition. Furthermore, Nb_3Al can be grown using similar vapor diffusion techniques as Nb_3Sn, making it a viable candidate for practical SRF applications. While it does not match Nb_3Sn in superconducting performance under ideal conditions, its improved tolerance to stoichiometry suggests that it could

be an important material for future studies. Incorporating our sample-specific TDGL framework into the study of NbZr, Nb_3Al, and other emerging materials would enable a more thorough understanding of their potential for SRF applications and allow for a direct comparison to Nb and Nb_3Sn.

As discussed in Chapter 7, there is also room to improve our GTDGL calculations. By incorporating DFT estimates of the inelastic electron-phonon scattering time, we could more accurately calculate the parameter γ, allowing for more specific predictions of the frequency dependence of H_{shRF}. Additionally, GTDGL offers a natural extension to TDGL for quality factor calculations, as such calculations require dealing with sinusoidal applied fields that prevent the system from reaching steady state. While GTDGL would not provide a completely quantitatively accurate solution, it would offer a significant improvement over TDGL in modeling time-dependent effects and the behavior of SRF cavities.

8.3 Final Remarks

This dissertation has provided a comprehensive exploration of the factors influencing the performance of superconducting radiofrequency (SRF) cavities, focusing particularly on the role of material defects and surface features in Nb and Nb_3Sn. By combining computational models, such as the sample-specific time-dependent Ginzburg-Landau (TDGL) framework we developed, with a detailed understanding of mesoscopic behavior, we have been able to uncover mechanisms that govern dissipation and high-field Q-slope (HFQS), and have offered insights into strategies for improving SRF cavity performance.

The results presented here highlight the critical importance of understanding material properties on a mesoscopic scale and how defects such as hydrides, Sn-deficient islands, and grain boundaries contribute to performance degradation. Through our analysis, we have demonstrated that these defects, even in small concentrations, can have significant effects on vortex behavior, dissipation, and overall cavity efficiency. In addition, our work on Nb_3Sn has provided valuable insights into how surface features and stoichiometry can impact cavity performance, with the potential to guide future research into optimizing material growth and treatment procedures.

Looking forward, there are numerous opportunities to build on this work, whether by expanding the computational framework to include temperature fields and more complex defect interactions, exploring new materials for SRF cavities, or refining the generalized TDGL model to provide more specific predictions for frequency-dependent behavior. The methods developed here provide a strong foundation for future research, and the findings presented in this dissertation offer new avenues for improving SRF cavity performance in the next generation of particle accelerators.

Ultimately, this work contributes to a deeper understanding of the microscopic and mesoscopic factors that influence superconducting materials and provides a roadmap for future improvements in SRF cavity design and technology. As we continue to push the boundaries of accelerator technology, the insights gained from this research will serve as a stepping stone toward achieving more efficient and cost-effective particle accelerators, enabling advancements in fundamental physics and a wide range of applied fields.

Appendix A

Miscellaneous Supplimentary Calculations

The folllowing chapter outlines several calculations which were either too onerous or out of scope for the main text.

A.1 Chapter 2 Appendices

The following section includes several of the appendices associated with the contents of Chapter 2, which include an abbreviated version of the TDGL nondimensionalizations (the next appendix section will go into this in much more detail), and several calculations related to our quality factor estimates.

A.1.1 Brief Overview of TDGL Non-dimensionalization

To nondimensionalize the TDGL equations, we start with Eqs. 2.1 and 2.2, and make the following coordinate transformations:

$$\begin{aligned}
\nabla &\longrightarrow \frac{1}{\lambda_0}\tilde{\nabla} \\
\frac{\partial}{\partial t} &\longrightarrow \frac{1}{\tau_{\psi_0}}\frac{\partial}{\partial \tilde{t}} \\
\mathbf{A} &\longrightarrow \sqrt{2}H_{c0}\lambda_0\tilde{\mathbf{A}} \\
\psi &\longrightarrow \sqrt{\frac{|\alpha_0|}{\beta_0}}\tilde{\psi} \\
\phi &\longrightarrow \phi_0\tilde{\phi}.
\end{aligned}$$

If we substitute in Eqs. 2.10, 2.11, 2.12, and 2.14 for α, β, Γ, and σ_n respectively, we can then define the quantities:

$$\begin{aligned}
\lambda_0 &= \sqrt{\frac{m_s c^2 \beta_0}{4\pi e_s^2 |\alpha_0|}} \\
\xi_0 &= \sqrt{\frac{\hbar^2}{2m_s |\alpha_0|}} \\
\kappa_0 &= \frac{\lambda_0}{\xi_0} \\
H_{c0} &= \sqrt{\frac{4\pi\alpha_0^2}{\beta_0}} \\
\tau_{\psi_0} &= \frac{\Gamma_0}{|\alpha_0|} \\
\tau_{j_0} &= \frac{\sigma_{n0} m_s \beta_0}{e_s^2 |\alpha_0|} \\
u_0 &= \frac{\tau_{\psi_0}}{\tau_{j_0}} \\
\phi_0 &= \frac{\hbar \kappa_0}{e_s \tau_{\psi_0}}.
\end{aligned}$$

Using these relations, the resulting equations under the above coordinate transformations simplify into Eqs. 2.15 and 2.16 (where we then drop the tildes).

A.1.2 Approximate Estimation of Normal-State Conductivity

We outline here a possible route to estimate σ_n using the Drude model [150], where the electrical conductivity is given by

$$\sigma = \frac{ne^2\tau}{m}, \tag{A.1}$$

with e and m the electron charge and mass, n the carrier density, and τ the mean free collision time. For the normal quasiparticle density at low temperatures, we adopt the approximation from Ref. 151,

$$n_n = 8ne^{-\Delta/k_bT}, \tag{A.2}$$

which leads to an expression for the normal-state conductivity in the Meissner regime:

$$\sigma_n = \frac{ne^2\tau}{m}\left(8e^{-\Delta/k_bT}\right). \tag{A.3}$$

We emphasize that this expression is approximate, and moreover that the energy gap Δ is inferred from the TDGL order parameter ψ, which is known to overestimate Δ at low temperatures [152]. Given these limitations, we regard this estimation primarily as a qualitative reference and have proceed with treating σ_n as a free parameter in the main text.

A.1.3 Quality Factor Derivation

We start with the quality factor:

$$Q = \frac{2\pi E}{\Delta E}. \tag{A.4}$$

These quantities (working in SI units for this section) can be expressed as integrals:

$$E = \frac{1}{2}\mu_0 \int_V dV \mathbf{H}^2 \tag{A.5}$$

$$\Delta E = \int_0^T dt \int_{V_{surf}} dV_{surf} D, \tag{A.6}$$

where V is the cavity volume, T is the RF period, and D is given by Equation 3.20. V_{surf} is the volume in the first few penetration depths of the cavity surface where essentially all of the dissipation occurs. TDGL simulation outputs are unit-free, so it is helpful to pull constants with units out of these integrals, leaving behind dimensionless functions which can be calculated from TDGL solutions. We start by expressing Equation A.5 in cylindrical coordinates:

$$E = \frac{1}{2}\mu_0 \int r dr \int d\phi \int dz \mathbf{H}^2$$

We then define some dimensionless quantities:

$$\tilde{r} = \frac{r}{R} \tag{A.7}$$

$$\tilde{z} = \frac{z}{L} \tag{A.8}$$

$$\tilde{\mathbf{H}} = \frac{\mathbf{H}}{H_a} \tag{A.9}$$

Where R is the maximum radius of the cavity, L is the length of the cavity in the axial direction, and H_a is the maximum value of the applied field at the surface of the cavity during an RF period. These quantities allow the definition of a unit-less integral that only depends on the cavity geometry:

$$I_H \equiv \int \tilde{r} d\tilde{r} \int d\tilde{z} \tilde{\mathbf{H}}^{\mathbf{2}} \tag{A.10}$$

Using these definitions with Equation A.5 and assuming that $\mathbf{H}$ has azimuthal symmetry results in

$$E = \pi \mu_0 H_a^2 L R^2 I_H. \tag{A.11}$$

Turning to the dissipated energy integral, suppose all of the dissipation occurs within a distance d below the cavity surface, where $d << R$. This allows the cylindrical integral to be converted into cartesian coordinates, with the azimuthal direction becoming the new x direction, the axial direction becoming the new y direction, and the radial direction becoming the new z direction. A diagram of these transformations is found in Figure A.1.

With these transformations, we have

$$\Delta E = \int_0^T dt \int_0^{2\pi R} dx \int_0^L dy \int_0^d dz D. \tag{A.12}$$

When calculating this from simulation outputs, the integral is necessarily calculated over a small region of the overall cavity surface. Let L_x and L_y be the simulation domain size in the x and y directions respectively, and let N be the total number of simulation areas needed to fully partition the cavity surface. Then the dissipation integral becomes

$$\Delta E = N \int_0^T dt \int_0^{L_x} dx \int_0^{L_y} dy \int_0^d dz D, \tag{A.13}$$

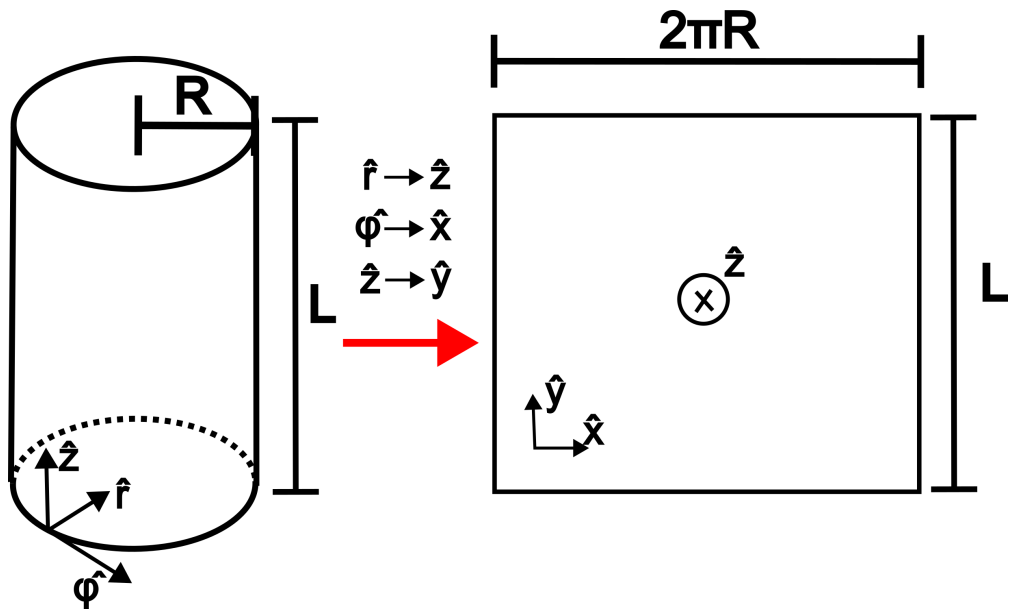

Figure A.1 Schematic of Transformations for the Quality Factor Calculation. The cylindrical geometry is shown on the left, with the cavity radius R and length L depicted, and the coordinate directions, $\hat{r}$, $\hat{\phi}$, and $\hat{z}$. Under the transformation (on the right) the coordinates become cartesian, with the $\hat{r}$ direction becoming the new $\hat{z}$ direction, the $\hat{\phi}$ direction becomes the $\hat{x}$ direction, and the old $\hat{z}$ direction becomes the $\hat{y}$ direction.

and N can be approximated as

$$N = \frac{2\pi RL}{L_x L_y}. \tag{A.14}$$

Contuining as before we again define dimensionless coordinates:

$$\tilde{x} = \frac{x}{\lambda} \tag{A.15}$$

$$\tilde{y} = \frac{y}{\lambda} \tag{A.16}$$

$$\tilde{z} = \frac{z}{\lambda} \tag{A.17}$$

$$\tilde{t} = \frac{T_{sim}}{T} t \tag{A.18}$$

where λ is the penetration depth and T_{sim} is the period in units of simulation time. These convert the integral to

$$\Delta E = \lambda^3 \frac{T}{T_{sim}} N \int_0^{T_{sim}} d\tilde{t} \int_0^{\frac{L_x}{\lambda}} d\tilde{x} \int_0^{\frac{L_y}{\lambda}} d\tilde{y} \int_0^{\frac{d}{\lambda}} d\tilde{z} D. \tag{A.19}$$

Additionally, under the temporal gauge ($\phi = 0$), Equation 3.20 can be expressed as

$$D = 2\mu_0 H_c^2 \frac{T_{sim}}{T} \left(\left| \frac{\partial \tilde{\psi}}{\partial \tilde{t}} \right|^2 + \sigma_n \mu_0 \lambda^2 \frac{T_{sim}}{T} \left(\frac{\partial \tilde{\mathbf{A}}}{\partial \tilde{t}} \right)^2 \right), \tag{A.20}$$

where $\tilde{\psi}$ and $\tilde{\mathbf{A}}$ are the unit-free versions of the vector potential and order parameter that are solved for with Eqs. 2.15 and 2.16 (a derivation of Equation A.20 can be found in the next section of the Appendix). Finally, we define some more dimensionless integrals over the TDGL solutions:

$$I_\psi \equiv \int_0^{T_{sim}} d\tilde{t} \int_0^{\frac{L_x}{\lambda}} d\tilde{x} \int_0^{\frac{L_y}{\lambda}} d\tilde{y} \int_0^{\frac{d}{\lambda}} d\tilde{z} \left| \frac{\partial \tilde{\psi}}{\partial \tilde{t}} \right|^2 \tag{A.21}$$

$$I_A \equiv \int_0^{T_{sim}} d\tilde{t} \int_0^{\frac{L_x}{\lambda}} d\tilde{x} \int_0^{\frac{L_y}{\lambda}} d\tilde{y} \int_0^{\frac{d}{\lambda}} d\tilde{z} \left(\frac{\partial \tilde{\mathbf{A}}}{\partial \tilde{t}} \right)^2 \tag{A.22}$$

Combining everything and noting that $\omega = \frac{2\pi}{T}$, we get

$$\Delta E = 2\mu_0 H_c^2 \lambda^3 \frac{2\pi RL}{L_x L_y} \left(I_\psi + \omega \frac{\sigma_n \mu_0 \lambda^2 T_{sim}}{2\pi} I_A \right). \tag{A.23}$$

Now using Equations A.4, A.11, and A.23 we get an expression for the quality factor,

$$Q = \frac{\tilde{H}_a^2 RL_x L_y I_H}{2\lambda^3 \left(I_\psi + \omega \frac{\sigma_n \mu_0 \lambda^2 T_{sim}}{2\pi} I_A \right)}, \tag{A.24}$$

where $\tilde{H}_a \equiv \frac{H_a}{\sqrt{2}H_c}$ is the applied field in simulation units. It is common to express the quality factor as

$$Q = \frac{G}{R_s}, \tag{A.25}$$

where R_s is the cavity surface resistance and G is a geometric factor that depends only on quantities which are determined by the cavity geometry. We can define these quantities under the framework we have presented as

$$G = \frac{1}{2}\mu_0 \omega R I_H \tag{A.26}$$

$$R_s = \frac{\mu_0 \omega \lambda^3}{\tilde{H}_a^2 L_x L_y}\left(I_\psi + \omega \frac{\sigma_n \mu_0 \lambda^2 T_{sim}}{2\pi} I_A\right). \tag{A.27}$$

For a typical 1.3 GHz 9-cell Nb TESLA cavity, $G = 270\ \Omega$ [105], so in practice we can just use this value or other known values of G, and only calculate R_s from Equation A.27.

A.1.4 Nondimensionalizing the TDGL Dissipation

We start with Equation 3.20,

$$D = 2\Gamma\left|\left(\frac{\partial \psi}{\partial t} + \frac{ie_s\phi\psi}{\hbar}\right)\right|^2 + \sigma_n \mathbf{E}^2$$

choosing the temporal gauge ($\phi = 0$) we have

$$D = 2\Gamma\left|\frac{\partial \psi}{\partial t}\right|^2 + \sigma_n\left(\frac{\partial \mathbf{A}}{\partial t}\right)^2.$$

Next, we make the same coordinate transformations as from the previous section (and the same time transformation as from the methods section) and use the expressions for τ_ψ and H_c on the first term:

$$\begin{aligned} D &= \frac{2\Gamma\alpha}{\beta}\frac{T_{sim}^2}{T^2}\left|\frac{\partial \tilde{\psi}}{\partial \tilde{t}}\right|^2 + 2\sigma_n H_c^2 \lambda^2 \frac{T_{sim}^2}{T^2}\left(\frac{\partial \tilde{\mathbf{A}}}{\partial \tilde{t}}\right)^2 \\ &= \frac{2\tau_\psi \alpha^2}{\beta}\frac{T_{sim}^2}{T^2}\left|\frac{\partial \tilde{\psi}}{\partial \tilde{t}}\right|^2 + 2\sigma_n H_c^2 \lambda^2 \frac{T_{sim}^2}{T^2}\left(\frac{\partial \tilde{\mathbf{A}}}{\partial \tilde{t}}\right)^2 \\ &= \frac{2H_c^2}{4\pi}\frac{T_{sim}}{T}\left|\frac{\partial \tilde{\psi}}{\partial \tilde{t}}\right|^2 + 2\sigma_n H_c^2 \lambda^2 \frac{T_{sim}^2}{T^2}\left(\frac{\partial \tilde{\mathbf{A}}}{\partial \tilde{t}}\right)^2, \end{aligned}$$

where in the last line we used the fact that $T = \tau_\psi T_{sim}$. Finally, this expression is in Gaussian units so we convert to SI units so that it is compatible with the other expressions in Section 2.2.5:

$$\begin{aligned} D &= 2\tau_\psi \mu_0 H_c^2 \frac{T_{sim}^2}{T^2} \left| \frac{\partial \tilde{\psi}}{\partial \tilde{t}} \right|^2 + 2\sigma_n \mu_0^2 H_c^2 \lambda^2 \frac{T_{sim}^2}{T^2} \left(\frac{\partial \tilde{\mathbf{A}}}{\partial \tilde{t}} \right)^2 \\ &= 2\mu_0 H_c^2 \frac{T_{sim}}{T} \left(\left| \frac{\partial \tilde{\psi}}{\partial \tilde{t}} \right|^2 + \sigma_n \mu_0 \lambda^2 \frac{T_{sim}}{T} \left(\frac{\partial \tilde{\mathbf{A}}}{\partial \tilde{t}} \right)^2 \right) \end{aligned}$$

A.2 Ginzburg-Landau Equation Nondimensionalization

A.2.1 Initial Equations and Useful Values

The Ginzburg-Landau equations are as follows:

$$\frac{1}{2m_s}\left(-i\hbar\nabla - \frac{e_s}{c}\mathbf{A}\right)^2\psi + \alpha\psi + \beta|\psi|^2\psi = 0 \text{ in the domain} \tag{A.28}$$

$$\nabla\times\nabla\times\mathbf{A} - \frac{2\pi i e_s\hbar}{m_s c}\left(\psi^*\nabla\psi - \psi\nabla\psi^*\right) - \frac{4\pi e_s^2}{m_s c^2}|\psi|^2\mathbf{A} = 0 \text{ in the domain} \tag{A.29}$$

$$\left(i\hbar\nabla\psi + \frac{e_s}{c}\mathbf{A}\psi\right)\cdot n = 0 \text{ on the boundary} \tag{A.30}$$

$$(\nabla\times\mathbf{A})\times n = \mathbf{H}\times n \text{ on the boundary} \tag{A.31}$$

To nondimentionalize these equations, we first start by getting a few useful constants from these equations. The coherence length, ξ, can be found by looking at Equation A.28, and letting $\mathbf{A} = 0$ (and thus ψ will be real):

$$\nabla^2\psi + \frac{1}{\xi^2}\left(\psi + \frac{\beta}{\alpha}\psi^3\right) = 0 \tag{A.32}$$

Where $\xi^2 = \frac{-\hbar^2}{2m_s\alpha}$. The coherence length is the length scale for the variance of ψ.

The penetration depth, λ, can be found by looking at Equation A.29 and considering the material to be perfectly superconducting, i.e. $\psi = \psi_0 = \left(\frac{-\alpha}{\beta}\right)^{\frac{1}{2}}$, this makes the second term in the equation go to 0 and we get:

$$\nabla\times\nabla\times\mathbf{A} + \frac{1}{\lambda^2}\mathbf{A} = 0 \tag{A.33}$$

Where $\lambda^2 = \frac{m_s c^2}{4\pi e_s^2 |\psi_0|^2} = \frac{-\beta m_s c^2}{4\pi e_s^2 \alpha}$. The penetration depth is a length scale for how deep magnetic field is able to penetrate into a superconducting material.

We now have the well known Ginzburg-Landau parameter, $\kappa = \frac{\lambda}{\xi} = \sqrt{\frac{\beta}{2\pi}} \frac{m_s c}{e_s \hbar}$. The material's thermodynamic critical field, $H_c = \frac{4\pi\alpha^2}{\beta}$ also becomes a useful constant later.

A.2.2 Nondimentionalization

To nondimentionalize the GL equations, we make a number of coordinate transformations: $x = \lambda x'$ (and therefore $\nabla = \frac{1}{\lambda}\nabla'$), $\mathbf{A} = \sqrt{2} H_c \lambda \mathbf{A}'$, and $\psi = \sqrt{\frac{-\alpha}{\beta}}\psi'$. Doing this to equation A.28:

$$\frac{1}{2m_s}\left(\frac{-i\hbar}{\lambda}\nabla' - \frac{\sqrt{2}H_c\lambda e_s}{c}\mathbf{A}'\right)^2 \sqrt{\frac{-\alpha}{\beta}}\psi' + \alpha\sqrt{\frac{-\alpha}{\beta}}\psi' + \beta\sqrt{\frac{-\alpha}{\beta}}^3 |\psi'|^2\psi' = 0 \tag{A.34}$$

Dropping the primes and dividing by $\alpha\sqrt{\frac{-\alpha}{\beta}}$ gives:

$$\frac{1}{2m_s\alpha}\left(\frac{-i\hbar}{\lambda}\nabla - \frac{\sqrt{2}H_c\lambda e_s}{c}\mathbf{A}\right)^2 \psi + \psi - |\psi|^2\psi = 0 \tag{A.35}$$

If we bring the $\frac{1}{2m_s\alpha}$ into the parentheses of the first term (square rooting it of course), and expand out the λs and Hc, you will see that the term in front of $\mathbf{A}$ goes to 1, and the term in front of the ∇ goes to $\frac{-i}{\kappa}$, so the final equation is:

$$\left(\frac{-i}{\kappa}\nabla - \mathbf{A}\right)^2 \psi + \psi - |\psi|^2\psi = 0 \tag{A.36}$$

If we make the same transformations for Equation A.29, we get the following:

$$\frac{\sqrt{2}H_c}{\lambda}\nabla\times\nabla\times\mathbf{A}' + \frac{2\pi i e_s\hbar\alpha}{m_s c\lambda\beta}\left(\psi'^*\nabla'\psi' - \psi'\nabla'\psi'^*\right) + \frac{4\pi e_s^2\alpha}{m_s c^2\beta}|\psi'|^2\sqrt{2}H_c\lambda\mathbf{A}' = 0 \tag{A.37}$$

Once again dropping the primes and then multiplying by $\frac{\lambda}{\sqrt{2}H_c}$ gives:

$$\nabla\times\nabla\times\mathbf{A} + \frac{2\pi i e_s\hbar\alpha}{m_s c\sqrt{2}H_c\beta}\left(\psi^*\nabla\psi - \psi\nabla\psi^*\right) + \frac{4\pi e_s^2\alpha\lambda^2}{m_s c^2\beta}|\psi|^2\mathbf{A} = 0 \tag{A.38}$$

Expanding H_c and λ again makes the coefficients in front of the second term reduce to $\frac{i}{2\kappa}$, and the terms in front of $|\psi|^2\mathbf{A}$ reduce to 1:

$$\nabla\times\nabla\times\mathbf{A}+\frac{i}{2\kappa}(\psi^*\nabla\psi-\psi\nabla\psi^*)+|\psi|^2\mathbf{A}=0 \tag{A.39}$$

For the first boundary condition, it follows the same process as for the first term in Equation A.36, and doing the transformations for the last boundary equation, there will be $\sqrt{2}Hc$ in front of both terms, which cancel, so the final nondimentionalized equations are:

$$\left(\frac{-i}{\kappa}\nabla-\mathbf{A}\right)^2\psi+\psi-|\psi|^2\psi=0 \tag{A.40}$$

$$\nabla\times\nabla\times\mathbf{A}+\frac{i}{2\kappa}(\psi^*\nabla\psi-\psi\nabla\psi^*)+|\psi|^2\mathbf{A}=0 \tag{A.41}$$

$$\left(\frac{i}{\kappa}\nabla\psi+\mathbf{A}\psi\right)\cdot n=0 \tag{A.42}$$

$$(\nabla\times\mathbf{A})\times n=\mathbf{H}\times n \tag{A.43}$$

A.2.3 α and β Spacial Dependence

Now we want to let α and β vary with space, this can represent different materials, or material defects. To do this, we make the transformations $\alpha=\alpha_0 a(\mathbf{r})$ and $\beta=\beta_0 b(\mathbf{r})$, where α_0 and β_0 are constant reference values with the same units as α and β, and a and b are dimensionless functions of position. Returning to our definitions of ξ and λ, we see that setting $\mathbf{A}=0$ in Equation A.28 and collecting terms gives:

$$\nabla^2\psi+\frac{1}{\xi_0^2}\left(a\psi+\frac{\beta_0}{\alpha_0}b\psi^3\right)=0 \tag{A.44}$$

Where $\xi_0^2=\frac{-\hbar^2}{2m_s\alpha_0}$. To find the other length scale we once again let the material be perfectly superconducting, but this time in terms of the reference α and β; $\psi=\psi_0=\left(\frac{-\alpha_0}{\beta_0}\right)^{\frac{1}{2}}$, this makes Equation A.29 go to:

$$\nabla\times\nabla\times\mathbf{A}+\frac{1}{\lambda_0^2}\mathbf{A}=0 \tag{A.45}$$

Where $\lambda_0^2 = \frac{m_s c^2}{4\pi e_s^2 |\psi_0|^2} = \frac{-\beta_0 m_s c^2}{4\pi e_s^2 \alpha_0}$. Similarly, H_c becomes $H_{c0} = \frac{4\pi\alpha_0^2}{\beta_0}$, and $\kappa_0 = \frac{\lambda_0}{\xi_0} = \sqrt{\frac{\beta_0}{2\pi}}\frac{m_s c}{e_s \hbar}$. We then do the same process as we did before, but replacing any λ, ξ, κ, or H_c with λ_0, ξ_0, κ_0, or H_{c0}. This will result in almost the same equations, but with an a and a b in front of the ψ and $|\psi|^2\psi$ terms:

$$\left(\frac{-i}{\kappa_0}\nabla - \mathbf{A}\right)^2 \psi + a\psi - b|\psi|^2\psi = 0 \tag{A.46}$$

$$\nabla \times \nabla \times \mathbf{A} + \frac{i}{2\kappa_0}\left(\psi^*\nabla\psi - \psi\nabla\psi^*\right) + |\psi|^2\mathbf{A} = 0 \tag{A.47}$$

$$\left(\frac{i}{\kappa_0}\nabla\psi + \mathbf{A}\psi\right)\cdot n = 0 \tag{A.48}$$

$$(\nabla \times \mathbf{A}) \times n = \mathbf{H} \times n \tag{A.49}$$

A.3 Time Dependent Ginzburg-Landau Equation Nondimensionalization

A.3.1 α and β constant

The Time Dependent Ginzburg-Landau equations are as follows:

$$\Gamma\left(\frac{\partial\psi}{\partial t}+\frac{ie_s\phi}{\hbar}\psi\right)+\frac{1}{2m_s}\left(-i\hbar\nabla-\frac{e_s}{c}\mathbf{A}\right)^2\psi+\alpha\psi+\beta|\psi|^2\psi=0 \quad \text{in the domain,} \tag{A.50}$$

$$\frac{4\pi\sigma_n}{c}\left(\frac{1}{c}\frac{\partial\mathbf{A}}{\partial t}+\nabla\phi\right)+\nabla\times\nabla\times\mathbf{A}-\frac{2\pi ie_s\hbar}{m_sc}\left(\psi^*\nabla\psi-\psi\nabla\psi^*\right)-\frac{4\pi e_s^2}{m_sc^2}|\psi|^2\mathbf{A}=0 \quad \text{in the domain,} \tag{A.51}$$

$$\left(i\hbar\nabla\psi+\frac{e_s}{c}\mathbf{A}\psi\right)\cdot n=0 \quad \text{on the boundary,} \tag{A.52}$$

$$(\nabla\times\mathbf{A})\times n=\mathbf{H}\times n \quad \text{on the boundary,} \tag{A.53}$$

$$-\left(\nabla\phi+\frac{\partial\mathbf{A}}{\partial t}\right)\cdot n=0 \quad \text{on the boundary.} \tag{A.54}$$

To nondimentionalize these equations, we first use the same definitions for λ, ξ, κ, and H_c as we defined in Section A.2.1. We also make the same change of variables as in Section A.2.2 in addition to letting $t=\tau_\Delta t'$ and $\phi=\phi_0\phi'$; For equation A.50, this gives us:

$$\begin{aligned}\frac{1}{2m_s}\left(\frac{-i\hbar}{\lambda}\nabla'-\frac{\sqrt{2}H_c\lambda e_s}{c}\mathbf{A}'\right)^2\sqrt{\frac{-\alpha}{\beta}}\psi'+\alpha\sqrt{\frac{-\alpha}{\beta}}\psi'+\beta\sqrt{\frac{-\alpha}{\beta}}^3|\psi'|^2\psi' \\ +\Gamma\sqrt{\frac{-\alpha}{\beta}}\left(\frac{1}{\tau_\Delta}\frac{\partial\psi'}{\partial t'}+\frac{ie_s\phi_0\phi'}{\hbar}\psi'\right)=0\end{aligned} \tag{A.55}$$

Dropping the primes and dividing by $\alpha\sqrt{\frac{-\alpha}{\beta}}$ gives:

$$\frac{1}{2m_s\alpha}\left(\frac{-i\hbar}{\lambda}\nabla-\frac{\sqrt{2}H_c\lambda e_s}{c}\mathbf{A}\right)^2\psi+\psi-|\psi|^2\psi+\frac{\Gamma}{|\alpha|}\left(\frac{1}{\tau_\Delta}\frac{\partial\psi}{\partial t}+\frac{ie_s\phi_0\phi}{\hbar}\psi\right)=0 \tag{A.56}$$

The first three terms reduce down to the same terms as in Equation A.36. We then let $\tau_\Delta=\frac{\Gamma}{|\alpha|}$ and $\phi_0=\frac{\hbar\kappa}{e_s\tau_\Delta}$ to get the final equation:

$$\left(\frac{-i}{\kappa}\nabla-\mathbf{A}\right)^2\psi+\psi-|\psi|^2\psi+\frac{\partial\psi}{\partial t}+i\phi\kappa\psi=0 \tag{A.57}$$

Making the same coordinate transformations for Equation A.51:

$$\begin{aligned}\frac{\sqrt{2}H_c}{\lambda}\nabla\times\nabla\times\mathbf{A}'+\frac{2\pi ie_s\hbar\alpha}{m_sc\lambda\beta}\left(\psi'^*\nabla'\psi'-\psi'\nabla'\psi'^*\right)\\ +\frac{4\pi e_s^2\alpha}{m_sc^2\beta}|\psi'|^2\sqrt{2}H_c\lambda\mathbf{A}'+\frac{4\pi\sigma_n}{c}\left(\frac{\sqrt{2}H_c\lambda}{c\tau_\Delta}\frac{\partial\mathbf{A}'}{\partial t'}+\frac{\phi_0}{\lambda}\nabla'\phi'\right)=0\end{aligned} \tag{A.58}$$

Dropping the primes and then multiplying by $\frac{\lambda}{\sqrt{2}H_c}$ gives:

$$\begin{aligned}\nabla\times\nabla\times\mathbf{A}+\frac{2\pi ie_s\hbar\alpha}{m_sc\sqrt{2}H_c\beta}\left(\psi^*\nabla\psi-\psi\nabla\psi^*\right)\\ +\frac{4\pi e_s^2\alpha\lambda^2}{m_sc^2\beta}|\psi|^2\mathbf{A}+\frac{4\pi\sigma_n}{c}\left(\frac{\lambda^2}{c\tau_\Delta}\frac{\partial\mathbf{A}}{\partial t}+\frac{\phi_0}{\sqrt{2}H_c}\nabla\phi\right)=0\end{aligned} \tag{A.59}$$

Once again the first 3 terms go the the same as Equation A.39. We then define $\tau_j=\frac{\sigma_n\beta m_s}{e_s^2|\alpha|}$, which gives:

$$\nabla\times\nabla\times\mathbf{A}+\frac{i}{2\kappa}\left(\psi^*\nabla\psi-\psi\nabla\psi^*\right)+|\psi|^2\mathbf{A}+\frac{\tau_j}{\tau_\Delta}\frac{\partial\mathbf{A}}{\partial t}+\frac{4\pi\sigma_n\phi_0}{\sqrt{2}H_cc}\nabla\phi=0 \tag{A.60}$$

If we define $u=\frac{\tau_\Delta}{\tau_j}$, then the coefficents in front of the time derivative go to $\frac{1}{u}$, and it turns out that if we substitute in the value for ϕ_0 we found earlier, the coefficients in front of the $\nabla\phi$ go to $\frac{1}{u}$:

$$\nabla\times\nabla\times\mathbf{A}+\frac{i}{2\kappa}\left(\psi^*\nabla\psi-\psi\nabla\psi^*\right)+|\psi|^2\mathbf{A}+\frac{1}{u}\left(\frac{\partial\mathbf{A}}{\partial t}+\nabla\phi\right)=0 \tag{A.61}$$

So the final equations are:

$$\left(\frac{-i}{\kappa}\nabla - \mathbf{A}\right)^2 \psi + \psi - |\psi|^2\psi + \frac{\partial \psi}{\partial t} + i\phi\kappa\psi = 0 \tag{A.62}$$

$$\nabla \times \nabla \times \mathbf{A} + \frac{i}{2\kappa}(\psi^*\nabla\psi - \psi\nabla\psi^*) + |\psi|^2\mathbf{A} + \frac{1}{u}\left(\frac{\partial \mathbf{A}}{\partial t} + \nabla\phi\right) = 0 \tag{A.63}$$

$$\left(\frac{i}{\kappa}\nabla\psi + \mathbf{A}\psi\right)\cdot n = 0 \tag{A.64}$$

$$(\nabla \times \mathbf{A}) \times n = \mathbf{H} \times n \tag{A.65}$$

$$-\left(\nabla\phi + \frac{\partial \mathbf{A}}{\partial t}\right)\cdot n = 0 \tag{A.66}$$

A.3.2 α and β vary with time and space

If we now let $\alpha = \alpha_0 a(\mathbf{r},t)$ and $\beta = \beta_0 b(\mathbf{r},t)$, we can do the same thing as we did in Section A.2.3, and let $\xi_0^2 = \frac{-\hbar^2}{2m_s\alpha_0}$, $\lambda_0^2 = \frac{m_s c^2}{4\pi e_s^2|\psi_0|^2} = \frac{-\beta_0 m_s c^2}{4\pi e_s^2\alpha_0}$, $H_{c0} = \frac{4\pi\alpha_0^2}{\beta_0}$, and $\kappa_0 = \frac{\lambda_0}{\xi_0} = \sqrt{\frac{\beta_0}{2\pi}}\frac{m_s c}{e_s\hbar}$. Additionally we also let $\tau_{\Delta 0} = \frac{\Gamma}{|\alpha_0|}$, $\tau_{j0} = \frac{\sigma_n\beta_0 m_s}{e_s^2|\alpha_0|}$, $u_0 = \frac{\tau_{\Delta 0}}{\tau_{j0}}$, and $\phi_0 = \frac{\hbar\kappa_0}{e_s\tau_{\Delta 0}}$. We can then follow the same steps as above with these new values and we get:

$$\left(\frac{-i}{\kappa_0}\nabla - \mathbf{A}\right)^2 \psi + a\psi - b|\psi|^2\psi + \frac{\partial \psi}{\partial t} + i\phi\kappa_0\psi = 0 \tag{A.67}$$

$$\nabla \times \nabla \times \mathbf{A} + \frac{i}{2\kappa_0}(\psi^*\nabla\psi - \psi\nabla\psi^*) + |\psi|^2\mathbf{A} + \frac{1}{u_0}\left(\frac{\partial \mathbf{A}}{\partial t} + \nabla\phi\right) = 0 \tag{A.68}$$

$$\left(\frac{i}{\kappa_0}\nabla\psi + \mathbf{A}\psi\right)\cdot n = 0 \tag{A.69}$$

$$(\nabla \times \mathbf{A}) \times n = \mathbf{H} \times n \tag{A.70}$$

$$-\left(\nabla\phi + \frac{\partial \mathbf{A}}{\partial t}\right)\cdot n = 0 \tag{A.71}$$

Bibliography

[1] P. Bagnaia and S. D. Ellis, "CERN collider results and the standard model," Annu. Rev. Nucl. Part. Sci. **38,** 659–703 (1988).

[2] M. M. Sabado, in *Supercollider 3*, J. Nonte, ed., (Springer US, Boston, MA, 1991), pp. 639–648.

[3] M. Silari, "Applications of particle accelerators in medicine," Radiation Protection Dosimetry **146,** 440–450 (2011).

[4] C. R. Wie], "High resolution x-ray diffraction characterization of semiconductor structures," Materials Science and Engineering: R: Reports **13,** 1 – 56 (1994).

[5] H. K. Onnes, "Further experiments with liquid helium: The resistance of pure mercury at helium temperatures," Communications from the Physical Laboratory of the University of Leiden (1911), original discovery of superconductivity.

[6] W. Meissner and R. Ochsenfeld, "Ein neuer Effekt bei Eintritt der Supraleitfähigkeit," Die Naturwissenschaften **21,** 787–788 (1933).

[7] A. Gurevich, "Theory of RF superconductivity for resonant cavities," Superconductor Science and Technology **30,** 034004 (2017).

[8] A. Pack, Master's thesis, Brigham Young University, 2017.

[9] J. Bardeen and M. J. Stephen, "Theory of the Motion of Vortices in Superconductors," Phys. Rev. **140,** A1197–A1207 (1965).

[10] D. B. Liarte, S. Posen, M. K. Transtrum, G. Catelani, M. Liepe, and J. P. Sethna, "Theoretical estimates of maximum fields in superconducting resonant radio frequency cavities: stability theory, disorder, and laminates," Superconductor Science and Technology **30,** 033002 (2017).

[11] S. Posen, N. Valles, and M. Liepe, "Radio Frequency Magnetic Field Limits of Nb and Nb_3Sn," Phys. Rev. Lett. **115,** 047001 (2015).

[12] H. London and F. London, "The electromagnetic equations of the supraconductor," Proceedings of the Royal Society A: Mathematical, Physical and Engineering Sciences **149,** 71–88 (1935).

[13] C. J. Gorter and H. Casimir, "On supraconductivity I," Physica **1,** 306–320 (1934).

[14] V. L. Ginzburg and L. D. Landau, "On the theory of superconductivity," Zhurnal Eksperimental'noi i Teoreticheskoi Fiziki **20,** 1064–1082 (1950).

[15] J. Bardeen, L. N. Cooper, and J. R. Schrieffer, "Theory of superconductivity," Physical review **108,** 1175 (1957).

[16] L. P. Gor'kov, "Microscopic derivation of the Ginzburg-Landau equations in the theory of superconductivity," Sov. Phys. JETP **9,** 1364–1367 (1959).

[17] A. Schmid, "A time dependent Ginzburg-Landau equation and its application to the problem of resistivity in the mixed state," Physik der kondensierten Materie **5,** 302 (1966).

[18] L. Gor'Kov and G. Eliashberg, "Generalization of the Ginzburg-Landau equations for non-stationary problems in the case of alloys with paramagnetic impurities," Sov. Phys. JETP **27,** 328 (1968).

[19] Y. M. Eliashberg, "Interelectronic interaction in superconductors with non-retarded electron-phonon interaction," Zhurnal Eksperimental'noi i Teoreticheskoi Fiziki **38,** 966–976 (1960).

[20] A. I. Larkin and Y. N. Ovchinnikov, "Nonuniform state of superconductors," Soviet Physics JETP **20,** 1200–1205 (1964), translated from Zh. Eksp. Teor. Fiz. 47, 1506–1512 (1964).

[21] G. Eilenberger, "Transformation of Gorkov's equation for type II superconductors into transport-like equations," Zeitschrift für Physik **214,** 195–213 (1968).

[22] K. D. Usadel, "Generalized diffusion equation for superconducting alloys," Physical Review Letters **25,** 507 (1970).

[23] M. Tinkham, *Introduction to Superconductivity* (Courier Corporation, 2004).

[24] N. Kopnin, *Theory of nonequilibrium superconductivity* (Oxford University Press, 2001), Vol. 110.

[25] H. Gao and W. Sun, "A New Mixed Formulation and Efficient Numerical Solution of Ginzburg–Landau Equations Under the Temporal Gauge," SIAM Journal on Scientific Computing **38,** A1339–A1357 (2016).

[26] M. S. Alnæs, J. Blechta, J. Hake, A. Johansson, B. Kehlet, A. Logg, C. Richardson, J. Ring, M. E. Rognes, and G. N. Wells, "The FEniCS project version 1.5," Archive of Numerical Software **3,** 9–23 (2015).

[27] L. Kramer and R. J. Watts-Tobin, "Theory of Dissipative Current-Carrying States in Superconducting Filaments," Phys. Rev. Lett. **40,** 1041–1044 (1978).

[28] R. J. Watts-Tobin, Y. Krähenbühl, and L. Kramer, "Nonequilibrium theory of dirty, current-carrying superconductors: Phase-slip oscillators in narrow filaments near T c," Journal of Low Temperature Physics **42,** 459–501 (1981).

[29] T. Tajima, A. Canabal, Y. Zhao, A. Romanenko, C. Nantista, S. Tantawi, L. Phillips, Y. Iwashita, I. Campisi, and B. Moeckly, "Tests on MgB_2 for Application to SRF Cavities," In *Proceedings of the European Particle Accelerator Conference (EPAC 2006)*, pp. 481–483 (Edinburgh, Scotland, 2006).

[30] P. Pizzol, A. Poudel, I. Nekrashevich, L. Civale, H. Salazar, D. Kelly, R. Schulze, and T. Tajima, "Progress of MgB2 Deposition technique for SRF cavities at LANL," In *Proc. 20th Int. Conf. RF Supercond*, pp. 482–484 (2021).

[31] W. Roach, J. Skuza, D. Beringer, Z. Li, C. Clavero, and R. Lukaszew, "NbN thin films for superconducting radio frequency cavities," Superconductor Science and Technology **25,** 125016 (2012).

[32] G. R. Stewart, "Superconductivity in the A15 structure," Physica C: Superconductivity and its Applications **514,** 28–35 (2015).

[33] S. E. Posen and M. U. Liepe, Ph.D. thesis, Cornell University, 2015.

[34] U. Pudasaini, G. V. Eremeev, J. W. Angle, J. Tuggle, C. E. Reece, and M. J. Kelley, "Growth of Nb3Sn coating in tin vapor-diffusion process," Journal of Vacuum Science & Technology A 37 (2019).

[35] Z. Sun, M. Liepe, T. Oseroff, R. Porter, T. Arias, N. Sitaraman, A. Connolly, J. Scholtz, and M. Thompson, "Electroplating of Sn film on Nb substrate for generating Nb3Sn thin films and post laser annealing," In *Proc. 19th Int. Conf. on RF Superconductivity (SRF'19)*, pp. 51–54 (2019).

[36] Z. Sun *et al.*, "Toward stoichiometric and low-surface-roughness Nb 3 Sn thin films via direct electrochemical deposition," Proc. SRF'21 pp. 516–521 (2021).

[37] N. S. Sitaraman, M. M. Kelley, R. D. Porter, M. U. Liepe, T. A. Arias, J. Carlson, A. R. Pack, M. K. Transtrum, and R. Sundararaman, "Effect of the density of states at the Fermi level on defect free energies and superconductivity: A case study of Nb_3Sn," Phys. Rev. B **103,** 115106 (2021).

[38] S. A. Willson, A. V. Harbick, L. Shpani, V. Do, H. Lew-Kiedrowska, M. U. Liepe, M. K. Transtrum, and S. Sibener, "Impact of submicron Nb 3 Sn stoichiometric surface defects on high-field superconducting radiofrequency cavity performance," Physical Review Research **6,** 043133 (2024).

[39] S. Posen, J. Lee, D. Seidman, A. Romanenko, B. Tennis, O. Melnychuk, and D. Sergatskov, "Advances in Nb3Sn superconducting radiofrequency cavities towards first practical accelerator applications," Superconductor Science and Technology 34 (2021), cited by: 19; All Open Access, Green Open Access, Hybrid Gold Open Access.

[40] Center for Bright Beams, "About,", https://cbb.cornell.edu/about, 2025, accessed: 2025-06-27.

[41] S. Posen and M. Liepe, "Advances in development of Nb_3Sn superconducting radio-frequency cavities," Phys. Rev. ST Accel. Beams **17,** 112001 (2014).

[42] S. Posen and D. L. Hall, "Nb_3Sn superconducting radiofrequency cavities: fabrication, results, properties, and prospects," Superconductor Science and Technology **30,** 033004 (2017).

[43] Z. Sun *et al.*, "ZrNb(CO) RF Superconducting Thin Film with High Critical Temperature in the Theoretical Limit," Advanced Electronic Materials **9,** 2300151 (2023).

[44] N. S. Sitaraman *et al.*, "Enhanced Surface Superconductivity of Niobium by Zirconium Doping," Phys. Rev. Appl. **20,** 014064 (2023).

[45] L. Kramer, "Stability Limits of the Meissner State and the Mechanism of Spontaneous Vortex Nucleation in Superconductors," Phys. Rev. **170,** 475–480 (1968).

[46] A. J. Dolgert, S. J. Di Bartolo, and A. T. Dorsey, "Superheating fields of superconductors: Asymptotic analysis and numerical results," Phys. Rev. B **53,** 5650–5660 (1996).

[47] M. K. Transtrum, G. Catelani, and J. P. Sethna, "Superheating field of superconductors within Ginzburg-Landau theory," Phys. Rev. B **83,** 094505 (2011).

[48] D. B. Liarte, M. K. Transtrum, and J. P. Sethna, "Ginzburg-Landau theory of the superheating field anisotropy of layered superconductors," Phys. Rev. B **94,** 144504 (2016).

[49] G. Catelani and J. P. Sethna, "Temperature dependence of the superheating field for superconductors in the high-κ London limit," Phys. Rev. B 78 (2008), cited by: 53; All Open Access, Green Open Access.

[50] F. P.-J. Lin and A. Gurevich, "Effect of impurities on the superheating field of type-II superconductors," Phys. Rev. B 85 (2012), cited by: 40; All Open Access, Green Open Access.

[51] T. Kubo, "Superheating fields of semi-infinite superconductors and layered superconductors in the diffusive limit: structural optimization based on the microscopic theory," Superconductor Science and Technology **34,** 045006 (2021).

[52] G. Müller, H. Piel, J. Pouryamout, P. Boccard, and P. Kneisel, "Proceedings of the Workshop on Thin Film Coating Methods for Superconducting Accelerating Cavities,", 2000.

[53] A. R. Pack, J. Carlson, S. Wadsworth, and M. K. Transtrum, "Vortex nucleation in superconductors within time-dependent Ginzburg-Landau theory in two and three dimensions: Role of surface defects and material inhomogeneities," Phys. Rev. B **101,** 144504 (2020).

[54] J. Carlson *et al.*, "Analysis of magnetic vortex dissipation in Sn-segregated boundaries in Nb_3Sn superconducting RF cavities," Phys. Rev. B **103,** 024516 (2021).

[55] B. Oripov and S. M. Anlage, "Time-dependent Ginzburg-Landau treatment of rf magnetic vortices in superconductors: Vortex semiloops in a spatially nonuniform magnetic field," Physical Review E 101 (2020), cited by: 13; All Open Access, Bronze Open Access, Green Open Access.

[56] B. Oripov *et al.*, "High-Frequency Nonlinear Response of Superconducting Cavity-Grade Nb Surfaces," Phys. Rev. Appl. **11,** 064030 (2019).

[57] J. Allmaras, A. Kozorezov, B. Korzh, K. Berggren, and M. Shaw, "Intrinsic Timing Jitter and Latency in Superconducting Nanowire Single-photon Detectors," Phys. Rev. Appl. **11,** 034062 (2019).

[58] M. Jönsson, R. Vedin, S. Gyger, J. A. Sutton, S. Steinhauer, V. Zwiller, M. Wallin, and J. Lidmar, "Current Crowding in Nanoscale Superconductors within the Ginzburg-Landau Model," Phys. Rev. Appl. **17,** 064046 (2022).

[59] L. Bishop-Van Horn, E. Mueller, and K. A. Moler, "Vortex dynamics induced by scanning SQUID susceptometry," Phys. Rev. B **107,** 224509 (2023).

[60] L. Bishop-Van Horn, "pyTDGL: Time-dependent Ginzburg-Landau in Python," Computer Physics Communications **291,** 108799 (2023).

[61] T. J. Rieger, D. J. Scalapino, and J. E. Mercereau, "Charge Conservation and Chemical Potentials in Time-Dependent Ginzburg-Landau Theory," Phys. Rev. Lett. **27,** 1787–1790 (1971).

[62] T. J. Rieger, D. J. Scalapino, and J. E. Mercereau, "Time-Dependent Superconductivity and Quantum Dissipation," Phys. Rev. B **6,** 1734–1743 (1972).

[63] S. Frota-Pessôa, J. A. Blackburn, and B. B. Schwartz, "Short weak link with distinct chemical potentials at the boundary," Phys. Rev. B **20,** 993–996 (1979).

[64] G. R. Berdiyorov, X. H. Chao, F. M. Peeters, H. B. Wang, V. V. Moshchalkov, and B. Y. Zhu, "Magnetoresistance oscillations in superconducting strips: A Ginzburg-Landau study," Phys. Rev. B **86,** 224504 (2012).

[65] G. Kimmel, A. Glatz, and I. S. Aranson, "Phase slips in superconducting weak links," Phys. Rev. B **95,** 014518 (2017).

[66] L. Peng, Y. Hu, Z. Li, K. Deng, Y. Zhu, L. Xu, and Y. Zhou, "Finite element treatment of vortex states in 3d mesoscopic cylindrical superconductors in a tilted magnetic field," Acta Physica Polonica A **133,** 152 – 156 (2018), cited by: 2; All Open Access, Bronze Open Access.

[67] K. Arutyunov, D. Golubev, and A. Zaikin, "Superconductivity in one dimension," Physics Reports **464,** 1–70 (2008).

[68] S. Michotte, S. Mátéfi-Tempfli, L. Piraux, D. Y. Vodolazov, and F. M. Peeters, "Condition for the occurrence of phase slip centers in superconducting nanowires under applied current or voltage," Phys. Rev. B **69,** 094512 (2004).

[69] B. Petukhov and V. Chechetkin, "Rate of penetration of a magnetic flux into type-II superconductors," Zh. Eksp. Teor. Fiz **65,** 1653–1657 (1973).

[70] L. Burlachkov, "Magnetic relaxation over the Bean-Livingston surface barrier," Physical Review B **47,** 8056 (1993).

[71] D. Feinberg, "Vortex lines in layered superconductors. I. From 3D to 2D behaviour," Journal de Physique III **4,** 169–208 (1994).

[72] H. Guo, C. L. Phillips, T. Peterka, D. Karpeyev, and A. Glatz, "Extracting, tracking, and visualizing magnetic flux vortices in 3D complex-valued superconductor simulation data," IEEE Transactions on Visualization and Computer Graphics **22,** 827–836 (2015).

[73] I. Sadovskyy, A. Koshelev, A. Glatz, V. Ortalan, M. Rupich, and M. Leroux, "Simulation of the vortex dynamics in a real pinning landscape of YBa 2 Cu 3 O 7- δ coated conductors," Physical Review Applied **5,** 014011 (2016).

[74] H. Guo, T. Peterka, and A. Glatz, "In situ magnetic flux vortex visualization in time-dependent Ginzburg-Landau superconductor simulations," In *2017 IEEE Pacific Visualization Symposium (PacificVis)*, pp. 71–80 (2017).

[75] E. Zhakina *et al.*, "Vortex motion in reconfigurable three-dimensional superconducting nanoarchitectures," arXiv preprint arXiv:2404.12151 (2024).

[76] S. Posen, N. Valles, and M. Liepe, "Radio Frequency Magnetic Field Limits of Nb and Nb_3Sn," Phys. Rev. Lett. **115,** 047001 (2015).

[77] Y. Trenikhina, S. Posen, A. Romanenko, M. Sardela, J.-M. Zuo, D. L. Hall, and M. Liepe, "Performance-defining properties of Nb3Sn coating in SRF cavities," Superconductor Science and Technology **31,** 015004 (2017).

[78] J. Lee, S. Posen, Z. Mao, Y. Trenikhina, K. He, D. L. Hall, M. Liepe, and D. N. Seidman, "Atomic-scale analyses of Nb3Sn on Nb prepared by vapor diffusion for superconducting radiofrequency cavity applications: a correlative study," Superconductor Science and Technology **32,** 024001 (2018).

[79] U. Pudasaini, G. V. Eremeev, J. W. Angle, J. Tuggle, C. E. Reece, and M. J. Kelley, "Growth of Nb3Sn coating in tin vapor-diffusion process," Journal of Vacuum Science & Technology A **37,** 051509 (2019).

[80] J. Lee, Z. Mao, K. He, Z. H. Sung, T. Spina, S.-I. Baik, D. L. Hall, M. Liepe, D. N. Seidman, and S. Posen, "Grain-boundary structure and segregation in Nb3Sn coatings on Nb for high-performance superconducting radiofrequency cavity applications," Acta Materialia **188,** 155–165 (2020).

[81] S.-H. Oh, D. Seol, Y.-J. Jeong, S.-H. Na, J. Kim, W.-S. Ko, J. B. Jeon, and B.-J. Lee, "Diffusion in A15 Nb3Sn: An atomistic study," Acta Materialia **234,** 118050 (2022).

[82] C. Becker, S. Posen, N. Groll, R. Cook, C. M. Schlepütz, D. L. Hall, M. Liepe, M. Pellin, J. Zasadzinski, and T. Proslier, "Analysis of Nb3Sn surface layers for superconducting radio frequency cavity applications," Applied Physics Letters **106,** 082602 (2015).

[83] E. Viklund, J. Lee, D. Seidman, and S. Posen, "Three-Dimensional Reconstruction of Nb3Sn Films by Focused Ion Beam Cross Sectional Microscopy," IEEE Transactions on Applied Superconductivity 33 (2023), cited by: 0.

[84] J. K. Freericks, A. Y. Liu, A. Quandt, and J. Geerk, "Nonconstant electronic density of states tunneling inversion for A15 superconductors: Nb_3Sn," Phys. Rev. B **65,** 224510 (2002).

[85] W. Markiewicz, "Elastic stiffness model for the critical temperature Tc of Nb3Sn including strain dependence," Cryogenics **44,** 767–782 (2004).

[86] M. G. T. Mentink, M. M. J. Dhalle, D. R. Dietderich, A. Godeke, F. Hellman, and H. H. J. ten Kate, "The effects of disorder on the normal state and superconducting properties of Nb3Sn," Superconductor Science and Technology **30,** 025006 (2016).

[87] M. M. Kelley, N. S. Sitaraman, and T. A. Arias, "Ab initio theory of the impact of grain boundaries and substitutional defects on superconducting Nb_3Sn," Superconductor Science and Technology **34,** 015015 (2020).

[88] A. E. Koshelev, I. A. Sadovskyy, C. L. Phillips, and A. Glatz, "Optimization of vortex pinning by nanoparticles using simulations of the time-dependent Ginzburg-Landau model," Phys. Rev. B **93,** 060508 (2016).

[89] I. Sadovskyy, A. Koshelev, C. Phillips, D. Karpeyev, and A. Glatz, "Stable large-scale solver for Ginzburg–Landau equations for superconductors," Journal of Computational Physics **294,** 639–654 (2015).

[90] M. P. Sørensen, N. F. Pedersen, and M. Ögren, "The dynamics of magnetic vortices in type II superconductors with pinning sites studied by the time dependent Ginzburg–Landau model," Physica C: Superconductivity and its Applications **533,** 40–43 (2017).

[91] S. J. Chapman, C. M. Elliott, A. K. Head, S. D. Howison, F. M. Leslie, J. R. Ockendon, J. Deang, Q. Du, M. Gunzburger, and J. Peterson, "Vortices in superconductors: modelling and computer simulations," Philosophical Transactions of the Royal Society of London. Series A: Mathematical, Physical and Engineering Sciences **355,** 1957–1968 (1997).

[92] A. Al Luhaibi, A. Glatz, and J. B. Ketterson, "Driven responses of periodically patterned superconducting films," Phys. Rev. B **106,** 224516 (2022).

[93] V. L. Ginzburg and L. D. Landau, in *On Superconductivity and Superfluidity: A Scientific Autobiography* (Springer Berlin Heidelberg, Berlin, Heidelberg, 2009), pp. 113–137.

[94] Q. Du, M. D. Gunzburger, and J. S. Peterson, "Analysis and Approximation of the Ginzburg–Landau Model of Superconductivity," SIAM Review **34,** 54–81 (1992).

[95] Q. Du, "Global existence and uniqueness of solutions of the time-dependent ginzburg-landau model for superconductivity," Applicable Analysis **53,** 1–17 (1994).

[96] C. Geuzaine and J.-F. Remacle, "Gmsh: A 3-D finite element mesh generator with built-in pre-and post-processing facilities," International journal for numerical methods in engineering **79,** 1309–1331 (2009).

[97] M. Tinkham, "Viscous Flow of Flux in Type-ii Superconductors," Phys. Rev. Lett. **13,** 804–807 (1964).

[98] H. London, "Production of heat in supraconductors by alternating currents," Nature **133,** 497–498 (1934).

[99] J. Halbritter, "On surface resistance of superconductors," Zeitschrift für Physik **266,** 209–217 (1974).

[100] J. Turneaure, J. Halbritter, and H. Schwettman, "The surface impedance of superconductors and normal conductors: The Mattis-Bardeen theory," Journal of Superconductivity **4,** 341–355 (1991).

[101] D. C. Mattis and J. Bardeen, "Theory of the anomalous skin effect in normal and superconducting metals," Physical Review **111,** 412 (1958).

[102] A. Abrikosov, L. Gor'Kov, and I. Khalatnikov, "A superconductor in a high frequency field," Sov. Phys. JETP **35,** 182 (1959).

[103] A. Gurevich, "Theory of RF superconductivity for resonant cavities," Superconductor Science and Technology **30,** 034004 (2017).

[104] A. Gurevich and T. Kubo, "Surface impedance and optimum surface resistance of a superconductor with an imperfect surface," Phys. Rev. B **96,** 184515 (2017).

[105] B. Aune *et al.*, "Superconducting TESLA cavities," Phys. Rev. ST Accel. Beams **3,** 092001 (2000).

[106] N. Sitaraman, "Private Correspondence,", 2025.

[107] M. G. T. Mentink, M. M. J. Dhalle, D. R. Dietderich, A. Godeke, W. Goldacker, F. Hellman, and H. H. J. ten Kate, "Towards analysis of the electron density of states of Nb3Sn as a function of strain," AIP Conference Proceedings **1435,** 225–232 (2012).

[108] E. Viklund, D. N. Seidman, D. Burk, and S. Posen, "Improving Nb3Sn Cavity Performance Using Centrifugal Barrel Polishing,", 2023.

[109] T. Proslier, J. F. Zasadzinski, L. Cooley, C. Antoine, J. Moore, J. Norem, M. Pellin, and K. E. Gray, "Tunneling study of cavity grade Nb: Possible magnetic scattering at the surface," Applied Physics Letters **92,** 212505 (2008).

[110] T. Kubo and A. Gurevich, "Field-dependent nonlinear surface resistance and its optimization by surface nanostructuring in superconductors," Phys. Rev. B **100,** 064522 (2019).

[111] S. Isagawa, "Influence of hydrogen on superconducting niobium cavities," Journal of Applied Physics **51,** 6010–6017 (1980).

[112] S. Isagawa, "Hydrogen absorption and its effect on low-temperature electric properties of niobium," Journal of Applied Physics **51,** 4460–4470 (1980).

[113] N. Jisrawi, M. Ruckman, T. Thurston, G. Reisfeld, M. Weinert, M. Strongin, and M. Gurvitch, "Reversible depression in the T c of thin Nb films due to enhanced hydrogen adsorption," Physical Review B **58,** 6585 (1998).

[114] J. Knobloch, "The "Q disease" in superconducting niobium RF cavities," In *AIP Conference Proceedings*, **671,** 133–150 (2003).

[115] F. Barkov, A. Romanenko, and A. Grassellino, "Direct observation of hydrides formation in cavity-grade niobium," Phys. Rev. ST Accel. Beams **15,** 122001 (2012).

[116] F. Barkov, A. Romanenko, Y. Trenikhina, and A. Grassellino, "Precipitation of hydrides in high purity niobium after different treatments," Journal of Applied Physics **114,** 164904 (2013).

[117] A. Romanenko, F. Barkov, L. D. Cooley, and A. Grassellino, "Proximity breakdown of hydrides in superconducting niobium cavities," Superconductor Science and Technology **26,** 035003 (2013).

[118] A. Romanenko, C. J. Edwardson, P. G. Coleman, and P. J. Simpson, "The effect of vacancies on the microwave surface resistance of niobium revealed by positron annihilation spectroscopy," Applied Physics Letters **102,** 232601 (2013).

[119] D. C. Ford, L. D. Cooley, and D. N. Seidman, "Suppression of hydride precipitates in niobium superconducting radio-frequency cavities," Superconductor Science and Technology **26,** 105003 (2013).

[120] A. Grassellino, A. Romanenko, D. Sergatskov, O. Melnychuk, Y. Trenikhina, A. Crawford, A. Rowe, M. Wong, T. Khabiboulline, and F. Barkov, "Nitrogen and argon doping of niobium for superconducting radio frequency cavities: a pathway to highly efficient accelerating structures," Superconductor Science and Technology **26,** 102001 (2013).

[121] M. Checchin and A. Grassellino, "High-field Q-slope mitigation due to impurity profile in superconducting radio-frequency cavities," Applied Physics Letters **117,** 032601 (2020).

[122] P. Dhakal, "Nitrogen doping and infusion in SRF cavities: A review," Physics Open **5,** 100034 (2020).

[123] R. D. Veit, R. G. Farber, N. S. Sitaraman, T. A. Arias, and S. J. Sibener, "Suppression of nano-hydride growth on Nb(100) due to nitrogen doping," The Journal of Chemical Physics **152,** 214703 (2020).

[124] M. Wenskat, J. Čižek, M. O. Liedke, M. Butterling, C. Bate, P. Haušild, E. Hirschmann, A. Wagner, and H. Weise, "Vacancy-Hydrogen Interaction in Niobium during Low-Temperature Baking," Scientific Reports **10,** 8300 (2020).

[125] T. Spina, A. Grassellino, and A. Romanenko, "Internal Friction Measures to Study Precipitates Formation in EP and N-Doped Bulk Nb for SRF Applications,", 2021.

[126] X. Fang, J.-S. Oh, M. Kramer, A. Romanenko, A. Grassellino, J. Zasadzinski, and L. Z. and, "Understanding mechanism of performance improvement in nitrogen-doped niobium superconducting radio frequency cavity," Materials Research Letters **11,** 108–116 (2023).

[127] Y. Tamashevich, A. Prudnikava, A. Matveenko, A. Neumann, O. Kugeler, and J. Knobloch, "Improved RF performance of niobium cavities via in-situ vacuum heat treatment technique," Superconductor Science and Technology **38,** 045006 (2025).

[128] J. Hauck, "Ordering of hydrogen in niobium hydride phases," Acta Crystallographica Section A: Crystal Physics, Diffraction, Theoretical and General Crystallography **33,** 208–211 (1977).

[129] J. S. Langer, "Statistical theory of the decay of metastable states," Annals of Physics **54,** 258–275 (1969).

[130] R. Sundararaman, K. Letchworth-Weaver, K. A. Schwarz, D. Gunceler, Y. Ozhabes, and T. A. Arias, "JDFTx: Software for joint density-functional theory," SoftwareX **6,** 278–284 (2017).

[131] J. P. Perdew, K. Burke, and M. Ernzerhof, "Generalized Gradient Approximation Made Simple," Physical Review Letter **77,** 3865–3868 (1996).

[132] K. F. Garrity, J. W. Bennett, K. M. Rabe, and D. Vanderbilt, "Pseudopotentials for high-throughput DFT calculations," Computational Materials Science **81,** 446–452 (2014).

[133] N. Marzari and D. Vanderbilt, "Maximally localized generalized Wannier functions for composite energy bands," Physical review B **56,** 12847 (1997).

[134] F. Giustino, M. L. Cohen, and S. G. Louie, "Electron-phonon interaction using Wannier functions," Physical Review B—Condensed Matter and Materials Physics **76,** 165108 (2007).

[135] R. Sundararaman, P. Narang, A. S. Jermyn, W. A. Goddard III, and H. A. Atwater, "Theoretical predictions for hot-carrier generation from surface plasmon decay," Nature communications **5,** 5788 (2014).

[136] A. M. Brown, R. Sundararaman, P. Narang, W. A. Goddard III, and H. A. Atwater, "Ab initio phonon coupling and optical response of hot electrons in plasmonic metals," Physical Review B **94,** 075120 (2016).

[137] G. Eliashberg, "Interactions between electrons and lattice vibrations in a superconductor," Sov. Phys. JETP **11,** 696–702 (1960).

[138] W. McMillan, "Transition temperature of strong-coupled superconductors," Physical Review **167,** 331 (1968).

[139] R. E. Ricker and G. R. Myneni, "Evaluation of the propensity of niobium to absorb hydrogen during fabrication of superconducting radio frequency cavities for particle accelerators," Journal of research of the National Institute of Standards and Technology **115,** 353 (2010).

[140] A. V. Harbick and M. K. Transtrum, "A Time-Dependent Ginzburg-Landau Framework for Sample-Specific Simulation of Superconductors for SRF Applications,", 2025.

[141] N. S. Sitaraman, Ph.D. thesis, Cornell University, 2022.

[142] D. Bafia, P. Berrutti, B. Giaccone, A. Grassellino, D. Neuffer, S. Posen, and A. Romanenko, "R+D Towards High Gradient CW SRF Cavities," JACoW (2022).

[143] M. Liepe, Private communication (2023).

[144] A. Larkin and Y. Ovchinnikov, "Nonlinear conductivity of superconductors in the mixed state," Sov. Phys. JETP **41,** 960–965 (1975).

[145] L. V. Keldysh, "Diagram technique for nonequilibrium processes," Zh. Eksp. Teor. Fiz. **47,** 1515–1527 (1964).

[146] U. Eckern and G. Schön, "Relaxation processes in superconductors," Journal of Low Temperature Physics **32,** 821–838 (1978).

[147] G. T. Gilbert, "Positive Definite Matrices and Sylvester's Criterion," The American Mathematical Monthly **98,** 44–46 (1991).

[148] J. Peatross, "Advancing the Maximum Accelerating Gradient of Niobium-3 Tin Superconducting Radiofrequency Accelerator Cavities: RF Measurements, Dynamic Temperature Mapping, and Material Growth," Ph.D. dissertation (Cornell University, Ithaca, N.Y., 2021).

[149] M. Jönsson, R. Vedin, S. Gyger, J. A. Sutton, S. Steinhauer, V. Zwiller, M. Wallin, and J. Lidmar, "Current Crowding in Nanoscale Superconductors within the Ginzburg-Landau Model," Phys. Rev. Appl. **17,** 064046 (2022).

[150] N. W. Ashcroft and N. D. Mermin, *Solid State Physics* (Holt, Rinehart and Winston, New York, 1976).

[151] T. E. Oseroff, Ph.D. thesis, Cornell University, 2022.

[152] K. Maki, "On persistent currents in a superconducting alloy. II," Progress of Theoretical Physics **29,** 333–340 (1963).